Electrically Assisted Propulsion & Power Systems for Short-Range Missions

Electrification of a Conventional Airbus A320neo

Sheng Chien Tan | 1507907

TU Delft

nlr

Electrically Assisted Propulsion & Power Systems for Short-Range Missions

Electrification of a Conventional Airbus A320neo

by

Sheng Chien Tan

in partial fulfillment of the requirements for the degree of

Master of Science
in Aerospace Engineering

at the Delft University of Technology,
to be defended publicly on Thursday 12 April, 2018 at 01:00 PM.

Student number:	1507907	
Thesis committee:	Dr. Arvind G. Rao,	TU Delft, chair and supervisor
	Drs. Wim Lammen,	NLR, supervisor
	Dr. Jianning Dong,	TU Delft, member
	Dr. ir. Roelof Vos	TU Delft, member

This thesis is confidential and cannot be made public until Thursday 12 April, 2018.

An electronic version of this thesis is available at: http://repository.tudelft.nl/.

Faculty of Aerospace Engineering · Delft University of Technology

Abstract

Over the last 50 years, the global airline industry has seen resilient growth in demand for passenger travel; this trend is expected to continue in the coming decades. With kerosene being the predominant source used as jet fuel, this increase in air traffic is expected to result in the depletion of non-renewable fossil fuels and undesired climate changes on a global scale. Therefore, the industry is currently exploring the electrification of aircraft taking into account advanced concepts such as more electric aircraft (MEA) and hybrid electric propulsion systems. This thesis addresses a combination of these two concepts characterised as an electrically assisted propulsion & power system (EAPPS). This system integrates a conventional turbofan engine with a network of electrical components, providing assistance to the aircraft propulsion and non-propulsive power systems. This secondary electrical system can be activated throughout the flight mission to assist the turbofan engine and increase the overall system efficiency. The amount of electrical power relative to the total power is defined as the power split ratio.

The objective of this study is to evaluate how gradual modifications in this EAPPS affect the overall performance of an Airbus A320neo (new engine option) aircraft in a short-range mission of 1,000 km. The proposed changes include the conversion to an electrical architecture of the non-propulsive power systems, the implementation of a fuel cell system, the installation of photovoltaic panels on the outer skin of the aircraft and the downscaling of the turbofan engine. To analyse these effects accordingly, two separate simulation models were developed within the MATLAB® environment to perform and verify a series of trade studies at two different time frames: near future (2020+) and far future (2040+).

The results revealed that each modification proved to be advantageous in terms of overall fuel and energy consumption; however, turning the A320neo into a MEA is the most effective approach. The inclusion of fuel cell and photovoltaic systems brings minor benefits, but also increases the complexity of the system. Nonetheless, the derived optimal setups for the 2020+ and 2040+ scenarios feature all modifications, but with a different power management strategy and engine scaling.

The optimal power management strategy for 2020+ includes fully electric taxiing, a take-off power split ϕ_{takeoff} of 17%, a climb power split ϕ_{climb} of 9% and a downscaled engine of 90%. Compared to the conventional A320neo, this setup will lower the fuel and energy consumption by 17% and 13%, correspondingly. Also, the CO_2 emissions are reduced by 16%. By 2040+, the optimal take-off power split ϕ_{takeoff} increases to 26% and the climb power split ϕ_{climb} to 43%. This allows the CFM LEAP-1A engine to be scaled down to 85%. The total relative savings of fuel, energy and CO_2 emissions equal 28%, 18% and 27%, respectively. The impact of the projected technological development in a time period of 20 years, from 2020+ to 2040+, is witnessed through the increased use of electrically assisted propulsion and significant greater amounts saved with respect to fuel, energy and engine emissions.

I dedicate this work to my father, Song Beng Tan,
who once had the dream of becoming an aerospace engineer.
Ultimately, a series of personal events stood in his way of achieving this goal.
To give him a sense of fulfillment in addition to my utmost respect,
I will complete this graduate degree on his behalf.

Preface

This thesis has been written to fulfill the graduation requirements of the Flight Performance & Propulsion track in the Aerospace Engineering MSc programme at the Delft University of Technology. The majority of the study was carried out during my internship at the Netherlands Aerospace Centre (NLR) in Amsterdam. I was engaged in conducting research and writing this thesis report from January 2017 to March 2018.

I am genuinely grateful to all the people that were involved in this study. In particular, I would like to thank my supervisors, Arvind Rao and Wim Lammen, for their exceptional guidance, persistent support and valuable feedback throughout my research. I would also like to express my gratitude towards Toni Kanakis for making this internship happen and providing me a productive and joyful work environment at NLR. Furthermore, I would like to give thanks to my former NLR colleagues: Jos Vankan for his useful insights and discussions during internal meetings, Joey Hoogendoorn for his cooperation in developing the battery and fuel cell models, Oscar Kogenhop for his assistance with GSP® software, Edward Rademaker for providing the CFM engine models, Alte de Boer for his insightful crash course on electrical systems and Peter van der Geest for developing the aircraft performance model which became the foundation of the EAPPS module. Moreover, I would like to thank Jianning Dong and Roelof Vos for being part of my exam committee and evaluating my work.

Along with these people, I wish to thank my family and my friends for their dedicated love and encouragement throughout my life outside academia. A special thanks to Andy for introducing me to NLR and giving me the ideal opportunity to complete my Master's degree and to Dejan for being my spiritual health/life guru and continuous support throughout personal setbacks. I would also like to express my gratitude to Frank for producing stunning hard copies of my thesis. Lastly, I would like to thank my sister Ling and parents for raising me in a caring home filled with unconditional love and acceptance; you are the real MVPs.

I hope this research provides new insights into hybrid electric aviation and the use of fuel cell and photovoltaic systems in a commercial aircraft environment, bringing us one step closer towards a sustainable future.

I sincerely wish you much pleasure reading this thesis.

Sheng Chien Tan

Haarlem, 28 March 2018

Table of Contents

List of Figures

List of Tables

List of Abbreviations

a-Si:H	amorphous silicon
ABS	anti-lock braking system
ACARE	Advisory Council for Aviation Research and Innovation in Europe
AEA	all electric aircraft
APU	Auxiliary Power Unit
ASM	available seat mile
ATRU	auto transformer rectifier unit
BPR	bypass ratio
CdTe	cadmium telluride
CIGS	copper indium gallium selenide/sulphide
CO	carbon monoxide
CO_2	carbon dioxide
c-Si	crystalline silicon
DFL	departure fuel load
DOC	direct operating costs
DOD	depth of discharge
DPL	design payload
DST	daylight saving time
EAPPS	electrically assisted propulsion & power system
EASA	European Aviation Safety Agency
ECS	Environmental Control System
ECTFE	ethylene chlorotrifluoroethylene
E & E	electronics and engineering
EGT	exhaust gas temperature
EGTS	Electric Green Taxiing System
EI	emissions index
EIA	Energy Information Administration
emf	electromotive force
EMS	energy management system
EOT	equation of time
FAA	Federal Aviation Administration
FBW	fly-by-wire
FF	fill factor

GaAs	gallium arsenide
GaINP	gallium indium phosphide
Ge	germanium
GHG	greenhouse gas
GSP®	Gas turbine Simulation Programme
H_2O	water vapour
HEPS	hybrid electric propulsion system
HP	high pressure
HPC	high pressure compressor
HPT	high pressure turbine
ICAO	International Civil Aviation Organization
ICE	internal combustion engine
IOC	indirect operating costs
IPM	Interior Permanent Magnet
IPS	Ice Protection System
ISA	International Standard Atmosphere
KIAS	Knots-Indicated Air Speed
LC	longitudinal correction
LCT	local clock time
Li-air	lithium-air
Li-ion	lithium-ion
Li-Po	lithium-polymer
Li-S	lithium-sulphur
LP	low pressure
LPC	low pressure compressor
LPT	low pressure turbine
LTO	landing and take-off
MEA	more electric aircraft
MM	mission mass
MPL	maximum payload
MPPT	maximum power point tracking
mono-Si	monocrystalline silicon
MTOM	maximum take-off mass
MZFM	maximum zero-fuel mass
NASA	National Aeronautics and Space Administration
neo	new engine option
NGV	nozzle guide vane
NiCd	nickel-cadmium
NiMH	nickel-metal hydride
NLR	Netherlands Aerospace Centre
NO_x	nitrogen oxide
NREL	National Renewable Energy Laboratory
O&M	operations and maintenance
OEM	operational empty mass
OPR	overall pressure ratio
PBW	power-by-wire
pc	Peukert constant
PEMFC	polymer electrolyte membrane fuel cell
PP	payback period

poly-Si	polycrystalline silicon
PV	photovoltaic
PVDF	polyvinylidene fluoride
ROI	Return on Investment
RPM	revolutions per minute
SFC	specific fuel consumption
slpm	standard litre per minute
SN	smoke number
SOC	state of charge
SOFC	solid oxide fuel cell
SO_x	sulphur oxide
SPM	Surface Permanent Magnet
SPS	SimPowerSystems
SRM	switched reluctance motor
STC	Standard Test Conditions
TeDP	Turbo-electric Distributed Propulsion
TiSD	Technology in Sustainable Development
TOC	total operating costs
UHC	unburnt hydrocarbon
US$	U.S. dollar
UTRC	United Technologies Research Center

List of Symbols

Greek Symbols

$\alpha_{I_{sc}}$	Temperature coefficient at short-circuit current [A/°C]
$\alpha_{V_{oc}}$	Temperature coefficient at open-circuit voltage [V/°C]
α	Angle of attack [rad]
α	Charge transfer coefficient [-]
α	Partial pressure of hydrogen [Pa]
β	Inclination angle of PV panels [rad]
β	Partial pressure of oxygen [Pa]
Δ	Change
Δ	Shape factor of electric motor [-]
δ	Partial pressure of water [Pa]
δ	Pressure ratio [-]
δ	Solar declination angle [rad]
$\dot{\gamma}$	Time derivative of flight path angle [rad/s]
$\dot{\varphi}$	Time derivative of bank angle [rad/s]
$\dot{\psi}$	Time derivative of heading angle [rad/s]
ε	Orbital eccentricity of the Earth [-]
η_{cell}	Photovoltaic cell efficiency [-]
$\eta_{elec,fc}$	Electrical efficiency of fuel cell [-]
η_F	Faradaic efficiency [-]
η_h	Packing density of hexagonal lattice [-]
η_{motor}	Motor efficiency [-]
η_{pv}	PV system efficiency [-]
η_{th}	Thermodynamic efficiency [-]
η_V	Voltaic efficiency [-]
γ	Azimuth angle [rad]
γ	Flight path angle [rad]
λ_{H_2}	Hydrogen stoichiometry [-]

μ_f	Fuel utilisation coefficient [-]
μ_{roll}	Rolling resistance coefficient [-]
μ	Magnetic permeability [H/m]
ω_b	Base rotational speed [rad/s]
$\omega_{max,LP}$	Maximum rotational speed of low pressure spool [rad/s]
ω_p	Critical rotational speed [rad/s]
ω	Hour angle [rad]
ω	Rotational speed [rad/s]
Φ_{fc}	Fuel cell power ratio [-]
φ	Bank angle [rad]
φ	Latitude angle [rad]
ψ	Heading angle [rad]
$\rho_{A,pv}$	Area mass density of solar skin [kg/m^2]
ρ_{mat}	Material density [kg/m^3]
σ_{disc}	Stress acting on the disc [N/m^2]
$\phi_{approach}$	Power split ratio during approach [-]
ϕ_{climb}	Power split ratio during climb [-]
ϕ_{cruise}	Power split ratio during cruise [-]
$\phi_{descent}$	Power split ratio during descent [-]
$\phi_{landing}$	Power split ratio during landing [-]
$\phi_{takeoff}$	Power split ratio during take-off [-]
ϕ_{taxiin}	Power split ratio during taxi-in [-]
$\phi_{taxiout}$	Power split ratio during taxi-out [-]
ϕ	Power split ratio, degree of hybridisation [-]
τ	Solar attenuation factor due to atmosphere [-]
θ	Incidence angle of incoming solar irradiance [rad]
θ	Temperature ratio [-]

Latin Symbols

$\bar{p}_{electricmotor}$	Specific power of electric motor [W/kg]
$\bar{p}_{fc}$	Specific power of fuel cell system [W/kg]
$\bar{p}_{inv}$	Specific power of inverter [W/kg]
$\dot{h}$	Time derivative of altitude [m/s]
$\dot{m}_{f,supp}$	Supplied fuel flow rate [kg/s]
$\dot{m}_{f,used}$	Used fuel flow rate [kg/s]
$\dot{m}_f$	Fuel flow rate [kg/s]
$\dot{m}_{H_2}$	Fuel flow rate of hydrogen [kg/s]
$\dot{m}$	Mass flow [kg/s]
$\dot{V}$	Time derivative of velocity [m/s^2]
$\dot{x}_{east}$	Time derivative of relative aircraft position towards the East [m/s]
$\dot{x}_{north}$	Time derivative of relative aircraft position towards the North [m/s]
A_{cell}	Exponential voltage coefficient of battery cell [V]
A_{cell}	Fuel cell area [m^2]

A_{disc}	Circumferential disc area [m^2]
$a_{landing}$	Acceleration during landing phase [m/s^2]
a_{mean}	Mean major axis length of the ellipse [m]
A_{pack}	Exponential voltage coefficient of battery pack [V]
A_{stack}	Total fuel cell stack area [m^2]
A_s	Specific electric loading [A-con/m]
$a_{takeoff}$	Acceleration during take-off phase [m/s^2]
a_{taxi}	Acceleration during taxi phase [m/s^2]
A	Exponential voltage coefficient [V]
A	Tafel slope [-]
a	Major axis length of the ellipse [m]
B_0	Initial guess vector for curve fitting battery data
B_v	Final vector for curve fitting battery data
B_{cell}	Exponential capacity coefficient of battery cell [1/Ah]
b_{mean}	Mean minor axis length of the ellipse [m]
$B_{p,0}$	Peak magnetic flux of hFan engine [T]
B_{pack}	Exponential capacity coefficient of battery pack [1/Ah]
B_p	Peak magnetic flux [T]
B	Exponential capacity coefficient [1/Ah]
B	Magnetic field [T]
b	Minor axis length of the ellipse [m]
c_0	Initial guess vector for curve fitting fuel cell data
C_{D_0}	Zero-lift drag coefficient [-]
$C_{D_{flaps}}$	Drag coefficient due to flap extension [-]
$C_{D_{gear}}$	Drag coefficient due to landing gear [-]
$C_{D_{mach}}$	Drag coefficient due to increased Mach numbers (compressibility) [-]
C_D	Drag coefficient [-]
C_{L_0}	Lift coefficient at zero angle of attack [-]
C_{L_α}	Lift curve slope [1/rad]
C_L	Lift coefficient [-]
C	Charge rate [1/h]
c	Final vector for curve fitting fuel cell data
d_n	Day of the year [-]
D_g	Ground drag [N]
D_r	Rotor diameter [m]
$D_{s,hFan}$	Stator diameter of hFan engine [m]
D_s	Stator diameter [m]
D	Drag [N]
D	Motor diameter [m]
E_0	Fuel cell potential at open-circuit conditions [V]
E_{batt}	Energy supplied by battery system [Wh]
e_{batt}	Specific energy of battery [Wh/kg]
E	Electromotive force [V]

E	Fuel cell voltage [V]
F_c	Centrifugal force [N]
$F_{N_{takeoff}}$	Thrust force at take-off [lbf]
f_s	Frequency [Hz]
F_{thrust}	Aircraft thrust [N]
F	Faraday constant [C/mol]
F	Lorentz force [N]
G_{op}	Operating irradiance [W/m^2]
G_{ref}	Nominal irradiance at Standard Test Conditions [W/m^2]
g	Air gap length [m]
g	Gravitational constant [m/s^2]
h_{cell}	Height of a single PV cell [m]
h	Altitude [m]
h	Arc length of the ellipse [m]
I_0	Diode reverse saturation current [A]
I_0	Peak phase current [A]
i_0	Exchange current density [A/m^2]
i_Δ	Limiting current density [A/m^2]
I_b	Current through battery (positive for discharge, negative for charge) [A]
I_{cell}	Photovoltaic cell current [A]
I_d	Diode current [A]
I_{fc}	Fuel cell current [A]
i_{max}	Maximum operating current [A]
$I_{mpp,cell}$	Photovoltaic cell current at maximum power point [A]
$I_{mpp,pv}$	Photovoltaic system current at maximum power point [A]
I_{op}	Operating current [A]
$I_{ph,ref}$	Reference photoelectric current of PV cell [A]
I_{ph}	Phase current [A]
I_{ph}	Photoelectric current [A]
I_{pv}	Operating current of PV system [A]
$I_{rat,cell}$	Rated discharge current of battery cell [A]
$I_{rat,pack}$	Rated discharge current of battery pack [A]
I_{rat}	Rated discharge current [A]
$I_{sc,cell}$	Short-circuit current of PV cell [A]
$I_{sc,ref}$	Reference short-circuit current of PV cell [A]
$I_{sc,system}$	Short-circuit current of PV system [A]
I_{sc}	Short-circuit current [A]
I_{stack}	Fuel cell stack current [A]
I	Current [A]
i	Current density [A/m^2]
i	Instantaneous time of the day, local solar time [h]
K_{cell}	Polarisation coefficient of battery cell [V]
K_c	Classical eddy current loss coefficient [$W/Hz^{1.5}\ T^{1.5}\ kg$]

K_e	Excess eddy current loss coefficient [W/Hz^2 T^2 kg]
K_h	Hysteresis loss coefficient [W/Hz^2 T^2 kg]
K_{pack}	Polarisation coefficient of battery pack [V]
K_t	Torque coefficient [Nm/A]
K_v	Voltage coefficient [V $\cdot$ s/rad]
K	Polarisation coefficient [V]
k	Induced drag factor [-]
k	Stefan Boltzmann's constant [J/K]
L_{curve}	Length of the curvature [m]
L_{EEbay}	Length of E & E bay [m]
$L_{fuse,eff}$	Effective fuselage length [m]
L_f	Length of magnetic field [m]
L_{motor}	Motor length [m]
L	Length of the wire [m]
L	Lift [N]
$m_{aircraft,init}$	Initial aircraft mass [kg]
$m_{aircraft,MZFM}$	Maximum zero-fuel mass [kg]
m_{batt}	Battery system mass [kg]
m_{batt}	Number of battery cells in parallel [-]
m_{cables}	Cable mass [kg]
$m_{conversion}$	Mass due to conversion to MEA [kg]
M_{cruise}	Cruise Mach number [-]
$m_{electricsystem}$	Electrical system mass [kg]
m_{engine}	Engine mass [lbs]
m_{fc}	Fuel cell system mass [kg]
m_{fuel}	Fuel mass [kg]
M_{H_2}	Molar mass of hydrogen [g/mol]
$m_{inv,batt}$	Inverter mass of battery system [kg]
$m_{inv,fc}$	Inverter mass of fuel cell system [kg]
$m_{inv,pv}$	Inverter mass of photovoltaic system [kg]
$m_{inverters}$	Mass of the inverters [kg]
m_i	Mass of the pollutant i [g]
m_{motor}	Mass of electric motor [kg]
$m_{pv,cell}$	Number of PV cells in parallel [-]
$m_{pv,module}$	Number of PV modules in parallel [-]
$m_{pv,total}$	Total number of PV cells in parallel [-]
m_{pv}	Photovoltaic system mass [kg]
m_{stack}	Number of fuel cells stacked in parallel [-]
M_{STP}	Molar mass at STP conditions [L/mol]
M_{ToC}	Mach number during Top of Climb phase [-]
M_{ToD}	Mach number during Top of Descent phase [-]
M	Mach number [-]
m	Aircraft mass [kg]

m	Concentration loss coefficient [V]
m	Number of phases in the electric motor [-]
n_{batt}	Number of battery cells in series [-]
n_{bear}	Number of bearings in the electric motor [-]
N_{fc}	Total number of fuel cells in fuel cell system [-]
$N_{max,hFan}$	Maximum rotational speed of hFan engine [rad/s]
N_{max}	Maximum rotational speed [rad/s]
N_{op}	Operating rotational speed [rad/s]
N_{pack}	Total number of cells in battery pack [-]
$n_{pv,cell}$	Number of PV cells in series [-]
$n_{pv,module}$	Number of PV modules in series [-]
$n_{pv,total}$	Total number of PV cells in series [-]
N_{pv}	Number of cells in PV system [-]
n_r	Number of rotors in the switched reluctance motor [-]
$n_{s,6/4SRM}$	Number of stators for a 6/4 SRM [-]
n_{stack}	Number of fuel cells stacked in series [-]
n_s	Number of stators in the switched reluctance motor [-]
N	Normal force [N]
N	Number of data points [-]
N	Number of windings in the electric motor [-]
N	Rotational speed [rpm]
n	Day number [-]
n	Diode ideality factor [-]
n	Exponential concentration loss coefficient [1/A]
n	Number of electrons [-]
p_0	Cubic polynomial coefficient [1/Ah]
p_1	Cubic polynomial coefficient [A]
p_2	Cubic polynomial coefficient [Ah]
p_3	Cubic polynomial coefficient [Ah^2]
P_{copper}	Copper losses [W]
$P_{electricmotor}$	Power provided by the electric motor [W]
$P_{electric}$	Electrical power [W]
P_{engine}	Turbofan engine power [W]
P_{fc}	Fuel cell power [W]
$P_{friction}$	Friction losses [W]
$P_{in,pv}$	Input power of the PV cell [W]
p_{inlet}	Inlet pressure [Pa]
P_{iron}	Iron losses [W]
$P_{loss,total}$	Total power losses [W]
P_{max}	Maximum power output of electric motor [W]
$P_{mpp,cell}$	Maximum power output of PV cell [W]
$P_{mpp,pv}$	Maximum power output of PV system [W]
P_{net}	Net power of fuel cell stack [W]

P_{op}	Operating power [W]
p_{op}	Operating pressure [Pa]
$P_{out,pv}$	Output power of the PV cell [W]
P_{pv}	Power generated by PV system [W]
p_{ref}	Reference pressure [Pa]
P_{total}	Total power [W]
$P_{windage}$	Windage losses [W]
P	Power [W]
p	Aircraft roll rate [rad/s]
Q_b	Nominal battery capacity [Ah]
q_{dyn}	Dynamic pressure [N/m^2]
Q_{pv}	Incoming solar irradiance [W/m^2]
$Q_{rat,cell}$	Rated capacity of battery cell [Ah]
$Q_{rat,pack}$	Rated capacity of battery pack [Ah]
Q_{rat}	Rated battery capacity [Ah]
q	Elementary charge [C]
R_0	Motor winding resistance [Ω]
R_b	Battery internal resistance [Ω]
R_{cell}	Internal resistance of battery cell [Ω]
r_m	Mean radius of the Earth [m]
r_{ohmic}	Area specific resistance of fuel cell [Ω/m^2]
R_{pack}	Internal resistance of battery pack [Ω]
$r_{perturn}$	Resistance per turn [mΩ]
R_p	Shunt resistance [Ω]
R_{stack}	Internal resistance of fuel cell stack [Ω]
R_s	Absolute reflectance of the stained filter material [-]
R_s	Series resistance [Ω]
$R_{wire,perturn}$	Wire resistance per turn [Ω]
R_w	Absolute reflectance of the clean filter material [-]
R	Universal gas constant of ideal gases [$J/K\dot{m}ol$]
r	Actual distance between the Earth and the Sun [m]
r	Area specific internal resistance of fuel cell [Ω/m^2]
$S_{cell,eff}$	Effective PV cell area [m^2]
$S_{cell,total}$	Total area of single PV cell [m^2]
$S_{fuse,eff}$	Total effective fuselage area [m^2]
$S_{pv,eff}$	Total effective surface area for PV panels [m^2]
$S_{tail,eff}$	Total effective tailplane area [m^2]
$S_{wing,eff}$	Total effective wing area [m^2]
S	Wing area [m^2]
T_A	Torque at point A [Nm]
T_B	Torque at point B [Nm]
T_{inlet}	Inlet temperature [K]
T_{op}	Operating temperature [K]

T_{ph}	Number of turns per phase [-]
T_{ref}	Reference temperature [K]
T_{ref}	Temperature at Standard Test Conditions [K]
t_{solar}	Solar time [h]
T_{t41}	Temperature at the nozzle guide vanes [K]
T_{t45}	Exhaust gas temperature [K]
T	Thrust [N]
T	Torque [Nm]
T	Transmittance of PV panels [-]
t	Time [h]
$V_{0,cell}$	Nominal voltage of battery cell [V]
$V_{0,pack}$	Nominal voltage of battery pack [V]
V_0	Battery nominal voltage [V]
V_{act}	Activation loss [V]
$V_{approach}$	Velocity during approach phase [m/s]
V_b	Battery terminal voltage [V]
V_{cell}	Photovoltaic cell voltage [V]
V_{climb1}	Velocity during first climb phase [m/s]
V_{climb2}	Velocity during second climb phase [m/s]
V_{conc}	Concentration loss [V]
$V_{descent1}$	Velocity during first descent phase [m/s]
$V_{descent2}$	Velocity during second descent phase [m/s]
V_{EEbay}	Volume of E & E bay [m^3]
V_{fc}	Fuel cell voltage [V]
V_{max}	Maximum operating voltage [V]
$V_{mpp,cell}$	Photovoltaic cell voltage at maximum power point [V]
$V_{mpp,pv}$	Photovoltaic system voltage at maximum power point [V]
$V_{nom,cell}$	Nominal voltage of battery cell [V]
$V_{nom,pack}$	Nominal voltage of battery pack [V]
$V_{oc,cell}$	Open-circuit voltage of PV cell [V]
$V_{oc,ref}$	Reference open-circuit voltage of PV cell [V]
$V_{oc,system}$	Open-circuit voltage of PV system [V]
V_{oc}	Open-circuit voltage [V]
V_{ohmic}	Ohmic loss [V]
V_{pv}	Operating voltage of PV system [V]
V_{stack}	Fuel cell stack voltage [V]
$V_{T_{cell}}$	Thermal cell voltage [V]
$V_{takeoff}$	Velocity during take-off phase [m/s]
V_{wind}	Wind velocity [m/s]
V	Velocity [m/s]
V	Voltage [V]
v	Wire velocity relative to the magnetic field [m/s]
w_{cell}	Width of a single PV cell [m]

W	Weight [N]
x_{east}	Relative position of the aircraft towards the East [m]
x_{north}	Relative position of the aircraft towards the North [m]
x	Independent variable matrix
y	Dependent variable vector

Subscripts

act	Activation
approach	Approach phase
A	Area
A	Point A
batt	Battery
bear	Bearing
B	Point B
b	Battery
cables	Cables
cell	Battery cell
cell	Photovoltaic cell
climb	Climb phase
conc	Concentration
conversion	Conversion
copper	Copper
cruise	Cruise phase
curve	Curvature
descent	Descent phase
dyn	Dynamic
D	Drag
d	Diode
east	East
EEbay	E & E bay
eff	Effective
electricmotor	Electric motor
electricsystem	Electrical system
elec	Electrical
engine	Turbofan engine
fc	Fuel cell system
friction	Friction
fuse	Fuselage
F	Faradaic
f	Fuel
f	Magnetic field
g	Ground
H_2	Hydrogen

h	Hexagonal lattice
init	Initial
inlet	Inlet
inverters	Total inverters
inv	Inverter
in	Input
iron	Iron
L_0	Lift at zero angle of attack
L_α	Lift curve slope
landing	Landing phase
loss	Loss
LP	Low pressure
L	Lift
mass	Mass
mat	Material
max	Maximum
mean	Mean value
module	Module
motor	Electric motor
mpp	Maximum power point
m	Mean
nom	Nominal
north	North
oc	Open-circuit
ohmic	Ohmic
op	Operating
out	Output
pack	Battery pack
ph	Phase
ph	Photoelectric
pv	Photovoltaic
p	Peak
rat	Rated
ref	Reference
roll	Rolling resistance
r	Rotor
sc	Short-circuit
solar	Solar
stack	Fuel cell stack
supp	Supplied
s	Stator
tail	Tailplane
takeoff	Take-off phase

taxiin	Taxi-in phase
taxiout	Taxi-out phase
thrust	Thrust
th	Thermodynamic
ToC	Top of Climb phase
ToD	Top of Descent phase
total	Total
used	Used
V	Voltaic
windage	Windage
wind	Wind
wing	Wing
wire	Wire

CHAPTER 1

Introduction

This chapter presents the research problem, the aim of this study and its methodologies to accomplish the objective. The main challenge of future aviation remains lessening its impact on the natural environment and the consumption of non-renewable fossil fuels. Current trends in the aircraft industry point towards the increased use of electrical power; the electrification of commercial aircraft can serve as a solution to this problem and will be discussed here in more detail.

First of all, the rationale for hybrid electric aviation and its underlying problems will be discussed in Section 1.1. From this, a research objective can be defined in Section 1.2, along with a list of secondary objectives. In Section 1.3, the scope and significance of this study will be briefly described. The research methods and procedure used to carry this project to a successful end will be presented in Section 1.4. Lastly, an outline of this thesis report will be covered in Section 1.5.

1.1 Problem Definition

In response to the ever-growing aviation industry and its impact on the natural environment, ambitious goals for future aviation have been set by the global aerospace industry. First introduced in the automotive sector and now making its way to the aviation industry, hybrid electric propulsion systems (HEPS) have been identified as a potential solution. These concepts attempt to reduce fuel consumption and emissions of traditional combustion engines through hybridisation via electrical energy sources. Another visible trend in this industry is the electrification of aircraft subsystem architectures; more electric aircraft (MEA), e.g. the Airbus A350 or the Boeing 787 Dreamliner, feature advanced electrically powered subsystems instead of conventional hydraulic and pneumatic counterparts.

Given the current state of technology, it is unlikely that electric flight can flourish in the present moment. Especially the specific power and energy values required for the electrical system impose a huge problem; such topologies will only become viable in the far future. It is expected that traditional gas turbines will play a crucial role in aircraft propulsion, possibly in combination with electric motors. HEPS cover a huge range of architectures. This thesis focuses on a pragmatic approach towards HEPS, coined as an electrically assisted propulsion & power system (EAPPS). An EAPPS can be defined as a coherent system which integrates a combustion engine with a network of electrical components, providing assistance to the aircraft propulsion and non-propulsive power systems via an electric motor and energy devices, respectively. This electrical network includes, but is not limited to: electric motors,

generators, power electronics, batteries, cables, fuel cell and photovoltaic systems. This EAPPS concept will serve as a stepping stone towards the realisation of fully electric aircraft.

1.2 Research Aim and Objectives

A former study has focused on the power management of HEPS in an A320 aircraft environment; the choice in power management strategy, along with the maturity level of electric technology, appear to be crucial for the feasibility of HEPS in commercial aviation [1, 2].

The purpose of this study is to extend this knowledge on HEPS applied in commercial aircraft. The main objective of the research project is to gradually assess the effects of several system modifications on fuel and energy consumption as well as engine emissions. When applying EAPPS, the following changes are taken into account: electrification of non-propulsive power systems, incorporating emerging technologies such as fuel cell systems or photovoltaics and engine scaling. Such modifications within a HEPS environment have not been addressed yet in current literature and thus provide new insights into the realm of hybrid electric propulsion, in the context of single-aisle commercial aircraft. Furthermore, a more in-depth analysis, by means of detailed modelling, is performed on the involved electrical components in order to assess the selected configurations and support the system sizing. The resulting EAPPS configuration and its associated electrical system can then be optimised with respect to fuel, energy and emission savings.

In order to realise this goal, a number of secondary objectives are formulated. These include but are not limited to:

- Identify the most suitable photovoltaic and fuel cell technologies for aircraft applications
- Find the optimal flight route based on available solar irradiance and sun hours
- Develop a flight mission analysis tool to simulate the performance of an A320neo hybrid electric aircraft with the aforementioned modifications
- Analyse the effect of these changes on the overall performance of the A320neo aircraft for a specified mission profile
- Find and validate well-known methods to model the dynamics of the electrical system and its individual components (i.e. electric motor, PV system, fuel cell system and batteries)
- Develop an energy management optimisation tool to accommodate the power demand of the aircraft and its subsystems
- Compare the results and define the optimised EAPPS configuration with power management strategy
- Identify the fuel, energy and emission savings with respect to the conventional A320neo aircraft
- Perform a sustainable impact assessment of the optimised EAPPS configuration

1.3 Research Scope

To keep this project manageable without missing any significant factors, several assumptions will be chosen carefully. The reference aircraft is an A320neo with a defined mission range of 1,000 km carrying the maximum capacity of 190 passengers. This range is supported by a sensitivity analysis that investigated the fuel savings of a HEPS-integrated aircraft as a function of mission length [1]. Beyond this range of 1,000 km, the additional electrical system will be carried over a longer distance, yielding increased fuel consumption and thus reduced benefits from HEPS [1]. The aircraft geometry will remain the same for all variations of the EAPPS and the components that make up this system will be based on technologies projected to be available in the near future (2020+) and the far future (2040+).

For this research, a full mission analysis is performed; each individual segment throughout flight will be considered. However, the most important segments are the take-off and the climb, where the turbofan engine will be assisted by an electric motor. The total required shaft power will be split between the conventional and electric components based on the chosen power management strategy. This, in turn, affects the fuel flow and battery discharge rate of the system.

The propulsion system used is a twin-spool turbofan engine; it will remain unaltered for the reference configuration, but scaled down accordingly for the hybrid electric configurations. Since the engine plays a key role in the overall aircraft efficiency, the secondary power off-takes for the aircraft subsystems will also be taken into account and analysed how this affects the engine performance. If traditional subsystems such as the Environmental Control System (ECS) and the Ice Protection System (IPS) are replaced by electrical counterparts, bleed air off-takes can be entirely eliminated at the cost of increased electrical power. In addition, conversion losses introduced by the generator as well as the generator mass can be avoided, if the electrical power is directly supplied by batteries; the results of this trade-off will be covered in this study. Keep in mind that detailed modelling of these aircraft subsystems (e.g. cabin thermal loads, heating requirements for de-icing, etc.) is beyond the scope of this project, electrical power requirements and other relevant data will be derived from existing literature.

All in all, the focus of the study will be on the overall performance and energy management of the Airbus A320neo equipped with EAPPS. The main purpose is to showcase the technical feasibility of different technologies with HEPS and determine whether this synergistic approach brings additional benefits. Cost and reliability aspects are not yet taken into account, as a proof of concept needs to be presented first. As stated before, integrating HEPS with other electrical components to form a co-operative system known as an EAPPS has not been documented yet in today's literature; this research will hopefully provide a better understanding of such systems and fill in this knowledge gap.

1.4 Research Methodology

For the majority of the time, the research project will be carried out at the Netherlands Aerospace Centre (NLR) in Amsterdam. The computing software MATLAB® and its integrated Simulink® environment will primarily be used for developing the aircraft flight performance model and the optimisation methods in the EAPPS module. To simulate the dynamics of the propulsion system, the internally developed Gas turbine Simulation Programme (GSP®) will be coupled to the simulation model. In addition, a separate model, the energy management system (EMS) module, will be built to replicate the dynamic behaviour of several components within an electrical system, for a more detailed analysis of these components.

The initial simulation model is able to analyse the performance of the reference aircraft, the Airbus A320neo. In addition, it supports hybridisation of the propulsive power by integrating electric

components and the associated power management control strategy based on a former study [1, 2]. Afterwards, various modifications will be introduced individually into the EAPPS simulation model: electrification of conventional subsystems, addition of fuel cell systems and the installation of PV panels. This arrangement can then be optimised through changes in the power management strategy and resizing the engine. Afterwards, the aircraft emissions will be modelled to analyse the environmental impact of the optimised configuration. To assess the assumptions used for the electrical system in the EAPPS module and provide additional insight into system behaviour, a more detailed EMS module will be developed separately, including the optimisation and sizing of the battery system. The implementation of these two simulation models for modelling the A320neo with EAPPS is discussed thoroughly in Section 3.11.

Ultimately, the result of this project will be two different simulation models. The first one is the EAPPS module, capable of comparing the performance of the reference aircraft with a conventional engine to the performance of the same aircraft with an EAPPS configuration; a parallel HEPS setup with several modifications including the electrification of conventional aircraft subsystems, installation of PV panels on the outer skin, addition of a complete fuel cell system and engine scaling. The second one is the EMS module and can evaluate the dynamic behaviour of the electrical system and find the optimal battery configuration that can provide the necessary electrical power to the aircraft propulsion and non-propulsive power systems.

1.5 Thesis Outline

The structure of the report is as follows: Chapter 2 will provide the essential background information to understand the basic concept of HEPS. Other associated topics such as the environmental impact of aviation and the electrification of aircraft as well as promising PV and fuel cell technologies for aircraft applications will also be discussed. Then, in Chapter 3, a thorough description of each individual system component and an overview of the two simulation models developed in this study will be given: one for the mission analysis (EAPPS module) and one for the energy management of the electrical system (EMS module). The development of both these modules will be explained comprehensively in Chapter 4 and Chapter 5, respectively; these include the model assumptions, the modelling approaches and all the validation and verification procedures performed. After running a series of trade studies with different EAPPS setups, the most important results and discoveries will be presented in Chapter 6. Also, additional insights will be given in separate discussion sections. Finally, in Chapter 7, the report will conclude with an extensive summary of all the important findings and a number of recommendations for future research regarding EAPPS.

CHAPTER 2

Background Information

This chapter introduces the topic of hybrid electric propulsion systems (HEPS) and its potential to bridge the gap between conventional and fully electric aircraft. Other subjects discussed include the environmental impact of aviation, the electrification of aircraft as well as potential applications of photovoltaics and fuel cell technologies in an aircraft environment. The information presented is mainly derived from previous literature research; the full literature survey can be accessed through Ref. [3].

Firstly, the environmental issues caused by the aircraft industry will be discussed in Section 2.1. Then, a short summary of HEPS and previous research work is given in Section 2.2. This is followed by the electrification of aviation in Section 2.3 and which challenges need to be faced to realise electric aircraft in the future. Two emerging technologies that are considered for an electrically assisted propulsion & power system (EAPPS), photovoltaics and fuel cell systems, will be described thoroughly in Section 2.4 and Section 2.5, respectively.

2.1 Environmental Impact of Aviation

Environmental issues such as air pollution have always been at the forefront of people's minds. The aircraft industry is one of the major contributors to air pollution and due to its rapid growth, it raises extra concern. Both leading aircraft manufacturers, Airbus and Boeing, predict that air travel will double in growth over the next twenty years [4, 5]; this is illustrated in Figure 2.1. Figure 2.1a shows that with an annual growth of 4.5%, the total global air traffic will double by the year 2030, with respect to the year 2015. Figure 2.1b illustrates how Boeing will expand from 22,510 airplanes in 2015 to an in-service fleet of 45,240 by 2035; note that 43% of the new airplanes will be used to replace older models.

With this in mind, the environmental impact caused by the aircraft industry should be investigated thoroughly. At current unsustainable rates of fossil fuel consumption, the non-renewable resources will inevitably run out. Aside from depletion, burning these fossil fuels brings undesired climate changes on a global scale. Aircraft engines generate thrust by accelerating air backwards. This is done by combusting a mixture of air and fuel, which releases heat, gases, particulates and noise; the most important greenhouse gases (GHGs) and particles include carbon dioxide (CO_2), nitrogen oxide (NO_x), water vapour (H_2O), soot and sulphate aerosols.

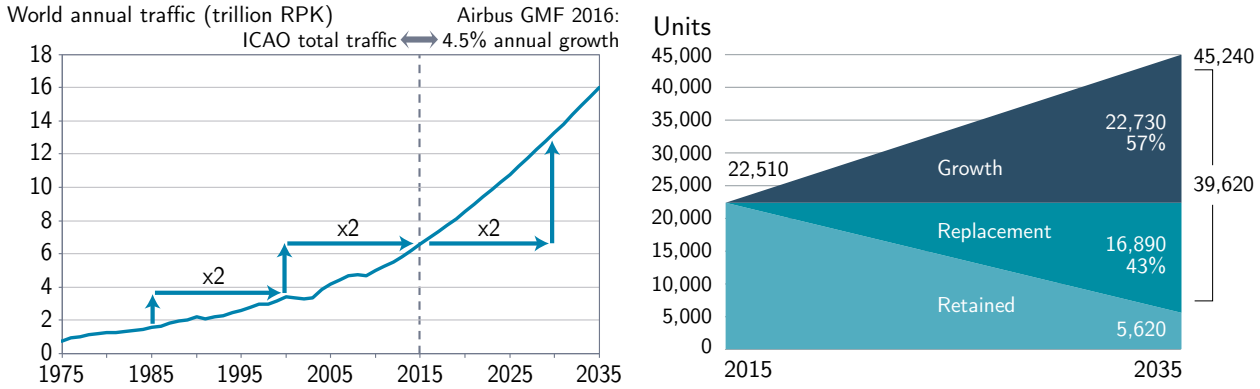

(a) Prediction of air traffic growth by Airbus [4].

(b) Prediction of fleet development by Boeing [5].

Figure 2.1: Global aviation forecast by the leading aircraft manufacturers.

To prevent escalation of environmental impact by the ever-increasing demand for aviation, challenging targets have been set by the Advisory Council for Aviation Research and Innovation in Europe (ACARE). The goals of Flightpath 2050 for future aviation are compared to the capabilities of typical new aircraft in 2000 and can be summarised as follows [6]:

- 75% reduction in CO_2 emissions per passenger kilometre
- 90% reduction in NO_x emissions
- 65% reduction in perceived noise emissions of flying aircraft
- emission-free aircraft movements when taxiing

Likewise, National Aeronautics and Space Administration (NASA) has set goals for future generations of advanced aircraft in the near, mid and far term (2015, 2025 and 2035) for which technologies should be ready by 2015, 2020 and 2025, correspondingly. Table 2.1 provides an overview of these targets for the next generations, also known as N+1, N+2 and N+3 [7–9].

Table 2.1: Goals set by NASA for future generation subsonic fixed wing aircraft [9].

Corners of the trade space	**N+1 (2015)[1] next generation tube-wing aircraft**	**N+2 (2020)[1] revolutionary hybrid wing body**	**N+3 (2025)[1] advanced aircraft concepts**
Aircraft fuel consumption[2]	- 33%	- 50%	- 60%
Noise (cumulative below Stage 4)	- 32 dB	- 42 dB	- 71 dB
LTO NO_x emissions (below CAEP 6)	- 60%	- 75%	- 80%
Cruise NO_x emissions (Relative to 2005 best in class)	- 55%	- 70%	- 80%
Aircraft field length	- 33%	- 50%	exploit metroplex concepts[3]

[1] Enabling technologies should reach TRL 4-6 by 2015, 2020 and 2025 for N+1, N+2 and N+3, respectively.
[2] Relative to a B737-800 with a CFM56/7B engine, representative of 1998 entry into service.
[3] Concepts that enable optimal use of runways at multiple airports within the metropolitan areas.

2.2 Hybrid Electric Propulsion Systems

The idea of electric propulsion is derived from the automotive industry; rapid development in battery technology has allowed a wide range of electric and hybrid electric cars to enter the global market. However, the realisation of fully electric commercial aircraft carrying hundreds of passengers is still farfetched given the current technology level. Aside from the take-off imposed power requirements, the problem of range limitation due to high battery mass impairs electric aviation even more than for ground-based transport. For this reason, the introduction of HEPS serves as an intermediate step between conventional and fully electric aircraft.

HEPS are considered to be a promising propulsion technology; the idea behind it is that the overall performance, consisting of a conventional internal combustion engine (ICE) combined with an electric motor, outweighs the individual performance of each component [10, 11]. Since less thrust is required by the engine, a reduction in emissions can be expected. Also, the ICE design is no longer dictated by the take-off phase, if additional thrust is provided by the electric motor, and could be optimised for the longer cruise phase, resulting in a smaller, more fuel efficient engine.

Figure 2.2 presents various electric propulsion arrangements. Different hybrid electric architectures depend on how the combustive and electric parts are combined: series (Figure 2.2a), parallel (Figure 2.2b) or a combination of both series and parallel (Figure 2.2c). The last option often results in more complex and heavier systems, far outside the scope of this project; therefore, this setup will not be considered. In a series configuration, the propeller fan is solely connected to an electric motor, which is consecutively driven by electrical power from an additional turbo generator. In a parallel configuration, the power comes from both the ICE and the electric motor, which is powered by a battery or any other energy storage device. These two will be further discussed in Section 2.2.1. The turbo-electric architectures are quite similar to the HEPS setups; the partial and full turbo-electric systems (Figure 2.2d and Figure 2.2e) are essentially the series-parallel and series hybrid setups without the use of batteries. These architectures cannot be installed on existing aircraft without a radical change in design, so these setups will not be discussed any further. The all electric architecture (Figure 2.2f) is the quintessential goal for future aviation and completely removes its dependence on kerosene, allowing zero emissions.

2.2.1 Trade-Off Study of Hybrid Electric Propulsion Systems

To perform this trade-off study, the advantages and disadvantages of the series and parallel HEPS architectures will be briefly described.

In a series HEPS configuration, the combustion engine is connected to a generator which converts mechanical into electrical power. Subsequently, the generated power is used to drive the fan through an electric motor. The advantage of series HEPS is that the engine is mechanically decoupled from the fan. This allows the engine to operate at an optimal RPM during the whole flight mission. The downside is an increased system weight due to the additional generator. Furthermore, this arrangement has the freedom to position the engine and fan separately from each other. This permits revolutionary aircraft configurations such as Turbo-electric Distributed Propulsion (TeDP), where a number of high-power electric motors drive a continuous array of propelling fans [9]. Distributed propulsion is being considered as a possible solution to increase aircraft efficiency, reduce fuel burn and lower emissions; however, further clarification is beyond the scope of this study.

In a parallel HEPS configuration, an electric motor is used to convert electrical power into mechanical power. This power provided by the motor is then added to the mechanical shaft power provided by the engine, which drives a fan. In a parallel configuration, the power supplied comes from both the ICE and the electric motor; therefore, each component can operate independently as well as together

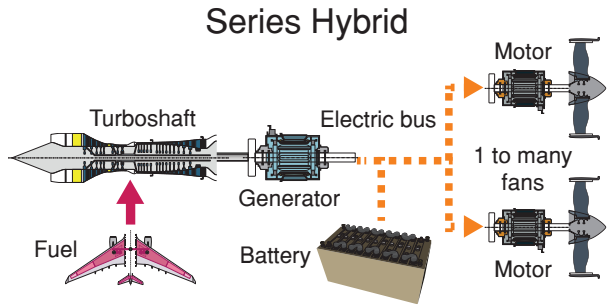

(a) Series hybrid electric propulsion.

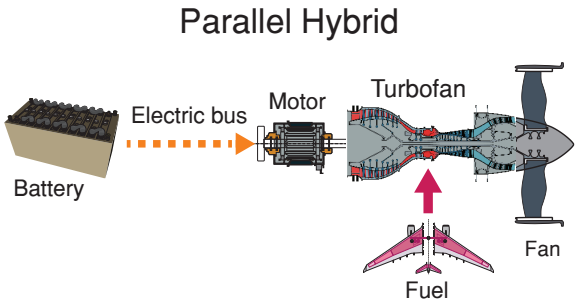

(b) Parallel hybrid electric propulsion.

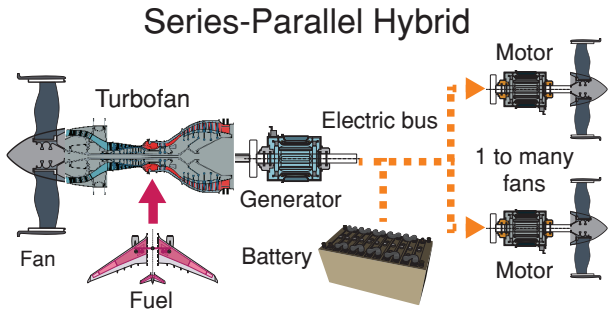

(c) Series-parallel hybrid electric propulsion.

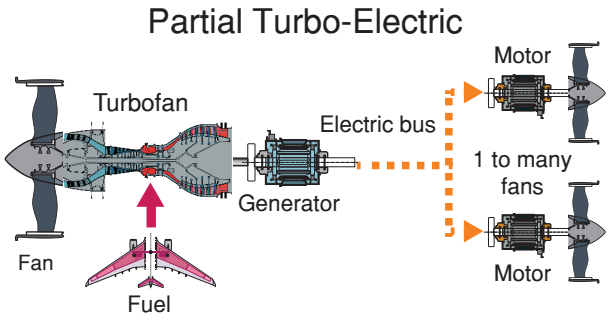

(d) Partial turbo-electric propulsion.

Figure 2.2: Different electric propulsion architectures; adapted from [12].

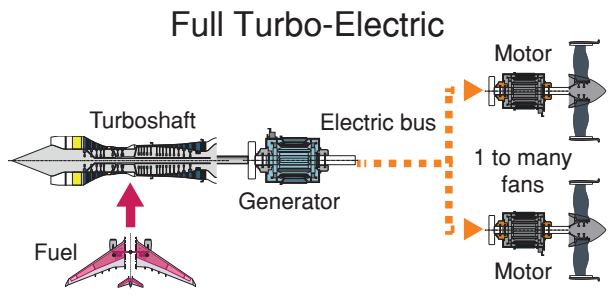

(e) Full turbo-electric propulsion.

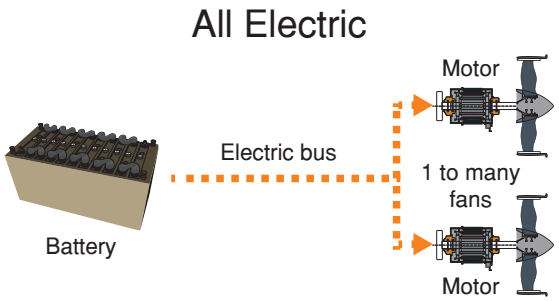

(f) All electric propulsion.

Figure 2.2: Different electric propulsion architectures; adapted from [12].

[13]. This arrangement also allows the power ratio between the two subsystems to be adjusted during operation. A major disadvantage of this layout is that the engine cannot operate at an optimal RPM throughout the whole flight mission, since it is mechanically linked to the fan [10].

Since parallel HEPS also offers the option of retrofitting on existing aircraft, this setup will be chosen for further investigation.

2.2.2 Degree of Hybridisation

Regardless of the selected electric propulsion architecture, the degree of hybridisation and accompanying power management strategy are crucial to the overall effectiveness of such a system. The degree of

hybridisation, or the power split ratio, is the percentage of electrical power available to the total power and non-linear in relation to the performance of the propulsion system; this is formulated in Equation 2.1.

$$\phi = \frac{P_{electric}}{P_{total}} \tag{2.1}$$

The power management strategy regulates when and how much electrical power will be supplied to the propulsion system during each flight phase. For instance, Ref. [2] concludes that the most optimal and feasible power management strategy for a parallel HEPS setup features a take-off power split of 24.9%, a climb power split of 13.6% and a downscaled engine of 90%; fuel savings of 7.5% can be achieved.

Despite the projected fuel savings of 7.5%, the target of 80% fuel savings by 2025 in Table 2.1 is still far from being reached. Hence, new advances in system configuration and propulsion integration are necessary to realise this sustainable future. To pave the way for this, a more synergistic approach is taken. The integration of photovoltaics and fuel cells into HEPS as well as the electrification of conventional subsystems could potentially change the metagame of aviation. This system is characterised as an EAPPS and will be the key focus of this study.

2.3 Electrification of Future Aircraft

In order to reach the realm of fully electric passenger aircraft in the next future, a crucial step change is required to commercialise this type of aircraft, both for propulsive and non-propulsive systems. New aircraft arrangements such as more electric aircraft (MEA) and HEPS are gently introduced to the aviation market; both these configurations strengthen the development of future electric aviation. These systems contribute to the environmental targets addressed in Section 2.1 and lower operating costs: more efficient and reliable power, low to zero emissions (depending on how electrical energy is generated), reduced noise and lower maintenance costs [14, 15].

2.3.1 Main Challenges of Electric Aircraft

One of the key challenges for electric aircraft is to realise the high power-to-mass ratios required in heavy machinery such as motors and generators. This is crucial to compete with conventional aircraft in terms of weight, flight performance and range. Current gas turbine engines hold specific power values in the range of 3-8 kW/kg. Only with advanced superconducting technology can conventional electric motors and generators surpass the power-to-mass ratios of today's gas turbines [16, 17]. Based on the assumption that the expected specific power values of superconductive cables and protection devices are greater than those of superconductive motors and generators, the system mass is more susceptible to the sizing of motors and generators than the sizing of the cables and protection devices [18]. By increasing system redundancy via additional cabling, the oversizing of motor and generator components may be reduced; significant mass reductions can be achieved.

It should be noted that a superconducting network needs to be kept at a specific temperature, requiring the use of a cryogenic cooling system which will add additional mass and power requirements to the system. Failure in the network or the cooling system can lead to system quenching, inducing a sudden loss of power to supply the propulsion motors and consequently jeopardise the safety of the aircraft [9]. Other mass considerations include the addition of redundant Auxiliary Power Units (APUs) for reliability and devices for monitoring system components to avoid electromagnetic interference due to the use of high-voltage DC [17, 19].

Another challenging task is the required storage of electrical energy in the form of batteries. In this context, only secondary batteries, which are rechargeable, are considered. A battery is rated in terms of its capacity, the amount of electric charge stored. The total battery energy, in watt hours, is the product of the capacity and voltage. The specific energy and energy density, measured in watt hours per kilogram and litre respectively, as well as specific peak power, measured in watts per kilogram, are important parameters in aircraft applications. Current energy storage devices used in the aircraft industry include lead-acid, nickel-cadmium (NiCd), nickel-metal hydride (NiMH), lithium-ion (Li-ion) and lithium-polymer (Li-Po) [20]. Several key characteristics of these batteries are summarised in Table 2.2.

Table 2.2: Key characteristics of current batteries in aircraft applications [20].

Parameter	Lead-acid	NiCd	NiMH	Li-ion	Li-Po
Specific energy [Wh/kg]	33 - 40	40 - 60	30 - 80	160	130 - 200
Energy density [Wh/L]	50 - 100	50 - 150	140 - 300	270	300
Specific power [W/kg]	80 - 300	200 - 500	250 - 1,000	1,800	2,800
Recharge time [h]	8 - 16	1	2 - 4	2 - 3	2 - 4
Life cycles	300	500	500 - 1,000	1,200	$>$ 1,000
Nominal voltage [V]	2	1.2	1.2	3.6	3.7

These batteries are acceptable as a means of energy storage in current conventional aircraft, but suffice no longer in advanced HEPS and all electric aircraft (AEA) applications. Even if Li-ion and Li-Po battery technologies reach their theoretical ceiling of 200-250 Wh/kg [21]; these specific energy values are still insufficient for future state-of-the-art aircraft concepts.

In order to realise these required specific energy and power targets, new promising lithium technologies have been introduced. The first one being lithium-sulphur (Li-S); the proven specific energy of 250-300 Wh/kg already exceed the theoretical limit of conventional batteries. Researchers predict potential specific energies of 500-1,500 Wh/kg for Li-S batteries, provided that challenges like poor life cyclability, self-discharge, capacity loss and high discharge currents will be overcome [21–24]. OXIS Energy, leading manufacturer of rechargeable Li-S batteries, has already commercialised Li-S batteries with a specific energy of 300 Wh/kg and are planning to push this boundary to 500 Wh/kg by 2020 [25]. Another promising battery technology is lithium-air (Li-air). The theoretical specific energy is equal to 11,680 Wh/kg, which is close to the specific energy of gasoline (around 13,000 Wh/kg) [26]. However, practical limits of specific energy lie between the range of 750 Wh/kg and 2,000 Wh/kg [27, 28].

An overview of current and projected characteristics regarding these lithium technologies can be found in Table 2.3. Note that no commercial Li-air batteries have been developed so far and it is still unclear whether the practical issues associated with these devices can be overcome [24]. Hence, the speculative values of Li-air for 2030 may have a larger margin of error than those of Li-S.

Table 2.3: Future developments regarding Li-S and Li-air batteries [25, 28–31].

	Li-S			Li-air	
Parameter	Current	2020	2030	Current	2030
Specific energy [Wh/kg]	250 - 300	500 - 600	800 - 1,500	$>$ 400	500 - 2,000
Energy density [Wh/L]	200	550	-	-	1,000
Specific power [W/kg]	2,800	-	$>$ 11,000	-	400 - 460

2.3.2 Aircraft Non-Propulsive Power Systems and Architectures

Conventional versus Electrical Architectures

The conventional aircraft integrates a number of subsystems, usually driven by a combination of different power types: pneumatic, mechanical, hydraulic and electrical power. The gas turbines provide all the power required for these subsystems. This power, which is separate from propulsive power, is often referred to as non-propulsive or secondary power [32]. An overview of the different power sources, along with the associated subsystems, is given in Table 2.4.

Table 2.4: Forms of power sources in conventional aircraft; adapted from [33, 34].

Power source type	Associated subsystems
Pneumatic	Environmental Control System (ECS), Ice Protection System (IPS)
Mechanical	Engine generators, hydraulic pumps, lubrication oil and fuel pumps
Hydraulic	Actuation & Flight Control Systems (AFCS), Landing Gear System (LGS)
Electrical	Avionics, Commercial Cabin Systems (CCS)

Currently, engines installed on a commercial aircraft supply these secondary power off-takes in two ways: shaft power and bleed air. Shaft power can be extracted from either the low or high pressure turbine shaft to drive a gear box; this is connected to hydraulic pumps and a generator providing electrical power. Bleed air can be extracted from different compressor stages and has two main purposes: cooling the internal parts of the engine and providing hot pressurised air for the IPS and ECS subsystems [35]. This conventional framework is mapped on the left side of Figure 2.3.

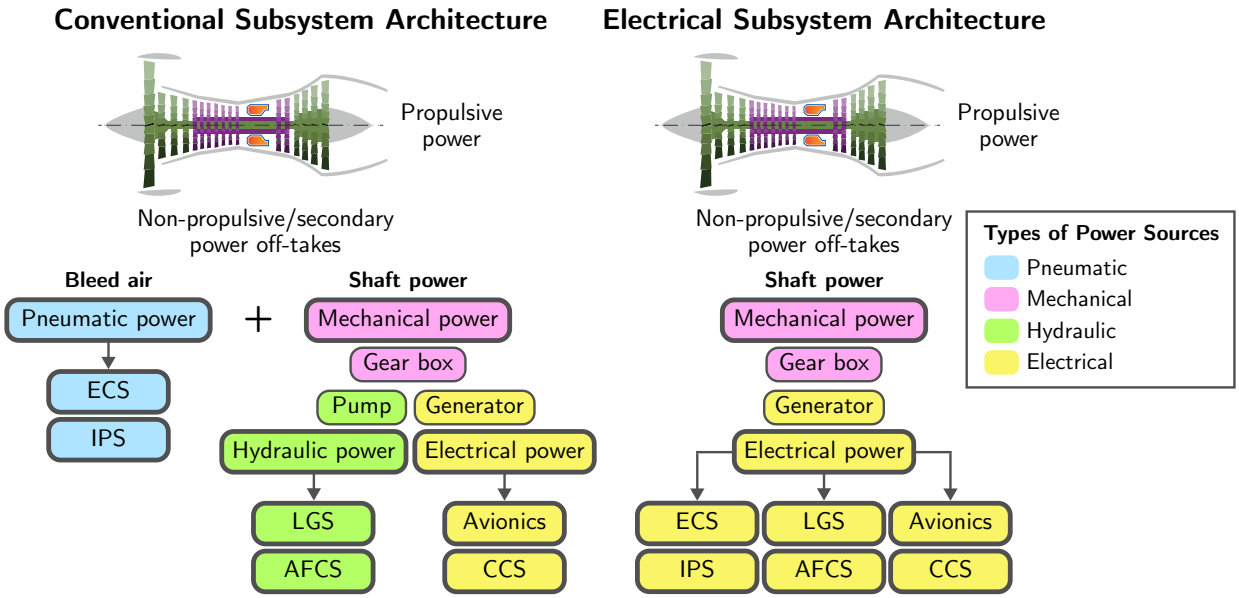

Figure 2.3: Transition from conventional to electrical subsystem architecture; adapted from [36].

The conventional subsystem architecture has proven to be reliable and effective in the past few decades. Inevitably, this conventionalism has reached its point of technology saturation; while modern commercial aviation seeks better and more advanced systems, large improvements in energy efficiency are no longer attainable in this outdated configuration. Rapid developments in power electronics and electric drives have allowed the focus to shift towards electrical architectures. Benefits of this more-electric approach

include higher component efficiencies due to the absence of conversion losses, reduction in overall system mass as well as lower operating and maintenance costs.

To make it clear within this study, a more electric aircraft (MEA) is defined as an aircraft which has several or all conventional mechanical, hydraulic and pneumatic subsystems replaced by electrical counterparts, while an AEA refers to an aircraft which also features fully electric propulsion. The main differences between the MEA and conventional aircraft can be summarised as follows: elimination of bleed air off-take, electric start of main engines and enhanced power generation capacity [33, 34]. The principal idea behind a MEA architecture is to replace the three individual mechanical, hydraulic and pneumatic secondary power systems with one electrical system, optimised for the entire aircraft [37]; this setup is shown on the right in Figure 2.3. Electrical power is the only type of power that could be utilised for all systems. This transition marks the end of a traditional 'fly-by-wire (FBW)' era towards the beginning of a new 'power-by-wire (PBW)' era.

Electrification of Aircraft Subsystems

Based on current conventional commercial aircraft, the following non-electric components or subsystems can be replaced with an electrical counterpart [17, 19, 38]:

- *Wing flaps*
  The flaps on the wing are currently controlled hydraulically. The hydraulic actuator of the flaps can be replaced by an electrical actuator. This component is part of the AFCS subsystem.
- *Landing gear*
  The landing gear retracts through the use of hydraulic struts with emergency extending if necessary. Each landing gear leg is equipped with a mechanical lock in both extreme positions, signalised by electro-block. Both the nose and main landing gear retraction can be controlled by electrical actuators. In emergency cases, the actuators must allow retraction. This component is considered a part of the LGS subsystem.
- *Brakes*
  The current brake system makes use of hydraulically controlled three-disk six-piston brake calipers, equipped with anti-lock braking system (ABS). The hydraulic brake system can be replaced by an electro-magnetic brake system. Also, regenerative braking can be integrated to store electrical energy when slowing down a landed airplane. This component is another part of the LGS subsystem.
- *Steering system*
  Using a hydro-mechanical cylinder, the nose landing gear can be controlled during ground movement. This cylinder is also used to prevent shimmy damping. Both functions can be replaced with electro-mechanical and electro-hydraulic actuators. Additionally, an electric drive system can be installed to move the airplane on the ground with zero pollution and minimal noise; using the engine thrust for taxiing at low speeds is inefficient and harmful to the environment. This component is also part of the LGS subsystem.
- *Environmental Control System (ECS)*
  The ECS includes the heating system as well as the pressurisation, ventilation and cooling system. Bleed air from the engines is used for powering the ECS and providing heat. The ventilation system operates by leading cold external air from the inlets through the heating system back to the cabin; the cold air is led to the mixing chamber to combine it with cabin recirculated air. The main difference lies in the heating system. In the conventional case, bleed air from the engine

is the source of hot air. In the electrical case, hot air can also be generated by heating ambient air with heat produced by fuel cells through a heat exchanger. For cooling, the same electric air conditioning cooling system can be installed: it consists of a compressor-condensation unit and two evaporators. The evaporators use ventilators to collect air from the cabin through inlets in the ceiling, cool it down and return it back to the cabin.

- *Ice Protection System (IPS)*
  The most common IPS for larger passenger aircraft is based on the bleed air system. Hot air is bled through piccolo tubes along the wings, tail and engine inlets to keep these surfaces above freezing temperatures; these sections are prone to ice accumulation and any malfunctions could lead to severe aircraft performance loss. Another method consists of a flexible rubber coating along the leading edges of the wing and control surfaces. When necessary, the pneumatic system inflates the rubber coating with compressed air to get rid of any ice buildup and then deflates again to its optimal shape. Electro-thermal and electro-impulse de-icing systems can be used to replace current practices; the former uses resistive circuits to generate heat inside the airframe structure, while the latter shatters ice by discharging a high-voltage electric current through coils inside the aircraft surface.

- *APU*
  The APU in current commercial aircraft is a gas turbine combined with a generator, usually located in the tail, that provides electricity to the entire aircraft when grounded, and pneumatic power to start the main engines. In present days, these tasks are still done by a small turbine, but in the near future it can be replaced by advanced battery or fuel cell systems.

Most of these subsystems are already installed in modern MEA such as the Airbus A380, the Airbus A350 and the Boeing 787 Dreamliner; an overview of the electrical subsystems is presented in Figure 2.4. The electrical load requirements of the aircraft depend chiefly on which subsystems are converted from mechanical, hydraulic or pneumatic power usage to electrical power usage [34].

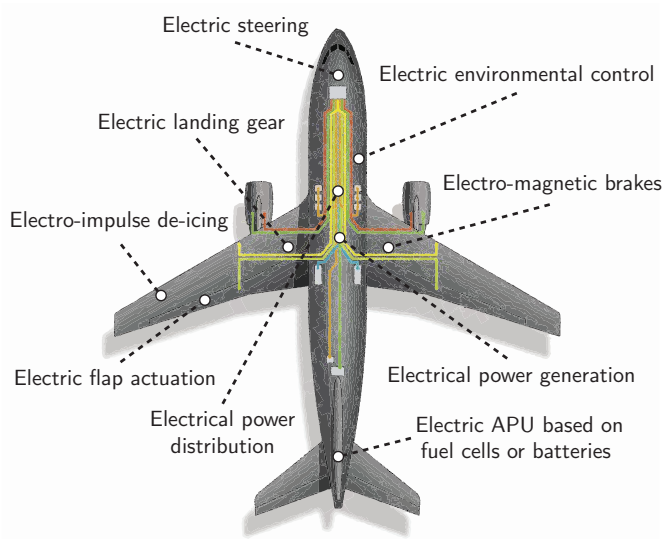

Figure 2.4: Electrical subsystems found in modern MEA; adapted from [14, 17, 37, 39].

2.3.3 Electrical Device Losses

The individual performance of the electrical machines determines the overall efficiency of the electrical system. To gain a better understanding, the various losses occuring in electrical devices will be discussed.

Power losses in electrical machines are important, because these losses ultimately determine the overall efficiency of these devices. The most common losses are briefly discussed and will be applicable to most electrical devices used in this study; electric motors, generators, power electronics, batteries, cables, etcetera.

- *Ohmic or copper losses [40]*
  Ohmic or copper loss refers to the heat produced by an electrical current flowing through a conductor; e.g. in case of an electric motor, the armature windings and in transmission cables, the wire itself. The copper loss is characterised by the following equation: $P_{copper} = I^2 \cdot R$.
- *Core or iron losses [40]*
  Core or iron losses are generally separated into two components: hysteresis loss and eddy current loss. The former occurs when a varying magnetic field is applied to a magnetic material. This leads to intermolecular friction, which in turn causes energy loss in the form of heat. The hysteresis loss increases proportionally with the maximum magnetic field. Eddy currents refer to circulating electric currents that are induced within the body of the conducting material when it is subjected to alternating magnetic fields. These currents produce power that is dissipated as heat; this waste of energy is known as eddy current loss.
- *Mechanical losses [41, 42]*
  Mechanical losses are divided into friction and windage losses. Friction loss refers to the heat generated in the bearings, bushings or brushes due to friction. In general, the frictional losses are proportional to the rotor speed. Windage loss is caused by the relative motion shearing of the fluid that flows between the rotor and stator. Windage losses are estimated as being proportional to the cube of the rotor speed.
- *Stray load losses [43]*
  Stray load losses arise from the variations in load and are difficult to measure precisely. Since the losses are relatively small compared to the others, these may be neglected. These losses include:
  - Ohmic loss due to skin effect: when an alternating current flows through a wire, the current-density tends to be higher near the skin of the wire
  - Additional core loss due to the flux from armature windings excited by load current
  - Eddy current loss in armature windings, bolts and other solid parts
  - Short-circuit loss of commutation

2.3.4 Types of Electric Motors

The basic operating principle of an electric motor is converting electrical energy via magnetic energy into kinetic energy. The first conversion from electrical to magnetic energy is based on Faraday's law of induction, shown in Equation 2.2, which describes how an electric current flowing through a wire produces a magnetic field.

$$B = \frac{N \cdot I \cdot \mu}{L_f} \tag{2.2}$$

B is the magnetic field in teslas, N is the number of windings, I is the current in amperes, μ is the magnetic permeability in henries per metre and L_f is the length of the magnetic field in metres. This magnetic field strength can be enhanced by increasing the number of windings, increasing the

current, increasing the magnetic permeability or decreasing the length of the magnetic field. The second conversion from magnetic to kinetic energy is made possible by Lorentz' force law. When a current carrying conductor is placed within a magnetic field, a Lorentz force F is created, as formulated in Equation 2.3:

$$F = B \cdot I \cdot L \tag{2.3}$$

where F is the Lorentz force in newtons, B is the magnetic field in teslas, I is the operating current in amperes and L is the length of the wire in metres. This Lorentz force can be enhanced by increasing the strength of the magnetic field, increasing the current or increasing the wire length. A wire moving relative to a magnetic field causes an electromotive force (emf), described by Equation 2.4:

$$E = B \cdot L \cdot v \tag{2.4}$$

where E is the emf in volts, B is the magnetic field in teslas, L is the length of the wire in metres and v is the wire velocity relative to the magnetic field in metres per second [44, 45]. By running a current through a wire loop in a magnetic field, the interaction of these fields will produce a twisting force, or torque, on the loop causing it to rotate. The moving component in an electric motor is called the rotor and the component that generates the force to turn this rotor is the stator. This is the basic working principle of an electric motor. A brief description of each common type of motor can be found below [46]:

- *AC commutator motor*
  These types make use of commutators, which periodically reverse the current direction of the rotor to maintain a uni-directional torque.
- *AC synchronous motor*
  The synchronous motor is characterised by the rotating speed being equal to the synchronous speed. This speed is determined by the frequency and number of magnetic poles. Various types include reluctance motors, hysteresis motors and inductor-type motors.
- *AC induction motor*
  This is also known as an asynchronous motor. Unlike the synchronous motor, the rotating speed of this motor is lower than the synchronous speed. Variants include squirrel-cage rotor type, eddy-current motor and wound-rotor type.
- *Switched reluctance motor (SRM)*
  The SRM uses a stator of concentrated winding and a salient-poled lamination rotor. SRMs are variable speed motors that have a simple and robust structure.
- *Surface Permanent Magnet (SPM) motor*
  The SPM has a structure in which permanent magnets are attached to the circumference of the rotor surface. It only uses magnetic torque from the magnet.
- *Interior Permanent Magnet (IPM) motor*
  The IPM motor has a rotor embedded with permanent magnets. Compared to the SPM, this type can reduce the risk of a magnet being peeled off by centrifugal force, and take advantage of reluctance torque through magnetic resistance in addition to magnetic torque.

A trade-off between the electric motors is summarised in Table 2.5. If each trade-off parameter is treated as equally important, the SRM seems like the best option for aircraft applications: an electric motor with the ability to perform under high temperatures and harsh environmental conditions [47].

Table 2.5: Trade-off between different types of electric motors [47].

Trade-off parameter	AC motor[1]	SRM	SPM	IPM
Useable in high temperature	good	intermediate	poor	poor
High rotational speeds	good	poor	poor	intermediate
High environment resistance	good	intermediate	poor	poor
Size and mass	intermediate	intermediate	good	good
Vibration and noise	intermediate/poor	good	intermediate	intermediate
Efficiency	intermediate	poor	good	good
Fixed output variation range	good	poor	poor	intermediate
Startup torque	good	intermediate	intermediate	good
Torque density	intermediate	poor	good	good
System cost	good	intermediate	intermediate	intermediate

2.4 Photovoltaic Applications in Aviation

The urge to search for alternative energy sources is growing due to the depletion of fossil fuels, the need to lower fuel demand and global climate change. PV technology can serve as a solution to this problem. Projects like the Sunseeker and Solar Impulse 2 have demonstrated that photovoltaics can serve as the primary energy source for sustained level flight [48]. Perhaps the first application of PV technology in commercial aircraft could be through the use of EAPPS.

The basic principle of solar powered aircraft is to have PV cells cover specific areas of the aircraft; often the wing and tail plane, as these parts are in a position facing upwards towards the Sun. When exposed to solar radiation, the cells convert solar energy into electrical energy. The total amount of energy produced depends on varying factors; the day of the year, the time of the day, the position on the Earth's surface, the inclination of the cells relative to the Sun and the degree of cloud cover [20]. Excess energy produced can be stored in batteries or fuel cells for later use e.g. during nighttime when the Sun is not available [49].

2.4.1 Photovoltaic System Technology and Development

Photovoltaics is defined as the direct conversion of solar energy into electricity using devices based on semiconductor materials. To make use of solar energy on aircraft, a complete stand-alone PV system is required. Other than PV modules, these system components include batteries, converters, charge controllers with maximum power point tracking (MPPT) and cables [50].

Currently, there are three main types of solar cells being produced: thin-film, single junction and multiple junction. For each type, the principle of energy generation is theoretically the same but differs in material and manufacture. Materials used in today's photovoltaics include monocrystalline silicon (mono-Si), polycrystalline silicon (poly-Si), amorphous silicon (a-Si:H), cadmium telluride (CdTe) and copper indium gallium selenide/sulphide (CIGS). A short description for each class of PV cells is presented below [20, 51]:

[1] AC motor refers to the commutator, synchronous and induction types of motor.

- *Single-junction crystalline wafers*
  Crystalline silicon (c-Si) wafers, also known as "first-generation" PV technology, are still the dominant semiconducting material used for solar cells; it covers 75% to 90% of the entire PV market. Their simplicity in p-n junction design and relatively high efficiency permit such dominance. These cells, however, are expensive from a manufacturing perspective. Also, the cell efficiency drops rapidly as the temperature rises, at a rate of 0.5%/°C. The highest conversion efficiencies for mono-Si and poly-Si technologies are set at 25% and 27.6%, respectively.

- *Thin-film technology*
  To lower the production costs, "second-generation" thin-film technologies have been developed that do not require expensive c-Si wafers. These can be made from a range of inorganic semiconducting materials such as CdTe and CIGS, as well as multi-junction a-Si:H. Laboratory efficiencies for CdTe, CIGS and a-Si:H are 22.1%, 23.3% and 13.6%, respectively.

- *Multi-junction cells*
  Multi-junction cells, one of the "third-generation" solar technologies, can capture and convert a much broader light spectrum than other designs, thus achieving greater efficiencies. Three-junction cells are generally made of gallium indium phosphide (GaINP), gallium arsenide (GaAs) and germanium (Ge) p-n junctions. A key feature is that these multi-junction cells do not drop in efficiency at increased temperatures. Various multi-junction cell efficiencies range from 31.6% to 46.0% depending on the number of junctions.

Every year, the National Renewable Energy Laboratory (NREL) presents a chart of compiled values of highest confirmed conversion efficiencies for research cells [52], from 1976 to the present, for a range of PV technologies, shown in Figure 2.5. The efficiencies of laboratory cells have steadily grown in the past and are expected to improve further with reduced costs in the coming decades. Both trends in solar cell development, lowering manufacturing costs and increasing energy conversion efficiencies, allow PV technology to expand and potentially be integrated in next-generation commercial aircraft.

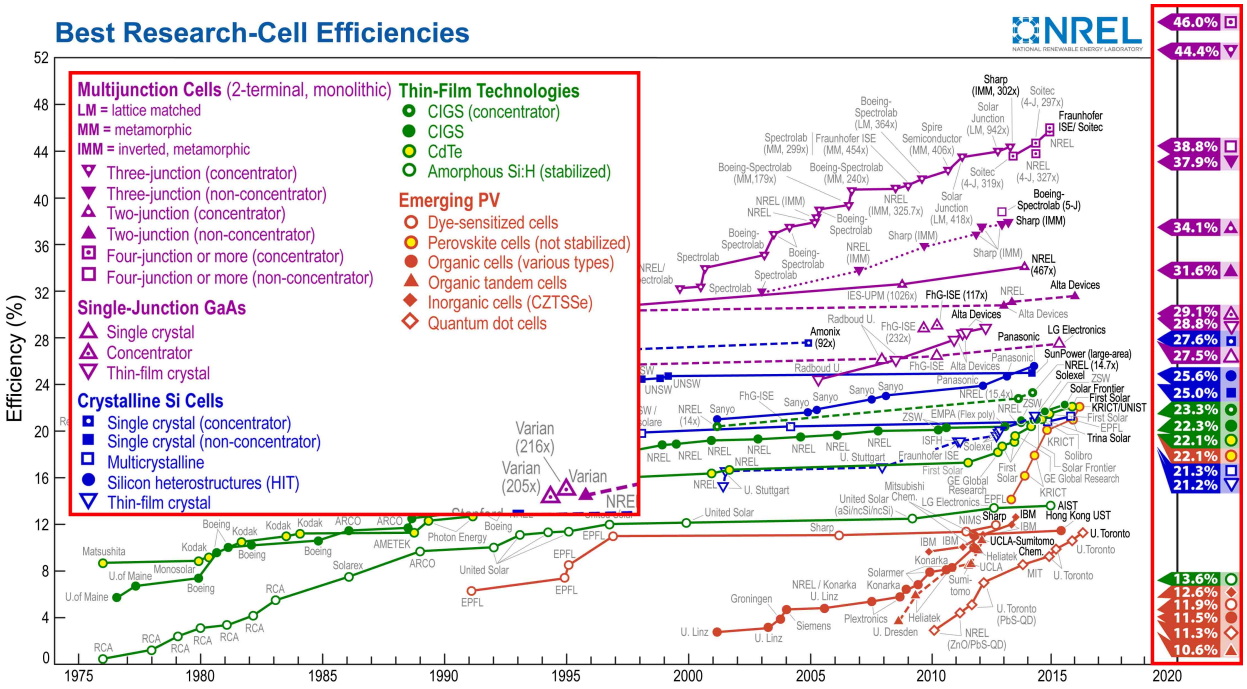

Figure 2.5: Current overview of the highest conversion efficiencies in PV technology; red-marked boxes are zoomed in for better readability [52].

2.4.2 Design Considerations for PV Integrated Aircraft

A fine balance between energy collection and energy consumption is crucial to the design of an aircraft completely reliant on solar power such as the Solar Impulse 2. If photovoltaics act as a secondary power source, this aspect is of less importance. Other key factors that should be taken into account are: the geographical area of operation, the orientation and inclination of the solar cell area, the weather (clouds, humidity and temperature), the mission profile and the payload. The operating altitude also affects the photovoltaic performance, as the solar power density increases with altitude, but this effect is significantly small [49, 53]. Since the PV modules will be installed on the outer skin of the aircraft, this will inevitably affect the aerodynamic and structural properties of the aircraft; however, this subject is considered beyond the scope of this study and will not be elaborated any further.

PV cells are also highly responsive to temperature; the efficiency degrades quickly with increasing temperature. This is due to the reduction of the band gap, rejecting the cell to absorb more energy from the photons. Fortunately, the wind has a positive impact causing convection heat transfer and lowering relative humidity and temperature, particularly effective on PV cells mounted on the wings of a flying aircraft. This allows the cells to reach higher efficiencies as a result of lower temperature [54].

Depending on the circumstances, the PV cells on the aircraft will also continuously generate varying amounts of power. Therefore, it is important to consider the use of MPPT. MPPT keeps the current and voltage levels such that the maximum power available is extracted from the PV cells regardless of changes in atmospheric or loading conditions. In case excess power is produced by the PV array, it can be stored in an energy storage device. This approach allows the system to optimally harvest the available solar radiation [49, 54].

Lastly, assuming that series-connected cells will be present, the one with the lowest irradiance e.g. due to wing curvature or a change in flight orientation will dictate the current for the remaining cells. This means that the maximum current flowing through the entire module or string is limited by this one cell [49, 54]. To prevent this problem from happening, bypass diodes can be installed to allow the current flow around the limited cell [50].

2.5 Fuel Cell Technology and Development

Another technology applicable to EAPPS is the use of fuel cell technology. Fuel cell systems are distinguished by the energy conversion components; these include fuel cell stacks, energy storage components, reactants, tankage and ancillary components. These systems can be categorised in two ways: regenerative and non-regenerative. The regenerative system splits hydrogen from oxygen through the use of an electrolyser stack. Whenever excess energy is generated, it is stored and used to disassociate water molecules. In addition, oxygen and hydrogen gases are then gathered in separate pressurised tanks. If power generation is required, the whole process will be reversed; hydrogen and oxygen will be fed back through the fuel cell to produce electricity and water as a by-product. The water will be stored in a tank until excess energy is available to repeat the process again. The non-regenerative system works on the same principle except the electrolyser is removed. As long as hydrogen and oxygen are supplied, the fuel cell will continuously generate electrical power along with heat and water.

Presently, there are different kinds of fuel cell technologies under development; these are shown in Table 2.6.

The two most favourable fuel cell types for advanced aircraft applications are the polymer electrolyte membrane fuel cell (PEMFC) and the solid oxide fuel cell (SOFC) [20, 55]. The PEMFC is a low-temperature device that allows quick start-up times, but requires the use of pure gaseous hydrogen

Table 2.6: Overview of fuel cell technologies [20].

Fuel cell type	Electrolyte	Operating temperature [°C]	Efficiency [%]	Power output [kW]
Polymer electrolyte membrane fuel cell (PEMFC)	Proton exchange membrane	50 - 100	35 - 60	$<$ 1 - 100
Alkaline fuel cell (AFC)	Aqueous potassium hydroxide solution	90 - 100	60	10 - 100
Phosphoric acid fuel cell (PAFC)	Liquid phosphoric acid	150 - 200	40	400
Molten carbonate fuel cell (MCFC)	Solution of lithium, sodium, and/or potassium carbonates	600 - 700	45 - 50	300 - 3,000
Solid oxide fuel cell (SOFC)	Solid zirconium oxide stabilised with yttrium	700 - 1,000	60	1 - 2,000

fuel. By increasing the operating temperature, the tolerance of impurities will improve and could possibly increase the specific power. Furthermore, PEMFC stacks generate a large amount of heat that is difficult to dissipate or to produce additional work. This necessitates some form of liquid cooling, particularly at higher potential specific power. The SOFC, contrary to PEMFCs, operates with far more airflow through the stack which provides sufficient heat removal; this eliminates the need and additional mass for a liquid cooling system [20].

For both fuel cell technologies, it holds that significant development in several areas is required for future implementation into EAPPS aircraft. These areas include increasing the specific power and energy, as well as improving the operability and durability of these fuel cell systems for flight applications. Current research and development programmes focus on developing reliable, low-cost, high-performance fuel cell system components for transportation applications [56].

CHAPTER 3

System Definition and Analysis

This chapter describes the characteristics of each individual system component and how these can be simulated within two separate models; one for the mission analysis (EAPPS module) and one for the in-depth energy management of the electrical system (EMS module).

First of all, Section 3.1 will cover the reference aircraft of this study, the Airbus A320neo. This is followed by a description of the CFM LEAP-1A26 turbofan engine in Section 3.2, which is the newest generation gas turbine installed on the A320neo. Afterwards, Section 3.3 will present a linear regression analysis for specific power and energy of the most important electrical system components: motor/generator, power electronics and batteries. Then, the dynamics and parameterisation of the electric motor and battery will be explained in Section 3.4 and Section 3.5, respectively. A brief summary on the power electronics and cables is given in Section 3.6. Subsequently, the fuel cell and photovoltaic systems will be discussed in Section 3.7 and Section 3.8, correspondingly. Since power and energy management are two essential and indispensable topics within this study, the strategies involved will be outlined in Section 3.9 and Section 3.10. Lastly, the implementation of the two different simulation models (EAPPS and EMS modules) using the aforementioned components will be specified in Section 3.11.

3.1 Reference Aircraft - Airbus A320neo (New Engine Option)

The reference aircraft chosen for this study is the Airbus A320neo with the new CFM LEAP-1A engine. The A320 aircraft is designed for short- to medium-range missions and considered one of the most successful single-aisle airliners with 4,333 units operable and 3,805 additional units to be delivered as of August 2017 [57]. Since there are many variants of this aircraft, the key characteristics of the selected version are shown in Table 3.1.

The mass breakdown of the A320neo can be found in Figure 3.1. In this research study, the maximum take-off mass (MTOM) is set as a limitation on the maximum allowable mass. This value is derived from the operational empty mass (OEM), design payload (DPL) and departure fuel load (DFL). To ensure no shortcomings, the aircraft must be able to carry the same maximum payload (MPL) as before. By subtracting the maximum zero-fuel mass (MZFM) from the MTOM, the mission mass (MM) can be computed. This MM value of 10,700 kg includes the fuel mass as well as any additional loads, such as the EAPPS, carried along the entire flight mission. Since the length of the reference mission is merely a distance of 1,000 km, no more than 4,000 kg of fuel needs to be carried on-board. This leaves a total of 6,700 kg for the EAPPS and its components.

Table 3.1: Main characteristics of the Airbus A320neo [58, 59].

General	
Typical seating (2-class) [pax]	165
Maximum seating (1-class) [pax]	190
Cruise Mach number [-]	0.78
Cruise altitude [ft]	37,000
Design range [km]	6,500
Masses	
Maximum take-off mass [kg]	73,500
Maximum zero-fuel mass [kg]	62,800

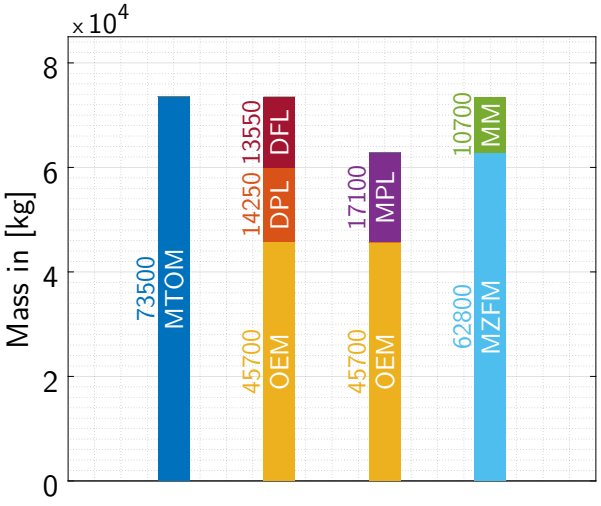

Figure 3.1: Mass breakdown of Airbus A320neo [59].

3.2 Turbofan Engine

The engine selected is the CFM LEAP-1A26 twin-spool turbofan engine installed on the Airbus A320neo (New Engine Option) aircraft; a cross-sectional view of the engine is illustrated in Figure 3.2. This engine was jointly certified in late 2010s by European Aviation Safety Agency (EASA) as well as Federal Aviation Administration (FAA) and entered into service in 2016 [58]. Key performance characteristics are presented in Table 3.2.

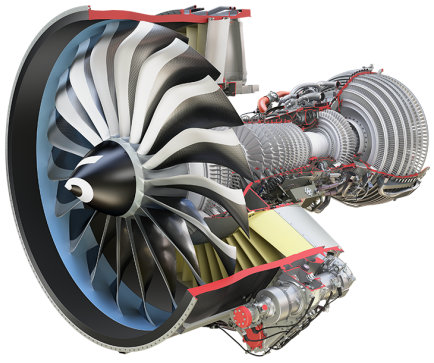

Figure 3.2: Cross-sectional view of the CFM LEAP-1A26 turbofan engine [60].

Table 3.2: Technical characteristics of the CFM LEAP-1A26 turbofan engine [61].

Parameter	Value
Engine mass (wet) [kg]	2,990
Take-off thrust [kN]	120.64
Maximum continuous thrust [kN]	118.68
Overall pressure ratio	40
LP rotor (N1 100%) [RPM]	3,856
HP rotor (N2 100%) [RPM]	16,645
Number of compressor stages (fan/LPC/HPC)	1/3/10
Number of turbine stages (HPT/LPT)	2/7

3.2.1 Power Off-Takes

As highlighted in Section 2.3.2, the secondary power off-takes can be divided into two parts: shaft power and bleed air.

Shaft Power

The shaft power is used to operate hydraulic pumps and electrical generators; the generated electrical power can then be directed towards different subsystems. The electrical power requirements for various subsystems in conventional and electrical architectures are presented in Table 3.3 and Table 3.4, respectively. A more in-depth explanation of how these values are estimated and verified against experimental data is given in Appendix A.

Note that the total AC and DC loads are noted in apparent power and shown separately. This apparent power is indicated by kVA and considers the differences in phase angle. For DC loads as well as AC resistive loads, the apparent power is always equal to the actual power; there is no phase differential between current and voltage. The ratio between actual and apparent power is called the power factor PF. Assuming a power factor of 1, these two can be combined to acquire a total sum in kilowatts.

Table 3.3: Electrical power requirements for conventional architecture of Airbus A320neo; adapted from [33, 36].

Subsystem	Taxi-out	Take-off	Climb	Cruise	Descent	Landing	Taxi-in
Actuation & landing gear	9.80	17.10	13.10	12.50	15.10	23.50	9.80
Avionics	31.59	34.13	41.23	41.23	41.23	34.62	31.59
Cabin equipment	7.50	6.50	6.50	49.40	6.50	6.50	7.50
Total AC [kVA]	*19.80*	*12.50*	*18.80*	*61.70*	*18.80*	*12.50*	*19.80*
Total DC [kVA]	*29.09*	*45.23*	*42.03*	*41.43*	*44.03*	*52.12*	*29.09*
Total [kW]	**48.89**	**57.73**	**60.83**	**103.13**	**62.83**	**64.62**	**48.89**

Bleed Air

The bleed air is mainly utilised for internal engine cooling and air supply towards the IPS and the ECS. To determine the bleed air requirements for the aircraft subsystems of the conventional Airbus

Table 3.4: Electrical power requirements for electrical architecture of Airbus A320neo; adapted from [33, 36].

Subsystem	Taxi-out	Take-off	Climb	Cruise	Descent	Landing	Taxi-in
Actuation	12.89	43.48	35.48	34.28	35.48	16.74	12.89
Avionics	41.59	34.13	41.23	41.23	51.23	47.92	41.59
Cabin equipment	7.50	6.50	6.50	49.40	6.50	6.50	7.50
ECS	135.00	5.00	125.00	130.40	125.00	5.00	135.00
IPS	4.33	8.23	26.29	26.29	26.29	0.00	4.33
Landing gear	5.10	3.80	0.00	0.00	0.00	31.20	5.10
Total AC [kVA]	*22.44*	*28.04*	*44.40*	*87.30*	*44.40*	*24.84*	*22.44*
Total DC [kVA]	*183.97*	*73.10*	*190.10*	*194.30*	*200.10*	*82.52*	*183.97*
Total [kW]	**206.41**	**101.14**	**234.50**	**281.60**	**244.50**	**107.36**	**206.41**

A320, a closer look is taken at the available flight data from Hamburg to Toulouse; these are shown in Table 3.5.

Table 3.5: Required bleed air off-takes; derived from actual Airbus A320 flight data (Hamburg-Toulouse) [62].

	Take-off	Climb	Cruise	Descent	Approach
Maximum bleed air off-take fan [kg/s]	0.463	0.308	0.186	0.332	0.453
Maximum bleed air off-take HPC [kg/s]	0.579	0.710	0.481	0.481	0.453
Maximum total bleed air off-take [kg/s]	1.042	1.018	0.667	0.761	0.906
Assumption: constant ECS bleed during flight (0.667 kg/s) and IPS inactive during cruise					
Environmental Control System [kg/s]	0.667	0.667	0.667	0.667	0.667
Ice Protection System [kg/s]	0.375	0.351	0	0.094	0.205

By assuming that the ECS bleed off-take is constant throughout the mission and that the IPS is inactive during cruise, the bleed consumption for the ECS and the IPS can be derived. The order of magnitude for the IPS (0.205-0.375 kg/s) is in line with values from an in-house developed model [63]. Another assumption is that taxiing requires no more than 0.75 kg/s of bleed air, equal to the other less heavily-loaded flight segments (cruise, descent and landing). The derived bleed air requirements for the subsystems on a conventional A320neo, as applied in the analysis of this thesis, is presented in Table 3.6; the electrical A320neo features a bleedless concept, therefore the required bleed flow in that case equals zero.

Table 3.6: Bleed air requirements for the aircraft subsystems of the conventional A320neo as applied within the present study.

	Taxi-out	Take-off	Climb	Cruise	Descent	Landing	Taxi-in
Required bleed flow [kg/s]	0.75	1	1	0.75	0.75	0.75	0.75

To find the corresponding bleed setting for each flight segment, Figure 3.3 can be used as a guideline. This graph shows the average mass flow for varying levels of bleed air extraction per flight phase. Given this illustration and the required bleed flow in Table 3.6, the desired bleed settings set as mass flow percentage of the engine air flow are derived and presented in Table 3.7.

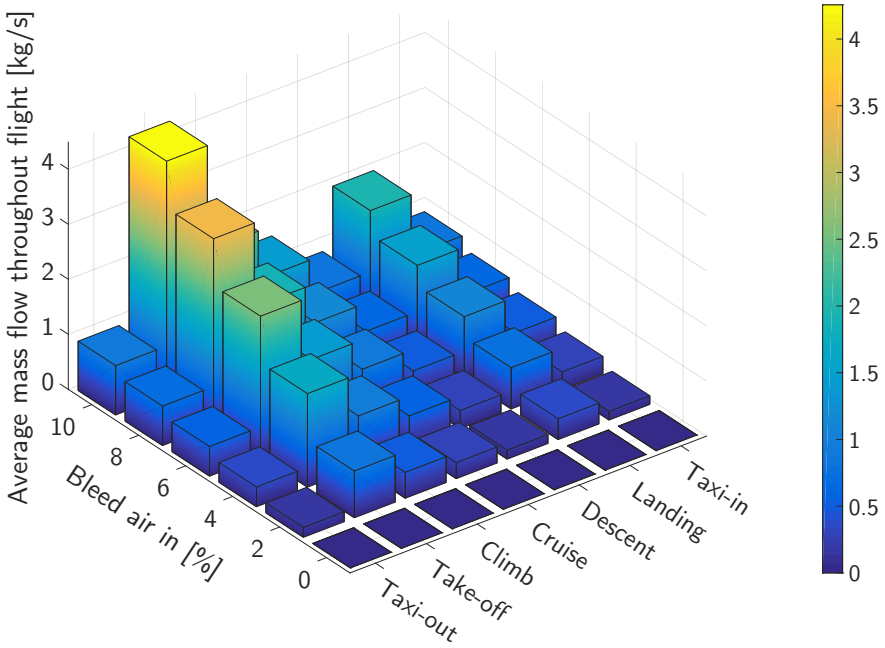

Figure 3.3: Effect of bleed extraction percentage on the average bleed mass flow throughout the flight mission.

Table 3.7: Selected bleed schedule for the aircraft subsystems of the conventional A320neo.

	Taxi-out	Take-off	Climb	Cruise	Descent	Landing	Taxi-in
Bleed air extraction [%]	10	3	5	6	10	4	10

3.2.2 Engine Scaling

Since an electric motor is utilised to assist the turbofan engine during the take-off and climb phases in this EAPPS setup, the maximum thrust of the initial CFM LEAP-1A26 engine is not required. This allows the CFM LEAP-1A26 gas turbine to be downscaled; it can be done via scaling the bypass ratio down or scaling the engine core mass flow down. In this study, the bypass ratio is kept constant, thus the engine core is scaled down.

The engine mass is related to the static take-off thrust $F_{N_{takeoff}}$ by Equation 3.1. This formula corresponds quite well to a database of 26 turbofan engines; the error using this correlation is within 10% of the actual engine mass [64]. Note that the input $F_{N_{takeoff}}$ is in pound-force (lbf), while the output m_{engine} is in pounds (lbs).

$$m_{engine} = 2.7 \cdot F_{N_{takeoff}}^{0.75} \tag{3.1}$$

The parameters for scaling the mass flow and the shaft speed are shown in Equation 3.2 and Equation 3.3, respectively [65]. When engine scaling is applied, these parameters must remain constant. If, for example, the engine core diameter DI is scaled down by 90%, the mass flow should be downscaled by the square of 90%. In turn, the shaft speed needs to increase by the inverse of 90%; this is required to keep the same tip Mach number of the engine blades, considering the compressibility effects [66, 67].

$$\text{mass flow scaling parameter} = \frac{\dot{m} \cdot \sqrt{\theta}}{DI^2 \cdot \delta} \tag{3.2}$$

$$\text{shaft speed scaling parameter} = \frac{DI \cdot N}{\sqrt{\theta}} \tag{3.3}$$

The two other variables in the aforementioned formulas, δ and θ, represent the parameters for the pressure and the temperature ratios, respectively, and are defined in Equation 3.4 and Equation 3.5. Here, the pressure and the temperature at International Standard Atmosphere (ISA) sea level static conditions are used as reference values.

$$\delta = \frac{p_{inlet}}{p_{ref}} \tag{3.4}$$

$$\theta = \frac{T_{inlet}}{T_{ref}} \tag{3.5}$$

By scaling the engine down and thus increasing the shaft speeds of the engine, the stresses on the discs are also affected. Within this study, these stresses are treated as proportional to the centrifugal force. This relation is shown in Equation 3.6, with A_{disc} being the circumferential area of the disc. To ensure safe engine operation and assure that the discs do not fail under the loads, the disc thickness and thus the disc mass is increased proportionally to the square of the rotational speed ω. The masses of the individual CFM LEAP-1A components can be estimated by using mass fractions stated in Table 3.8. These are derived from a PW4056 engine in a turbine performance simulation software called GasTurb [68].

$$\sigma_{disc} = \frac{F_c}{A_{disc}} \tag{3.6}$$

Table 3.8: Mass fractions of individual components of PW4056 engine [68].

Component	Mass [kg]	Fraction [%]
Fan	840.63	22.1
LPC	253.58	6.7
HPC	455.54	12.0
HPT	119.63	3.1
LPT	265.41	7.0
Other	1,871.64	49.2
Total	**3,806.43**	**100**

The scaled engine mass is obtained in two steps. First, the total mass of the non-rotating components is determined using the mass fraction of 49.2% mentioned in Table 3.8 and proportionally lowered by the applied scale. Then, in a similar way, the masses of the rotating components are calculated and increased proportionally to the square of the rotational speed. The results for varying scales of the CFM LEAP-1A engine are found in Table 3.9; these masses include the reinforced discs and are valid for the A320neo aircraft.

The last but most important aspect is that scaling should be done within the engine limitations. Even though the mass of the discs may be increased with increasing shaft speeds, the maximum allowable temperatures for nozzle guide vanes (NGVs) T_{t41} and exhaust gas temperature (EGT) T_{t45} remain unchanged. More details on engine limitations are provided in Section 4.9.2.

Table 3.9: Masses of different scales of CFM LEAP-1A engine.

Scale	Engine mass [kg]	Total mass [kg]
100%	2,879.90	5,759.8
95%	2,796.65	5,593.3
90%	2,675.15	5,350.3
85%	2,543.00	5,086.0
80%	2,410.05	4,820.1

3.2.3 Engine Emissions

To monitor the engine emissions, the International Civil Aviation Organization (ICAO) has set standards limiting the production of soot, unburnt hydrocarbons (UHCs), carbon monoxides (COs) and nitrogen oxides (NO_x) from turbofan engines. Each pollutant is characterised by the so-called emissions index (EI), expressed in Equation 3.7. This is the ratio between the mass of the pollutant i in grams and the mass of the fuel used in kilograms [69].

$$EI_i = \frac{m_i}{m_{fuel}} \tag{3.7}$$

The expected EI values for each pollutant produced by the turbofan engine are displayed in Table 3.10. First of all, carbon dioxide (CO_2) and water vapour (H_2O) are products of complete combustion and only dependent on the total fuel burnt throughout the mission. CO, UHC and soot are products of incomplete combustion and thus determined by the thrust setting. NO_x is a by-product of complete combustion and along with sulphur oxide (SO_x), are products of fuel impurities. Since SO_x emission levels are low for jet fuels used in aircraft engines, this parameter may be disregarded.

Table 3.10: Indicative emissions indices of Jet A-1 fuel [70].

Substance	EI [g/kg fuel]	Emission depends on
CO_2	3,150	fuel consumption
H_2O	1,250	
CO	0.4 - 65	thrust setting: maximum production at idle
UHC	0.2 - 12	
Soot	$\pm$ 0.015	thrust setting: maximum production at full thrust
NO_x	4 - 30	
SO_x	0.02 - 6	

The formation of CO and UHC decreases with higher thrust settings, while the production of soot, NO_x and SO_x increases [70]. This trend is clearly visible in Figure 3.4.

Here, soot is represented by the smoke number (SN); it is the plume opacity of the engine exhaust and rated on a scale of 0 to 100. By staining a filter sample, the SN can be determined using Equation 3.8; where R_s and R_w are the absolute reflectance readings of the stained and clean filter material, respectively [69].

$$SN = 100 \cdot \left(1 - \frac{R_s}{R_w}\right) \tag{3.8}$$

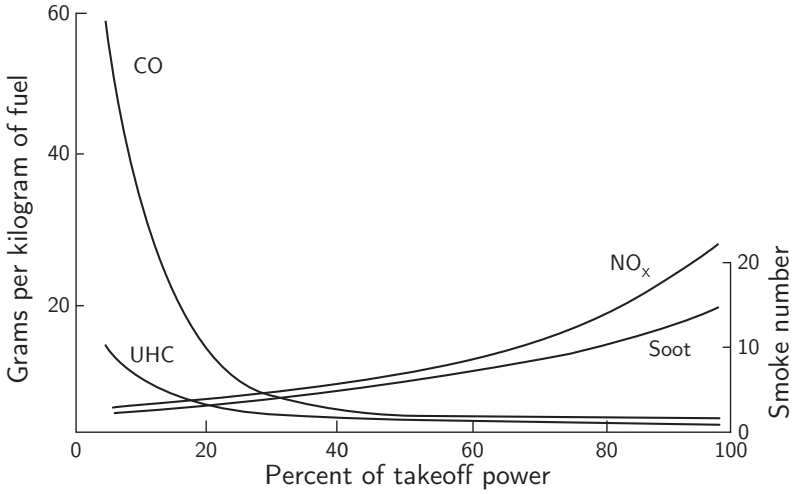

Figure 3.4: Emission trends of CO, UHC, soot and NO_x; adapted from [60, 70].

3.3 Electrical System

The minimal setup of the electrical system comprises an electric motor/generator, an inverter, a battery and cables for transmission. In this particular study, fuel cells and PV systems can also be implemented to become part of the electrical system. Each component will be discussed in the following sections: the electric motor in Section 3.4, the batteries in Section 3.5, the power electronics and cables in Section 3.6, the fuel cells in Section 3.7 and the PV system in Section 3.8. The advancement and current state of these individual components ultimately decide the overall performance on the system level. To account for such technological developments, the performance characteristics of each component will be determined at two different time frames: near term (2020+) and far term (2040+).

The most important parameters are efficiency, specific power and specific energy. The specific power describes the amount of power a component can supply per unit mass (in watts per kilogram). The specific energy gives the amount of energy a battery can store per unit mass (in watt hours per kilogram). A linear regression analysis is performed to find the specific power and energy values for the most important components: electric motor, generator, power electronics and batteries. Numerous journal articles, conference papers and reports have been used to create a data map: $N = 26$ for motors/generators, $N = 6$ for power electronics and $N = 11$ for batteries. The results of this linear regression fit are shown in Figure 3.5. The symbols marked in green are the numeric values considered for the electrical components in 2020+ and 2040+. Keep in mind that these specific power and energy values are based on non-cryogenic technology; including cryogenics would significantly increase these values but also raise concerns about safety and other aspects.

Additionally, the power density (watts per litre) is used for batteries and fuel cells, to determine the volume needed for the stacks and hydrogen fuel storage. Also, the area mass density is specified, in kilograms per square metre, to determine the total mass of the PV panels.

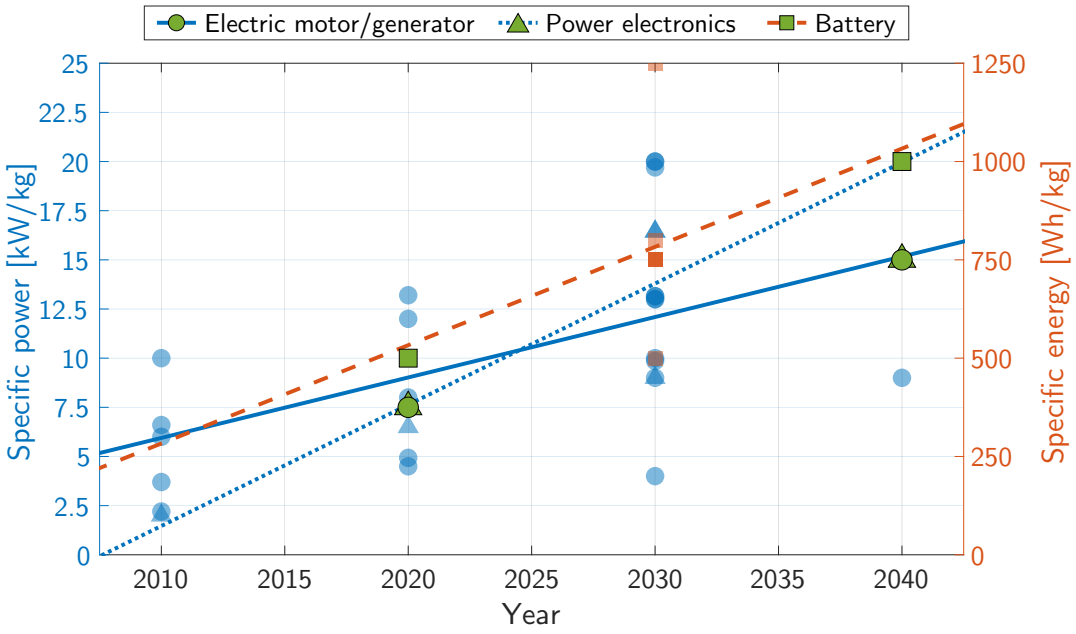

Figure 3.5: Linear regression fit of various components for specific power and energy as function of year: electric motor/generator (circle) [12, 33, 47, 71–77], power electronics (triangle) [12, 71, 74, 78, 79] and battery (square) [12, 25, 76, 78]. The symbols marked in green are the values used within this study for 2020+ and 2040+.

3.4 Electric Motor

The electric motor is a device that turns electrical power into mechanical power; see Section 2.3.4 for some background information. If the mechanism is reversed, it essentially operates as a generator. In this study, the focus lies on the modelling of the motor functionality; the generator part is only addressed in a limited way (as a fixed efficiency). The motor selected for this study will be a switched reluctance motor (SRM) similar to the one used for the SUGAR Volt, the hFan motor [78]. It is assumed that the hFan characteristics do not change and can be applied for the power requirements of the flight mission. In the simplified motor model, the electric motor will be parameterised to only include a fixed efficiency and specific power for each time frame, stated in Table 3.11.

Table 3.11: Simplified characteristics of the electric motor in 2020+ and 2040+ [47, 72, 80].

Parameter	2020+	2040+
Efficiency [%]	95	98
Specific power [W/kg]	7,500	15,000

In the advanced motor model, the electric motor will be sized and modelled dynamically, with the efficiency depending on power output and rotational speed. The corresponding formulas to determine the motor characteristics and its losses are described in the following paragraphs.

3.4.1 Electric Motor Parameterisation

Before the motor sizing procedure, it is essential to understand the operational behaviour of an SRM. In general, any type of electric motor works on the same principle: the rotational speed is proportional to the voltage applied and the torque is proportional to the current drawn. The motor power output

is the product of the torque and rotational speed. These fundamental torque-speed relationships are formulated in Equation 3.9 to 3.11, where K_v and K_t are the voltage and torque coefficients, respectively. For a specified motor design, these parameters are assumed to remain constant [78].

$$P = T \cdot \omega \tag{3.9}$$

$$V = K_v \cdot \omega \tag{3.10}$$

$$T = K_t \cdot I \tag{3.11}$$

The torque-speed characteristics of an SRM are illustrated in Figure 3.6.

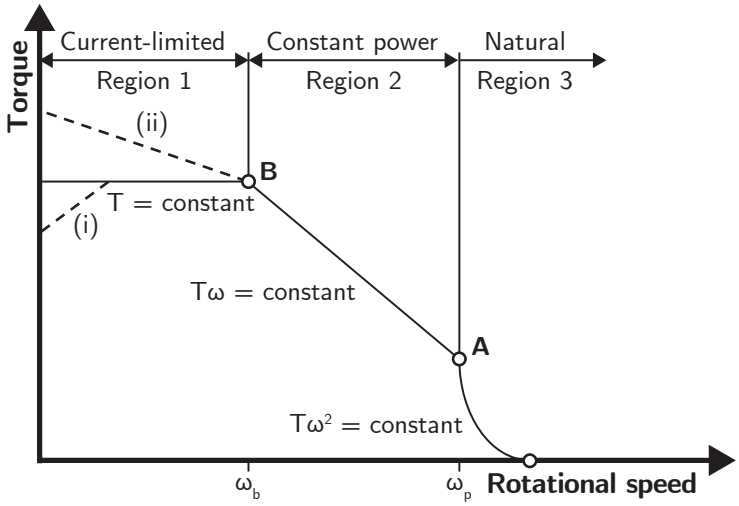

Figure 3.6: Torque-speed characteristics of an SRM; adapted from [81].

At low rotational speeds, the torque is limited by the maximum allowable current (region 1). As speed increases, the torque-limited region will persist until the rotor reaches a point where the back electromotive force (emf) can no longer draw more current, given the nominal voltage supplied, and thus no longer produce maximum torque. This point is characterised by the base speed, ω_b. After this point, the downward sloping curve shows the maximum permissible torque at each speed representing a constant maximum power output (region 2); the core and windage losses increase rapidly with speed. At even higher speeds (beyond the critical speed ω_p), the back emf increases and the shaft output power will drop following the natural characteristic of the SRM, i.e. the torque decreasing with the square of the rotational speed (region 3). Keep in mind that operation below this line is allowed; however, higher efficiencies are generally achieved near the power rating of the motor.

Depending on the circumstances, deviations from this curve may occur. The first is at very low speeds (line i): e.g. if the chopping frequency[1] is limited by the use of gate turn-off thyristors[2]; since high peak currents cannot be controlled in a safe manner, the maximum allowable current may be lowered. If core and windage losses are negligibly low, higher torques can be obtained (line ii) by temporarily drawing more current through the coils, thus increasing the copper losses [81].

By making use of the correlation between torque and speed illustrated in Figure 3.6, the voltage and torque coefficients can be determined for any given SRM. The first step is to specify the maximum power output required by the electric motor for the electrification of propulsion. In addition, the maximum rotational speed can be specified by assuming that the motor is directly mounted on the LP shaft. Assuming that operation in region 3 is undesirable, with the torque declining rapidly with the inverse

[1] The chopping frequency is the rate at which a switching device (chopper) switches on and off.

[2] The gate turn-off thyristor is a high-power semiconductor device that acts as a fully-controllable switch, albeit with relatively long switch-off times.

of the rotational speed squared, point A can now be defined. The torque at point A can be calculated using Equation 3.12:

$$T_A = \frac{P_{max}}{\omega_{max,LP}} \tag{3.12}$$

Using the maximum operating voltage V_{max}, the voltage coefficient follows from Equation 3.13:

$$K_v = \frac{V_{max}}{\omega_{max,LP}} \tag{3.13}$$

To determine point B, a value must be chosen for the base speed ω_b; this is defined as a ratio of the maximum rotational speed ω_{max}. With the base speed known, the maximum torque can be determined using Equation 3.14:

$$T_B = \frac{P_{max}}{\omega_b} \tag{3.14}$$

Then, the maximum current is estimated with an empirical formula (Equation 3.15) [78]. A value is assumed for the motor winding resistance R_0, in Ohms.

$$i_{max} = 0.5 \cdot \frac{\sqrt{K_v^2 \cdot \omega_b^2 + 1.63299 \cdot P_{max} \cdot R_0} - K_v \cdot \omega_b}{R_0} \tag{3.15}$$

With both the maximum current and torque known at point B, the torque coefficient K_t can finally be obtained using Equation 3.16:

$$K_t = \frac{T_B}{i_{max}} \tag{3.16}$$

By determining the two coefficients K_v and K_t for a given SRM setup, the motor is now properly defined. When two inputs for power, torque, rotational speed, current or voltage are specified, any remaining unknown parameters can be solved using Equation 3.10 and Equation 3.11.

3.4.2 Electric Motor Losses

The individual losses (copper, iron, friction and windage) of an SRM, described in Section 2.3.3, can be estimated by means of semi-empirical relationships published in available literature [40, 47, 78]. These predictions are based on the operating current and rotational speed as well as the motor dimensions. First, the diameter and length of the motor are calculated using Equation 3.17 and Equation 3.18. These formulas are based on the findings of another hybrid electric aircraft study led by Boeing [78]. The stator diameter D_s is equal to the motor diameter D here.

$$D = D_s = 0.0713950 \cdot \log(P_{max}) - 0.1572667 \tag{3.17}$$

$$L_{motor} = \frac{0.4}{0.48} \cdot D \tag{3.18}$$

With Equation 3.19 and Equation 3.20, the rotor diameter D_r and the air gap length g can be approximated [47]. To calculate the mass of the electric motor, the shape will be simplified into a simple

cylinder. A shape factor Δ is introduced to correct for mass changes without considering each motor element; this factor changes depending on the number of stators and rotors in an SRM configuration. Equation 3.21 calculates the motor mass as a function of shape factor Δ, material density ρ_{mat} and stator diameter D_s.

$$D_r = 0.5 \cdot D_s \tag{3.19}$$

$$g = 0.0083 \cdot D_r \tag{3.20}$$

$$m_{motor} = \Delta \cdot \rho_{mat} \cdot \pi \cdot \left(\frac{D_s}{2}\right)^2 \cdot L_{motor} \tag{3.21}$$

Once the motor dimensions are established, the various motor losses can be estimated. The copper losses are caused by the current going through the windings. First, the resistance per turn $r_{perturn}$ is estimated based on AWG wire sizing charts [78] in Equation 3.22, followed by the total wire resistance per turn $R_{wire,perturn}$ in Equation 3.23.

$$r_{perturn} = 48.83 \cdot i_{max}^{-1.001259} \tag{3.22}$$

$$R_{wire,perturn} = \frac{D \cdot \pi \cdot r_{perturn}}{10^3} \tag{3.23}$$

To obtain the number of turns per phase T_{ph} in Equation 3.24, the values for the specific electric loading A_s and the phase current I_{ph} need to be determined. Equation 3.25 shows an estimation of the specific electric loading A_s as a function of the stator diameter D_s only [47]. With Equation 3.26, the phase current is acquired with the power and speed ratios, relative to the peak phase current I_0.

$$T_{ph} = \frac{\pi \cdot A_s \cdot D_s}{2 \cdot m \cdot I_{ph}} \tag{3.24}$$

$$A_s = 4.6e^{-7} \cdot D_s^6 - 1.4e^{-4} \cdot D_s^5 + 0.02 \cdot D_s^4 - 1.3 \cdot D_s^3 + 61.5 \cdot D_s^2 - 2242 \cdot D_s + 73022 \tag{3.25}$$

$$I_{ph} = I_0 \cdot \frac{P_{op}}{P_{max}} \cdot \frac{N_{op}}{N_{max}} \tag{3.26}$$

Now all the parameters are known to determine the copper losses using Equation 3.27. This formula shows that the copper losses are dictated by the operating current.

$$P_{copper} = I_{op}^2 \cdot R_{wire,perturn} \cdot T_{ph} \tag{3.27}$$

The iron losses are calculated with Equation 3.28 to 3.30 based on the Steinmetz equation, which considers the hysteresis and eddy current losses separately.

$$f_s = \frac{2 \cdot N_{op} \cdot n_s}{60} \tag{3.28}$$

$$B_p = \left[B_{p,0} \cdot \left(\frac{n_{s,6/4SRM}}{n_s}\right)^{\frac{n_s}{n_r \cdot m}}\right] \left(\frac{D_s}{D_{s,hFan}}\right)^{\frac{N_{max}}{N_{max,hFan}}} \tag{3.29}$$

$$P_{iron} = \left[K_h \cdot B_p^2 \cdot f_s + K_c \cdot (B_p \cdot f_s)^2 + K_e \cdot (B_p \cdot f_s)^{1.5}\right] \cdot m_{motor} \tag{3.30}$$

Equation 3.28 calculates the frequency based on the operational speed N_{op} and number of stators n_s. The peak magnetic flux density B_p follows from Equation 3.29; this formula relates the motor characteristics to the peak flux density and features of the hFan, the SRM used for Boeing's SUGAR Volt. Here, $B_{p,0}$ is the peak flux density of the hFan, n_r is the number of rotors, m is the number of phases, $D_{s,hFan}$ is the hFan stator diameter and $N_{max,hFan}$ is the hFan maximum rotational speed. The iron losses are then calculated with Equation 3.30, where K_h, K_c and K_e are the coefficients for the hysteresis, classical eddy current and excess eddy current losses, respectively.

The mechanical losses consist of the friction and windage losses; these can be estimated using the semi-empirical relations derived from Ref. [40]. The friction losses in the bearings are described by Equation 3.31, where n_{bear} is the number of bearings used. The windage losses are calculated with Equation 3.32.

$$P_{friction} = \frac{\frac{3}{2} \cdot n_{bear} \cdot m_{motor} \cdot N_{op}}{10^3} \tag{3.31}$$

$$P_{windage} = \frac{2 \cdot D_s^3 \cdot L_{motor} \cdot N_{op}^3}{10^6} \tag{3.32}$$

As shown in Equation 3.33, the copper, iron, friction and windage losses can then be summed to obtain a final value for the total power lost. The motor efficiency follows by substituting the operating power P_{op} and the total losses $P_{loss,total}$ into Equation 3.34. This efficiency varies throughout flight, as the required power changes along with its accompanying losses, which are dependent on operating current and rotational speed. The resulting efficiency map of the electric motor can be found in Section 5.3.

$$P_{loss,total} = P_{copper} + P_{iron} + P_{friction} + P_{windage} \tag{3.33}$$

$$\eta_{motor} = \frac{P_{op} - P_{loss,total}}{P_{op}} \tag{3.34}$$

3.5 Battery

As discussed before in Section 2.3.1, the development in battery technology plays a huge role in the realisation of HEPS and EAPPS concepts. Higher specific energy values are necessary to keep the overall system weight low; beyond a certain limit, the benefits are negated. By picking two time frames separated by 20 years of technological development, the feasibility of advanced hybrid electric configurations can be presented clearly. As current development leans towards lithium technologies, a lithium-based battery is used. The features of this battery for the EAPPS module are shown in Table 3.12.

Table 3.12: Technical characteristics of the battery in 2020+ and 2040+ [72, 80, 82].

Parameter	2020+	2040+
Efficiency [%]	92.5	95
Specific energy [Wh/kg]	500	1,000

In the EMS module, the dynamics of discharging and charging the battery will also be taken into account. The battery characteristics and how these performance parameters can be extracted from experimental data through curve fitting will be described in Section 3.5.1 and Section 3.5.2.

3.5.1 Battery Dynamics

To simulate the battery dynamics, various models exist throughout literature. One of the most common and simple battery models is Shepherd's battery model [83]. The original model for discharging is shown in Equation 3.35.

$$V_b = V_0 - K \cdot \frac{Q_b}{Q_b - I_b \cdot t} + A \cdot e^{-B \cdot I_b \cdot t} - I_b \cdot R_b \tag{3.35}$$

The first term, after V_0, takes care of the voltage drop due to cell reactant depletion near the maximum battery capacity. The exponential term accounts for activation and concentration polarisation to initiate and drive the chemical reaction. The last term represents the internal voltage losses in the battery [84].

The modified version of Shepherd's model considers both charging and discharging, and consists of two formulas: one in discharge mode and one in charge mode. These are shown as Equation 3.36 and Equation 3.37, respectively.

$$V_b = V_0 - K \cdot \frac{Q_b}{Q_b - I_b \cdot t} \cdot I_b \cdot t - K \cdot \frac{Q_b}{Q_b - I_b \cdot t} \cdot I_b + A \cdot e^{-B \cdot I_b \cdot t} - I_b \cdot R_b \tag{3.36}$$

$$V_b = V_0 - K \cdot \frac{Q_b}{Q_b - I_b \cdot t} \cdot I_b \cdot t - K \cdot \frac{Q_b}{I_b \cdot t - 0.1 \cdot Q_b} \cdot I_b + A \cdot e^{-B \cdot I_b \cdot t} - I_b \cdot R_b \tag{3.37}$$

Within these formulas, the following applies: V_b is the battery terminal voltage, V_0 is the battery nominal voltage, R_b is the battery internal resistance, I_b is the current through the battery (positive for discharge, negative for charge), Q_b is the nominal battery capacity, K is the polarisation coefficient, A is the exponential voltage coefficient and B is the exponential capacity coefficient. The last three parameters are considered curve fitting parameters and will be elaborated upon in Section 3.5.2.

The generic battery model, readily available in the SimPowerSystems (SPS) environment of Simulink®, is based on these two equations [85]. The difference between the original Shepherd (Equation 3.35) and the modified Shepherd (Equation 3.36 and Equation 3.37) lies mainly in the additional term called the polarisation resistance. This expression takes care of the steep voltage slopes at the end of the discharge curve and at the beginning of the charging curve. In particular, for batteries with low internal resistance (in the order of μΩ), this term will help significantly. In this study, the lithium-ion battery used will be in the order of mΩ, therefore this term will not be of substantial importance [83].

3.5.2 Curve Fitting Analysis

Using the original Shepherd model from Equation 3.35, a curve fitting analysis can be performed on experimental data to obtain the unknown fitting parameters; details of this curve fitting approach will be covered in Section 5.4. To fit multiple discharge curves simultaneously and accurately, a method provided by Ref. [84] is applied. It makes use of a cubic polynomial equation to model the current dependence of the exponential capacity coefficient B on the discharge current, described by Equation 3.38.

$$B = p_3 \cdot C^3 + p_2 \cdot C^2 + p_1 \cdot C + p_0 \tag{3.38}$$

The C in the formula is the discharge rate normalised to the battery capacity and is given by Equation 3.39:

$$C = \frac{I_b}{Q_{rat}} \tag{3.39}$$

The decrease in battery capacity at high discharge rates is invoked by the Peukert effect; to take this into account, the battery capacity is derated with increasing current drawn to obtain the actual battery capacity Q_b, expressed as:

$$Q_b = Q_{rat} \cdot \left(\frac{I_{rat}}{I_b}\right)^{pc-1} \tag{3.40}$$

where Q_{rat} is the rated battery capacity, I_{rat} is the rated discharge current and pc is the Peukert constant. This constant usually varies between 1.0 and 1.04 [84]. The state of charge (SOC) and depth of discharge (DOD) are each other's complement; one increases as the other decreases and vice versa. The definition can be found in Equation 3.41.

$$SOC = 1 - DOD = 1 - \frac{\int I_b \cdot dt}{Q_{rat}} \tag{3.41}$$

3.5.3 Battery System Sizing

Battery packs can be sized for the operating voltage required by the electrical system or the minimum capacity necessary to complete the mission. In short, the desired operating voltage or battery capacity can be reached by connecting the cells in series or in parallel, respectively. A combination of series and parallel connections is also possible; note that such a configuration should only be designed with the same battery type to avoid mismatches in voltage and capacity.

Therefore, the characteristics of a battery system or pack are ruled by the number of identical battery cells in series (indicated by n_{batt}) and in parallel (indicated by m_{batt}). The important features are described by Equation 3.42 to Equation 3.49; these are derived by applying Kirchhoff's laws.

$$V_{nom,pack} = V_{nom,cell} \cdot n_{batt} \tag{3.42}$$
$$Q_{rat,pack} = Q_{rat,cell} \cdot m_{batt} \tag{3.43}$$
$$I_{rat,pack} = I_{rat,cell} \cdot m_{batt} \tag{3.44}$$
$$R_{pack} = R_{cell} \cdot \frac{n_{batt}}{m_{batt}} \tag{3.45}$$
$$V_{0,pack} = V_{0,cell} \cdot n_{batt} \tag{3.46}$$
$$K_{pack} = K_{cell} \cdot \frac{n_{batt}}{m_{batt}} \tag{3.47}$$
$$A_{pack} = A_{cell} \cdot n_{batt} \tag{3.48}$$
$$B_{pack} = \frac{B_{cell}}{m_{batt}} \tag{3.49}$$

The total number of cells needed to assemble the battery pack is then found by:

$$N_{pack} = n_{batt} \cdot m_{batt} \tag{3.50}$$

3.6 Supplementary System Components

Other components needed in a functional electrical system are the power electronics and the cables, covered in Section 3.6.1 and Section 3.6.2, respectively.

3.6.1 Power Electronics

Power electronics refers to all sorts of power conversion systems needed to deliver power at the appropriate voltage levels and type of current. This includes rectifiers (AC to DC), inverters (DC to AC) and converters (AC to AC, DC to DC). Each device requires a different power conversion e.g. electric motor versus PV system. To simplify this matter, the properties of all power conversion devices are assumed to be similar; these are summarised in Table 3.13.

Table 3.13: Technical characteristics of the power electronics in 2020+ and 2040+ [71, 72].

Parameter	2020+	2040+
Efficiency [%]	95	98
Specific power [W/kg]	7,500	15,000

3.6.2 Cables

The electrical cables connect all the individual components into one co-operative system. Each connection requires special attention with respect to length, power type, transmitted power, voltage drop and required current. From this, a cable may be selected from a wire stranding chart, which allows the mass of the cable to be calculated. Since cable management is an art of its own and outside the scope of this study, it is assumed that the cables presently take up 15% of the simplified system mass (electric motor, inverter and battery). This fraction is assumed to decrease to 10% in the future, as an advanced power distribution system incorporates less cables and makes better use of dynamic power management [33]. The technical details of the power distribution are presented in Table 3.14.

Table 3.14: Technical characteristics of the cables in 2020+ and 2040+ [33, 72].

Parameter	2020+	2040+
Efficiency [%]	99	99.6
Mass fraction of simplified system [%]	15	10

3.7 Fuel Cell System

One of the options is to include a fuel cell system covering a part of the electrical load required for HEPS and the aircraft subsystems. The complete fuel cell system consists of fuel cell stacks, compressors, humidifiers, coolers, reactants and tankage. In the context of this study, a system of the non-regenerative type will be addressed; it is assumed that the hydrogen tank will carry sufficient fuel for the whole mission. Since these fuel cell systems may take up more space than conventional systems, the total volume including its fuel will also be taken into account; this procedure is described in Appendix B. Furthermore, power electronics will be required to regulate the power between the fuel cell system and the electrical network. As mentioned in Section 2.5, both PEMFCs and SOFCs are currently favoured within the aircraft industry. Throughout this study, the PEMFC type will be used

for its quick start-up and shut-down times. The system properties are indicated in Table 3.15; the size of the fuel cell system is assumed to decrease by 30% through 20 years of development.

Table 3.15: Technical characteristics of the fuel cell system in 2020+ and 2040+ [20, 72, 86, 87].

Parameter	2020+	2040+
Efficiency [%]	60	75
Specific power [W/kg]	500	1,000
Power density [W/L]	350	500

The characteristics of a fuel cell are in general defined by a polarisation curve, which shows the voltage output for a given current. In order to gain a better understanding, the characterisation of a fuel cell stack, along with its typical losses, will be discussed in Section 3.7.1. Moreover, the expansion of this stack into a fully-working fuel cell system will be described in Section 3.7.2.

3.7.1 Polarisation Curve of Fuel Cell Stack

The polarisation curve of a typical low-temperature fuel cell is illustrated in Figure 3.7. The open-circuit voltage V_{oc} is already lower than the ideal voltage and the curve stops at the limiting current I_L. Note that the horizontal axis of the curve may be expressed in current I or current density i, current per unit area. The latter is more often used, as it allows the user to compare the characteristics of different-sized fuel cells.

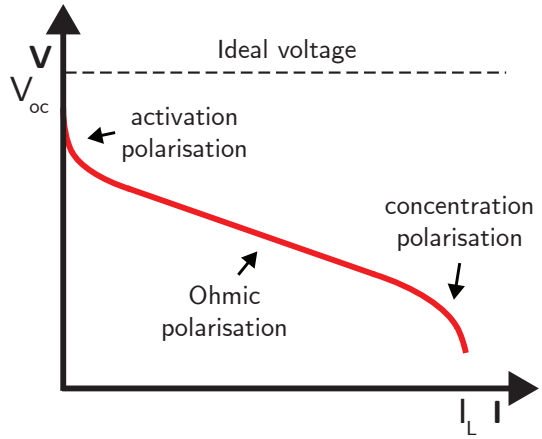

Figure 3.7: Example of a typical low-temperature fuel cell polarisation curve.

The ideal electrochemical performance of a fuel cell can be modelled in several ways. One of the most common methods to characterise this ideal performance is based on the Nernst potential, usually noted as E. This voltage term represents the reversible cell voltage or highest voltage that could exist at a given temperature and pressure. This allows the user to model the ideal performance for a range of temperatures and pressures; in general, the performance improves with increasing temperature or pressure. The Nernst equation is shown in Equation 3.51. Here, E_0 is the emf or cell potential at open-circuit conditions, R is the universal constant of ideal gases (8.314 $J/(K \cdot mol)$), F is the Faraday constant (96,485.33 C/mol), T_{op} is the operating temperature and p_{op} is the operating pressure. The three Greek parameters α, β and δ represent the partial pressures of hydrogen, oxygen and water, respectively [88, 89].

$$E = E_0 + \frac{R \cdot T_{op}}{2 \cdot F} \cdot \ln\left(\frac{\alpha \cdot \beta^{\frac{1}{2}}}{\delta}\right) + \frac{R \cdot T_{op}}{4 \cdot F} \cdot \ln(p_{op}) \tag{3.51}$$

In an ideal fuel cell, the cell voltage E is independent of the current drawn. In practice, this reversible cell voltage cannot be realised due to irreversible processes during fuel cell operation. This difference between actual cell voltage at a given current and ideal cell voltage is known as overpotential. Three major sources of overpotential in a fuel cell are activation, Ohmic and concentration losses [90].

Activation losses are prominent at low current densities and represent the fact that the cell requires a certain amount of energy to start electron circulation and create or break chemical bondings in the anode and the cathode. This explains the significant voltage drop at low currents in both electrodes. The activation loss V_{act} can be related to the current density i by Equation 3.52; A is the slope of the Tafel line and is given by Equation 3.53. Equation 3.52 is better known as the Tafel equation, where α is the charge transfer coefficient, n is the number of electrons involved, i is the current density and i_0 is the exchange current density at which the voltage drop occurs. This equation is only valid when the current density i is higher than the exchange current density i_0 ($i > i_0$).

$$V_{act} = A \cdot \ln\left(\frac{i}{i_0}\right) \tag{3.52}$$

$$A = \frac{R \cdot T_{op}}{\alpha \cdot n \cdot F} \tag{3.53}$$

The Ohmic losses arise due to the resistance of current flow in the electrolyte and in the electrodes. This voltage drop V_{ohmic} follows Ohm's law and can be expressed as Equation 3.54. Here, i is the current density and r_{ohmic} is the cell area specific resistance. The value of internal resistance is heavily dependent on cell humidity and temperature levels [89]. This voltage loss occurs in the middle part of the polarisation curve and is mainly linear.

$$V_{ohmic} = i \cdot r_{ohmic} \tag{3.54}$$

The last form of losses are the concentration or diffusion losses. These are the result of changes in the concentration of reactants while they are consumed by the electrochemical reaction. The effects of voltage drop V_{conc} are mostly evident at high current densities and can be described by Equation 3.55. In this formula, i is the current density and i_Δ is the limiting current density at which the operating fuel rate equals the maximum fuel supply rate.

$$V_{conc} = \frac{R \cdot T_{op}}{n \cdot F} \cdot \ln\left(1 - \frac{i}{i_\Delta}\right) \tag{3.55}$$

Another approach for expressing the concentration losses that is highly favoured, but purely empirical, is given by Equation 3.56. This formula fits experimental results very well, provided that the fitting parameters m and n are chosen properly [88]. This expression will actually be preferred over Equation 3.55 for the curve fitting procedure of an experimental polarisation curve in Section 5.6.

$$V_{conc} = m \cdot \exp(n \cdot i) \tag{3.56}$$

By taking into account all the losses, the actual cell voltage V_{fc} can then be described by Equation 3.57, or more accurately, by Equation 3.58:

$$V_{fc} = E - V_{act} - V_{ohmic} - V_{conc} \tag{3.57}$$

$$V_{fc} = E - \frac{R \cdot T_{op}}{\alpha \cdot n \cdot F} \cdot \ln\left(\frac{i}{i_0}\right) - i \cdot r_{ohmic} + \frac{R \cdot T_{op}}{n \cdot F} \cdot \ln\left(1 - \frac{i}{i_\Delta}\right) \tag{3.58}$$

When the voltage drops as a result of the various losses, the efficiency of the fuel cell decreases. The total or electrical efficiency of the fuel cell $\eta_{elec,fc}$ can be defined in many ways; here, it is computed using Equation 3.59. The electrical efficiency is defined as the ratio of the power output and the amount of fuel utilised. In this formula, $\dot{m}_f$ is the fuel flow rate and LHV_f is the lower heating value of the fuel used; for PEMFCs, this is usually hydrogen and LHV_{H_2} equals 120 MJ/kg [91].

$$\eta_{elec,fc} = \frac{P_{fc}}{\dot{m}_f \cdot LHV_f} = \frac{I_{fc} \cdot V_{fc}}{\dot{m}_f \cdot LHV_f} \tag{3.59}$$

Alternatively, the efficiency $\eta_{elec,fc}$ can also be written as Equation 3.60. This notation is preferred by Ref. [91] to identify where the largest efficiency losses occur.

$$\eta_{elec,fc} = \eta_{th} \cdot \eta_F \cdot \eta_V \cdot \mu_f \tag{3.60}$$

Here, η_{th} is the thermodynamic or theoretical maximum efficiency, which equals 98.1% for hydrogen. η_F is the Faradaic efficiency, which accounts for the charge transfer losses. Electrons may cause unwanted side reactions or leak through the electrolyte membrane; both causes a reduction in Faradaic efficiency. η_V is the voltaic efficiency and decreases with increasing operating current. Finally, μ_f is the fuel utilisation coefficient. This coefficient μ_f is defined by Equation 3.61, as the ratio between the actual fuel consumed and the amount of fuel supplied.

$$\mu_f = \frac{\dot{m}_{f,used}}{\dot{m}_{f,supp}} \tag{3.61}$$

According to Ref. [91], the low electrical efficiency at reduced power settings is mainly caused by the low Faradaic efficiency. At high power settings, the fuel cell operates at a lower voltage, thus yielding a low voltaic efficiency and electrical efficiency.

The next subject to be discussed is the fuel flow rate or hydrogen consumption rate. This parameter is typically specified in standard litres per minute (slpm) or in kilograms per second. The conversion from slpm to kg/s is described by Equation 3.62, where M_{H_2} is the molar mass of hydrogen (2.016 g/mol) and M_{STP} is the molar mass at STP conditions (22.4 L/mol).

$$\dot{m}_{H_2}[kg/s] = \frac{\dot{m}_{H_2}[slpm]}{60 \cdot 10^3} \cdot \frac{M_{H_2}}{M_{STP}} \tag{3.62}$$

A relationship between the hydrogen consumption rate and the operating current is shared by Ref. [92]; this expression is shown in Equation 3.63.

$$\dot{m}_{H_2} = \frac{I_{fc} \cdot \lambda_{H_2} \cdot M_{H_2}}{2 \cdot F} \tag{3.63}$$

Here, I_{fc} is the operating fuel cell current, λ_{H_2} is the hydrogen stoichiometry (typically between 1.1 and 2), M_{H_2} is the molar mass of hydrogen and F is the Faraday constant. Note that the hydrogen consumption rate $\dot{m}_{H_2}$ is now calculated in kg/s.

Lastly, the H_2O emissions can be calculated by applying the mole ratio from the half and net reactions involved in a fuel cell, as described by Equation 3.64 to Equation 3.66 [92]:

$$2H_2 \rightarrow 4H^+ + 4e^- \quad \text{Anode, release of electrons (oxidation)} \tag{3.64}$$

$$O_2 + 4H^+ + 4e^- \rightarrow 2H_2O \quad \text{Cathode, capture of electrons (reduction)} \tag{3.65}$$

$$2H_2 + O_2 \rightarrow 2H_2O \quad \text{Net reaction (redox)} \tag{3.66}$$

Equation 3.66 reveals that 2 moles of hydrogen reacts into 2 moles of water. In terms of kilograms, this translates to 1 kg of hydrogen consumed produces 8.94 kg of H_2O emissions.

3.7.2 Fuel Cell System Sizing

Individual cells can be stacked, similar to batteries, to form a fuel cell stack for high-power and high-voltage applications. Raising the number of cells in a stack increases the voltage, while enlarging the surface area of the cells increases the current. Such a fuel cell stack is finished with end plates and connections for easier use. The stack voltage V_{stack} can be determined by the number of cells stacked in series n_{stack}, as shown in Equation 3.67.

$$V_{stack} = n_{stack} \cdot V_{fc} \tag{3.67}$$

With the operating stack voltage V_{stack} and current density i known, the total stack area A_{stack} required for a defined power output P_{fc} can be calculating using Equation 3.68. Subsequently, the number of cells m_{stack} to produce this required stack area can then be found with Equation 3.69 [78].

$$A_{stack} = \frac{P_{fc}}{V_{stack} \cdot i} \tag{3.68}$$

$$m_{stack} = \frac{A_{stack}}{A_{cell}} \tag{3.69}$$

Finally, the total number of cells necessary to form the complete fuel cell stack for a specified power output P_{fc} is given by Equation 3.70:

$$N_{fc} = n_{stack} \cdot m_{stack} \tag{3.70}$$

The hydrogen consumption rate of Equation 3.63 can then be expressed as:

$$\dot{m}_{H_2} = \frac{N_{fc} \cdot I_{stack} \cdot \lambda_{H_2} \cdot M_{H_2}}{2 \cdot F} \tag{3.71}$$

3.8 Photovoltaic System

In the context of this study, a PV system is also addressed to generate additional electrical power; see Section 2.4 for background information on PV. Later in this section, the efficiency and sizing of PV on aircraft will be discussed.

A possible method to implement PV is to install a thin film of PV cells on the A320neo aircraft; this technique is mimicked from a recently developed solar powered aircraft, the Solar Impulse 2, shown in Figure 3.8.

Figure 3.8: Example of a successful solar powered aircraft project, the Solar Impulse 2 [93].

The wings, fuselage and horizontal stabiliser of the Solar Impulse 2 are covered by a so-called solar skin of PV cells. These cells are less than 120 µm thick and have a commercial module efficiency of 23.6%. To protect the PV panels, an ultra-thin film made from Halar® ethylene chlorotrifluoroethylene (ECTFE) is placed on both sides. This resin has a thickness of 20 µm and ideal properties for PV applications; UV resistant, highly transparent and waterproof. In addition, Solstick® adhesive tape (based on the Solef® polyvinylidene fluoride (PVDF) polymer) covers the 5 mm gap between the panels; this improves the aerodynamics of the wings and adds wing flexibility during flight [94–96]. An illustrative representation of the solar skin is found in Figure 3.9.

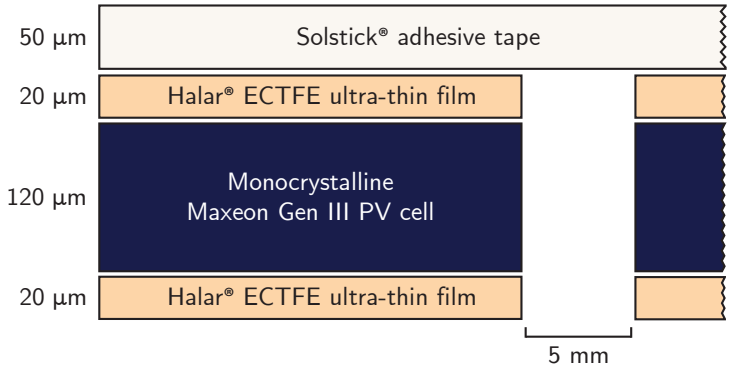

Figure 3.9: Cross-sectional view of the solar skin on Solar Impulse 2.

To calculate the total area density of the solar skin used on the Solar Impulse 2, the volumetric mass density and thickness of each individual component are required. These are summarised in Table 3.16. It is assumed that the monocrystalline Maxeon Gen III solar cell has similar mass density as silicon and that the Solstick® adhesive tape has a thickness of 50 µm (similar to regular adhesive tape).

Table 3.16: Specifications of the solar skin on Solar Impulse 2 [94, 97, 98].

Individual layer of solar skin	Density [g/cm^3]	Thickness [µm]	Area density [kg/m^2]
Monocrystalline Maxeon Gen III PV cell	2.3296	120	0.2796
Halar® ECTFE ultra-thin film	1.68	20	0.0336
Solstick® adhesive tape	1.8	50	0.0900

Assuming that the solar skin consists of the monocrystalline Maxeon Gen III solar cell, two thin films of Halar® ECTFE and Solstick® adhesive tape along the aircraft's surface, the overall area mass density for the solar skin becomes $0.4368\,kg/m^2$. This value is assumed to reduce down to a conservative value of $0.35\,kg/m^2$ by 2040. To complete the PV system, necessary power electronics will be installed to interact with the existing electrical network including a charge controller and batteries to store the generated energy. Additional features of the PV system can be found in Table 3.17.

Table 3.17: Technical characteristics of the PV system in 2020+ and 2040+ [94, 97–100].

Parameter	2020+	2040+
Efficiency [%]	23.6	35
Area mass density [kg/m^2]	0.4368	0.35

In reality, the PV system will be operating on a current and voltage (I-V) curve. To model this accurately in the EMS module, some theory on I-V characteristics and basic equivalent circuit models will be discussed in Section 3.8.1. Furthermore, expanding and sizing the PV cell towards a complete PV system is outlined in Section 3.8.2.

3.8.1 I-V Characterisation of Illuminated Photovoltaic Cell

A photovoltaic cell converts direct sunlight into electricity. This working principle is based on the photovoltaic effect, i.e. the generation of a potential difference at the junction of two different semiconductor materials in response to electromagnetic radiation. Essentially, three basic processes can be distinguished: generation of charge carriers due to the absorption of photons, subsequent separation of the carriers at the p-n junction and collection of these photo-generated carriers at the terminals of the device [50, 101]. Going into the physics behind semiconductor materials is outside the scope of this report; the reader is advised to consult literature on PV fundamentals such as Ref. [50].

One of the most common ways to represent an I-V curve of an illuminated PV cell is through the use of a simple equivalent circuit as shown in Figure 3.10. The diode is connected to a current source in parallel. The I-V characteristics are given by Shockley's ideal diode formula in Equation 3.72, where the thermal voltage V_T is expressed as Equation 3.73. In this case, the PV cell behaves as an ideal diode, therefore the diode ideality factor n is omitted from the formula.

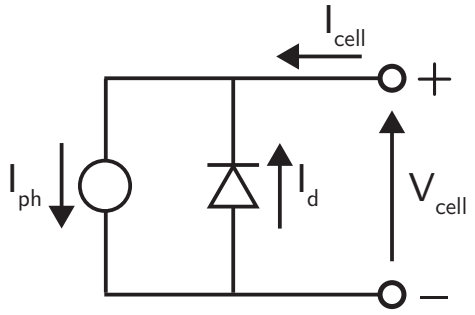

Figure 3.10: Example of a simple equivalent circuit model for an ideal PV cell; adapted from [50].

$$I_{cell} = I_{ph} - I_d = I_{ph} - I_0 \left[\exp\left(\frac{V_{cell}}{V_{T_{cell}}} \right) - 1 \right] \tag{3.72}$$

$$V_{T_{cell}} = \frac{k \cdot T_{op}}{q} \tag{3.73}$$

Here, I_{ph} is the photoelectric current, I_d is the diode current, I_0 is the diode reverse saturation current, V_{cell} is the operating cell voltage, k is the Stefan Boltzmann's constant ($1.38 \cdot 10^{-23}$ J/K), T is the operating cell temperature expressed in kelvins and q is the elementary charge ($1.602 \cdot 10^{-19}$ C).

To model the I-V curve more realistically, the equivalent circuit from Figure 3.10 can be expanded to include a series resistance R_s and a shunt resistance R_p; the result is shown in Figure 3.11. These terms take the parasitic power losses into account. A sensitivity study on how each parameter affects the performance can be found in Section 5.8.3. This circuit is also known as the five parameter model and Equation 3.74 shows the governing formula using Kirchhoff's current law. Note that the diode ideality factor n is present to account for additional recombination losses [50].

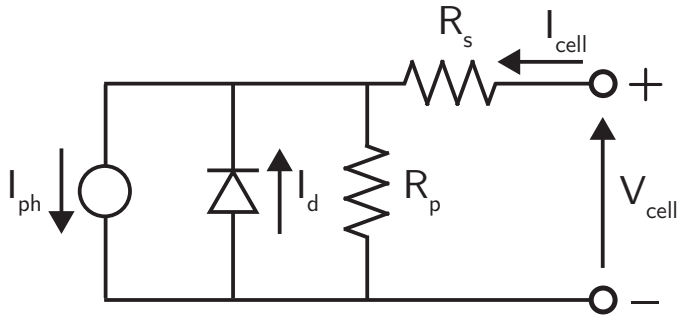

Figure 3.11: Example of a complex equivalent circuit model for PV characterisation; adapted from [50].

$$I_{cell} = I_{ph} - I_d - I_p = I_{ph} - I_0 \left[\exp\left(\frac{V_{cell} + I_{cell} \cdot R_s}{n \cdot V_{T_{cell}}} \right) - 1 \right] - \frac{V_{cell} + I_{cell} \cdot R_s}{R_p} \tag{3.74}$$

If the user connects a load to this modified circuit in Figure 3.11 and sweeps the voltage across the measuring load from zero to the open-circuit voltage V_{oc}, an I-V curve of the illuminated PV cell can be obtained. The generated power can be calculated by multiplying the current with the voltage. Examples of these characteristic curves are illustrated in Figure 3.12.

When modelling the performance of a PV system, two important factors need to be kept in mind: the effect of temperature and the effect of solar radiation.

The performance of a cell is highly sensitive to the operating temperature. When a solar cell is exposed to higher temperatures, the short-circuit current I_{sc} will increase slightly while the open-circuit voltage V_{oc} decreases a significant amount; this shift is illustrated in Figure 3.13a. The effect of temperature on the short-circuit current I_{sc}, the open-circuit voltage V_{oc}, the reverse saturation current I_0 and the photoelectric current I_{ph} is formulated in Equation 3.75 to Equation 3.78.

$$I_{sc,cell} = I_{sc,ref} + \alpha_{I_{sc}} \cdot (T_{op} - T_{ref}) \tag{3.75}$$

$$V_{oc,cell} = V_{oc,ref} + \alpha_{V_{oc}} \cdot (T_{op} - T_{ref}) \tag{3.76}$$

$$I_0 = \frac{I_{sc,cell} + \alpha_{I_{sc}} \cdot (T_{op} - T_{ref})}{\exp\left(\frac{V_{oc,cell} + \alpha_{V_{oc}} \cdot (T_{op} - T_{ref})}{n \cdot V_{T_{cell}}} \right) - 1} \tag{3.77}$$

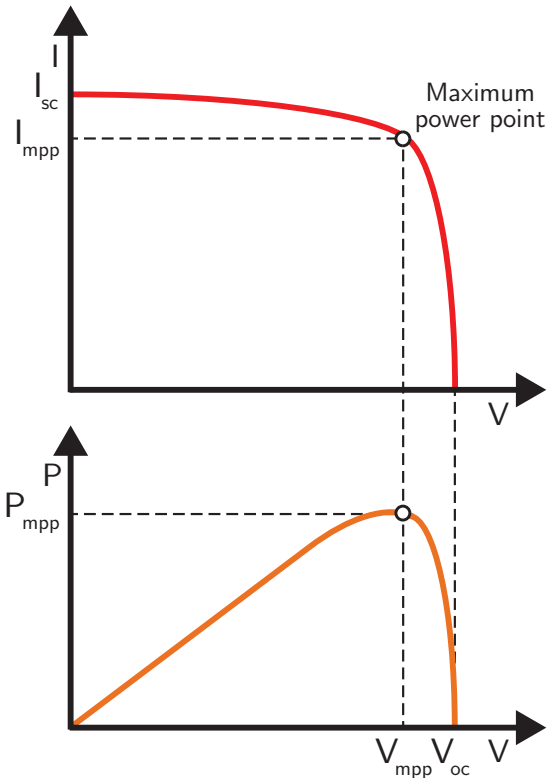

Figure 3.12: Examples of the I-V and P-V curves for an illuminated PV cell.

$$I_{ph} = \left(I_{ph,ref} + \alpha_{I_{sc}} \cdot (T_{op} - T_{ref})\right) \cdot \frac{G_{op}}{G_{ref}} \tag{3.78}$$

In these formulas, $\alpha_{I_{sc}}$ and $\alpha_{V_{oc}}$ are temperature coefficients, while T_{ref} and G_{ref} refer to the temperature and nominal irradiance at Standard Test Conditions (STC); usually 25°C and 1,000 W/m^2, respectively. From Equation 3.78 can also be derived that the photoelectric current I_{ph} is directly proportional to the solar irradiance G_{op}. This causes the current to drop quickly with reduced sunlight, as shown in Figure 3.13b.

To measure how efficient a PV cell behaves, a fill factor (FF) can be determined. This is the ratio between the maximum power generated and the product of the short-circuit current I_{sc} and the open-circuit voltage V_{oc} described in Equation 3.79. This fill factor refers to the degree at which the actual operating conditions performs compared to its potential power; it can never reach a value of 1.

$$FF = \frac{P_{mpp,cell}}{I_{sc,cell} \cdot V_{oc,cell}} = \frac{I_{mpp,cell} \cdot V_{mpp,cell}}{I_{sc,cell} \cdot V_{oc,cell}} \tag{3.79}$$

Another way is to simply calculate the cell efficiency with Equation 3.80. Here, $S_{cell,eff}$ is the effective area of a single PV cell.

$$\eta_{cell} = \frac{P_{out,pv}}{P_{in,pv}} = \frac{V_{oc,cell} \cdot I_{sc,cell} \cdot FF}{G_{op} \cdot S_{cell,eff}} \tag{3.80}$$

Using the newfound relationship between the fill factor and the maximum power, Equation 3.80 can also be written as:

$$\eta_{cell} = \frac{P_{mpp,cell}}{G_{op} \cdot S_{cell,eff}} = \frac{I_{mpp,cell} \cdot V_{mpp,cell}}{G_{op} \cdot S_{cell,eff}} \tag{3.81}$$

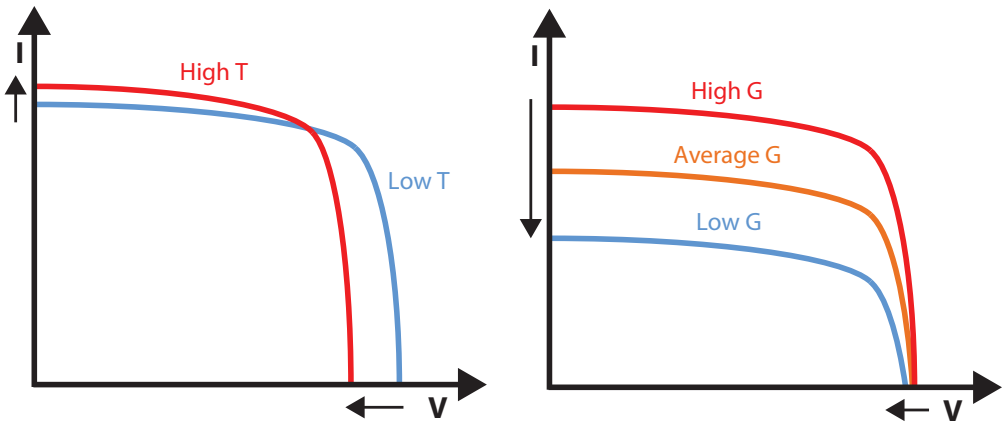

(a) Effect of temperature on the I-V curve.

(b) Effect of solar irradiance on the I-V curve.

Figure 3.13: Effect of temperature and solar irradiance on the I-V curve and cell performance; adapted from [50].

3.8.2 Photovoltaic System Sizing

The shape of the I-V curve, presented in Figure 3.12, is similar for a PV module or array. However, the values for short-circuit current I_{sc} and open-circuit voltage V_{oc} will scale based on the number of cells connected in series (indicated by n_{cell}) and in parallel (indicated by m_{cell}); a similar procedure is used for batteries in Section 3.5.3. If n cells are connected in series, the short-circuit current I_{sc} is multiplied by n; if m cells are connected in parallel, the open-circuit voltage V_{oc} is multiplied by m. The effect of this sizing procedure is shown in Figure 3.14.

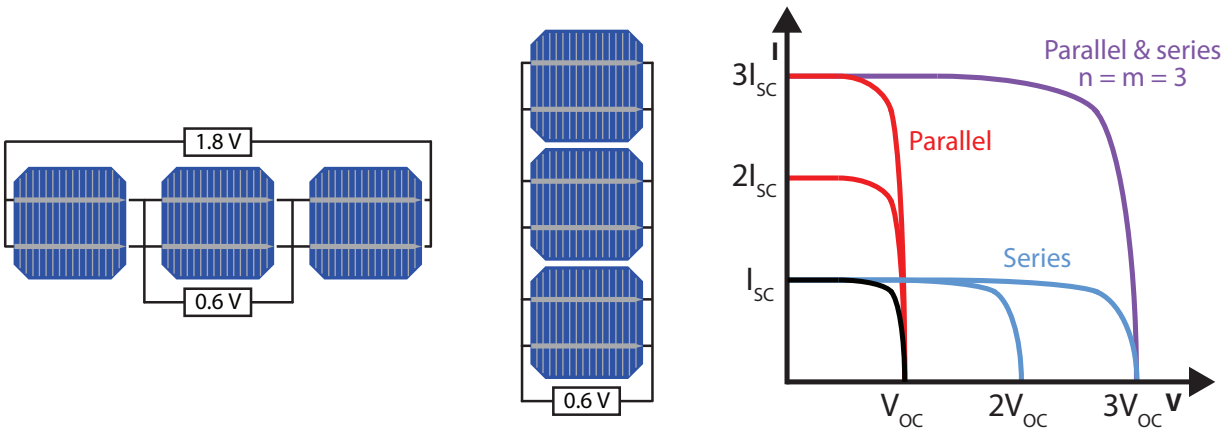

(a) Cells in series: n = 3.

(b) Cells in parallel: m = 3.

(c) I-V curves of cells in series and in parallel.

Figure 3.14: I-V characteristics of PV cells in series and in parallel; adapted from [50].

A PV module is defined as a larger device in which many cells are connected in series and in parallel. In turn, these modules can be connected in series to form a PV string and multiple strings in parallel together are specified as a PV array [50]. The accompanying formulas are described by Equation 3.82

to Equation 3.86.

$$n_{pv,total} = n_{pv,cell} \cdot n_{pv,module} \tag{3.82}$$
$$m_{pv,total} = m_{pv,cell} \cdot m_{pv,module} \tag{3.83}$$
$$N_{pv} = n_{pv,total} \cdot m_{pv,total} \tag{3.84}$$
$$I_{sc,system} = I_{sc,cell} \cdot m_{pv,total} \tag{3.85}$$
$$V_{oc,system} = V_{oc,cell} \cdot n_{pv,total} \tag{3.86}$$

For a complete PV system, Equation 3.74 turns into the following formula:

$$I_{pv} = m_{pv,total} \cdot I_{ph} - m_{pv,total} \cdot I_0 \left[\exp\left(\frac{V_{pv} + n_{total} \cdot I_{pv} \cdot R_s}{n_{pv,total} \cdot n \cdot V_T} \right) - 1 \right] - \frac{V_{pv} + n_{pv,total} \cdot I_{pv} \cdot R_s}{n_{pv,total} \cdot R_p} \tag{3.87}$$

It is assumed that all cells are identical within the whole PV system; in reality, this is not the case as there are manufacturing imperfections and ageing effects [101]. Also, the temperature and solar irradiance are assumed to be uniform across all cells. Using these two assumptions and Equation 3.81, the system efficiency can be defined as:

$$\eta_{pv} = \frac{P_{mpp,pv}}{G_{op} \cdot S_{pv,eff}} = \frac{I_{mpp,pv} \cdot V_{mpp,pv}}{G_{op} \cdot n_{pv,total} \cdot m_{pv,total} \cdot S_{cell,eff}} \tag{3.88}$$

3.9 Power Management Strategy and Optimisation

The overall performance of the EAPPS from a mission perspective is based on the power management strategy applied. It describes when and how much power is provided throughout the mission from two different sources: the turbofan engine and the electric motor. From this, the power split ratio ϕ can be calculated using Equation 2.1:

$$\phi = \frac{P_{electric}}{P_{total}} = \frac{P_{electric\ motor}}{P_{engine} + P_{electric\ motor}} \tag{3.89}$$

Since this approach determines the amount of electrical power and energy required for the complete mission, the electrical system can be sized accordingly. In turn, the additional mass of this electrical system must be justified by its improvement in overall performance and efficiency.

While taxiing, the main engines operate inefficiently at power settings of approximately 7-15% [102]; this leads to excessive fuel burn between gate and runway. For short and medium-haul flights this becomes even more prominent, as the taxiing procedure takes up a lot of time, compared to the actual length of the flight [103]. By performing this phase electrically, fuel and emission savings can be achieved. During the take-off and climb segments, the overall system efficiency increases due to the assistance of a highly efficient electric motor. Considering that the sizing of the turbofan engine is no longer dictated by the maximum take-off thrust, the engine can be sized and optimised for the cruise phase. In the time of descent and approach, the battery can be recharged by the turbofan via a generator. The final landing and taxi-in procedures are, once again, carried out electrically.

The choice to perform electric aircraft taxiing is in line with current advancements. Airbus and Safran have recently developed an Electric Green Taxiing System (EGTS) for the A320 family; it will be

released in the near future and available as both a retrofit and forward fit option. The benefits of electric taxiing include reduction in operating costs as well as lower carbon footprints [104].

The power management strategy proposed for the EAPPS is summarised below and mapped in Figure 3.15 (inactivity is indicated as transparent):

1. Taxi-out: electric motor only ($\phi_{taxiout} = 1$)
2. Take-off: turbofan engine is assisted by the electric motor (based on $\phi_{takeoff}$)
3. Climb: turbofan engine is assisted by the electric motor (based on ϕ_{climb})
4. Cruise: turbofan engine only ($\phi_{cruise} = 0$)
5. Descent & approach: turbofan engine can recharge the batteries ($\phi_{descent}, \phi_{approach} = 0$)
6. Landing & taxi-in: electric motor only ($\phi_{landing}, \phi_{taxiin} = 1$)

In this study, the power split ratio is applied on the average total power required in each flight phase; this ensures that the electrical power supplied is constant throughout each phase.

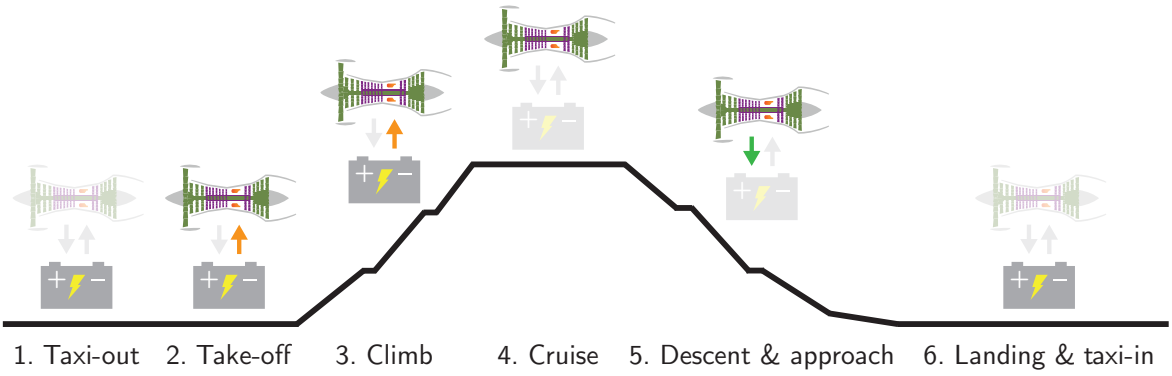

Figure 3.15: Selected power management strategy throughout mission (inactivity is indicated as transparent).

The optimal power management strategy in the EAPPS simulation model is the one which leads to the lowest fuel and energy consumption, while the total aircraft mass stays below the MTOM limit. To find this optimal configuration with near future technology (2020+), the power management strategy will vary from 0% to 40% with increments of 10% for both take-off and climb power splits ($\phi_{takeoff}$ and ϕ_{climb}). This gives a set of 25 different configurations per case. Ideally, smaller increments are preferred, but due to time constraints, this is not achievable within this project.

Since far future technology (2040+) results in lower electrical system mass and thus enables greater degrees of hybridisation, the power split ratios will range from 0% to 50% with increments of 10%. This yields a total of 36 power management strategies to be analysed per case.

3.10 Energy Management Strategy and Optimisation

The electrical system consists of three different energy providers: the PV system, the PEMFC system and the battery system. The electrical power and energy received from PV is determined by the incoming solar irradiance, while the power supply of the PEMFC system is specified by the user. This implies that

only the battery system can be optimised; the energy management optimisation is simply determining the minimal battery system setup that can provide the required power within certain operating range.

The optimal battery system setup in the EMS module is the one with the smallest battery pack or the lowest total amount of batteries. In this analysis, the number of cells in series n_{batt} is varied from 600 to 740 and the number of cells in parallel m_{batt} is varied from 2 to 800; these cell ranges are based on the required power requirements and operating limitations. A total of 112,659 different battery combinations will be investigated.

3.11 System Modelling of Airbus A320neo with EAPPS

In order to investigate the flight performance of the Airbus A320neo equipped with a selected EAPPS configuration, two simulation models will be developed: the EAPPS module and the EMS module. The two separate modules along with the associated input and output parameters are illustrated in Figure 3.16.

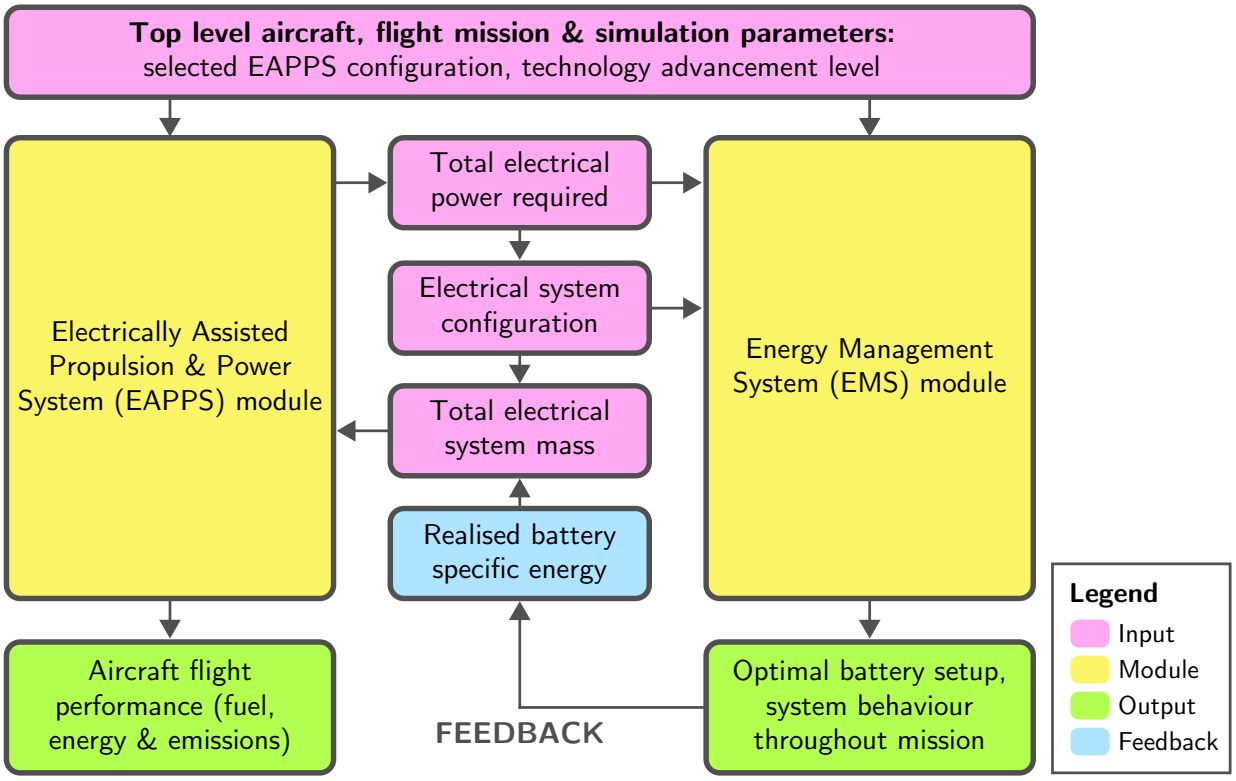

Figure 3.16: Schematic overview of modelling the Airbus A320neo flight performance with EAPPS.

For both modules, the same aircraft, flight mission and simulation parameters are specified as input; this ensures that the results will be consistent. The EAPPS simulation model is essentially an advanced flight mission analysis tool which can compute the performance of a hybrid electric aircraft through several simulation steps (see Section 4.1). In this case, the electrical system is represented as a low-fidelity model, which only accounts for fixed system parameters. The most important outputs of this module are the fuel and energy consumption as well as the aircraft emissions.

The EMS module is an in-depth simulation model of the electrical system only and considers the internal dynamics of four components: the electric motor, the PV system, PEMFC system and the

battery system. The main inputs are the total power required, by the electric motor and the non-propulsive power systems, as well as the configuration of this electrical system. Its output is the most optimal battery system setup which can conform to the defined power requirements and operating limitations. Also, the behaviour of the aforementioned components throughout the entire mission will be available. This module provides valuable feedback on the realised specific energy of the battery system, which leads to a new electrical system mass. This updated mass value can be put back into the EAPPS module to re-evaluate the aircraft performance and increase the model's level of fidelity.

These two modules will be covered in more detail in Chapter 4 and Chapter 5, respectively.

CHAPTER 4

EAPPS Simulation Model

To put this altogether, an advanced flight simulation and analysis tool is required to accurately model the aircraft performance of the Airbus A320neo as well as the technologies addressed in Chapter 3; the result of this integration is an EAPPS configuration. This chapter will cover the whole arrangement of the EAPPS simulation model, from assumptions to modelling approaches to validation and verification.

In the first place, the method used to implement the electrification of the propulsion system within the simulation will be explained in Section 4.1. This concludes with a schematic overview of this EAPPS module. Then, the associated model assumptions and limitations will be described in Section 4.2, followed by the mission profile in Section 4.3. The approaches and accompanying formulas used to simulate the aircraft and engine performances are covered in Section 4.4 and Section 4.5, respectively. Afterwards, the aspects regarding the aircraft mass can be found in Section 4.6. Then, in Section 4.7, the solar irradiation model is discussed along with some important equations to convert between local clock and solar times. The chosen EAPPS configuration for this study will then be illustrated in Section 4.8. Lastly, the verification and validation procedures of various component models can be found in Section 4.9.

4.1 Schematic Overview

In terms of turbomachinery, the hybridisation of the Airbus A320neo can be realised by physically connecting the electric motor to the low pressure (LP) shaft of the CFM LEAP1A-26 engine. This allows the motor to supplement additional shaft power to the fan. The electrification of the propulsion system, conforming to the power management strategy outlined in Section 3.9, can be simulated by separating the hybridisation approach into four discrete simulation steps. These steps are indicated in a flow diagram of the EAPPS module, illustrated in Figure 4.1 and summarised in Table 4.1. This methodology was conceived by United Technologies Research Center (UTRC) [105] and has been further developed in Ref. [1].

The first step of the procedure is to simulate the reference mission; this is done to determine the power requirements of the LP shaft throughout flight. From this, the power split ratios defined by the power management strategy can be applied in step 2, resulting in reduced LP shaft power requirements. This additional shaft power supplied by the electric motor will be added as a negative power off-take to the LP shaft within the GSP® model. The mission will then be simulated with the new LP shaft power

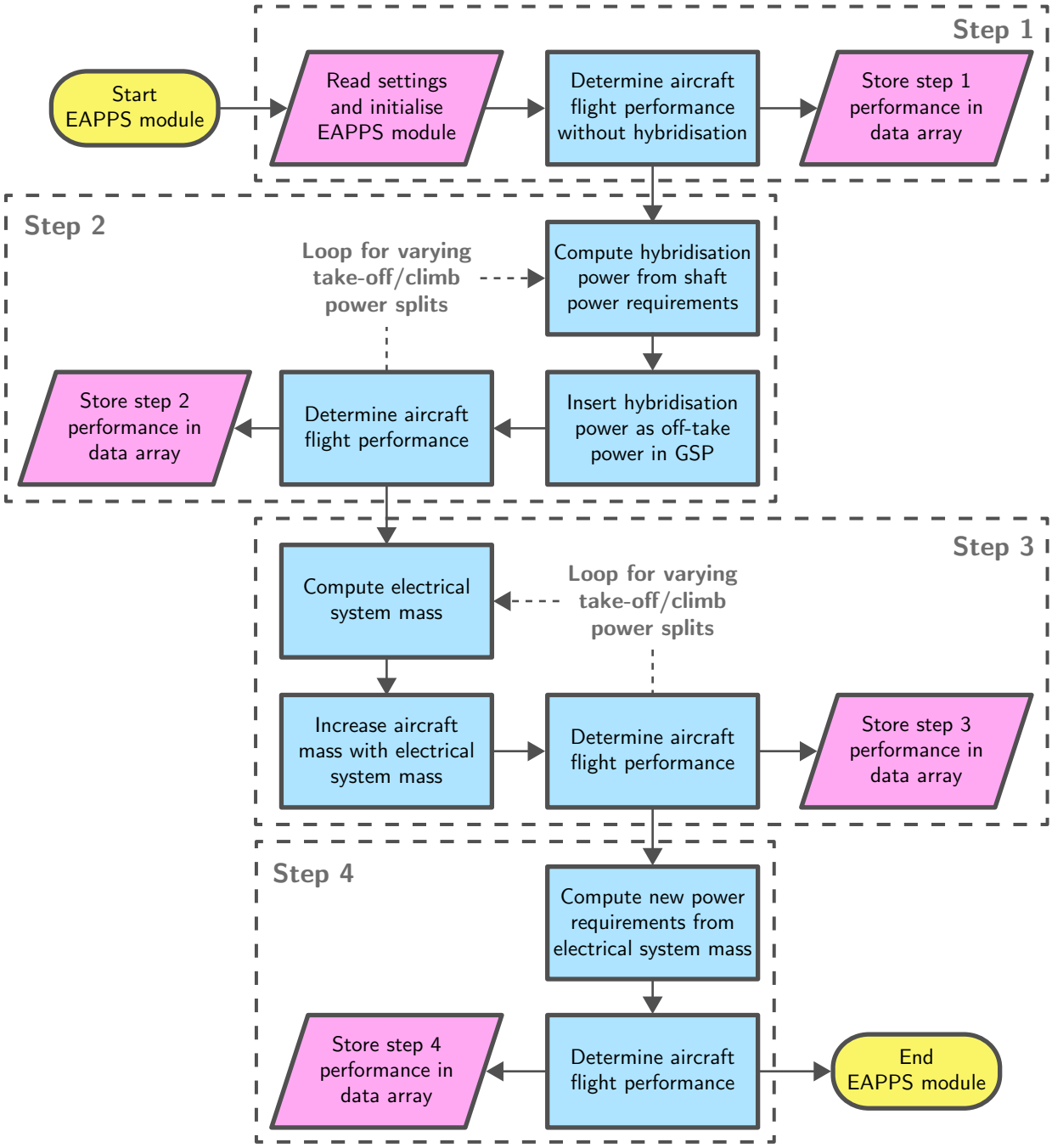

Figure 4.1: Schematic overview of the EAPPS module, including four discrete simulation steps.

requirements and additional electrical power, but without taking the mass of the electrical system into account. In step 3, this electrical system mass will be calculated based on the power supplied by the electric motor. Again, a full mission is simulated; this time keeping the LP shaft power requirements unaltered, but including the mass of the electrical system. This produces new values for the LP shaft power to meet the new thrust requirements due to increased aircraft mass. In the last step, the electrical shaft power calculated in step 2 will be added to the new LP shaft power requirements from step 3. Once more, a full simulation will be performed to obtain the final results of the electrification. Keep in mind that the resulting power split ratios in step 4 will be lower than in step 2, because the LP shaft power requirements used in step 2 did not account for the electrical system mass.

Table 4.1: Electrification methodology in four discrete simulation steps; adapted from [1, 105].

Step	Description	Power of electrical system	Mass of electrical system
1	Simulate reference flight mission		
2	Compute peak power and energy required from electrical system based on $\phi_{takeoff}$ and ϕ_{climb}	▪	
3	Determine and apply electrical system mass		▪
4	Finalise electrification of propulsion system	▪	▪

4.2 Model Assumptions and Limitations

The main assumptions and limitations used within the EAPPS model are as follows:

- *Full mission profile*
  The model covers the whole flight mission from taxi-out to taxi-in for a mission range of 1,000 km; details are described in Section 4.3. Within this mission, a power management strategy can be applied; refer to Section 3.9 for more information.
- *Horizontal runway*
  The runway at the airport is assumed to be horizontal; no elevation is present.
- *Thrust in direction of velocity*
  The thrust vector of the engine acts in the same direction as the velocity vector of the aircraft.
- *Only steady and symmetrical flight*
  The aircraft is constrained to lateral manoeuvres (pitch) only; the aircraft neither turns (yaw) or banks (roll). In reality, an aircraft will often perform a combination of these three movements to fly a specified mission from A to B.
- *Only longitudinal stability*
  Only longitudinal stability and control is taken into account, as the flight is assumed to be symmetrical.
- *No wind disturbances*
  The aircraft is not affected by any wind disturbances in the model.
- *MTOM as absolute mass limitation*
  The MTOM of the conventional A320neo is taken as the maximum limit on the aircraft mass, including all equipment that represents the EAPPS. A detailed mass breakdown is given in Figure 3.1.
- *Constant aircraft geometry and aerodynamics*
  The aircraft geometry stays the same. When photovoltaic panels are installed on the outer skin of the aircraft or when the engine is being downscaled, the aerodynamic characteristics are assumed to remain unchanged.
- *Constant payload*
  The payload remains constant and is equal to the maximum payload of 190 passengers (17,100 kg) for the conventional A320neo configuration. With an OEM of 45,700, this implies that the MZFM stays constant as well, at a total mass of 62,800 kg.

- *Initial fuel mass of 4,000 kg*
  The initial fuel mass is assumed to be a total of 4,000 kg, as mentioned in Section 3.1. This amount is based on a reference flight mission of 1,000 km, including taxi and trip fuel.
- *Constant battery mass*
  The mass of the batteries in the electrical system is assumed to stay constant throughout the mission. Future battery technologies may make use of advanced chemical compositions, allowing the mass to significantly change while charging or discharging.
- *No electrical system overhead*
  The equipment for monitoring and cooling the electrical components is not taken into account.
- *Minimum battery state of charge is 10%*
  The state of charge (SOC) of the lithium-ion battery is limited to 10% due to safety reasons; discharging the battery beyond the cut-off voltage can lead to permanent damage such as reduced battery lifetime or even explosions. Therefore, the device cannot be discharged below 10% SOC within this study.
- *Sufficient hydrogen on-board*
  It is assumed that there is enough hydrogen on-board to carry out the full mission. In addition, the mass of the required hydrogen is negligible compared to the total aircraft mass and will not be taken into account.
- *Near and far future technology level*
  The system components that form the electrical system for the EAPPS is based on the technology level projected for the near future (2020+) and far future (2040+). The assumed mass-related parameters and efficiencies are based on linear regression analyses (Section 3.3) and multiple sources in literature.
- *Constant aircraft engine performance and mass*
  The performance and mass of the CFM LEAP-1A engine are considered to stay the same within a time span of 20 years (from 2020+ to 2040+); in reality, the gas turbine performance will deteriorate over time which also implies that more maintenance is required. Aircraft engines are usually replaced entirely with newer and more efficient models instead of applying engine upgrades; these are more common in the automotive industry than in aviation.
- *Electric motor attached to LP shaft*
  The electric motor is assumed to be physically attached to the LP shaft of the turbofan engine. This implies that the additional shaft power supplied by the motor is added to the LP shaft of the engine, as part of the hybridisation approach.
- *Only shaft speed and temperature as engine limitations*
  Only the limitations on the LP and HP shaft speeds, exhaust gas temperature (EGT) and HPT NGV temperatures are considered for the CFM LEAP-1A engine. The limits on shaft speeds N_1, N_2 and EGT (T_{t45}) are stated in Ref. [61]. An EGT margin of 75°C is selected and the NGV temperature T_{t41} is assumed to be 2,000 K. Note that the EGT is merely used as an indicator and not a hard limitation; the user may decide whether to apply this boundary condition or not.
- *Engine bleed occurs at 10th stage of HPC*
  The bleed air for powering the aircraft subsystems and engine cooling is extracted at the last stage of the high pressure compressor (HPC). In reality, the CFM LEAP-1A makes use of an advanced bleed air system: this system controls several bleed valves at various locations according to a detailed engine bleed schedule.

- *Linear engine scaling*
  The CFM LEAP-1A engine will be scaled linearly according to scaling parameters defined in Ref. [65]. In practice, this does not hold for components such as casing wall thicknesses, trailing edge radii, etcetera. Also, by downscaling the engine, a certain point will be reached when required tip clearances cannot be produced due to manufacturing limitations; this would have a significant impact on the overall engine performance.

4.3 Mission Profile

The mission profile of a commercial passenger airliner can usually be broken down into several phases: taxiing, take-off, climb, cruise, descent, approach and landing. Figure 4.2 shows a schematic diagram of a typical flight mission for an Airbus A320neo. The altitudes and velocities are based on values indicated in the Airbus Flight Operations Manual [106].

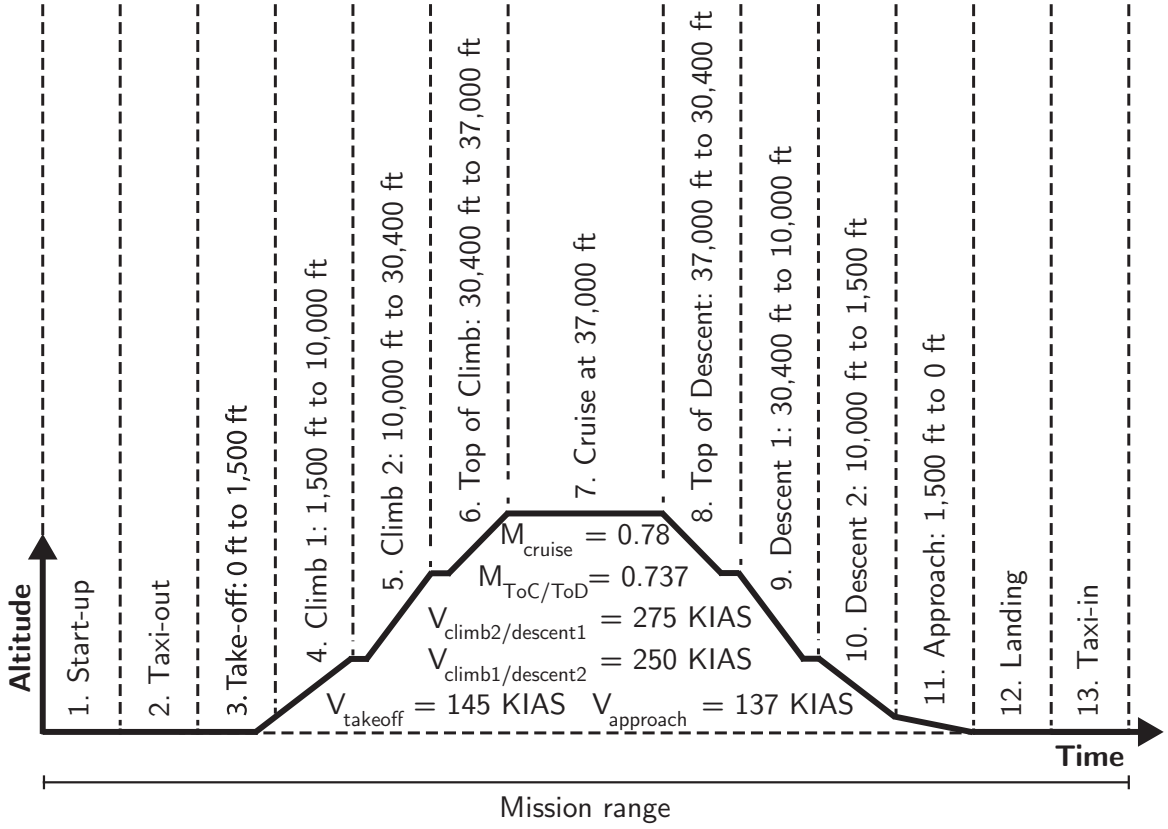

Figure 4.2: Typical mission profile of Airbus A320neo; based on [106].

The mission begins with the aircraft parked at the airport gate to start up the engine and other systems (segment 1). Soon after all passengers are boarded, the aircraft will taxi out towards the runway (segment 2). The take-off phase is one of the most critical phases throughout the mission and covers everything from ground level till 1,500 ft (segment 3). From here on, the aircraft climbs with a constant speed of 250 Knots-Indicated Air Speed (KIAS) from 1,500 ft to 10,000 ft (segment 4). Then, the aircraft will accelerate to 275 KIAS before climbing further to 30,400 ft (segment 5). This is known as the crossover altitude, where the aircraft will climb at a constant Mach number of 0.737 until 37,000 ft (segment 6). At cruise altitude, the aircraft will accelerate to a Mach number of 0.78 and keep this constant throughout cruise (segment 7). Right before the descent phase, the aircraft will decelerate to Mach 0.737. The descent phase is carried out in the same fashion as for the climb phase, but mirrored;

the first leg of the descent is flown at a constant Mach number of 0.737 (segment 8), followed by two legs of constant KIAS (segment 9 and 10). The approach starts at an altitude of 1,500 ft with a speed of 137 KIAS till touchdown (segment 11). The mission ends with the aircraft decelerating during landing (segment 12) and taxiing back to the airport apron (segment 13).

In this study, the reference flight mission is based on a range of 1,000 km, following the mission profile described above.

4.4 Aircraft Flight Performance

Each mission segment can be modelled separately, based on different sets of equations of motion. Since the taxi, take-off and landing segments are of short duration compared to the other segments, these ground performance models will be reduced to two-dimensional form. The free body diagrams can be found in Figure 4.3, along with the accompanying simplified equations of motion.

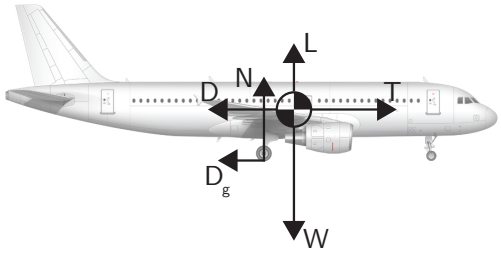

$$\left.\begin{aligned} T - D - D_g &= m \cdot a_{taxi} \\ N &= W - L \\ D_g &= \mu_{roll} \cdot N \end{aligned}\right\} \quad T - D - \mu_{roll} \cdot (W - L) = m \cdot a_{taxi}$$

a) Taxi

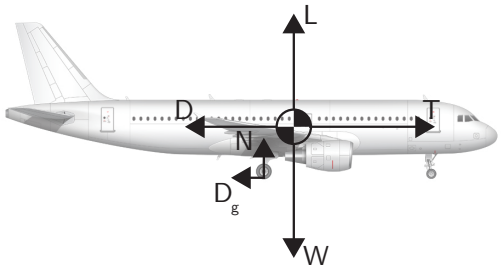

$$\left.\begin{aligned} T - D - D_g &= m \cdot a_{takeoff} \\ N &= W - L \\ D_g &= \mu_{roll} \cdot N \end{aligned}\right\} \quad T - D - \mu_{roll} \cdot (W - L) = m \cdot a_{takeoff}$$

b) Take-off

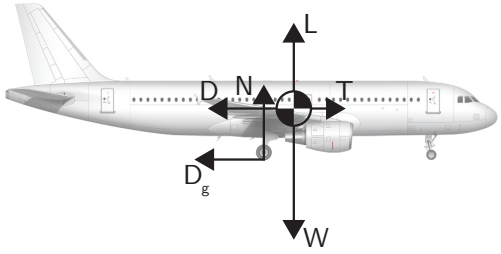

$$\left.\begin{aligned} T - D - D_g &= m \cdot a_{landing} \\ N &= W - L \\ D_g &= \mu_{roll} \cdot N \end{aligned}\right\} \quad T - D - \mu_{roll} \cdot (W - L) = m \cdot a_{landing}$$

c) Landing

Figure 4.3: Free body diagrams and simplified equations for taxi, take-off and landing phases.

To solve these equations, the aerodynamic forces lift and drag need to be determined. The lift coefficient C_L can be computed using Equation 4.1:

$$C_L = C_{L_0} + C_{L_\alpha} \cdot \alpha \tag{4.1}$$

Subsequently, the lift L can be calculated from Equation 4.2:

$$L = C_L \cdot q_{dyn} \cdot S \tag{4.2}$$

The drag coefficient consists of five components: zero-lift drag C_{D_0}, induced drag, drag due to flap extension $C_{D_{flaps}}$, drag due to landing gear $C_{D_{gear}}$ and compressibility drag due to increased Mach numbers $C_{D_{mach}}$. Putting this together results in Equation 4.3:

$$C_D = C_{D_0} + k \cdot {C_L}^2 + \Delta C_{D_{flaps}} + \Delta C_{D_{gear}} + \Delta C_{D_{mach}} \tag{4.3}$$

Similar to the lift force, the drag D can be expressed using the drag coefficient C_D, the dynamic pressure q_{dyn} and the wing area S. This is shown in Equation 4.4:

$$D = C_D \cdot q_{dyn} \cdot S \tag{4.4}$$

Since fuel is being consumed throughout the flight mission, the mass of the aircraft is not considered to be constant. This change in aircraft mass due to fuel flow Δm is formulated in Equation 4.5:

$$\Delta m = -\dot{m}_f \tag{4.5}$$

The GSP® add-on calculates this fuel flow based on the state of the aircraft (Mach number M, altitude h and required thrust F_{thrust}). The resultant change in aircraft mass can then be fed back into the next iteration.

For the other flight segments (climb, cruise and descent), a more sophisticated flight performance model is used governed by three-dimensional point-mass differential equations. This set of equations results in seven state variables:

- V; the velocity in [m/s]
- h; the altitude in [m]
- γ; the flight path angle in [rad]
- φ; the bank angle in [rad]
- ψ; the heading angle in [rad]
- x_{north}; the relative position of the aircraft towards the North in [m]
- x_{east}; the relative position of the aircraft towards the East in [m]

Assuming that the angle of attack α is relatively small and no wind is present ($V_{wind} = 0$), the aircraft equations of motion become (Equation 4.6 to 4.12):

$$\dot{V} = \frac{F_{thrust} - D}{m} - g \cdot \sin\gamma \tag{4.6}$$

$$\dot{h} = V \cdot \sin\gamma \tag{4.7}$$

$$\dot{\gamma} = \frac{L}{m \cdot V} \cdot \cos\varphi - \frac{g}{V} \cdot \cos\gamma \tag{4.8}$$

$$\dot{\varphi} = p \tag{4.9}$$

$$\dot{\psi} = \frac{g \cdot \tan\varphi}{V} \tag{4.10}$$

$$\dot{x}_{north} = V \cdot \cos\gamma \sin\psi \tag{4.11}$$

$$\dot{x}_{east} = V \cdot \cos\gamma \cos\psi \tag{4.12}$$

Along with the previous equations for lift, drag and change of mass (Equation 4.1 to 4.5), the aircraft flight performance can be computed for the remaining segments. More details and information of this flight performance model can be found in Ref. [107].

4.5 Engine Performance

The performance of the CFM LEAP-1A26 turbofan engine can be reproduced using GSP® software developed by Netherlands Aerospace Centre (NLR). To determine the unknown engine parameters, alterations are made iteratively until the output data corresponds to the available data. The design temperature of the nozzle guide vanes (NGVs) T_{t41} of the HPT is assumed to be at 2,000 K.

To initialise the engine model, the rotor speeds and bypass ratio (BPR) are used as input values. Then, the pressure ratios of the fan, HPC and low pressure compressor (LPC) will be adjusted until a desired overall pressure ratio (OPR) is reached. A similar procedure follows with the take-off thrust by changing the design mass flow rate at the inlet [1]. To ensure the engine is optimised for specific fuel consumption (SFC), the jet velocity ratio should be between 0.7 and 0.9 depending on the overall conditions [68, 108]. This ideal jet velocity ratio can be achieved by varying the outer fan pressure ratio. Figure 4.4 shows the CFM LEAP-1A26 engine model in the GSP® environment.

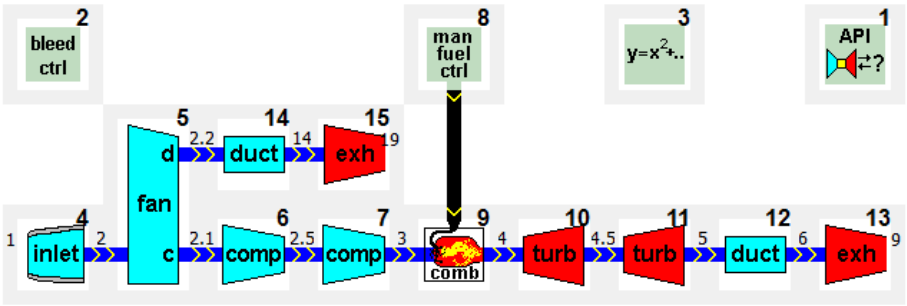

Figure 4.4: GSP® model of the CFM LEAP-1A26 turbofan engine.

Engine Emissions

The engine emissions are also modelled within the GSP® environment. To do so, emission data is taken from the ICAO Aircraft Engine Emissions Databank [102] and implemented into the engine model. As input, GSP® requires the emissions indices (EIs) for UHC, CO and NO_x as well as the smoke number (SN) throughout each phase of the LTO cycle (take-off, climb out, approach and idle). In addition, the fuel flow, total pressure and temperature after the HPC (indicated as point 3 in Figure 4.4) are given. Table 4.2 presents the emission data for the CFM LEAP-1A26 as input for GSP®.

Table 4.2: Emission data from ICAO Aircraft Engine Emissions Databank for the CFM LEAP-1A26 engine [102].

Mode	$\dot{m}_{fuel}$ [kg/s]	T_{t3} [K]	P_{t3} [bar]	EI_{UHC}	EI_{CO}	EI_{NO_x}	SN
take-off	0.855	1,050.5	44.946	0.02	0.22	18.77	1.30
climb out	0.705	994.1	38.996	0.02	0.27	11.16	1.17
approach	0.242	713.1	18.461	0.04	2.74	8.67	1.31
idle	0.088	560.7	7.384	0.28	21.4	4.63	1.25

4.6 Mass Breakdown

The complexity of the mass model is reduced to only account for the aircraft mass, the change in mass due to transitioning from conventional to electrical subsystem architecture, the amount of fuel

burnt and the system components of the electrical system. The initial aircraft mass is calculated using Equation 4.13.

$$m_{aircraft,init} = m_{aircraft,MZFM} + \Delta m_{conversion} + m_{fuel} + m_{electricsystem} \tag{4.13}$$

The MZFM is equal to 62,800 kg, as stated earlier in Table 3.1. The conversion mass change $\Delta m_{conversion}$ is described in Table 4.3; these values are based on detailed subsystem sizing methods and empirical relationships from a systems architecture design tool called Pacelab SysArc. These practices were presented in a study comparing the performance of conventional and electrical subsystem architectures for a single-aisle narrowbody aircraft such as the Airbus A320neo. Other components include additional wiring, increased auto transformer rectifier units (ATRUs) and the removal of generators due to the use of batteries [36].

Table 4.3: Mass changes for converting from conventional to electrical subsystem architecture [36].

Description	Change in mass [kg]
Actuation	- 725
Landing gear	- 100
IPS	- 101
ECS	- 55
Other components	+182
Total	**- 799**

The initial fuel mass is assumed to be 4,000 kg for this study, as mentioned before in Section 3.1. The mass of the electrical system equals the mass of the electric motor, inverters, batteries and cables. If fuel cells and/or PV panels are installed, these masses will be included as well. The masses are obtained by using the mass-related parameters stated in Section 3.3 to Section 3.8. The corresponding formulas are shown below (Equation 4.14 to 4.21):

$$m_{electricsystem} = m_{electricmotor} + m_{inverters} + m_{batt} + m_{cables} + m_{fc} + m_{pv} \tag{4.14}$$

$$m_{electricmotor} = \frac{P_{electricmotor}}{\bar{p}_{electricmotor}} \tag{4.15}$$

$$m_{inverters} = m_{inv,batt} + m_{inv,fc} + m_{inv,pv} \tag{4.16}$$

$$m_{inv,x} = \frac{P_{inv,x}}{\bar{p}_{inverter}} \tag{4.17}$$

$$m_{batt} = \frac{E_{batt}}{e_{batt}} \tag{4.18}$$

$$m_{cables} = m_{electricsystem} \cdot \%_{mass,electricsystem} \tag{4.19}$$

$$m_{fc} = \frac{P_{fc}}{\bar{p}_{fc}} \tag{4.20}$$

$$m_{pv} = \rho_{A,pv} \cdot S_{pv,eff} \tag{4.21}$$

The instantaneous aircraft mass can then be determined using Equation 4.22:

$$m_{aircraft} = m_{aircraft,init} - \int \dot{m}_f \cdot dt \tag{4.22}$$

4.7 Solar Irradiation

The solar irradiance, which varies slightly throughout the year, can be determined by calculating the actual distance between the Earth and the Sun, r, at a given time of the year. In this procedure, the following formulas are applied:

$$r = r_m \cdot \frac{(1-\varepsilon^2)}{(1+\varepsilon \cdot \cos(\alpha))} \tag{4.23}$$

$$\alpha = \left(\frac{2\pi \cdot (n-4)}{365}\right) \tag{4.24}$$

$$SF = SF_m \cdot \tau \frac{r_m^2}{r^2} \tag{4.25}$$

where the mean radius of the Earth r_m is $1.496 \cdot 10^8$ km, the Earth's orbital eccentricity ε is 0.017, the mean solar irradiance at orbit SF_m is 1,367 W/m^2 and the day number n is based on the day of the year (for January 1st, $n = 1$). The solar attenuation factor due to the atmosphere τ is assumed to be 0.80 for this study [109].

The incidence angle of incoming solar irradiance θ depends on the solar declination angle δ, the orientation of the panels characterised by the inclination angle β and the azimuth angle γ, the latitude φ and the time of the day expressed as the hour angle ω. The equation becomes:

$$\begin{aligned}\theta =& \operatorname{acos}\Big(\sin(\delta)\sin(\varphi)\cos(\beta) - \sin(\delta)\cos(\varphi)\sin(\beta)\cos(\gamma) + \\ & \cos(\delta)\cos(\varphi)\cos(\beta)\cos(\omega) + \cos(\delta)\sin(\varphi)\sin(\beta)\cos(\gamma)\cos(\omega) + \\ & \cos(\delta)\sin(\beta)\sin(\gamma)\sin(\omega)\Big)\end{aligned} \tag{4.26}$$

The declination angle δ changes with the day of the year d_n. This parameter d_n is based on the vernal equinox in the Northern hemisphere (e.g. $d_n = 1$, if the date is March 21st), the instance at which the Sun shines directly on the Earth's equator. This declination angle can be calculated with the following equation:

$$\delta = 0.4091 \cdot \sin\left(\frac{2\pi \cdot d_n}{365}\right) \tag{4.27}$$

The declination angle is the same anywhere across the globe on any given day; Figure 4.5 shows the variation throughout the year. In the Northern hemisphere, March 21st and September 21st are known as the vernal and autumnal equinoxes. On these two days, the length of day and night are approximately the same. June 21st and Dec 21st are known as the summer and winter solstices, when the longest and shortest period of daylight can be experienced. The period of the Earth's revolution around the Sun does not coincide exactly with the calendar year, therefore the declination angle varies slightly on the same day from year to year. For the Southern hemisphere, the equinoxes and solstices are reversed [110].

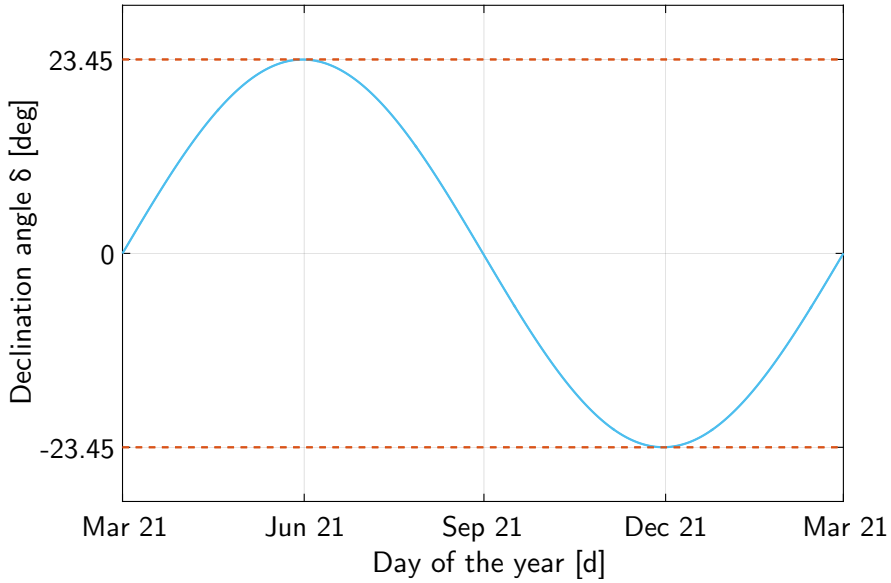

Figure 4.5: Variation in declination angle δ throughout the year.

The hour angle ω can be expressed as Equation 4.28:

$$\omega = 2\pi \cdot \frac{i - 11.968}{23.935} \tag{4.28}$$

where i is the instantaneous time of the day or local solar time in hours. The convention for ω is negative before noon, zero at noon and positive after noon. The solar time depends on the location (more specifically, the longitude) and is, in general, different from the local clock time (LCT), which is defined by the specified time zone.

The input for the solar irradiation model can either be given in LCT or solar time t_{solar}; one can be converted to another if the following parameters are known: daylight saving, local longitude, day number and time zone [111].

The difference between mean solar time and apparent solar time on a given date is called the equation of time (EOT). This deviation is caused by the definition of the solar time; the Sun is not always due South at 12AM noon on any given day. An approximation of the EOT is given by Equation 4.29 in minutes and accurate within 30 seconds during daylight hours.

$$EOT = 0.258 \cdot \cos(x) - 7.416 \cdot \sin(x) - 3.648 \cdot \cos(2x) - 9.228 \cdot \sin(2x) \tag{4.29}$$

where x is the angle defined in Equation 4.30 as function of the day number n.

$$x = \frac{360 \cdot (n - 1)}{365.242} \tag{4.30}$$

The time conversion from LCT to solar time t_{solar} is realised by Equation 4.31 in 24-hour decimal format:

$$t_{solar} = LCT + \frac{EOT}{60} - LC - DST \tag{4.31}$$

where the LCT is given in 24-hour decimal format, the EOT is expressed in minutes, the daylight saving time (DST) is either 0 or 1 (when it is in effect) and the longitudinal correction (LC) in hours is defined as:

$$LC = \frac{\text{local longitude} - \text{longitude of timezone}}{15} \tag{4.32}$$

To convert from local solar time to LCT, Equation 4.31 can be rephrased as follows:

$$LCT = t_{solar} - \frac{EOT}{60} + LC + DST \tag{4.33}$$

The inclination angle of the PV panels β is comparable to the flight path angle of the aircraft. However, since the change in flight path angle throughout flight is small, β may be safely assumed to be equal to zero. This allows Equation 4.26 to be simplified into Equation 4.34 [110]:

$$\theta = \text{acos}\Big(\sin(\delta)\sin(\varphi) + \cos(\delta)\cos(\varphi)\cos(\omega)\Big) \tag{4.34}$$

The incoming solar irradiance can then be expressed as:

$$Q_{pv} = SF \cdot T \cdot \cos(\theta) \tag{4.35}$$

where T is the transmittance of the PV panels. From the manufacturer's data sheet, it is found that this value equals 0.91 [97]. Finally, the generated PV power P_{pv} can be determined with Equation 4.36:

$$P_{pv} = \eta_{pv} \cdot Q_{pv} \cdot S_{pv,eff} \tag{4.36}$$

where η_{pv} is the efficiency of the installed PV panels (see Section 3.8.1) and $S_{pv,eff}$ is the total effective surface area; the derivation of the latter is thoroughly described in Appendix C.

4.8 Selected EAPPS Configuration

The selected EAPPS setup integrates the conventional turbofan engine with an electric motor in a parallel HEPS configuration. A fundamental aspect is that the EAPPS and its electrical network can be retrofitted into the existing A320neo aircraft. The electrical system consists of the electric motor, power electronics, batteries and cables. Also, fuel cell and PV systems are available as add-ons. An overview of the EAPPS configuration is depicted in Figure 4.6.

The purpose of this illustration is to indicate how the engine (marked in light blue) and the electrical system (yellow) interact with each other. The drawing also shows the connections and efficiencies between the individual system components to form the complete electrical network; the ones being modelled in MATLAB® are indicated in yellow. Since the aircraft subsystems are only represented by constant values of electrical power required per flight phase (see Section 3.2.1), these elements are marked pink. To distinguish between the usage of the electric motor or the generator, two situations are shown: discharge mode (in orange) and charge mode (in green).

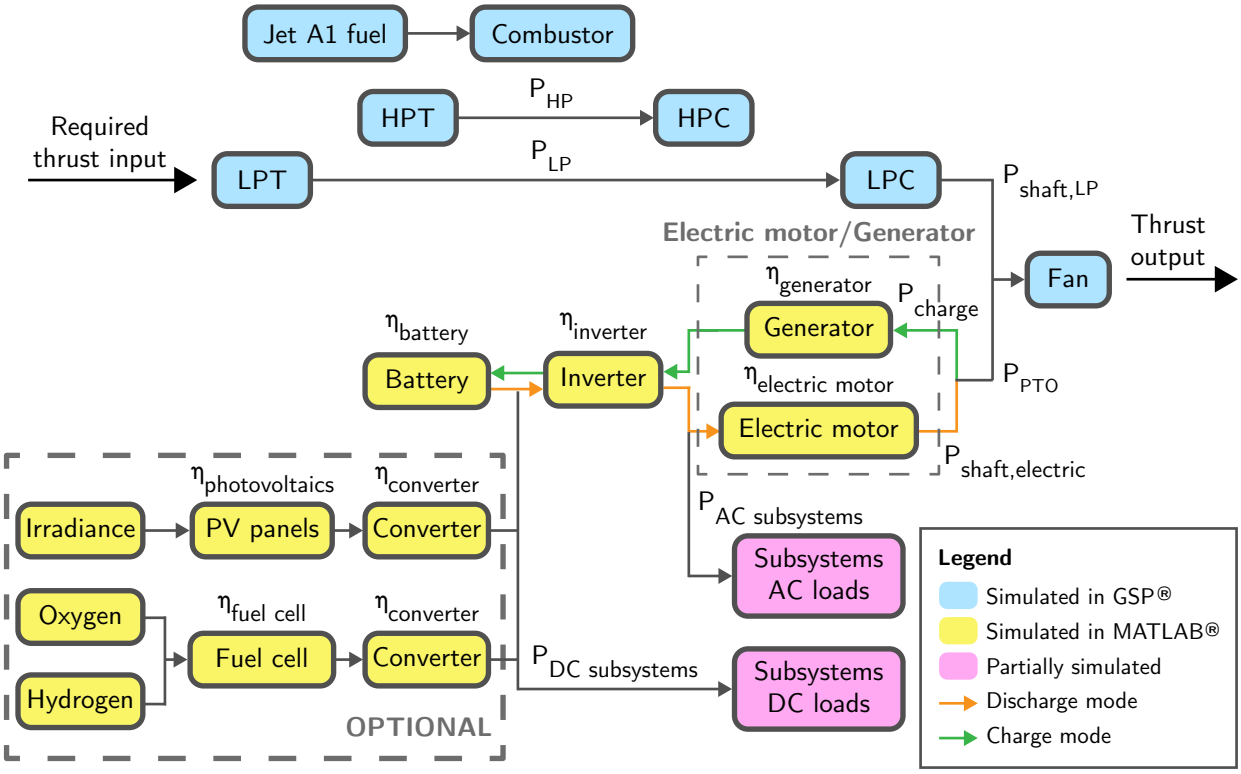

Figure 4.6: Detailed overview of the selected EAPPS configuration.

4.9 Model Verification and Validation

To make sure that the individual parts are modelled correctly, these models will be verified and validated against existing data. First of all, the output data from the aircraft flight performance model will be compared to that from Piano-X® in Section 4.9.1. Then, in Section 4.9.2, the engine model will be validated with certification sheets from the CFM LEAP-1A engine. Lastly, the solar irradiance model will be tested by checking the output for three different flight missions in Section 4.9.3.

4.9.1 Validation of Aircraft Flight Performance Model

To validate the flight performance model from Section 4.4, the output data of the simulation is compared to the performance data from Piano-X®. Piano-X® is a commercial mission analysis tool that computes fuel consumption, environmental emissions, drag and performance characteristics of any aircraft with various range and payload combinations, for the majority of the mission; this tool only computes data for altitudes above 1,500 ft. The selected reference mission is an Airbus A320 flying a distance of 1,000 km; the initial aircraft mass is around 65,000 kg. Figure 4.7 shows the outputs of both models for various flight parameters. When comparing both simulations, it can be seen that the altitude, thrust, Mach number and flight path angle are nearly identical. The marginally higher Mach number during the descent phase can be explained by looking at the calibrated airspeed; the performance model has some difficulty in keeping this speed setting constant. Since the calibrated airspeed and required thrust are slightly off in comparison to Piano-X®, the fuel flow has similar inconsistencies in those relevant mission segments.

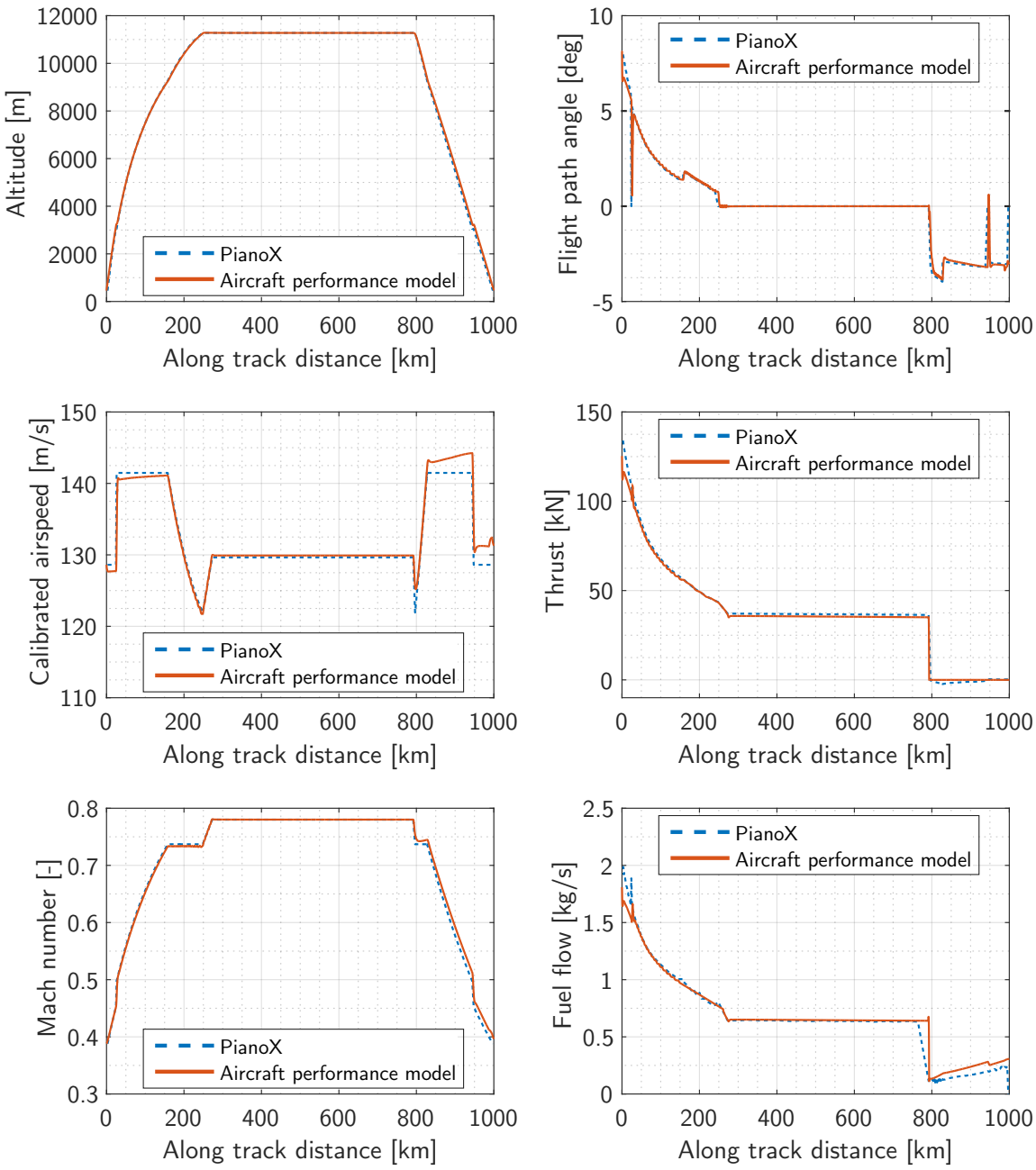

Figure 4.7: Validation of the aircraft performance model with Piano-X® [112].

4.9.2 Validation of Engine Performance Model

To validate the engine performance model of the CFM LEAP-1A, the output data from GSP® is compared to the key characteristics from certificate data sheets [61]. Table 4.4 summarises the acquired data from the GSP® model and the data sheets provided by European Aviation Safety Agency (EASA).

The certificate data sheets provide limitations on the EGT T_{t45} and bleed extraction of the CFM LEAP-1A engine; these are indicated in Table 4.5 and Table 4.6.

Table 4.4: Validation of the GSP® engine model with certificate data sheets [61].

Parameter	GSP®	Certified data
OPR [-]	40.6	40
N1 (100%) [rpm]	3,856	3,856
N2 (100%) [rpm]	16,645	16,645
Take-off thrust [kN]	120.63	120.64

Table 4.5: Airflow limitations of the CFM LEAP-1A engine [61].

Bleed location	LP rotor speed	Airflow limit
Bypass duct	Above minimum idle	2% of secondary airflow
HPC 4th stage[1]	Above minimum idle	9.97% of primary airflow[2]
HPC 7th stage	Below 2,314 rpm N1K[3]	2.9% of primary airflow
HPC 7th stage	Above 2,314 rpm N1K[3]	2.45% of primary airflow
HPC 10th stage[1]	Above minimum idle	15% of primary airflow

Table 4.6: Exhaust gas temperature limitations of the CFM LEAP-1A engine [61].

Phase	EGT limit [°C]
Take-off	1,060
Maximum continuous	1,025
Ground start	750
In-flight start	875

Temperature & Bleed Flow Limitations

To ensure these engine limits are not exceeded, bleed flows need to be carefully selected; sufficient bleed air for powering the aircraft subsystems and engine cooling, while staying below the maximum indicated airflow limits. Since a detailed bleed schedule for the CFM LEAP-1A engine is not available, it is assumed that all bleed occurs at the 10th stage of the HPC. This imposes an airflow limit of 15%, according to Table 4.5.

The EGT margin is defined as the difference between the peak EGT during take-off and the certified redline EGT, which is the absolute maximum without causing damage to the engine. This measure is introduced to evaluate the engine's health and account for engine deterioration over its lifetime [113]. All engines will eventually reach its certified redline EGT limit. Typical EGT margins for new, lower rated engines are between 75°C and 100°C [114]; for this study, a conservative EGT margin of 75°C has been chosen. In addition, the maximum temperature for the HPT nozzle guide vanes T_{t41} is assumed to be 2,000 K.

Figure 4.8 and Figure 4.9 depict the cooling bleed variation of a conventional and electrical A320 setup, with T_{t41} and T_{t45} limitations throughout a full mission. The NGV temperature T_{t41} is shown in the two upper graphs; the left one presents the temperatures of the different flight segments and the right one highlights the limiting segment, the take-off. The T_{t45} limitations at the low pressure

[1] It is not allowed to extract air from the 4th and 10th stages simultaneously.
[2] Absolute maximum; refer to the LEAP-1A Installation Manual for a detailed HPC 4th stage bleed schedule.
[3] Temperature corrected fan rotor speed.

turbine (LPT) depend on various operating conditions, as formulated in Table 4.6, and correspond to the lower three graphs: ground, take-off and in-flight. The solid red line indicates the maximum allowed temperatures for the HPT and LPT, including the EGT margin of 75°C. The dashed red line is the T_{t45} limit without the margin. Each dot represents the maximum temperature experienced during the segment with a specified cooling bleed setting; it is marked grey when it surpasses the temperature limit or when the cooling bleed, including the required bleed for the aircraft subsystems (conventional A320neo setup only), exceeds the airflow limitations stated in Table 4.5.

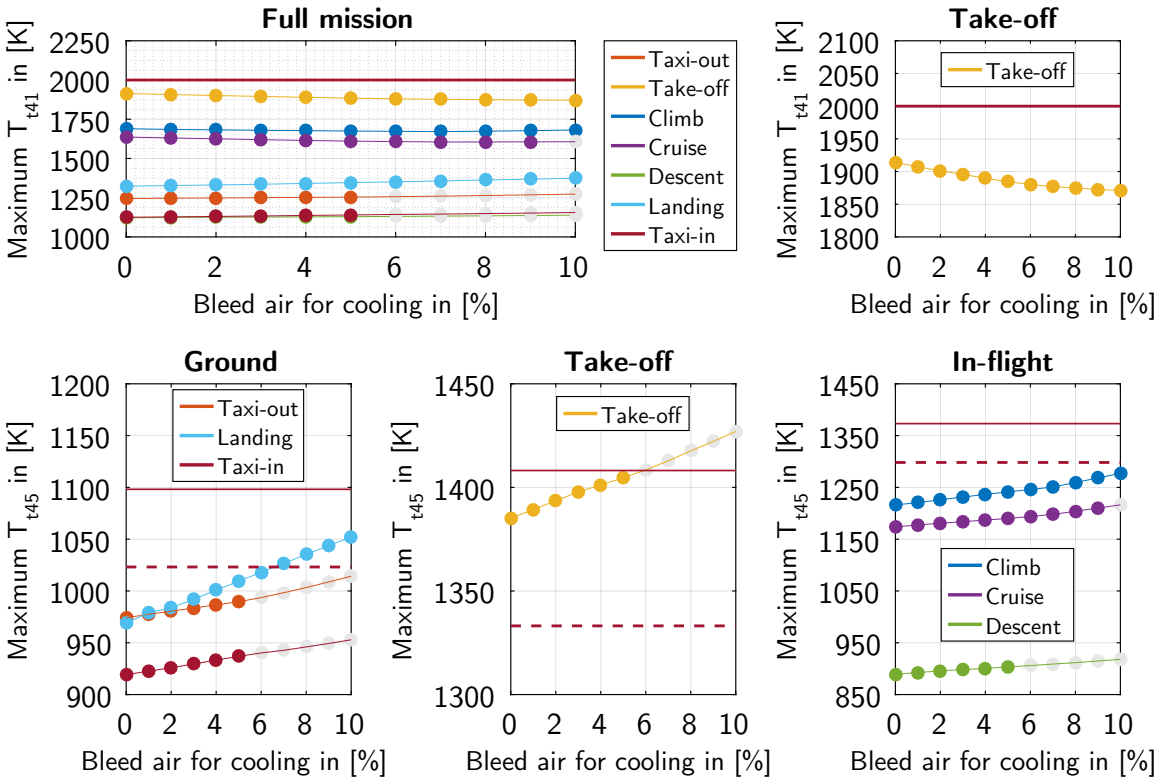

Figure 4.8: Effect of cooling bleed variation on conventional A320neo with NGV temperature (T_{t41}) and EGT (T_{t45}) limitations.

Figure 4.8 reveals that by increasing the bleed air percentage for cooling, the NGV temperature T_{t41} goes down. This is expected as the bleed air is used specifically for cooling the NGVs. On the contrary, the EGT T_{t45} goes up, because more 'cold' air is extracted from the core flow, which leaves less air available for heat dissipation after combustion. From Figure 4.8 can be concluded that only the take-off segment exceeds the maximum allowable temperatures for T_{t41} and T_{t45}. The cooling bleed for take-off can be set between 0% and 5% without surpassing the limits; a setting of 0% is chosen because operating at a lower T_{t45} prolongs the engine's life. T_{t41} poses no limitation during take-off. For the taxi-out, climb, cruise, descent and taxi-in segments, the settings will be equal to the maximum allowable bleed. The cooling bleed for landing will be set at 6% to stay below the dashed red line (T_{t45} limit without margin); this will push back the point at which the engine will pass the certified redline EGT limit.

From Figure 4.9, it can be deduced that the temperatures experienced throughout the mission will never exceed the engine limitations. This implies that no cooling bleed is required to keep the temperatures below maximum allowable T_{t41} and T_{t45} (solid red lines). Also, this result is in line with the concept of bleedless engines: one that does not supply internal airflow towards the pneumatic system. In certain conditions, a small amount of bleed air may be needed for internal cooling (e.g. during hot take-off)

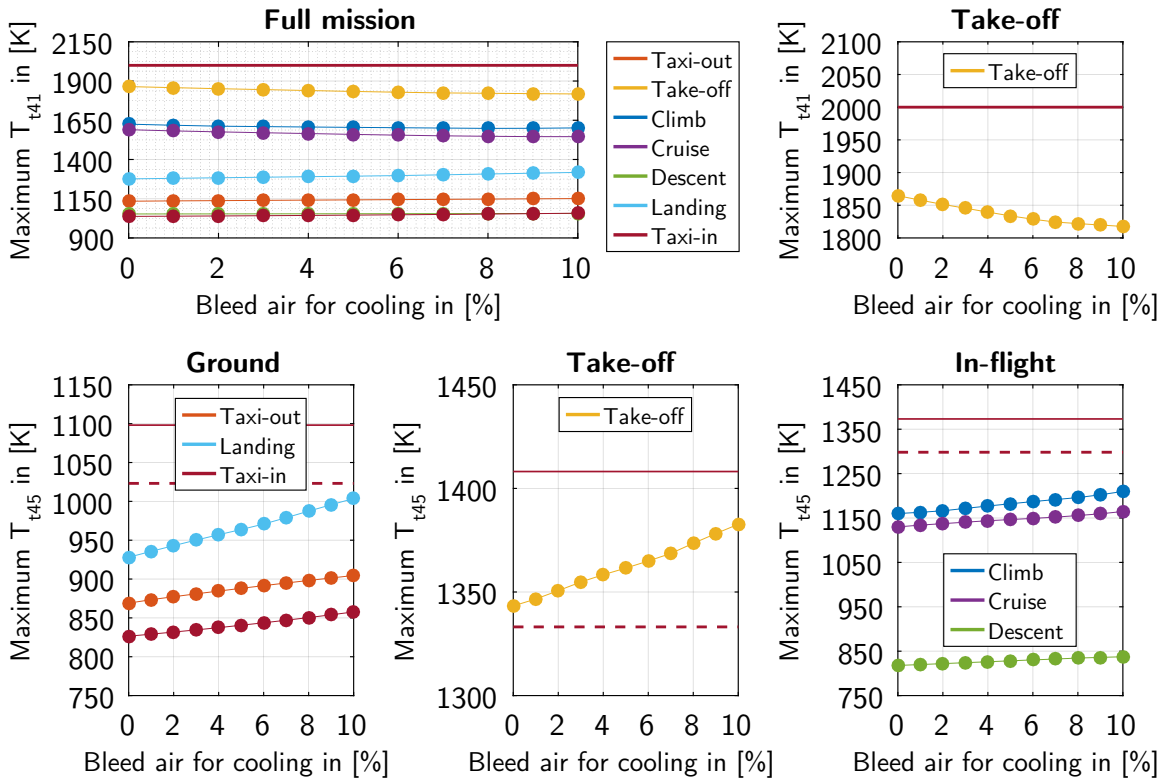

Figure 4.9: Effect of cooling bleed variation on electrical A320neo with NGV temperature (T_{t41}) and EGT (T_{t45}) limitations.

or engine stability (e.g. during compressor surge), but in general this is not necessary.

A summary of the selected cooling bleed settings for the conventional and electrical Airbus A320neo setup throughout the mission can be found in Table 4.7.

Table 4.7: Settings for cooling bleed extraction on conventional and electrical Airbus A320neo.

	Taxi-in	Take-off	Climb	Cruise	Descent	Landing	Taxi-out
Conventional	5%	0%	10%	9%	5%	6%	5%
Electrical	0%	0%	0%	0%	0%	0%	0%

Engine Emissions

Finally, the engine emissions can also be validated with output data from Piano-X®. Since the aircraft type used within Piano-X® is the A320-214, the following engine variants could be used for simulating the emissions [59]: CFM56-5B4, CFM56-5B4/P, CFM56-5B4/2P or CFM56-5B4/3 engine. A short comparison study is conducted for the emissions characteristics and the CFM56-5B4/P engine seems to match the most; the emission characteristics of this variant can be found in Table 4.8.

Figure 4.10 shows the total fuel burn dependent emissions, CO_2 and H_2O, for the entire flight mission obtained from Piano-X® and GSP® for the CFM56-5B4/P engine. From Figure 4.10a can be observed that the values of the absolute emissions differ no more than 4%. Figure 4.10b displays identical distribution for both simulations.

The engine dependent emissions, CO, UHC and NO_x, are presented in Figure 4.11; emissions data is only available when the aircraft is airborne. As shown in Figure 4.11a and Figure 4.11b, the absolute

Table 4.8: Emission data from ICAO Aircraft Engine Emissions Databank for the CFM56-5B4/P engine [102].

Mode	$\dot{m}_{fuel}$ [kg/s]	T_{t3} [K]	P_{t3} [bar]	EI_{UHC}	EI_{CO}	EI_{NO_x}	SN
take-off	1.132	792.9	27.522	0.9	0.25	28.0	5.4
climb out	0.935	769.1	24.651	0.9	0.16	23.2	4.1
approach	0.120	654.5	14.744	2.3	3.24	10.0	0.2
idle	0.104	491.9	4.097	23.4	32.07	4.3	0.5

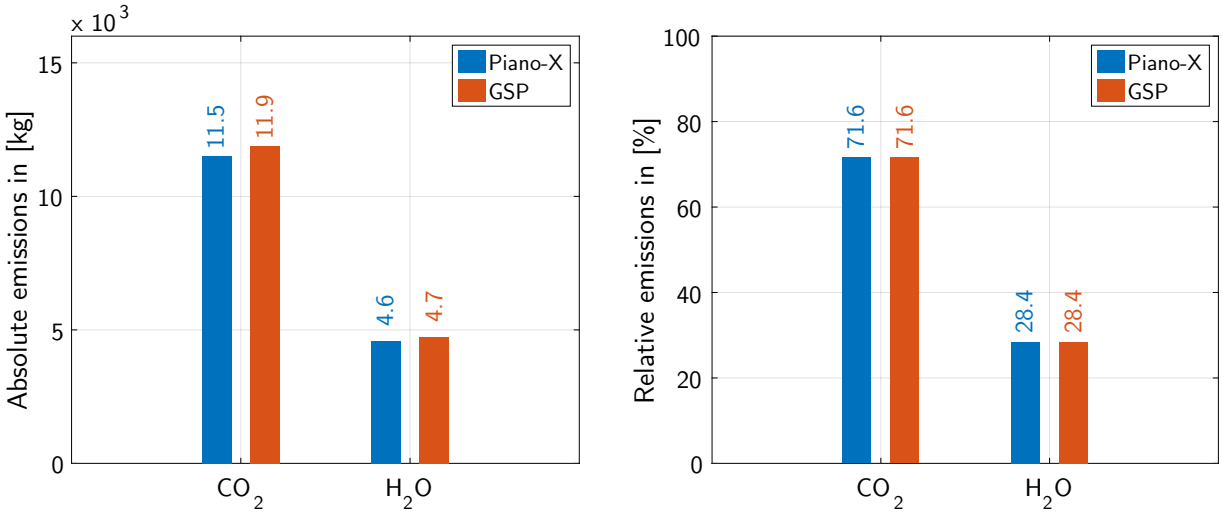

(a) Total emission masses. **(b)** Distribution of emissions.

Figure 4.10: Comparison of fuel burn dependent emissions for the CFM56-5B4/P engine derived from Piano-X® and GSP®.

and relative emissions for CO and UHC are slightly different. The trend of underpredicting CO and overestimating UHC is clearly visible in the aforementioned graphs.

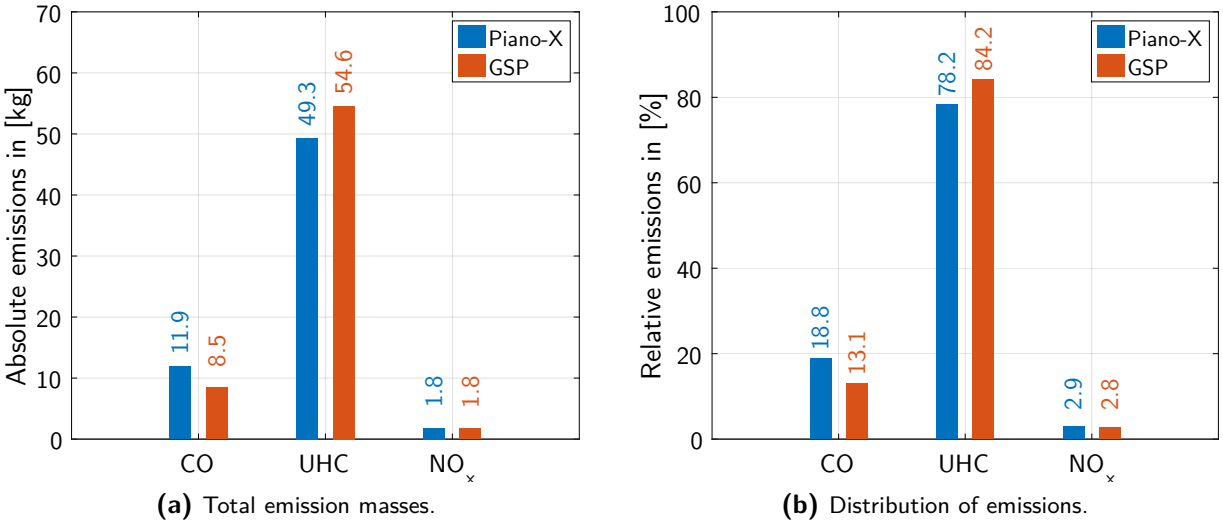

(a) Total emission masses. **(b)** Distribution of emissions.

Figure 4.11: Comparison of engine dependent emissions derived from Piano-X® and GSP®.

These emission charts are used to indicate whether GSP® is accurate enough to predict the engine

emissions for this study; this seems to be the case, as similar trends are observed for the output data from Piano-X®. Moreover, the exact variant of the CFM56-5B4 used within Piano-X® cannot be determined. If this identification problem can be solved, the GSP® results could even match closer to those of Piano-X®.

4.9.3 Verification of Solar Irradiation Model

To verify that the incoming solar irradiance is modelled correctly, three different flight missions of approximately 1,000 km across the world have been selected; these are indicated in Table 4.9 and the corresponding irradiances are presented in Figure 4.12.

Table 4.9: Selected flight missions with a range of approximately 1,000 km.

#	Departure	Arrival	Distance [km]
1	Toulouse, France (TLS)	Amsterdam, The Netherlands (AMS)	998
2	Guayaquil, Ecuador (GYE)	Bogota, Colombia (BOG)	991
3	Hobart, Tasmania (HBA)	Sydney, Australia (SYD)	1,037

Figure 4.12a shows the solar irradiance for a flight mission from Toulouse to Amsterdam. It can be seen that the solar irradiance reaches a daily high at 12PM (solar noon). Since the flight takes place in the Northern hemisphere, the summer solstice (blue line) corresponds to the longest day in the summer and the winter solstice (green line) to the shortest day in the winter. The two equinoxes (orange and red line) are similar. Figure 4.12b depicts the solar irradiance for a flight mission between Guayaquil and Bogota. As both locations are close to the equator, the variation in solar irradiance throughout the year is minimal and thus highly desired for PV installations. Figure 4.12c presents the solar irradiance for a flight mission from Hobart to Sydney. Considering that this flight occurs in the Southern hemisphere, the solstices and equinoxes should be the exact opposite of Figure 4.12a; this trend in solar irradiance is apparent, indicating that the irradiation model works correctly.

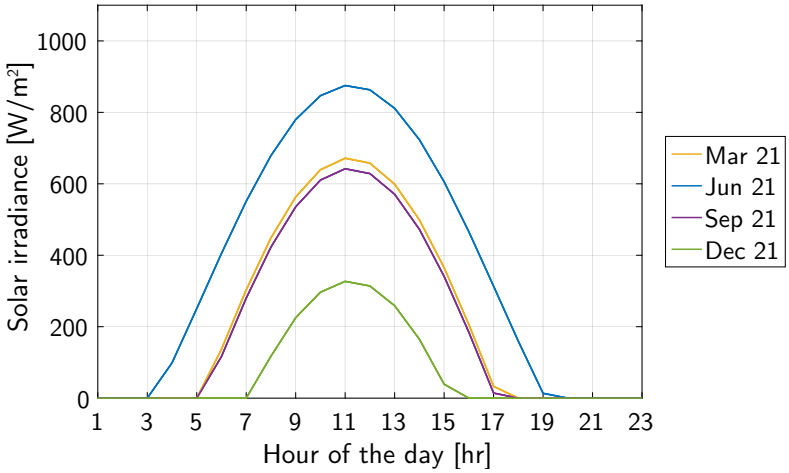

(a) Flight mission from Toulouse to Amsterdam.

Figure 4.12: Variation of solar irradiance for three different flight missions of approximately 1,000 km: Toulouse - Amsterdam, Guayaquil - Bogota and Hobart - Sydney.

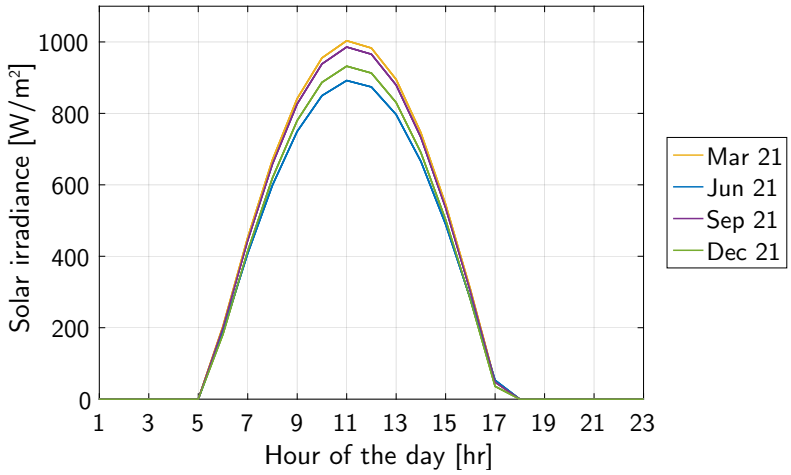

(b) Flight mission from Guayaquil to Bogota.

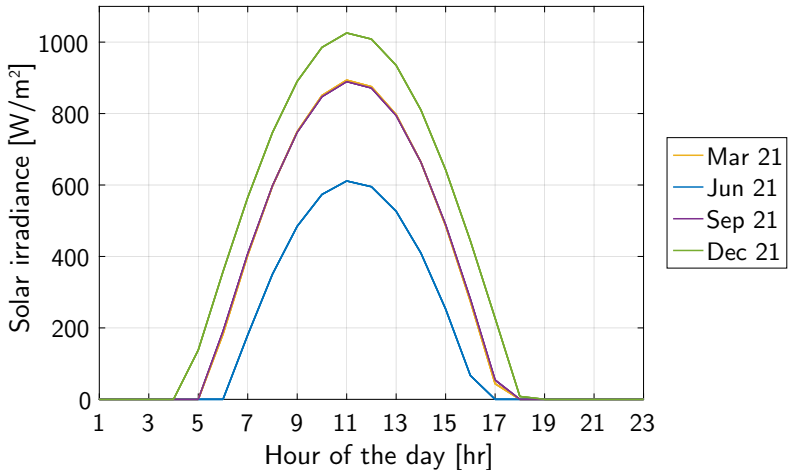

(c) Flight mission from Hobart to Sydney.

Figure 4.12: Variation of solar irradiance for three different flight missions of approximately 1,000 km: Toulouse - Amsterdam, Guayaquil - Bogota and Hobart - Sydney.

CHAPTER 5

EMS Simulation Model

To gain a better understanding of the dynamics involved within the electrical system, a more in-depth system analysis is carried out. This results in a separate simulation and sizing tool of solely the electrical system: the EMS module. This chapter will, similarly as Chapter 4 for the EAPPS module, describe the design and implementation of the EMS simulation model.

First of all, a schematic overview on a system-level scale will be shown in Section 5.1. This is followed by the assumptions and limitations regarding the EMS model in Section 5.2. The electric motor will be characterised by a contour map, where the efficiency depends on the power output and rotational speed; this figure can be found in Section 5.3. Next, the battery discharge characteristics will be extracted from experimental data of the Panasonic NCR20700A lithium-ion battery; the entire procedure is explained in Section 5.4. Both Section 5.5 and Section 5.6 will describe various methods to fit simulated data with experimental data obtained from existing literature for photovoltaic (PV) and fuel cell systems, respectively. Then, the configuration used to model the electrical system within the EMS module will be illustrated in Section 5.7. Finally, Section 5.8 can be consulted for verification and validation procedures of the different models.

5.1 Schematic Overview

The EMS module is essentially a more detailed model and used to simulate the dynamics of the electrical system accurately. This is only carried out after results of the EAPPS module are available; this post-correction method provides a more realistic value for the battery specific energy, which leads to a new electrical system mass. This updated mass value can then be fed back into the EAPPS module. The sequential steps are described in Figure 5.1.

First, the power requirements for the electric motor and the non-propulsive power systems are extracted from the flight mission data, acquired from the EAPPS simulation model. Then, the solar irradiance throughout the mission is modelled as a function of location, time and date. This allows the user to precisely determine the electrical power received from the PV system. Also, the power output from the PEMFC system can be derived from predetermined user settings. With all these different power requirements known, the actual electrical power that the battery system needs to provide at each timestep can be established.

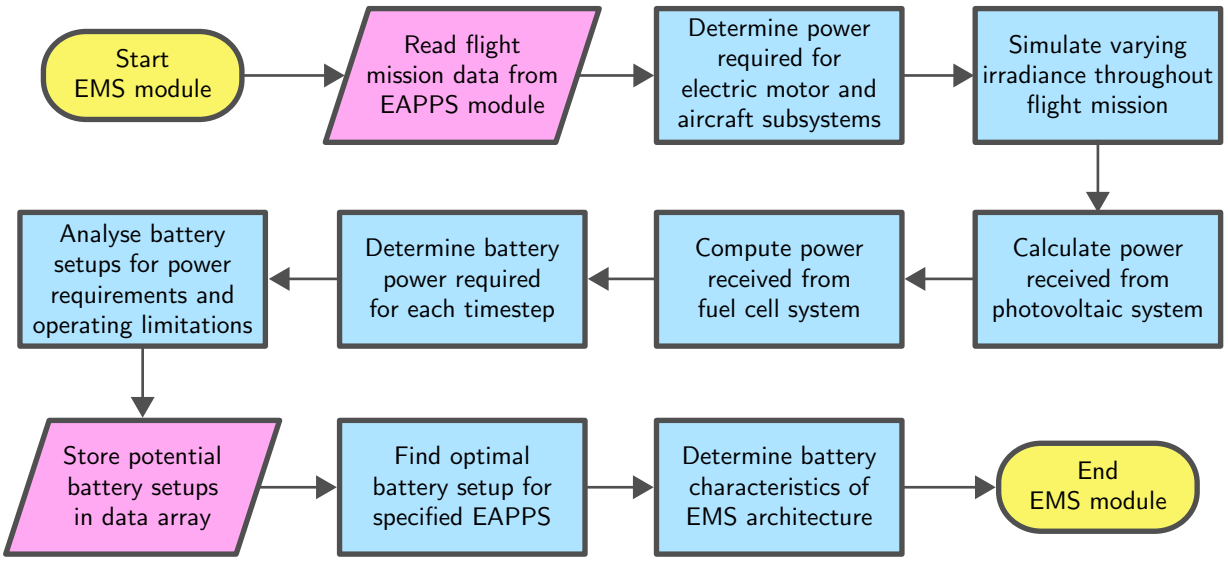

Figure 5.1: Schematic overview of the EMS module.

Now, by varying the number of cells in series and parallel, all potential battery configurations which satisfy the power requirements and operating limitations (see Section 5.2) are identified and stored into a data array. The optimal battery setup is the one which has the lowest amount of batteries within the entire battery pack. With the mass and volume specifications from the data sheet, one can determine which battery characteristics can be realised and used as feedback for the EAPPS module.

5.2 Model Assumptions and Limitations

The main assumptions and limitations used within the EMS model are as follows:

- *Mission parameters based on optimised EAPPS setup*
  This model uses the mission parameters from the optimised EAPPS configuration as input. This means the EMS module can be adopted as a verification tool to see if appropriate parameters have been used, taking into account a more detailed analysis of the various component efficiencies.
- *Steady-state modelling of electrical system*
  The dynamic behaviour of the electrical system will be simulated as steady-state. This implies that the characteristics of each component will remain constant over time. The time step size of the simulation is set to 1 s. For systems with fast response times such as batteries and PV modules, the dynamics will be modelled accurately. PEMFCs have an average response of 30 seconds, which means that changes within this time period will not be precise. Since the fuel cell system within this module will only provide constant power, it is assumed that the simulation begins when the fuel cell power supply is steady. The start-up of the fuel cell system will happen beforehand, e.g. when the aircraft is parked.
- *Operating voltage and current limited to 3,000 V and 4,000 A/6,000 A (2020+/2040+)*
  To avoid the effects of arcing, the operating voltage limit is set at 3,000 V. This value is also based on the E-Fan X, a project led by Airbus to incorporate a series-hybrid architecture into a BAe 146 airliner [115]. In addition, a current limit of 4,000 A is selected to avoid high Ohmic losses and heavy cabling for the near term projection (2020+). This current limit is raised to 6,000 A for the far future (2040+), to be able to provide the increased electrical power required.

- *Electric motor characterisation*
  The characteristics of the electric motor is derived from the hFan engine used by Boeing's SUGAR Volt [78]; see Section 3.4.1. The electrical losses are based on empirical relations found in existing literature and are dependent on rotational speed and power output only; see Section 3.4.2. This also implies that technological development is not taken into account, the same efficiency map is used for near future (2020+) and far future (2040+).

- *Battery discharge characteristics*
  The discharge characteristics extracted from the data sheet are assumed to be valid for a wide range of operating conditions. Also, the discharge curves are treated the same for charging procedures; see Section 3.5.1.

- *Minimum battery state of charge is 10%*
  The state of charge (SOC) of the lithium-ion battery is limited to 10% due to safety reasons; discharging the battery beyond the cut-off voltage can lead to permanent damage such as reduced battery lifetime or even explosions. Therefore, the device cannot be discharged below 10% SOC within this study.

- *Constant battery internal resistance*
  The internal resistance of the battery is assumed to be constant during charge and discharge cycles. It does not vary with the amplitude of the operating current or the state of charge.

- *No temperature and self-discharge effects on battery*
  The battery characteristics are assumed to be independent of operating temperature. In real life, the battery heats up during discharge and charge procedures. Also, the available capacity decreases with lower temperatures. Furthermore, self-discharge effects will be ignored; it can be modelled by e.g. adding a large parallel resistance. In general, lithium-ion batteries possess good self-discharge characteristics compared to other types such as lead-acid or nickel-cadmium batteries [116].

- *Identical PV cells*
  All cells throughout the PV system are assumed to be identical. In reality, this is never the case as manufacturing defects, imperfections and ageing effects are always present [101].

- *Uniform cell temperature and irradiance distribution*
  Each PV cell is subjected to the same operating conditions. This means that a constant cell temperature and irradiance can be used for analysing the system performance. Hot spots are usually present within a string of PV modules or cells, where one or multiple cells experience lower currents due to partial shading or manufacturing defects. This can have a significant impact on the overall system performance by limiting its operating current.

- *Solar charge controller with maximum power point tracking (MPPT) is present*
  To manage the power generated by the PV system, it is assumed that a solar charge controller will be present. This device regulates the voltage and/or current to keep the batteries from overcharging and make sure the system operates at the maximum power point.

- *Near and far future technology level*
  The applied values for the specific power and energy as well as for the power and energy densities in the EMS module correspond with the values used in the EAPPS module. The parameters that configure the electrical system for the EAPPS is based on the technology level projected for the near future (2020+) and far future (2040+). The assumed power densities and efficiencies are based on linear regression analyses (Section 3.3) and multiple sources in literature.

5.3 Electric Motor

Due to the lack of performance specifications of an advanced SRM, the motor cannot be modelled with a generic SimPowerSystems (SPS) model; not all parameters can be specified. By using empirical relations from existing literature, various power losses can be estimated based on motor power output. The procedure and accompanying formulas are thoroughly described in Section 3.4.2. The assumed parameters are stated in Table 5.1 and the resulting efficiency map is illustrated in Figure 5.2.

Table 5.1: Assumed scaling parameters of electric motor for obtaining efficiency map [47, 78].

Motor scaling parameters	**Value**
Maximum power output P_{max} [MW]	6
Maximum rotational speed N_{max} [rpm]	5,000
Maximum operating voltage V_{max} [V]	3,000
Number of stators n_s [-]	6
Number of rotors n_r [-]	4
Number of bearings n_{bear} [-]	2
Break speed ratio ω_b [-]	0.6
Shape factor for a 6/4 SRM $\Delta_{6/4SRM}$ [-]	1.195
Density of laminated steel $\rho_{mat,steel}$ [kg/m^3]	7,650
Number of phases m [-]	3
Peak value of phase current I_0 [A]	2,000
Maximum rotational speed for hFan engine $N_{max,hFan}$ [rpm]	3,300
Peak magnetic flux for hFan $B_{p,0}$ [T]	1.5
Hysteresis loss coefficient K_h [W/Hz^{2}T^{2}kg]	0.0275
Classical eddy current loss coefficient K_c [W/Hz$^{1.5}$T$^{1.5}$kg]	0.0000183
Excess eddy current loss coefficient K_e [W/Hz^{2}T^{2}kg]	0.0000277

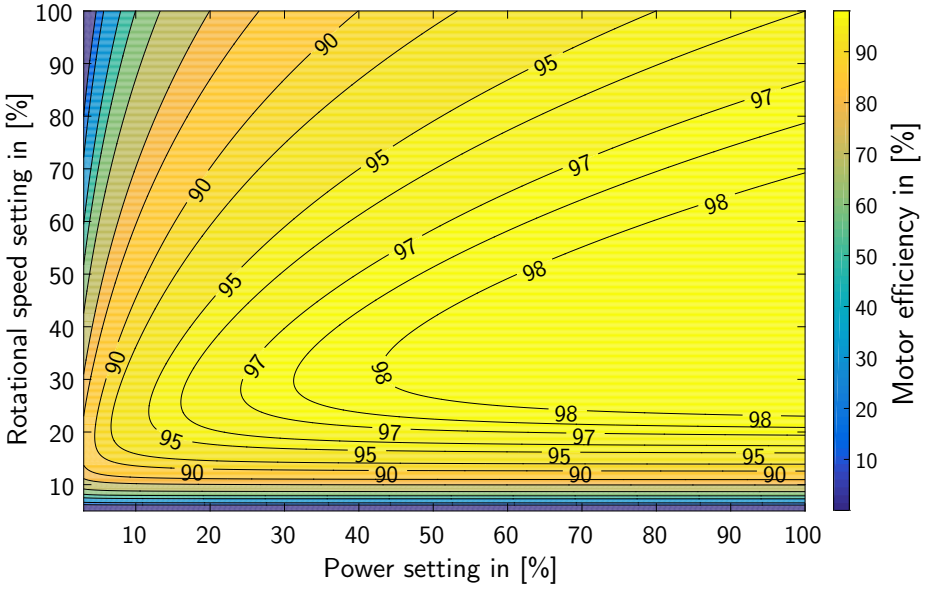

Figure 5.2: Motor efficiency as function of power and rotational speed settings.

Figure 5.2 shows that the electric motor is most efficient at high power settings and intermediate rotational speeds. To prove its validity, the characteristic features of this efficiency map will be compared to that of the hFan engine used in the SUGAR Volt aircraft; this validation procedure can be found in Section 5.8.1.

5.4 Lithium-Ion Battery System

The lithium-ion battery characteristics are based on experimental discharge data of the Panasonic NCR20700A lithium-ion battery with a typical capacity of 3,300 mAh and high discharge currents up to 30 A [117]; the discharge curves at different rates are shown in Figure 5.3. Note that the discharge curves are obtained by following a constant current strategy.

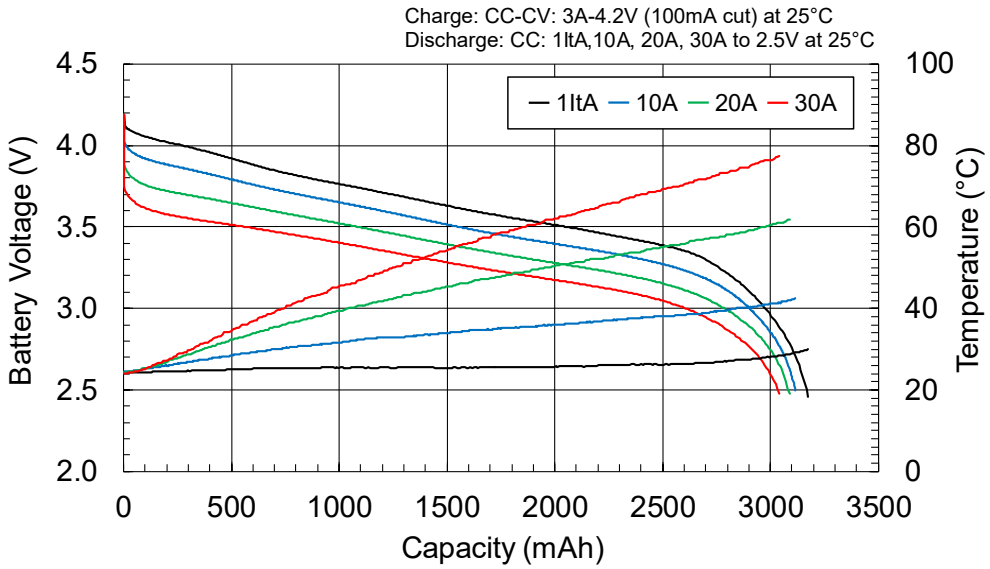

Figure 5.3: Discharge characteristics of the Panasonic NCR20700A battery [117].

First, data points are extracted from Figure 5.3 using *ScanIt* by AmsterChem. This software allows the user to define the plot axes, trace the discharge curves and collect the data points for each curve. Since Equation 3.35 needs to be fitted for four discharge curves, the discharge current I_b changes for each curve. This makes it a multiple regression analysis, where the formula changes slightly for each data set. This regression fit can be performed in MATLAB® by using the *fminsearch* function. This algorithm uses the simplex search method from Ref. [118], which can be applied with varying currents I_b and an initial guess vector B_0. The main disadvantage of using this algorithm is that it does not always converge to a local minimum.

To do the multiple regression analysis, three arrays need to be set up first: an independent variable matrix x, a dependent variable vector y and a coefficient vector B.

Each data point corresponds to three values, as shown in Equation 5.1. The x represents the independent variable matrix, where x(:,1) is the discharge current per curve and x(:,2) is the time it has discharged, and the y-vector is the dependent variable vector, where y(:,1) is the corresponding voltage.

The last vector required is called the coefficient vector B and it contains all the curve fitting parameters, displayed in Equation 5.2.

$$x = \begin{bmatrix} I_{b,1C} & t_{1C_1} \\ \vdots & \vdots \\ I_{b,1C} & t_{1C_k} \\ I_{b,10A} & t_{10A_1} \\ \vdots & \vdots \\ I_{b,10A} & t_{10A_k} \\ I_{b,20A} & t_{20A_1} \\ \vdots & \vdots \\ I_{b,20A} & t_{20A_k} \\ I_{b,30A} & t_{30A_1} \\ \vdots & \vdots \\ I_{b,30A} & t_{30A_k} \end{bmatrix} \qquad y = \begin{bmatrix} V_{1C}(t_{1C_1}) \\ \vdots \\ V_{1C}(t_{1C_k}) \\ V_{10A}(t_{10A_1}) \\ \vdots \\ V_{10A}(t_{10A_k}) \\ V_{20A}(t_{20A_1}) \\ \vdots \\ V_{20A}(t_{20A_k}) \\ V_{30A}(t_{30A_1}) \\ \vdots \\ V_{30A}(t_{30A_k}) \end{bmatrix} \tag{5.1}$$

$$B = \begin{bmatrix} V_0 & K & pc & A & p_3 & p_2 & p_1 & p_0 & R \end{bmatrix} \tag{5.2}$$

In MATLAB®, a vector norm is applied to the objective function; this is also known as the L^2-norm or magnitude of a vector. The objective function to be minimised is shown in Equation 5.3.

$$J = |\bar{y} - \bar{y}_{data}| = \sqrt{\sum (y(i) - y_{data}(i))^2} \tag{5.3}$$

The calculated norm of this least-squares method is 0.488776 after 3,251 iterations and 4,653 function evaluations; the total data set consists of 480 data points. The optimisation settings are presented in Table 5.2. The *fminsearch* algorithm stops when both *TolFun* and *TolX* tolerances are satisfied. This means that if the solver attempts to take a step that is smaller than *TolX* and *TolFun*, the iteration procedure ends.

Table 5.2: Optimisation settings for the non-linear multiple regression fit of the Panasonic NCR20700A battery.

Option	Value	Description
MaxIter	10,000	Bound on number of solver iterations
MaxFunEvals	10,000	Bound on number of function evaluations
TolX	1E-7	Lower bound on step size for subsequent iterations
TolFun	1E-7	Lower bound on function evaluation changes for subsequent iterations

The resulting fit is highly sensitive to the initial values provided for vector B_0. The values have been changed until a decent fit was achieved. The initial B_0 and final B_v values for the curve fitting parameters are given in Table 5.3.

Table 5.3: Curve fitting parameters for the Panasonic NCR20700A battery.

Vector	V_0 [V]	K [V]	pc [-]	A [V]	p_3 [Ah^2]	p_2 [Ah]	p_1 [A]	p_0 [Ah^{-1}]	R [Ω]
B_0	3.2	0.055	1.0	2.4	0.03	-0.01	0.04	1.5	0.015
B_v	3.3439	0.0424	1.0069	0.8586	0.0011	-0.0179	0.0663	0.4311	0.0162

The result of this fit of multiple datasets can be found in Figure 5.4. The graph shows a good correlation between experimental and simulation data, even at higher discharge rates. This gives the impression that the non-linear regression method is done correctly with *fminsearch* in MATLAB®.

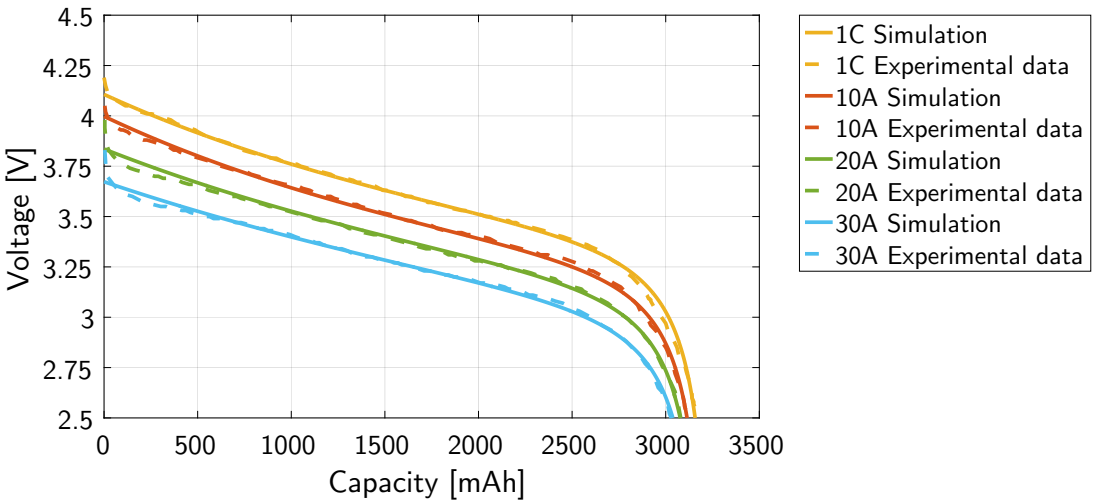

Figure 5.4: Curve fit of four discharge curves for the Panasonic NCR20700A battery [117].

5.5 Photovoltaic System

The solar skin covering the wings, fuselage and horizontal stabiliser will be implemented as a PV array built of strings of PV modules in parallel. The PV cells used are the monocrystalline Maxeon Gen III cells from SunPower; the main parameters are summarised in Table 5.4.

Table 5.4: Main characteristics of the SunPower Maxeon Gen III cell at STC (1,000 W/m^2, AM 1.5 and cell temperature of 25°C) [119].

Parameter	Value
Power at maximum power point P_{mpp} [W]	3.63
Cell efficiency η [%]	23.7
Open-circuit voltage V_{oc} [V]	0.73
Short-circuit current I_{sc} [A]	6.15
Voltage at maximum power point V_{mpp} [V]	0.632
Current at maximum power point I_{mpp} [A]	5.9
Temperature coefficient of V_{oc} $\alpha_{V_{oc}}$ [mV/°C]	-1.74
Temperature coefficient of I_{sc} $\alpha_{I_{sc}}$ [mA/°C]	0.52
Temperature coefficient of P α_P [%/°C]	0.30
Width and height of a single cell w_{cell},h_{cell} [m]	0.125

To make use of the complex equivalent circuit model and Equation 3.74 described in Section 3.8.1, the following parameters need to be determined: the photoelectric current I_{ph}, the diode reverse saturation current I_0, the diode ideality factor n, the series resistance R_s and the parallel resistance R_p.

These unknown parameters can be obtained by using the values from Table 5.4 and implement them in the generic PV array model from Simulink®. This model uses an optimisation algorithm to find the unknown values that best fit the input parameters; the resulting I-V and P-V curves are shown in Figure 5.5 along with the fitting errors. The obtained fitting parameters for a single cell are shown in Table 5.5.

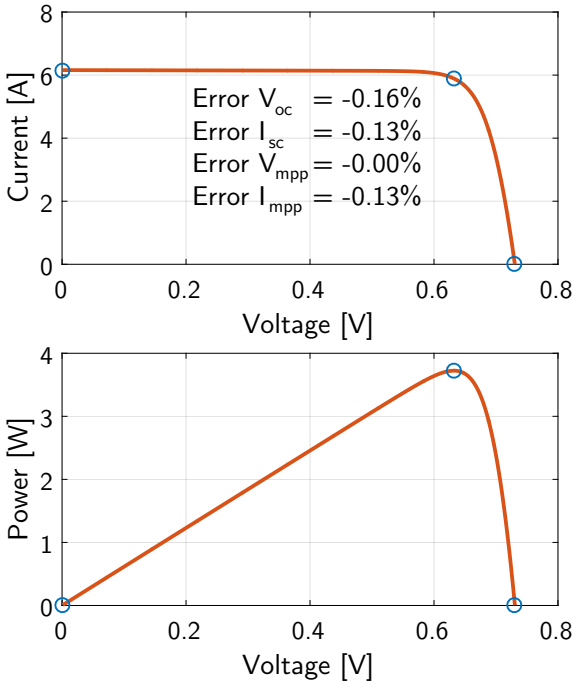

Figure 5.5: Characterisation of the SunPower Maxeon Gen III cell within Simulink® [120].

Table 5.5: Optimal fitting parameters for the SunPower Maxeon Gen III cell [120].

Parameter	Value
Photoelectric current I_{ph} [A]	6.159
Diode reverse saturation current I_0 [A]	$1.18{\cdot}10^{-12}$
Diode ideality factor n [-]	0.97046
Series resistance R_s [Ω]	0.0028854
Parallel resistance R_p [Ω]	23.075

The saturation current I_0 can also be acquired using Equation 3.77. For a cell temperature of 25°C, the value for I_0 becomes $1.173{\cdot}10^{-12}$ A; this is only an error percentage of 0.6%. The advantage of using Equation 3.77 over the optimisation algorithm is that the operating temperature can be varied over a range of temperatures.

To determine the maximum amount of Maxeon Gen III cells that can be installed on the A320neo, the total area of a single cell $S_{cell,total}$ needs to be calculated; note that this is not the same as the effective cell area $S_{cell,eff}$, which depicts just the cell. Assuming a gap of 5 mm between each cell, as presented in Figure 5.6, the total cell area becomes $0.13 \cdot 0.13 = 0.0169$ m^2.

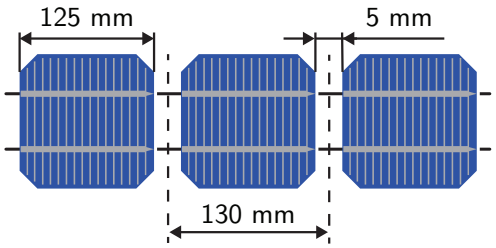

Figure 5.6: Spacing of the SunPower Maxeon Gen III cell; adapted from [119].

Now the maximum number of cells N_{pv} follows from Equation 5.4:

$$N_{pv} = \frac{S_{pv,eff}}{S_{cell,total}} = \frac{209.91}{0.0169} \approx 12420 \text{ cells} \tag{5.4}$$

With the total number of cells known, the PV system can be sized accordingly with the following considerations: low operating current for reduced power losses and decent voltage range for different solar irradiance and temperatures. Taking these factors into account, the following PV configuration has been chosen: $n_{pv,total} = 540$ and $m_{pv,total} = 23$. The key system characteristics are given in Table 5.6.

Table 5.6: Main characteristics of the complete PV system.

Parameter	Value
Number of cells in series $n_{pv,total}$ [-]	540
Number of cells in parallel $m_{pv,total}$ [-]	23
Power at maximum power point P_{mpp} [kW]	46.31
Open-circuit voltage V_{oc} [V]	394.20
Short-circuit current I_{sc} [A]	141.45
Voltage at maximum power point V_{mpp} [V]	341.28
Current at maximum power point I_{mpp} [A]	135.7
Effective area of a single cell $S_{cell,eff}$ [m^2]	0.015625

To show the operating current and voltage ranges for this selected system, the flight mission from Toulouse to Amsterdam has been selected. During this mission, the solar irradiance will vary between 570 W/m^2 and 730 W/m^2. To mimick various weather conditions, the temperature will fluctuate from -15°C to 45°C. Figure 5.7 and Figure 5.8 show the corresponding I-V and P-V curves for these temperature and irradiance limits.

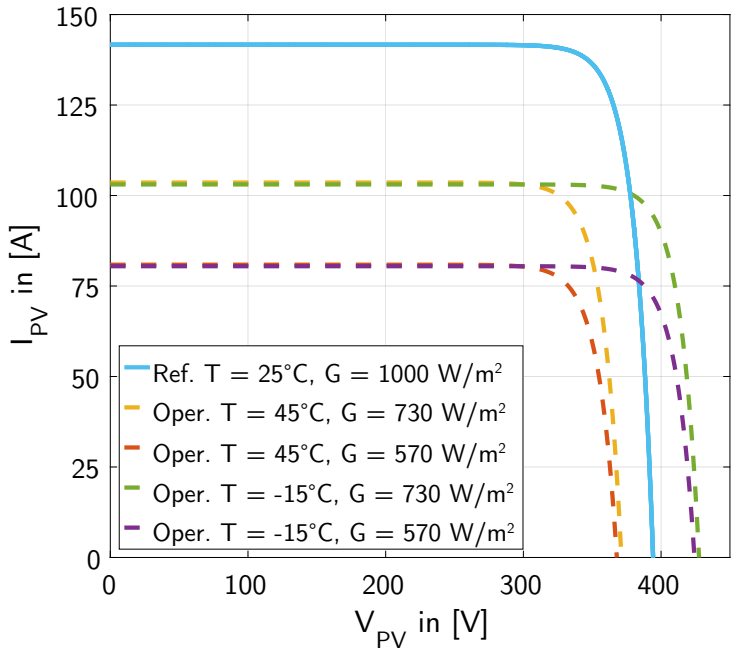

Figure 5.7: I-V curves of selected PV system for varying temperatures and solar irradiance.

From Figure 5.7 can be derived that the variation in solar irradiance manipulates the operational current range between 80 A and 103 A, while the temperature change commands the voltage range between 370 V and 430 V. Such insights are important for selecting devices with specific current and voltage ratings like power electronics.

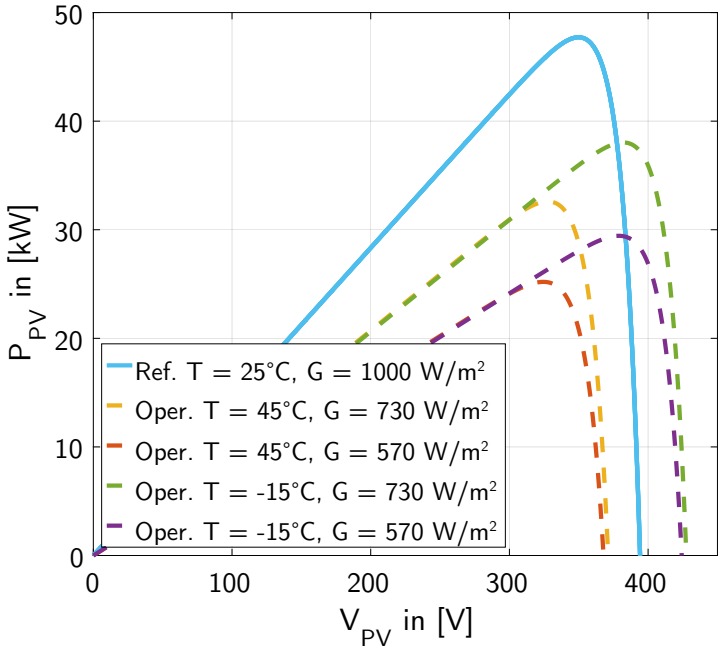

Figure 5.8: P-V curves of selected PV system for varying temperatures and solar irradiance.

Figure 5.8 presents the maximum power points for these different operating conditions. From this graph, the exact operating voltage and current can be determined. The maximum power point actually shifts continuously as function of incoming irradiance and cell temperature; it is assumed that a charge controller will be present to ensure that the system always operates at its maximum power point. Also, the efficiency of the entire PV system can be calculated with Equation 5.5, allowing the user to analyse the fluctuations in efficiency throughout flight.

$$\eta_{pv} = \frac{I_{mpp,pv} \cdot V_{mpp,pv}}{G_{op} \cdot N_{pv} \cdot S_{cell,eff}} = \frac{I_{mpp,pv} \cdot V_{mpp,pv}}{G_{op} \cdot 12420 \cdot 0.015625} \tag{5.5}$$

5.6 Fuel Cell System

The fuel cell system characteristics are based on the experimental data of the PowerCell MS-20 PEMFC with a nominal output of 20 kW [121]. This system is designed for mobile applications such as battery-operated vehicles and features the PowerCell S2 fuel cell stack, which is scalable between 5-35 kW [122]. The voltage and power curves against stack current are displayed in Figure 5.9. Note that the net power is slightly lower than the stack power; this is because the built-in humidifier, cooler and air compressor also require power to operate.

Again, *ScanIt* is used to extract the data from the polarisation curves in Figure 5.9. The governing formula for the stack voltage is rather identical to that of a single cell (Equation 3.58), with the addition of the term n_{stack}. However, this formula will not be applied, as numerous studies on fuel cells have demonstrated that a different equation is more suited for curve fitting [88, 89, 91]; this empirical formula is described by Equation 5.6:

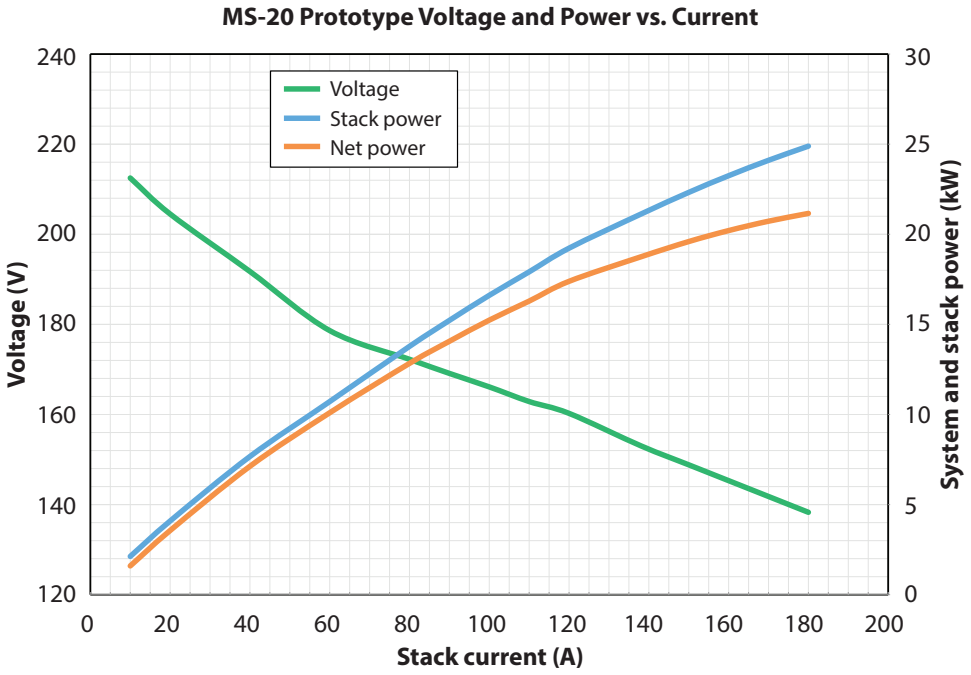

Figure 5.9: System and stack characteristics of the PowerCell MS-20 fuel cell [121].

$$V_{stack} = V_0 - B \cdot \ln(I_{stack}) - I_{stack} \cdot R_{stack} - m \cdot \exp(n \cdot I_{stack}) \tag{5.6}$$

Here, V_0 is the open-circuit potential, B is the activation loss coefficient, I_{stack} is the operating current, R_{stack} is the internal resistance, m is the concentration loss coefficient and n is the exponential concentration loss coefficient. It is also possible to use the current density i_{stack} instead of the current I_{stack}; subsequently, the internal resistance R needs to be interchanged with the area specific resistance r.

For this optimisation problem, three vectors need to be arranged. The xdata and ydata vectors, shown in Equation 5.7, contain the corresponding stack currents and voltages from the polarisation curve. The final vector is the coefficient vector c with the five unknown fitting parameters and presented in Equation 5.8.

$$\text{xdata} = \begin{bmatrix} I_{stack,1} \\ I_{stack,2} \\ \vdots \\ I_{stack,k} \end{bmatrix} \qquad \text{ydata} = \begin{bmatrix} V_{stack,1} \\ V_{stack,2} \\ \vdots \\ V_{stack,k} \end{bmatrix} \tag{5.7}$$

$$c = \begin{bmatrix} V_0 & B & R & m & n \end{bmatrix} \tag{5.8}$$

To solve this non-linear problem, a least-squares regression fit is done using the *lsqcurvefit* function within MATLAB®. This operation uses the same algorithm as *lsqnonlin*, but provides a more user-friendly interface for data-fitting problems; requirements are that an user-defined formula and initial guess c_0 need to be included. The following form is used, where the sum of squares is minimised:

$$\min_x ||F(x, \text{xdata}) - \text{ydata}||_2^2 = \min_x \sum_i (F(x, \text{xdata}_i) - \text{ydata}_i)^2 \tag{5.9}$$

The data set contains 299 reference points and the tolerances for *TolFun* and *TolX* are set at 1E-7. In addition, lower and upper bound constraints have been defined to ensure realistic values; these are stated in Table 5.7.

Table 5.7: Lower and upper bounds for the curve fit optimisation of the PowerCell MS-20 fuel cell.

Option	V_0 [V]	B [V/ln(A)]	R [Ω]	m [V]	n [1/A]
Lower bound	220	-inf	0	-inf	-inf
Upper bound	inf	inf	inf	inf	inf

After running the optimisation tool, the problem was solved after 43 iterations and 264 function evaluations. Again, the goodness of the fit is greatly dependent on the initial vector c_0; these values have been varied repeatedly until an acceptable fit was obtained. Table 5.8 shows the initial guess and final values for the curve fitting parameters.

Table 5.8: Curve fitting parameters for the PowerCell MS-20 fuel cell.

Vector	V_0 [V]	B [V/ln(A)]	R [Ω]	m [V]	n [1/A]
c_0	250	2	0.5	-0.00002	0.085
c	250.508	14.278	0.19	0.00259	0.042

The resulting fit is presented in Figure 5.10; due to the nature of the experimental polarisation curve, a greater fit cannot be obtained using Equation 5.6. Nevertheless, it still proves that the empirical formula is practical for curve fitting.

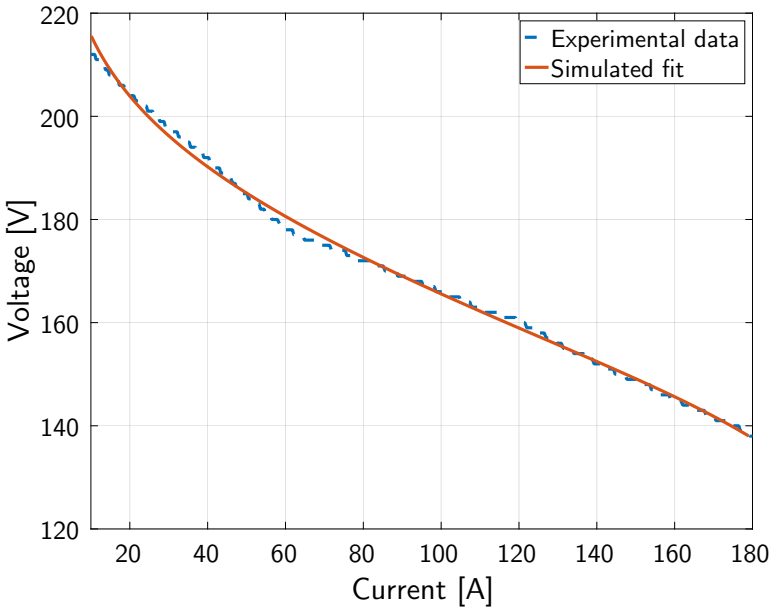

Figure 5.10: Curve fit of the polarisation curve for the PowerCell MS-20 fuel cell [121].

To see how this discrepancy affects the power curve, a comparison between the experimental and simulated stack power will be made. In addition, the fuel cell power ratio Φ_{fc} between the net and stack power will be determined by employing Equation 5.10, which varies as a function of stack current. This term signifies how much stack power is available for use and how much is consumed by auxiliary components such as humidifiers, compressors and coolers within the fuel cell system.

$$\Phi_{fc}(I_{stack}) = \frac{P_{net}}{P_{stack}} \tag{5.10}$$

To derive the net power curve, the power ratio Φ_{fc} will be multiplied by the simulated stack power. The experimental and simulated results for both the stack and net power values are displayed in Figure 5.11.

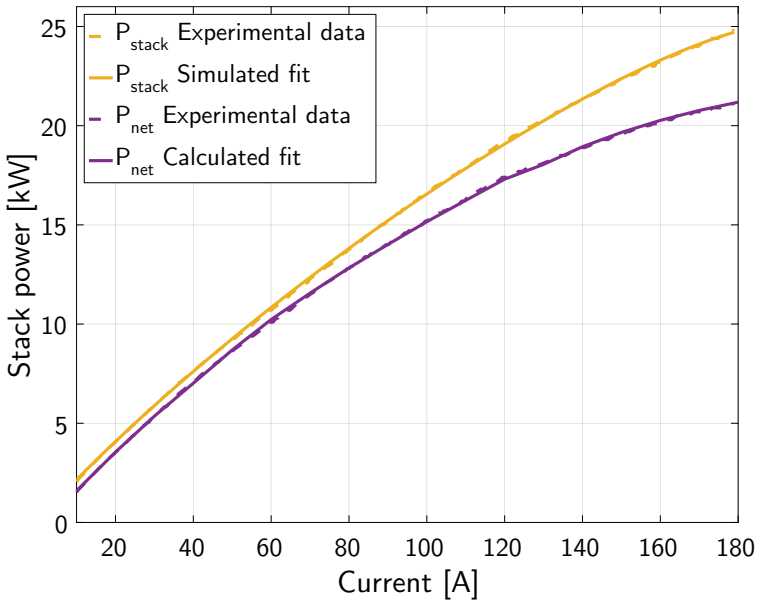

Figure 5.11: Curve fit of the stack and net power curves for the PowerCell MS-20 fuel cell [121].

This graph reveals that the variations in the V-I polarisation curve does not affect the stack power in any manner; the correlation between experimental and simulated data is nearly identical. Furthermore, the net power curves are also in agreement, indicating that the power ratio Φ_{fc} is applied correctly.

The hydrogen consumption rate $\dot{m}_{H_2}$ of the PowerCell MS-20 can be determined by applying Equation 3.71. The number of cells stacked in series is estimated using Equation 3.67, where the single cell voltage V_{cell} is assumed to be 0.7 V [123]. For a net power of 20 kW, a stack voltage V_{stack} of 147 V is needed, as derived from Figure 5.9; this corresponds to 210 cells in series. The stoichiometric value for hydrogen λ_{H_2} is chosen to be 1.2, which is a typical value for PEMFCs [92]. Now, the variation in hydrogen consumption rate can be plotted as a function of net power; see Figure 5.12.

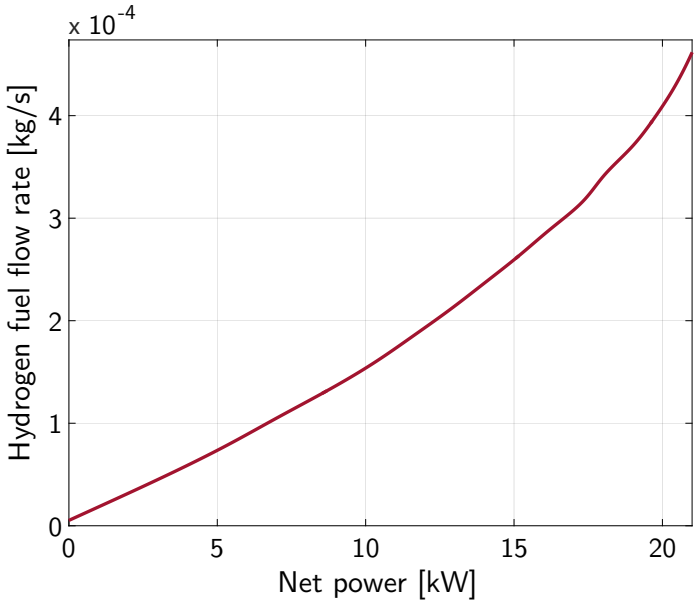

Figure 5.12: Hydrogen consumption rate for the PowerCell MS-20 fuel cell, as a function of net power.

For a constant net power supply of 20 kW, the value for $\dot{m}_{H_2}$ becomes $4.092 \cdot 10^{-4}$ kg/s. This corresponds to $3.657 \cdot 10^{-3}$ kg/s for the H_2O emissions, using the mole ratio in Equation 3.66.

The efficiency of the fuel cell η_{fc} varies with hydrogen consumption rate and generated power, as expressed in Equation 3.59. Assuming a fuel utilisation coefficient μ_f of 100%, the efficiency is plotted as a function of net power in Figure 5.13.

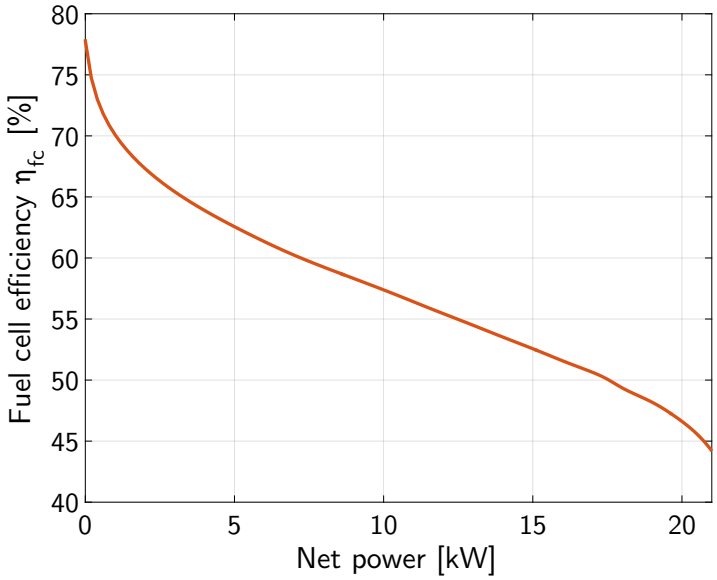

Figure 5.13: Efficiency curve of the PowerCell MS-20 fuel cell, as a function of net power.

However, it should be noted that the presented efficiency curve of the PowerCell MS-20 fuel cell is for indicative purposes only. In order to determine the efficiency of this fuel cell accurately, its true operating conditions need to be specified. The actual performance is influenced by many factors: voltage level per cell V_{cell}, utilisation of hydrogen (hydrogen stoichimetry λ_{H_2}) and operating pressure level [123].

5.7 Selected EMS Configuration

The selected EMS setup focuses on the dynamics of several components within the electrical system: the electric motor, the PV, the PEMFC and the battery systems. Similar to the EAPPS module, the fuel cell and PV systems are available as add-on options, even though these two components are always included in the optimised setup. An overview of the EMS configuration is illustrated in Figure 5.14.

The purpose of this overview is to show to what extent each component is modelled within the MATLAB® environment. The most complex devices are the aircraft subsystems and the power electronics (marked in pink); these are merely modelled as static values in the form of electrical power requirements (see Section 3.2.1) and fixed efficiencies (see Section 3.6.1), respectively. The electric motor is simulated semi-dynamically (marked in yellow), meaning that its efficiency will be determined as a function of the power output and the rotational speed. Last but not least, the most essential components that make the EAPPS (PV, fuel cell and battery systems) are marked in light blue. The system dynamics are modelled accurately after available devices on the current market; SunPower Maxeon Gen III for the PV system, PowerCell MS-20 for the PEMFC system and Panasonic NCR20700A for the battery system. Specific operating conditions and limitations are defined for each system, which may affect the performance significantly.

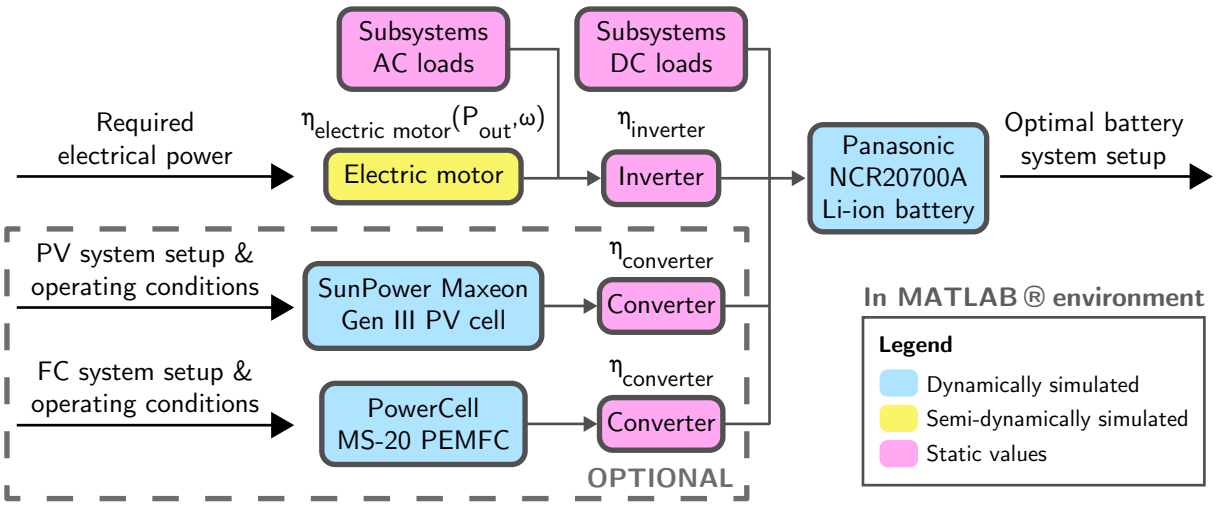

Figure 5.14: Detailed overview of the selected EAPPS configuration.

5.8 Model Verification and Validation

Again, to make sure that the different models are simulated correctly, each one will be verified and validated against existing data. First of all, the electric motor model will be checked by comparing the efficiency map to that of the hFan engine in Section 5.8.1. Then, the curve fitting method for the lithium-ion battery will be assessed by reproducing results from reference data in Section 5.8.2. In Section 5.8.3, a sensitivity study will be performed on the I-V curve of the PV system model. Finally, the curve fitting approach used for fuel cells will be tested against experimental data in Section 5.8.4.

5.8.1 Validation of Electric Motor Model

To approve the electric motor model, the trends of the efficiency map will be compared to that of the hFan engine from a NASA report covering Boeing's SUGAR Volt aircraft [78]. The performance map of this particular engine is given in Figure 5.15.

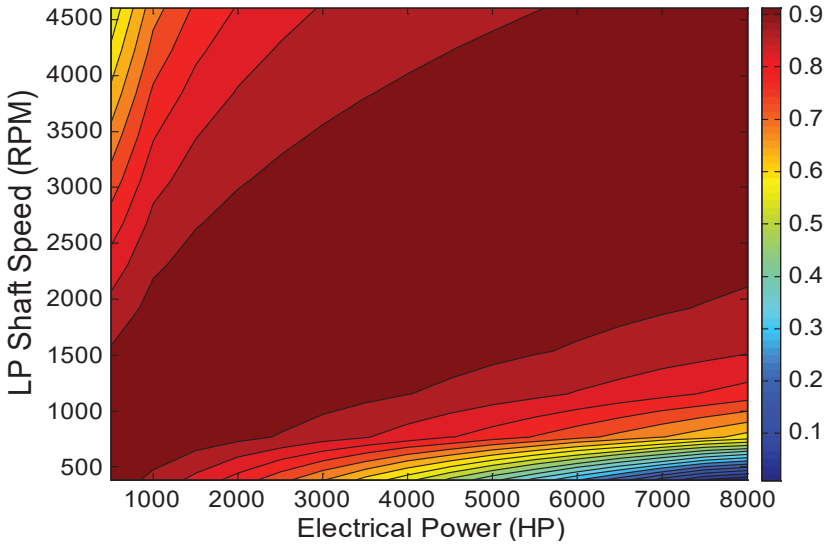

Figure 5.15: Performance map of the hFan motor efficiency as function of electrical power output and rotational speed; adapted from [78].

When comparing the two maps from Figure 5.2 and Figure 5.15, it is evident that the trends at high RPMs are well in agreement. On the contrary, the efficiency at low RPM settings, below 25%, seems to be modelled too optimistically, while the hFan shows a linearly decreasing efficiency with increasing power setting. This means the electric motor will not be modelled accurately enough at RPM settings below 25% in combination with high power outputs. Fortunately, the lowest operating RPMs are during taxiing (around 20%) at low power settings, implying that any discrepancies can be avoided.

5.8.2 Validation of Lithium-Ion Battery Model (Curve Fitting Method)

To validate the battery model from Section 5.4, the curve fitting method will be tested on reference data to see if the same results can be achieved. This non-linear least-squares regression method will be based on Equation 3.35 and Equation 3.38 to Equation 3.40, as described in Ref. [84]. The discharge characteristics come from a 6-cell 1,300 mAh high-C Li-Po battery with a nominal voltage V_0 of 22.2 V (or 3.7 V per cell). Figure 5.16 shows the original graph next to the reproduced plots, with the accompanying curve fitting parameters summarised in Table 5.9. The solid line shows the actual experimental data and the dashed line represents the simulated curve fit. Both graphs are nearly indistinguishable, which means that the curve fitting method is applied correctly. An important battery characteristic presented in the graphs is that the battery capacity is dependent on the discharge rate; higher discharge rates tend to lower the battery energy content, which means that lower discharge rates are favoured.

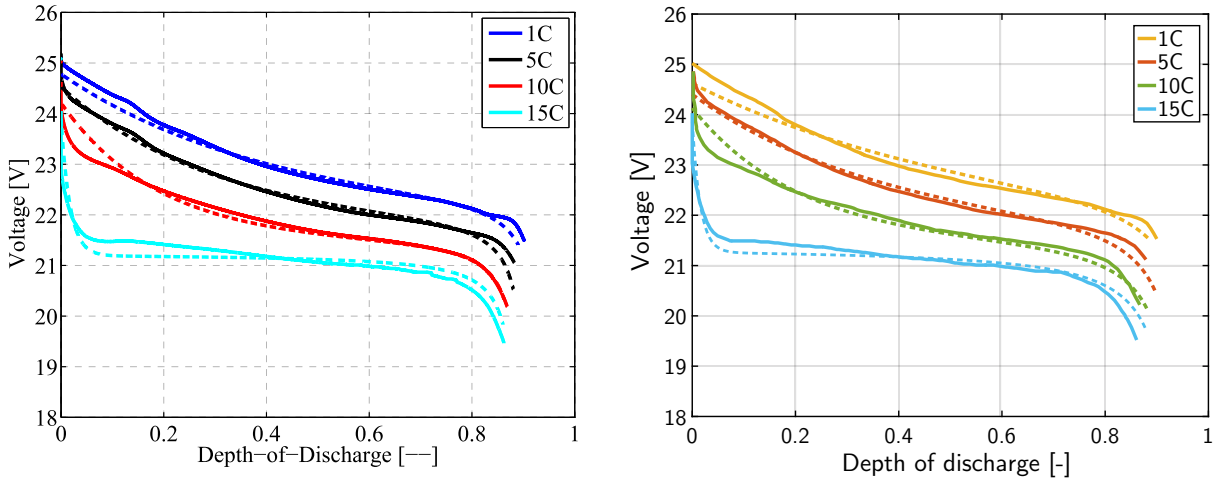

(a) Results from reference data; adopted from [84].

(b) Replicated results with same curve fitting method.

Figure 5.16: Curve fitting results for the 6-cell 1,300 mAh high-C Li-Po battery; experimental data (solid) and simulated fit (dashed).

Table 5.9: Curve fitting parameters for the 6-cell 1,300 mAh high-C Li-Po battery [84].

Data type	K [V]	pc [-]	A [V]	p_3 [Ah^2]	p_2 [Ah]	p_1 [A]	p_0 [Ah^{-1}]	R [Ω]
Reference	0.05832	1.019	2.7020	0.05308	-0.8332	3.5110	-0.7699	0.04865
Replicate	0.12380	1.019	2.5979	0.06220	-0.9781	4.1073	-1.6769	0.04180

5.8.3 Verification of Photovoltaic System Model

To verify the five parameter model, a parametric sensitivity study is done for the series resistance R_s, the parallel resistance R_p, the cell temperature T and the solar irradiance G. The effects of each parameter on the I-V and P-V curves are shown in Figure 5.17 to Figure 5.19.

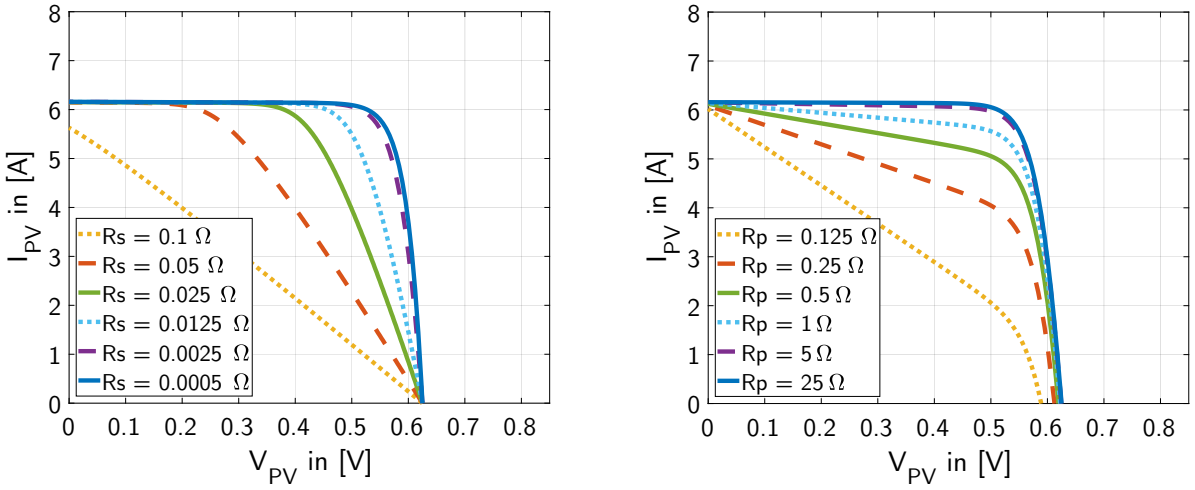

(a) Effect of series resistance on I-V curve.

(b) Effect of parallel resistance on I-V curve.

Figure 5.17: Sensitivity study on the series resistance R_s and the parallel resistance R_p.

Figure 5.17a presents the effect of different values for the series resistance R_s on the I-V curve. Both the maximum power and fill factor decreases with higher resistances. The series resistance affects the I-V curve such that the constant current area becomes smaller or larger; at higher resistances, the voltage becomes lower for the same current. This also means that the voltage at which the current starts to drop is lower for increasing resistances, resulting in lower currents at the maximum power point. From this graph can be said that the ideal series resistance should be as low as possible.

Figure 5.17b demonstrates the effect of different values for the parallel resistance R_p on the I-V curve. The parallel resistance works similar as the series resistance, only for the voltage instead of the current. This time, the maximum power and fill factor decreases with lower resistances. Hence, the ideal parallel resistance should be as high as possible.

Figure 5.18a and Figure 5.18b show the effect of different values for the cell temperature T_{cell} on the I-V and P-V curves. With increasing temperatures, the short-circuit current I_{sc} increases while the open-circuit voltage V_{oc} lowers. This is in line with Equation 3.75 and Equation 3.76. The largest impact of temperature is on the maximum power output: the power output decreases significantly with increasing cell temperature, as shown in Figure 5.18b. The temperature coefficient for the power is equal to -0.115 W/°C or 0.3%/°C, which is identical to the value stated in the specification sheet [119].

Figure 5.19a and Figure 5.19b illustrate the effect of different values for the solar irradiance G on the I-V and P-V curves. The photoelectric current I_{ph} is directly related to the solar irradiance by Equation 3.78, which explains the huge current drop with decreasing irradiance. This in turn affects the maximum power output of the PV cell depicted in Figure 5.19b.

With that being said, the presented graphs seem to agree with perceivable trends in PV literature as well as the data sheet for the Maxeon Gen III cell, suggesting that the five parameter model works correctly.

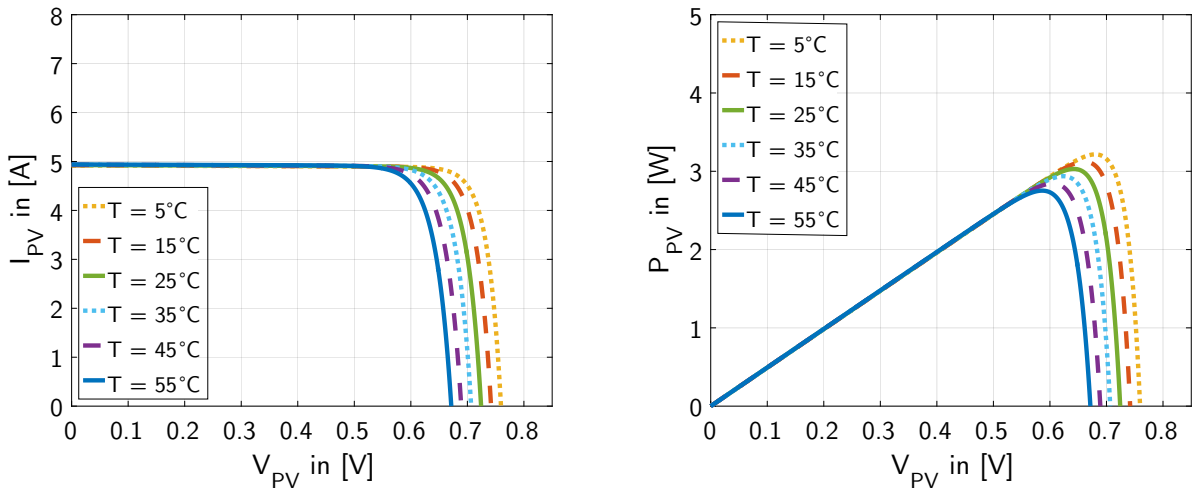

(a) Effect of cell temperature on I-V curve.

(b) Effect of cell temperature on P-V curve.

Figure 5.18: Sensitivity study on the cell temperature T.

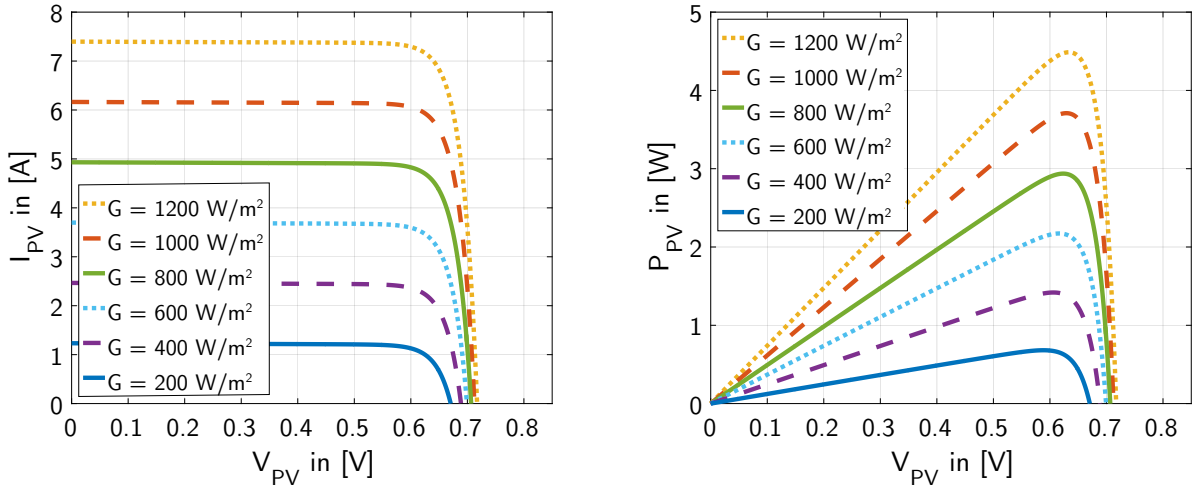

(a) Effect of solar irradiance on I-V curve.

(b) Effect of solar irradiance on P-V curve.

Figure 5.19: Sensitivity study on the solar irradiance G.

5.8.4 Validation of Fuel Cell System Model (Curve Fitting Method)

To validate the fuel cell system model, the same approach for polarisation curve fitting will be applied on reference data, provided by Ref. [91]. For this, the characteristic formula described by Equation 5.6 will be used. The polarisation curve data stems from the AeroStack 200W PEMFC manufactured by Horizon Energy Systems. The curve fitting parameters are given in Table 5.10.

Table 5.10: Curve fitting parameters for the 200W AeroStack fuel cell [91].

Data type	V_0 [V]	B [V$\ln(A)^{-1}$]	R [Ω]	m [V]	n [A^{-1}]
Reference	30.480	0.4947	0.5002	$1.972 \cdot 10^{-4}$	0.6826
Replicate	30.497	0.4850	0.5070	$1.458 \cdot 10^{-4}$	0.7010

In Figure 5.20, the original reference data with the applied curve fit is displayed on the left and the reproduced graph on the right. The circles represent the reference data from AeroStack and the solid

line is the curve fit obtained using Equation 5.6.

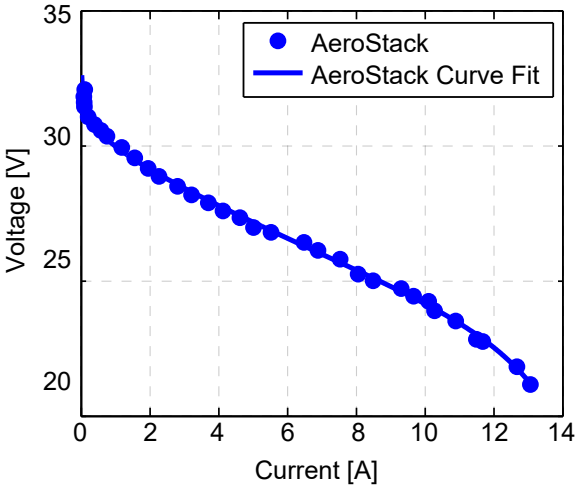

(a) Results from reference data; adapted from [91].

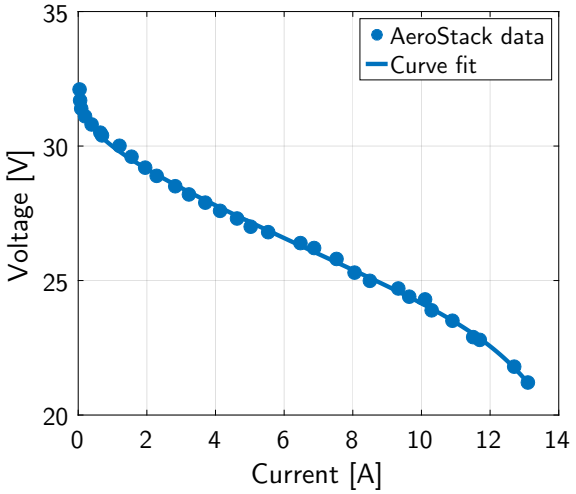

(b) Replicated results with same curve fitting method.

Figure 5.20: Curve fitting results for the 200W AeroStack fuel cell; experimental data (circle) and simulated fit (solid line).

It is clear that both graphs agree well to each other, implying correct use of the curve fitting method described in Section 5.6.

CHAPTER 6

Results and Discussion

After constructing both the EAPPS and EMS modules, a series of trade studies with different EAPPS setups can be performed. This chapter will contain the most important findings from both simulation models regarding the EAPPS setup and overall aircraft flight performance. The focus is primarily on the potential fuel, energy and emission savings.

Firstly, Section 6.1 will present the results of a conventional A320neo with hybrid electric propulsion system (HEPS) only, similar to a former study by Ref. [1, 2]. Then, in Section 6.2, a set of gradual system changes will be introduced to the conventional A320neo using the EAPPS module. These modifications include the electrification of the traditional non-propulsive power systems, the inclusion of fuel cell systems, the installation of PV panels on the outer skin of the A320neo aircraft and downscaling the CFM LEAP-1A engine. This is followed by a projection study of the EAPPS configuration with far future technology (2040+) in Section 6.3. The results from the previous sections are two optimised EAPPS setups in 2020+ and 2040+, respectively. Then, using the EMS module, the dynamic behaviour of the electrical system for both setups will be studied in Section 6.4; this leads to corrective measures for the battery specific energy, which can be fed back into the EAPPS module. After the final corrected results for both time frames are obtained, the overall performance can then be compared to that of the conventional A320neo aircraft in Section 6.5; the absolute and relative savings in terms of fuel, energy and emissions will be discussed in more detail.

6.1 Conventional A320neo with HEPS (2020+)

This section describes the analysis of a conventional A320neo only equipped with HEPS, based on near term technology (2020+); these parameters can be found in Chapter 3.

First of all, the effect of power management strategy on the fuel and energy consumption will be discussed in Section 6.1.1. This is an extension of a former study described in Ref. [1, 2]. This is followed by a Pareto efficiency plot in Section 6.1.2, which suggests that both fuel and energy consumption cannot be optimised at the same time. Furthermore, a closer look is taken at three different battery charging strategies. The chosen approach determines the total electrical system mass to be carried throughout the mission and thus affects the overall aircraft performance. Section 6.1.3 and Section 6.1.4 will cover its effect on mass as well as fuel and energy consumption, respectively. Lastly, some insights regarding power management and battery charging strategies will be shared in Section 6.1.5.

6.1.1 Effect of Power Management Strategy on Fuel and Energy Consumption

Using the EAPPS module, the take-off and climb power split ratios have been varied independently between 0% and 40%. Larger values of power splits are not feasible as in those cases the total aircraft mass, caused by the increased electrical system mass, will exceed the maximum take-off mass (MTOM).

Figure 6.1 shows the relative fuel consumption as a function of the take-off split $\phi_{takeoff}$ and climb power split ϕ_{climb}, with respect to the conventional A320neo without HEPS.

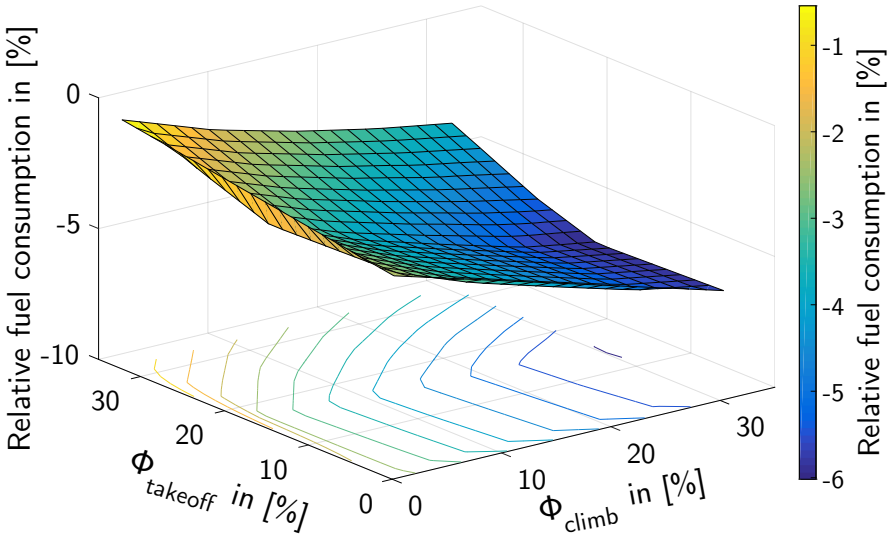

Figure 6.1: Effect of power management strategy on relative difference in fuel consumption.

This graph indicates that by lowering the take-off power split $\phi_{takeoff}$ and increasing the climb power split ϕ_{climb}, the fuel consumption can be reduced. The downward trend of fuel consumption as function of ϕ_{climb} is explained by the amount of fuel saved during the climb phase, which offsets the additional fuel burnt for carrying along the electrical system mass. This is generally not the case for the take-off power split, as the fuel saved during the short period of time at take-off is less than the additional fuel consumed for the inclusion of the electrical system mass. This mass is mainly determined by the peak power sizing requirements; increasing $\phi_{takeoff}$ and thus the peak power leads to a heavier system. At $\phi_{takeoff} = 0$ and $\phi_{climb} = 0$, the reduction in relative fuel consumption is around 3%; this is because fully electric taxiing is applied in each case, which saves fuel by avoiding inefficient use of the turbofan engine during taxiing. This percentage is similar to the estimations made by Safran and Airbus [103].

To justify the use of HEPS, the total energy consumption should also be considered within this research; this is illustrated in Figure 6.2. The total energy consumed comprises the chemical energy stored as fuel and the electrical energy in the form of batteries. The relative energy consumption is the difference with respect to the energy consumption of the conventional A320neo without HEPS.

The implementation of HEPS results in reduced fuel consumption for power splits up to 35%, however, this is not always the case for energy consumption. This is observed better in Figure 6.3, a contour plot of Figure 6.2. The graph shows a distinct orange border where the relative energy consumption breaks even. This boundary, which extends to different combinations of power split ratios, should be kept in mind when selecting an optimised HEPS configuration.

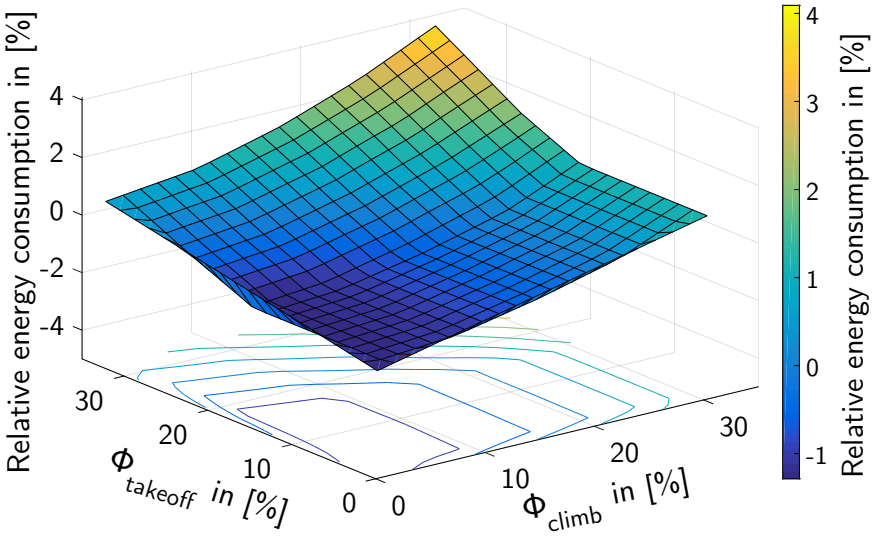

Figure 6.2: Effect of power management strategy on relative difference in energy consumption.

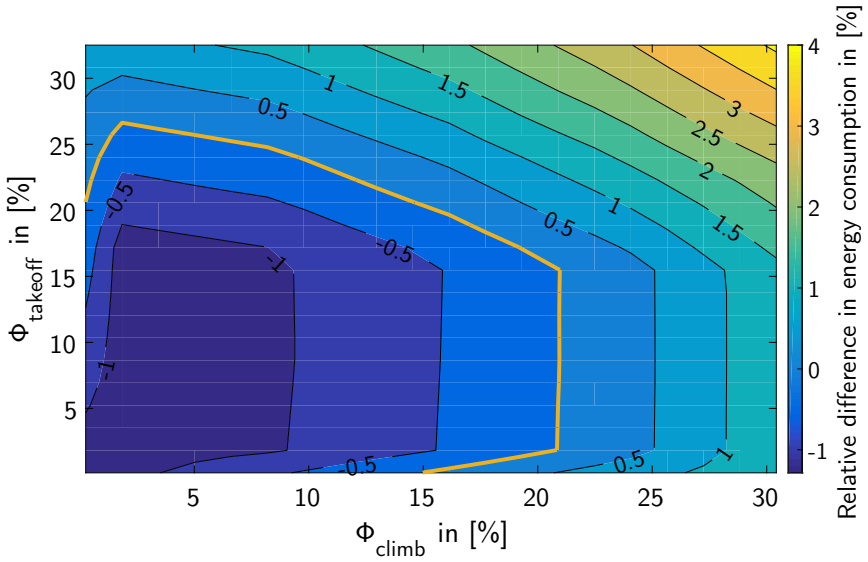

Figure 6.3: Effect of power management strategy on relative difference in energy consumption in a contour plot; break-even border is marked orange.

The trends shown in Figure 6.1 and Figure 6.2 as a function of power management strategy agree well with the results from Ref. [1]. Since the assumed time frame and electrical system characteristics from the previous study are significantly different than those from this study, further quantitative comparison is not provided here.

6.1.2 Pareto Representation of Conventional A320neo with HEPS (2020+)

Since fuel and energy consumption cannot be optimised simultaneously without compromising each other, the Pareto efficiency is plotted in Figure 6.4, following a multi-objective approach as in Ref. [1]. This graph illustrates different power management strategies as individual points corresponding to various fuel and energy consumption. If the total aircraft mass for a combination of take-off and climb power splits exceeds the MTOM, that specific point is marked grey. The reference point of the conventional A320neo without any modifications is marked dark blue.

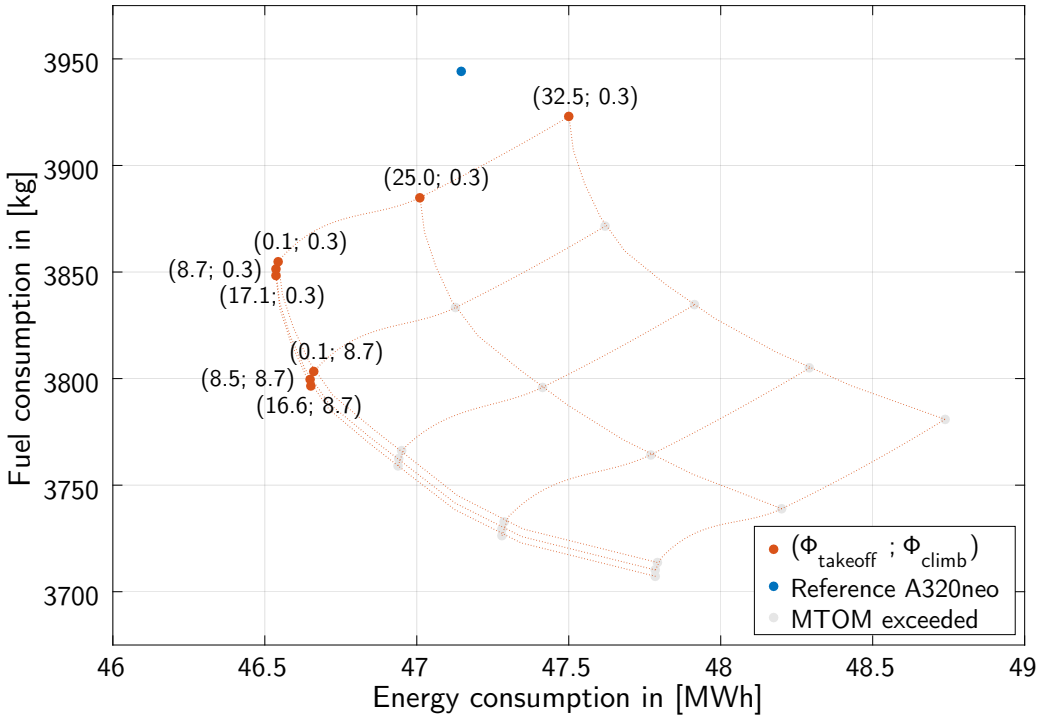

Figure 6.4: Pareto efficiency of conventional A320neo with HEPS (2020+).

6.1.3 Effect of Battery Charging Strategy on Electrical System Mass

The mass of the electrical system depends on the power splits during take-off and climb, $\phi_{takeoff}$ and ϕ_{climb}, respectively; in essence, the power management strategy. In addition to that, the choice of charging strategy affects the total amount of batteries to be carried and thus contributes to the change in electrical system mass. Keep in mind that the state of charge (SOC) is limited to a minimum of 10% to maintain safe operation. Another alternative is to keep the SOC between 25% and 85% to prolong battery life [124]. Since this study mainly focuses on the feasibility and potential of HEPS, this approach will not be investigated; it can be considered as a topic for future research.

The following charging strategies are available during the descent phase:

- *No charging*
  If batteries are not charged in-flight during descent, more capacity needs to be carried along to perform the landing and taxi-in segments electrically. The batteries will be sized for the full mission without additional fuel and energy consumption. The SOC will be a minimum of 10% at the end of the mission.

- *Partially charging*
  Another option is to charge the batteries to a certain capacity such that the landing and taxi-in sequences can be completed electrically. This way the battery is sized only for the taxi-out, take-off and climb phases; however, additional fuel will be used by the engine to charge the batteries. The SOC is limited to 10% at the end of the mission.

- *Fully charging*
  The last alternative is to fully charge the batteries during descent; it is the least fuel efficient choice, but results in a near-full battery (SOC $>$ 75%) at the end of the mission. This can be crucial for quick turnaround times at the airport. Again, the battery can be sized for the first

three segments (taxi-out, take-off and climb) only, at the cost of consuming extra fuel during descent.

Since average turnaround times for the A320 are at least 30 to 35 minutes, sufficient time is available to recharge the batteries to full capacity on-ground [125]. This eliminates the latter strategy of fully charging. The remaining two options will be analysed for the same range of power split ratios as applied previously.

Figure 6.5 and Figure 6.6 depict the masses of the electrical system at various power management strategies for the two different charging approaches, respectively. The red solid line indicates the electrical system mass limitation of 6,700 kg (mission mass of 10,700 kg minus fuel mass of 4,000 kg).

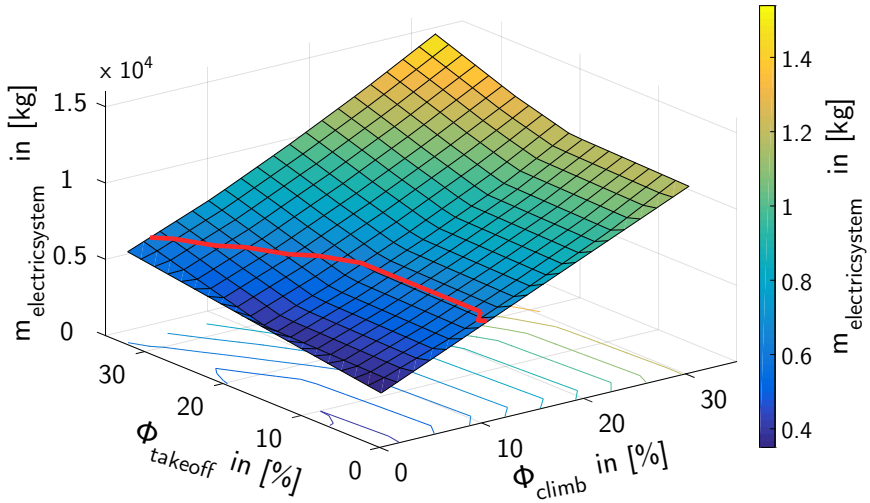

Figure 6.5: Effect of power management strategy on electrical system mass, assuming no charging; mass limitation of 6,700 kg is marked red.

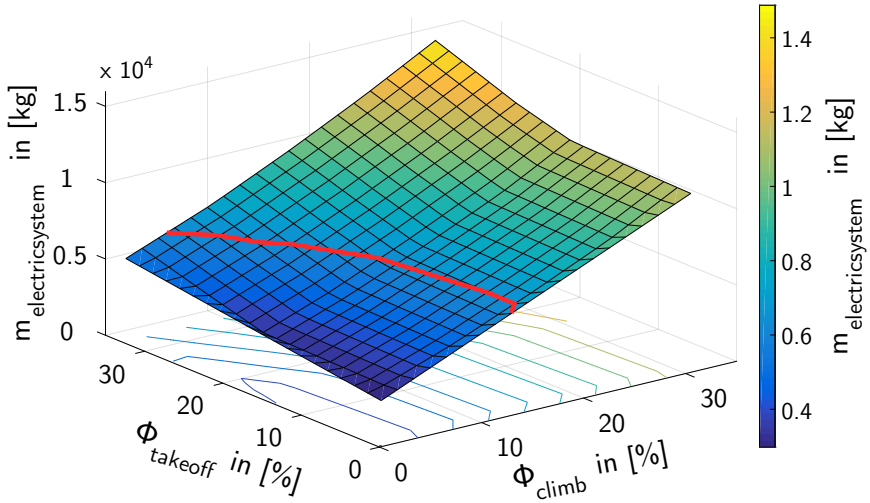

Figure 6.6: Effect of power management strategy on electrical system mass, assuming partially charging; mass limitation of 6,700 kg is marked red.

From Figure 6.5 and Figure 6.6 can be deduced that the electrical system mass is more affected by the power split of the climb phase than the power split from take-off. The mass of the batteries is determined by its energy, which is the produced power multiplied by its duration of supply. The masses

of the electric motor and the inverter are only based on the maximum power supplied. Even though the power required during climb is significantly lower, resulting in a smaller motor and inverter, the overall electrical system mass is dictated by the batteries. The duration of the climb phase is notably longer than the take-off phase, which causes the batteries to be sized much larger to provide sufficient energy. This explains the steeper slope in the direction of the climb power split ϕ_{climb}, which hints that the system mass is primarily governed by the mass of the batteries. Furthermore, at $\phi_{takeoff} = 0$ and $\phi_{climb} = 0$, the electrical system masses for no charging and partially charging are equal to 3,500.7 kg and 2,984 kg, respectively; this is required for performing the taxiing phase electrically.

Since the mass trends of the two charging strategies are nearly indistinguishable, the relative difference in mass between the two is plotted in Figure 6.7, as a contour plot.

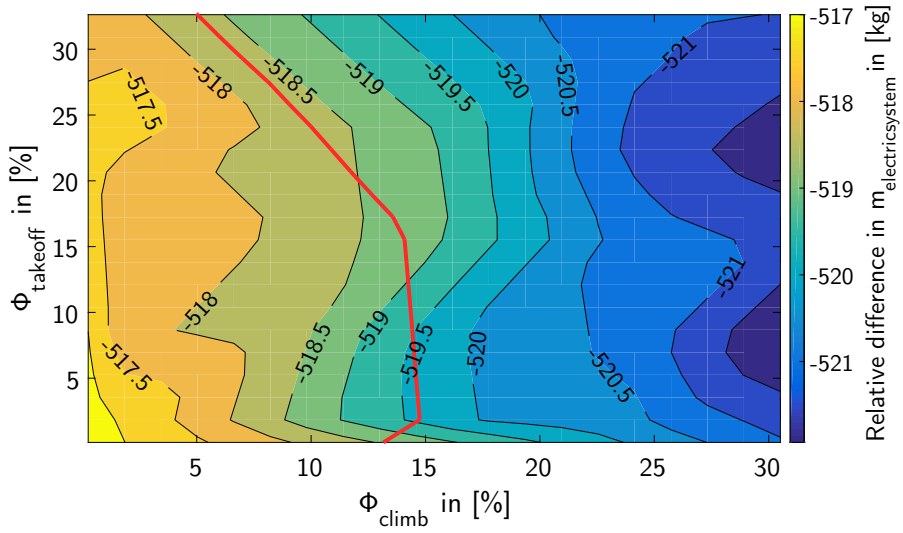

Figure 6.7: Effect of power management strategy on relative difference in electrical system mass between no charging and partially charging; mass limitation of 6,700 kg is marked red.

It can be observed that if the battery is partially charged during descent, the electrical system will be sized slightly smaller; approximately 520 kg of mass is saved for any given power management strategy. To see how this mass change affects the overall mission performance, both charging strategies will be investigated further on its fuel and energy consumption in Section 6.1.4.

6.1.4 Effect of Battery Charging Strategy on Fuel and Energy Consumption

Charging the battery during flight will inevitably lead to additional fuel and energy consumption. Taking into account the differences in electrical system mass, Figure 6.8 and Figure 6.9 illustrate the relative differences between no charging and partially charging of fuel and energy consumption, respectively. A positive value suggests that the fuel and energy consumption are higher for partially charging than no charging, and vice versa when it is negative.

Figure 6.8 presents the relative fuel consumption between the two charging strategies. The effect of the take-off power split $\phi_{takeoff}$ on the relative fuel consumption is rather insignificant compared to the effect of the climb power split ϕ_{climb}. This can be led back to the fact that the climb segment lasts much longer than the take-off segment. As the battery size grows with higher climb power splits, the energy required for the taxi-in phase will increase as well, due to the added electrical system mass. This leads to a higher amount of capacity that needs to be recharged, which in turn contributes to more fuel consumed during the descent phase.

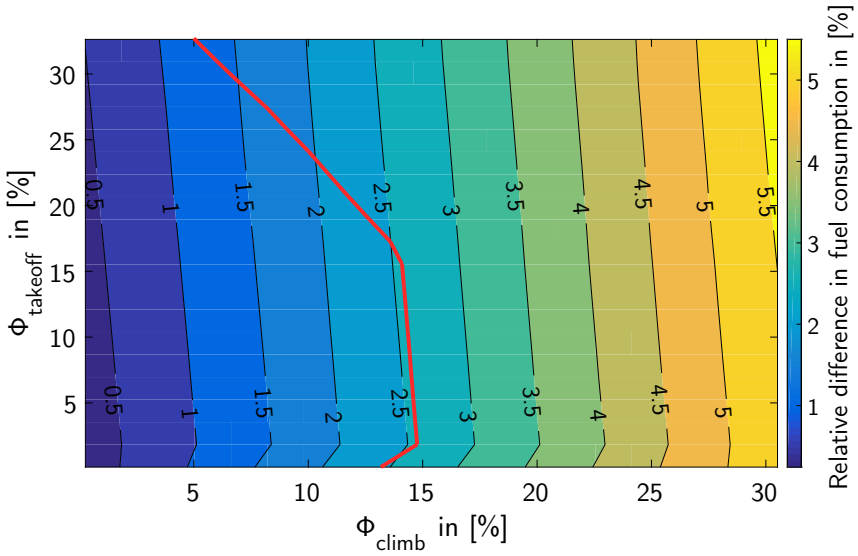

Figure 6.8: Effect of power management strategy on difference in relative fuel consumption between no charging and partially charging; mass limitation of 6,700 kg is marked red.

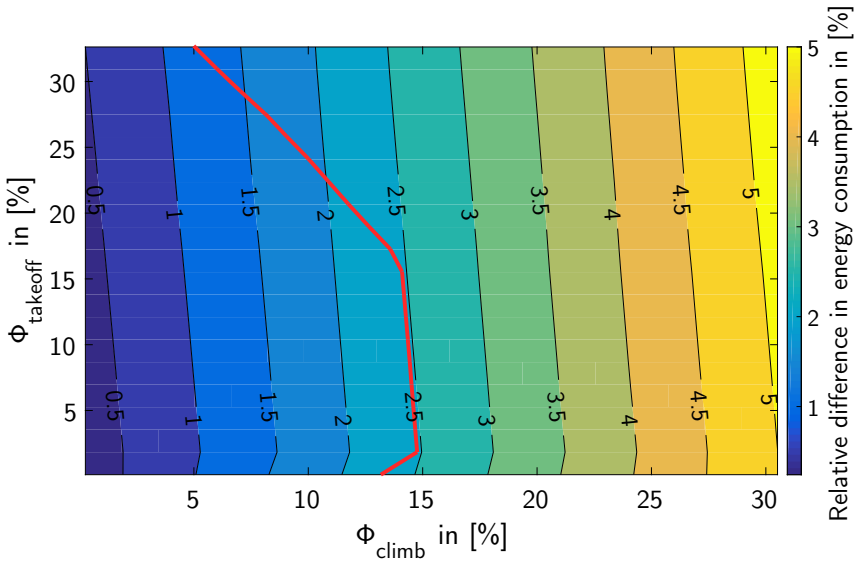

Figure 6.9: Effect of power management strategy on relative difference in energy consumption between no charging and partially charging; mass limitation of 6,700 kg is marked red.

A similar relationship between the charging strategies is shown for the energy consumption in Figure 6.9. Again, the influence of the climb power split ϕ_{climb} dictates over that of the take-off power split $\phi_{takeoff}$.

From Figure 6.8 and Figure 6.9 can be concluded that the strategy of partially charging is not beneficial in terms of fuel and energy consumption for any power management strategy. The fuel and energy required to charge the batteries during descent does not offset the lower fuel and energy consumption due to the smaller and lighter electrical system.

This is better illustrated in Figure 6.10, where the absolute amounts of fuel and energy consumed during the mission are plotted for a power management strategy of $\phi_{takeoff} = 16.7\%$ and $\phi_{climb} = 8.7\%$. Also, as shown by the plateaus in the beginning and the end of the mission, the taxi-out and taxi-in phases are performed fully electric. The descent phase and thus the charging procedure starts about 4,000 seconds into the mission. After a short amount of time, the consumption by the partial charging

approach overtakes that of the approach without charging; for this particular setup, the differences in fuel and energy consumed are 63.1 kg and 0.75 MWh, respectively.

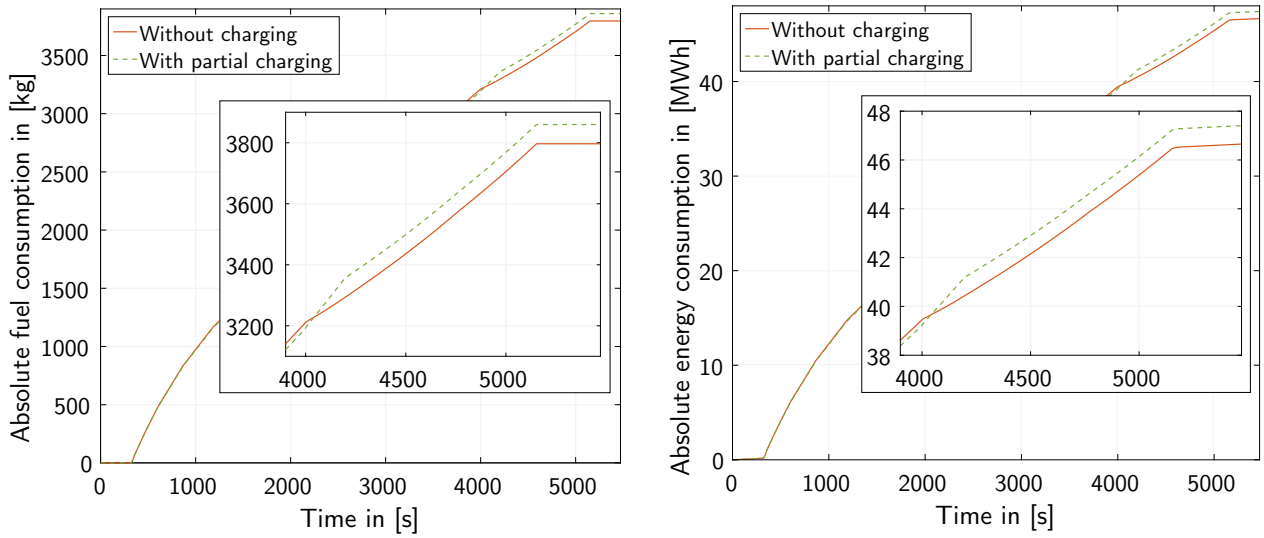

(a) Effect of battery charging strategy on absolute fuel consumption.

(b) Effect of battery charging strategy on absolute energy consumption.

Figure 6.10: Effect of battery charging strategy on absolute fuel and energy consumption.

6.1.5 Discussion

The first investigation of the conventional A320neo aircraft with HEPS (see Section 6.1.1) demonstrates that one should aim for higher power split values, within the aircraft MTOM limitations, to reduce fuel consumption. However, when taking the total energy consumption into account, a constraint appears illustrating a break-even point where the increased electrical power does not outperform the increase in electrical system weight anymore. The priority of propulsive electrification lies in optimising the climb power split ϕ_{climb}, as benefits grow with longer operating times. Furthermore, fully electric taxiing already reduces the fuel and energy consumption by 3% and 1%, respectively. Lastly, the batteries used for HEPS should be recharged on-ground, as in-flight charging only results in less fuel and energy savings.

6.2 A320neo with EAPPS Modifications (2020+)

After the first analyses with the baseline aircraft described in Section 6.1, the aircraft will be modified incrementally to investigate potential optimisations of the EAPPS. These changes include the conversion of the traditional non-propulsive power systems into an electrical subsystem architecture (MEA), the implementation of a fuel cell system (including hydrogen storage), the installation of PV on the outer skin and the downscaling of the turbofan engine. The projected technology level of the components used in the electrical system will be from the near future (2020+).

First, the baseline aircraft is converted into a MEA by introducing an electrical subsystem architecture; the effect of this modification on its fuel and energy consumption can be found in Section 6.2.1. Afterwards, three different EAPPS configurations are applied to the MEA with varying fuel cell output power. The results will be compared in Section 6.2.2. Additionally, PV panels are installed on the outer skin of the aircraft to see whether this EAPPS setup can be beneficial or not. The outcome of this

analysis is described in Section 6.2.3. A Pareto graph, similar to Figure 6.4 in Section 6.1.2, is then constructed in Section 6.2.4 to find the optimal power split values to be investigated. Furthermore, the effect of engine scaling will be analysed in Section 6.2.5. An additional PV study is performed in Section 6.2.6 to see how the flight mission impacts the overall performance of the EAPPS configuration. Lastly, the findings and the optimised EAPPS setup for this specific time frame (2020+) will be expressed in Section 6.2.7.

6.2.1 Effect of Electrical Subsystem Architecture on Fuel and Energy Consumption

The first alteration is the electrification of traditional aircraft subsystems; here, the pneumatic and hydraulic systems have been replaced by electrical counterparts, as mentioned earlier in Section 2.3.2. This means that bleed air off-takes are no longer required from the engine, allowing a more efficient operation of the engine. Figure 6.11 and Figure 6.12 show the impact of this modification on the relative fuel and energy consumption, respectively. Note that the electrical system mass limitation is now increased to 7,499 kg due to the resultant mass change of MEA conversion (Table 4.3).

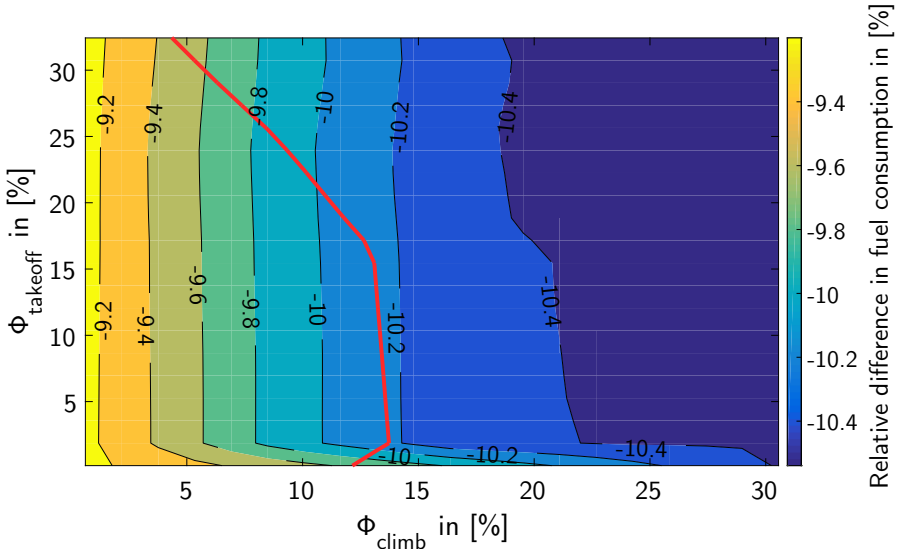

Figure 6.11: Effect of power management strategy on relative difference in fuel consumption, assuming electrical subsystem architecture; mass limitation of 7,499 kg is marked red.

The relative change in fuel consumption with respect to the reference case from Section 6.1.1 is illustrated in Figure 6.11. This architecture conversion is beneficial regardless of any take-off power split $\phi_{takeoff}$ and climb power split ϕ_{climb} combination. This means that the HEPS always compensates for its additional electrical system mass. It also helps that an A320neo with an electrical subsystem architecture carries 799 kg less in aircraft equipment than for the conventional configuration, as depicted in Table 4.3.

The same trend is seen for the relative energy consumption, as shown in Figure 6.12. Here, the MEA can save up to 9.4% of energy consumed compared to the baseline aircraft. In relative terms, the optimal power management strategy should operate at take-off power splits above 25% and climb power splits between approximately 18% and 25%. Unfortunately, the aircraft mass limitation only allows a maximum reduction of 9.2% for a take-off power split ratio of around 12% and a climb power split ratio between 2% and 18%. Keep in mind that this optimum may not hold true in absolute senses; the absolute gains with respect to the conventional A320neo aircraft will be presented later in Section 6.2.4.

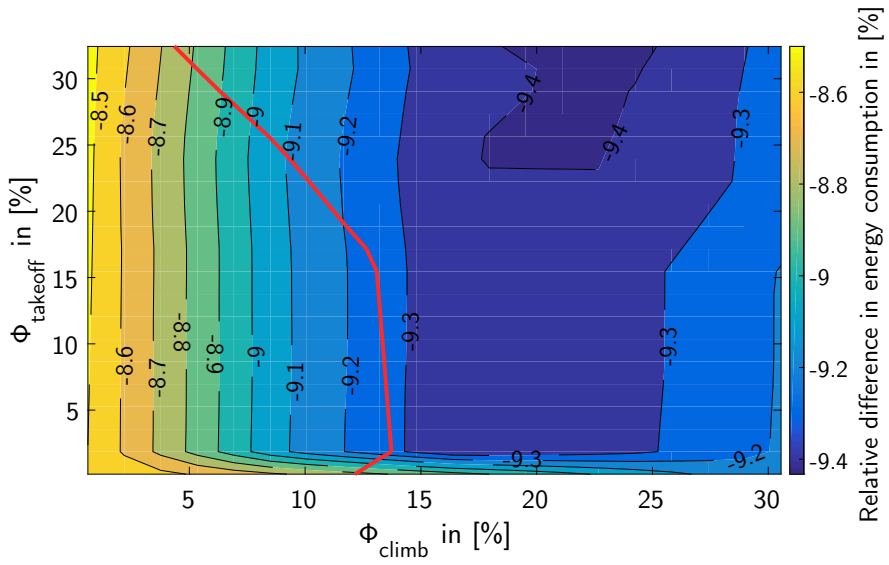

Figure 6.12: Effect of power management strategy on relative difference in energy consumption, assuming electrical subsystem architecture; mass limitation of 7,499 kg is marked red.

6.2.2 Effect of Fuel Cells on Fuel and Energy Consumption

The next adjustment is the addition of a fuel cell system to alleviate the required load from the batteries. The principal idea behind this is that the hydrogen used has a higher specific energy than batteries, so fuel cells will perform far better in endurance. However, the sizing of the fuel cell and its auxiliary devices (e.g. compressor, humidifier, fuel storage and supply, etc.) is defined by the maximum power the system has to provide.

For the same power output, the initial system mass of batteries is lower than that of fuel cells; however, as the operating time increases, more batteries need to be added to supply sufficient energy, while fuel cells only require additional hydrogen. With the far superior specific energy of hydrogen, this means that at some point the fuel cell system mass becomes lower than the battery system mass. Hence, a careful trade-off between maximum fuel cell power and operating time needs to be made to allow a reduction in total electrical system mass.

To investigate this matter, three configurations with varying maximum fuel cell power will be examined; these are described below.

- *Configuration 1: Constant power supply of 200 kW*
  The first configuration is a 200 kW fuel cell system which provides continuous power throughout the whole mission. The value of 200 kW is based on the minimum electrical power required by the various non-propulsive aircraft subsystems of the MEA. The fuel cell size is defined by the maximum power of 200 kW.
- *Configuration 2: Constant power of 200 kW and 5% of the electrically provided propulsive power during take-off/climb*
  The second configuration extends the first configuration and also provides 5% hybridisation power towards the electric motor during take-off and climb phases. This means that the fuel cell system will be sized for the highest power value between 5% of electric take-off power and 5% of electric climb power, depending on the chosen power management strategy.
- *Configuration 3: Constant power of 200 kW and 10% of the electrically provided propulsive power during take-off/climb*

The last configuration is similar to the second one, only now sized for 10% hybridisation power during take-off and climb. The fuel cell system size is dictated by the highest power value between 10% of electric take-off power and 10% of electric climb power, depending on the chosen power management strategy.

The changes in fuel consumption as a function of the power management strategy for the three configurations are shown in Figure 6.13a to Figure 6.13c.

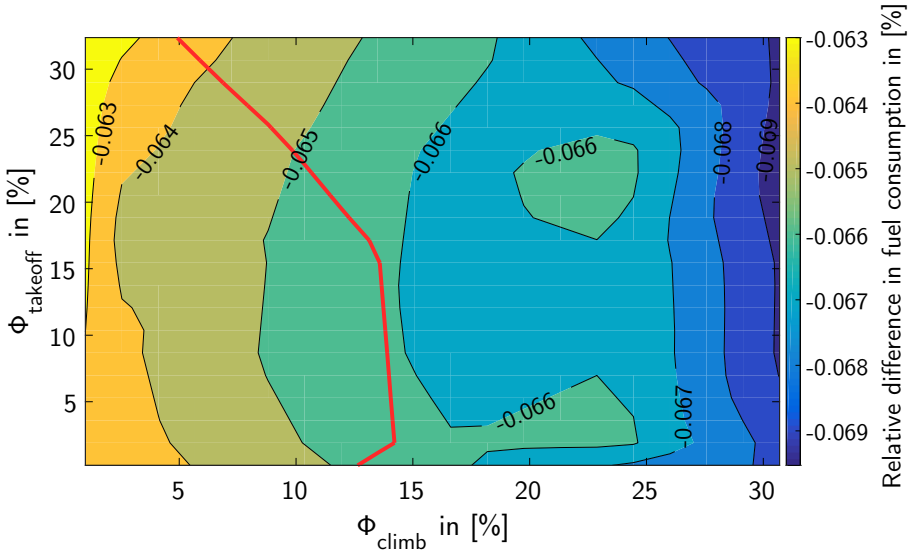

(a) Configuration 1: Constant supply of 200 kW and no additional power provided during take-off/climb.

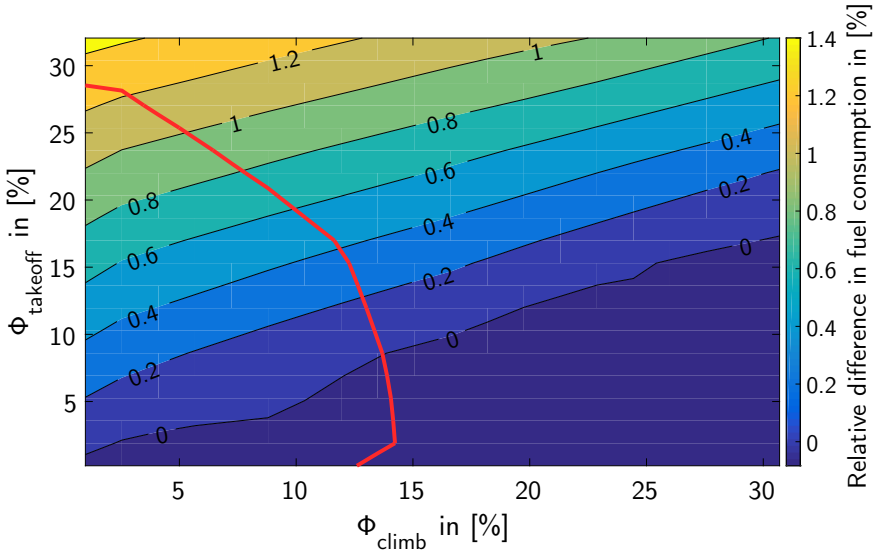

(b) Configuration 2: Constant supply of 200 kW and 5% of required power provided by fuel cells during take-off/climb.

Figure 6.13: Effect of power management strategy on relative difference in fuel consumption, assuming varying fuel cell power; mass limitation of 7,499 kg is marked red.

Analysing these graphs, it can be said that the only configuration worth pursuing is the first one: a fuel cell system that provides a constant power supply of 200 kW. Figure 6.13a shows that the inclusion of fuel cells could still lead to an improvement in fuel burn, albeit much less than what the first modification achieved. Compared to the modified A320neo with only an electrical subsystem

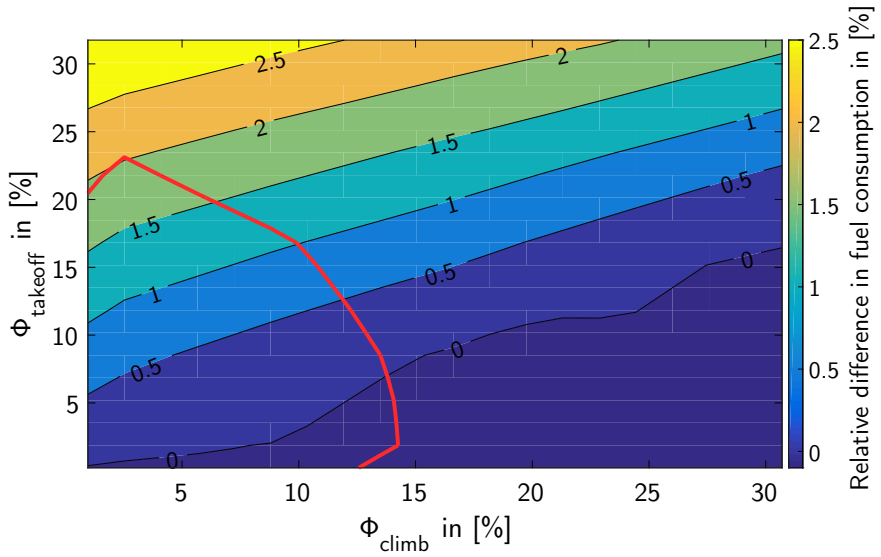

(c) Configuration 3: Constant supply of 200 kW and 10% of required power provided by fuel cells during take-off/climb.

Figure 6.13: Effect of power management strategy on relative difference in fuel consumption, assuming varying fuel cell power; mass limitation of 7,499 kg is marked red.

architecture in Section 6.2.1, the overall gain is slightly more than 0.06% of fuel saved for any chosen power management strategy. As said before, this improvement is possible due to the higher specific energy of the hydrogen fuel; the overall mass of the electrical system becomes less when part of the batteries is replaced by a fuel cell system. Both Figure 6.13b and Figure 6.13c show an increase in fuel consumption. This indicates that sizing the fuel cell system for 5% or 10% of the required hybridisation power is inefficient and eliminates all benefits of installing such a system.

Figure 6.14 presents the change in energy consumption for configuration 1, relative to the MEA described in Section 6.2.1. Now the total energy consumed consists of the chemical energy stored in kerosene and hydrogen as well as the electrical energy in the form of batteries.

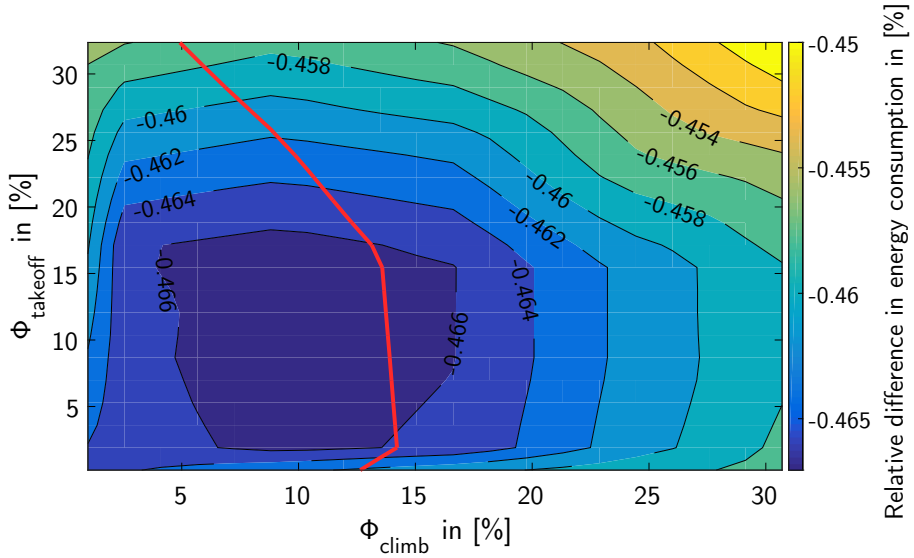

Figure 6.14: Effect of power management strategy on relative difference in energy consumption, assuming configuration 1; mass limitation of 7,499 kg is marked red.

Contrary to the fuel consumption, the overall energy consumption does lower by a higher amount

of around 0.5% for any arbitrary chosen power management strategy. This implies that the process of generating electrical power throughout the mission using fuel cell systems is more efficient than extracting it directly from lithium-ion batteries for this mission length of 1,000 km. Do keep in mind that, from an economical point of view, this approach might not be effective yet, as today's kerosene prices are still lower than the current energy equivalent price of hydrogen [126].

6.2.3 Effect of Photovoltaics on Fuel and Energy Consumption

To demonstrate the impact of photovoltaics, a specific flight mission has been selected: the aircraft departs from Toulouse at solar noon on 21st of March 2017 towards Amsterdam, covering a total distance of 998 km. The changes in fuel and energy consumed for this mission, relative to the modified aircraft in Section 6.2.2, are presented in Figure 6.15 and Figure 6.16, correspondingly. In this case, the total energy consumption is equal to the chemical energy stored in kerosene and hydrogen as well as the electrical energy provided by the batteries, minus the electricity generated by the PV system.

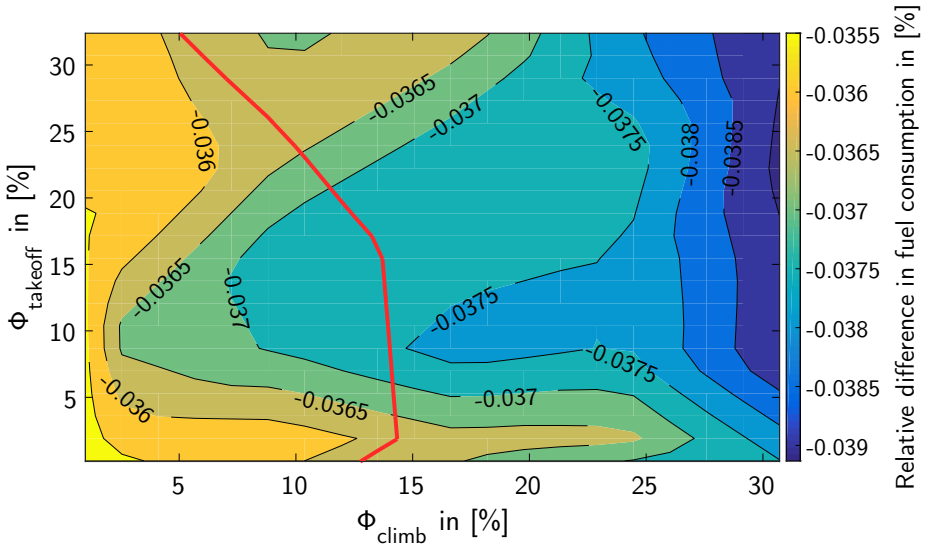

Figure 6.15: Effect of power management strategy on relative difference in fuel consumption; mass limitation of 7,499 kg is marked red.

Figure 6.15 reveals that photovoltaics is of limited use on this chosen flight, for any chosen power management strategy. A maximum of 0.04% of fuel can be saved compared to the previous configuration; this corresponds to 1.4 kg of kerosene. It can be argued whether this amount of fuel saved is meaningful enough to design and install a complete PV system on the A320neo.

As shown in Figure 6.16, installing PV panels on the A320neo saves energy irrespective of power management strategy; the energy consumed can be reduced by about 0.25%. It should also be mentioned that the energy generated by photovoltaics is sustainable: it is 'free' and does not produce any emissions during operation.

Nonetheless, the resulting fuel and energy savings can be quite deceiving, as the mission received the highest solar irradiance at that particular day during solar noon. In reality, the position of the Sun changes throughout the day, so flying at different times might not even lead to savings. The effectiveness of photovoltaics is greatly dependent on location, time and date; therefore, another PV analysis will be done for multiple flight missions at different times of the day (morning, afternoon and evening), once the most effective EAPPS configuration in terms of fuel and energy savings has been determined. This analysis can be found in Section 6.2.6.

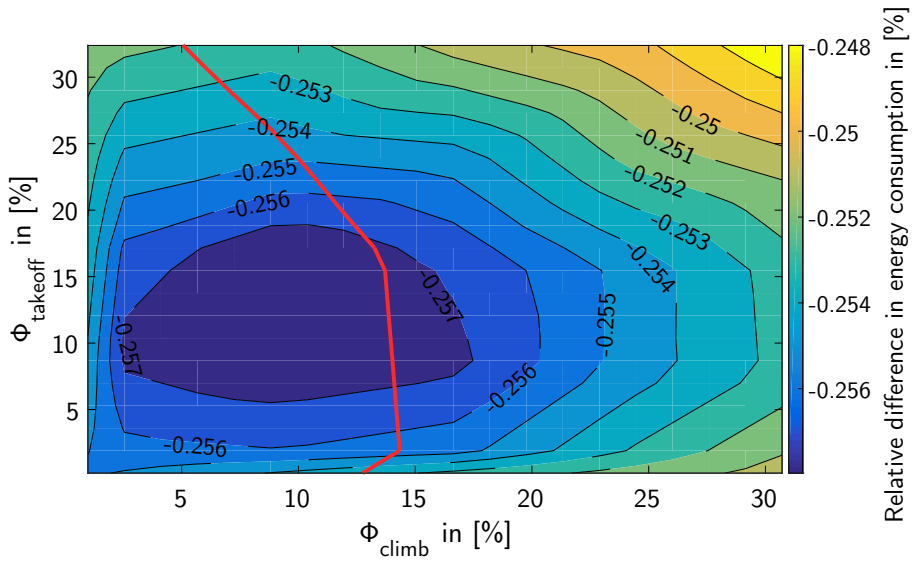

Figure 6.16: Effect of power management strategy on relative difference in energy consumption, assuming photovoltaics for flight from Toulouse to Amsterdam; mass limitation of 7,499 kg is marked red.

6.2.4 Pareto Representation of A320neo with EAPPS Modifications (2020+)

The absolute fuel and energy consumption for the baseline aircraft with all three modifications (electrical subsystems, fuel cells and photovoltaics), with respect to the conventional A320neo are presented in Figure 6.17 and Figure 6.18, respectively.

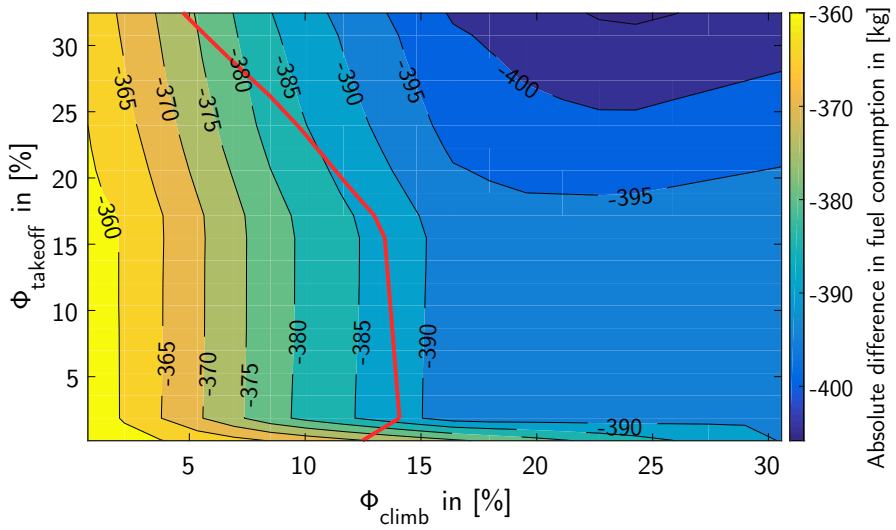

Figure 6.17: Effect of power management strategy on absolute difference in fuel consumption, assuming the baseline aircraft with all three modifications (electrical subsystems, fuel cells and photovoltaics); mass limitation of 7,499 kg is marked red.

The Pareto efficiency for this aircraft is shown in Figure 6.19. From all the simulated take-off and climb power split combinations, the best results which consume the least amount of fuel and energy, without exceeding the mass limit, are marked purple in the graph and arranged in Table 6.1.

As downsizing the engine has not been considered yet, this will be the subject of focus in Section 6.2.5.

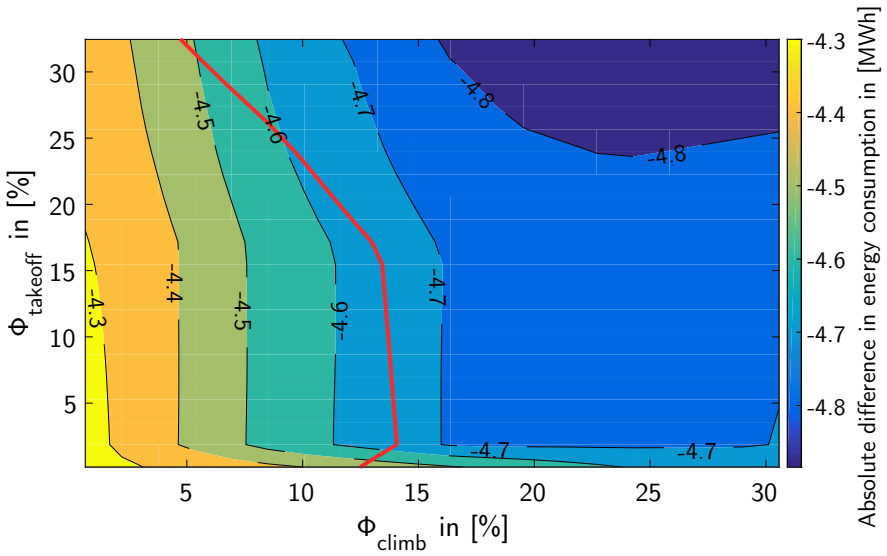

Figure 6.18: Effect of power management strategy on absolute difference in energy consumption, assuming the baseline aircraft with all three modifications (electrical subsystems, fuel cells and photovoltaics); mass limitation of 7,499 kg is marked red.

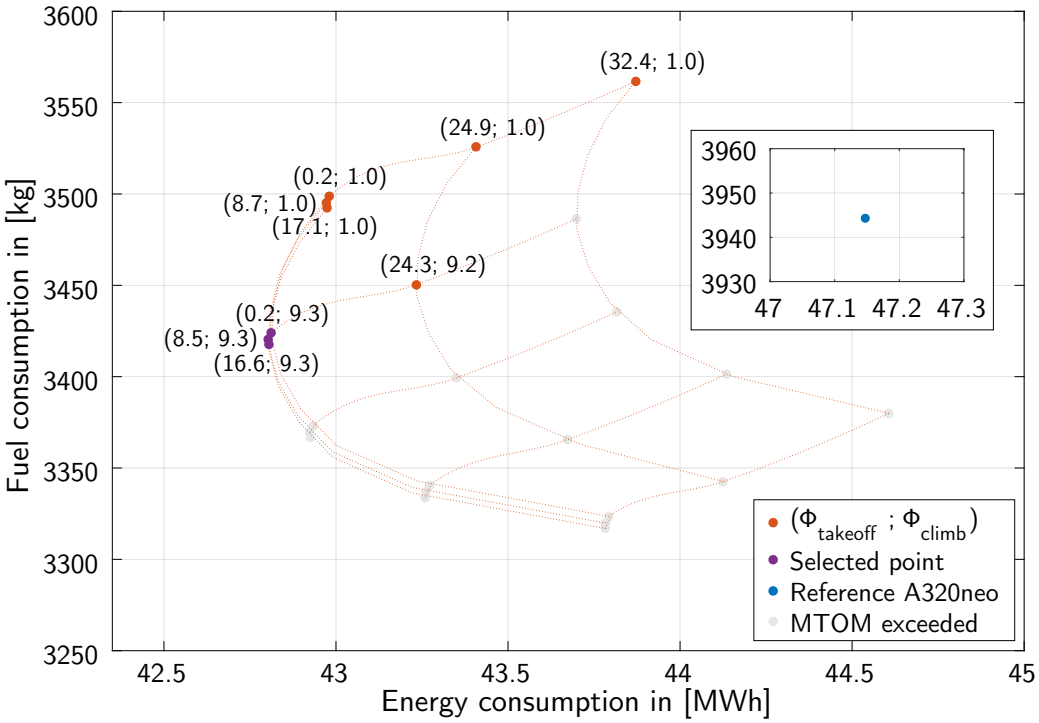

Figure 6.19: Pareto efficiency of modified A320neo with EAPPS (2020+).

Table 6.1: Optimal Pareto points for modified A320neo with EAPPS (2020+).

Pareto point	$\phi_{takeoff}$ in [%]	ϕ_{climb} in [%]
1	0.2	9.3
2	8.5	9.3
3	16.6	9.3

6.2.5 Effect of Engine Scaling on EAPPS Performance

When a power management strategy is selected for the baseline aircraft with all three modifications, the required thrust will be partially covered by the electric motor during take-off and climb. This means that the sizing of the engine is not governed by the required take-off thrust anymore, yielding a smaller and lighter powerplant. The optimal power split combinations considered for this analysis were mentioned earlier in Table 6.1.

Figure 6.20 illustrates the fuel and energy consumption at the three different Pareto points for five engine sizes between 80% and 100% of the standard CFM LEAP-1A26 engine. The various operating points are indicated by shapes (circle, triangle and square), while the engine scaling is marked in different colours (yellow, orange, green, light blue and purple).

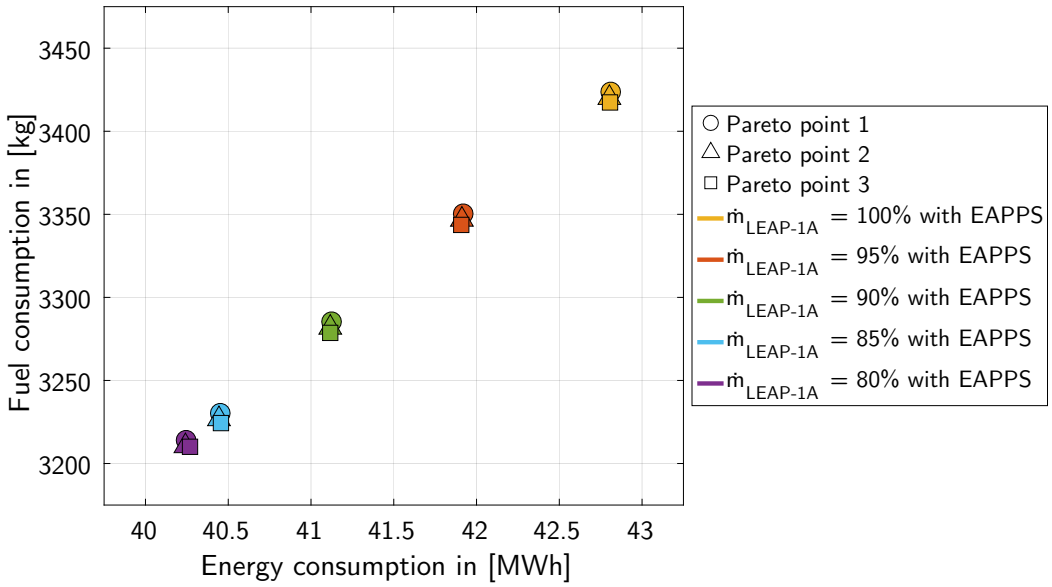

Figure 6.20: Pareto efficiency of modified A320neo with EAPPS (2020+) as function of power management strategy and engine scaling.

The effect of engine scaling on the consumption is clearly displayed: less fuel and energy is spent as the engine gets smaller and lighter. Of the three Pareto points, the power management strategy with the largest take-off power split $\phi_{takeoff}$ of 16.6% (Pareto point 3) is the most efficient strategy in terms of saving fuel and energy. By increasing the take-off power split and thus lowering the thrust required from the turbofan engine during take-off, the design point (take-off) will essentially shift towards the off-design point (cruise). This means that the engine will operate at a higher overall system efficiency throughout the mission, resulting in lower fuel and energy consumption.

Since applying EAPPS and downscaling affect the engine operating conditions, the limitations on the maximum shaft speeds and temperatures will be re-examined in the following paragraphs.

Figure 6.21 presents the maximum LP and HP shaft speeds (N_1 and N_2) for each configuration individually. The dark blue starred marker is the reference A320neo configuration without EAPPS. The graph reveals that by increasing the take-off power split (from point 1 to point 3), the maximum rotational speed on the HP spool N_2 decreases significantly; in some cases, lower HP shaft speeds than for the reference case can be attained. Essentially, with the assistance of the electric motor on the LP shaft during take-off, a part of the work required by the HP shaft is alleviated. However, when employing smaller powerplants, both shaft speeds will be greatly increased; this will affect the lifespan of the disc blades due to larger centrifugal stresses.

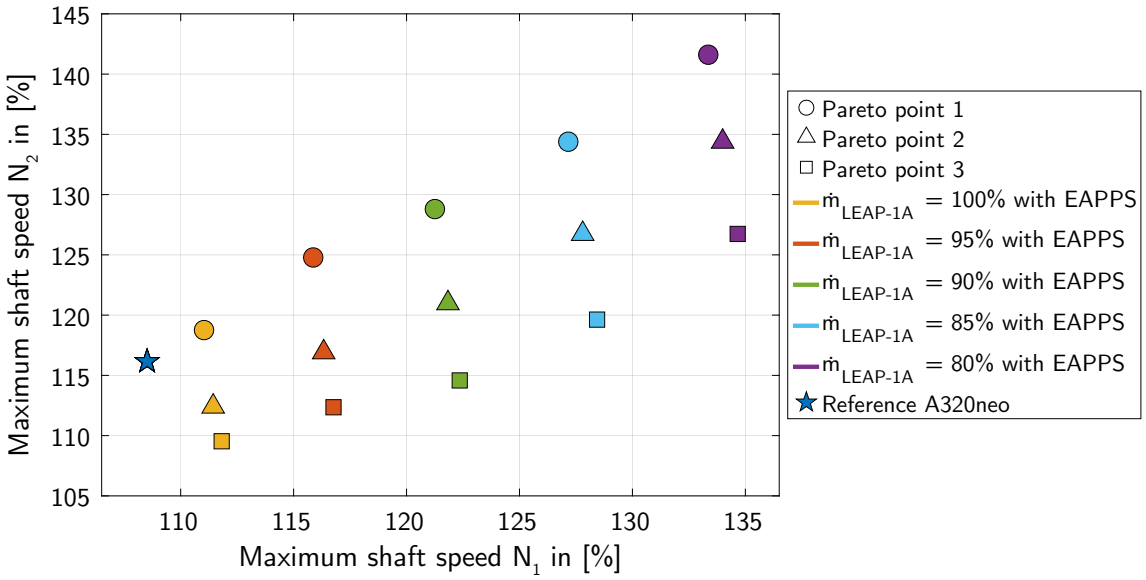

Figure 6.21: Effect of power management strategy and engine scaling on maximum shaft speeds, assuming modified A320neo with EAPPS (2020+).

Figure 6.22 displays the effect of scaling on the engine mass. The reference case, marked in light blue, shows the mass of the engine for scaling from 80% to 100%, as function of its thrust output (applying Equation 3.1). The remaining lines represent the engine mass at the three Pareto points. As smaller-sized engines face higher rotational speeds, all turbine and compressor blades will be strengthened to withstand the increased disc loads; this happens in accordance with Equation 3.6. The difference in mass between the Pareto points and the reference mark at each engine size is the extra mass required for disc reinforcements.

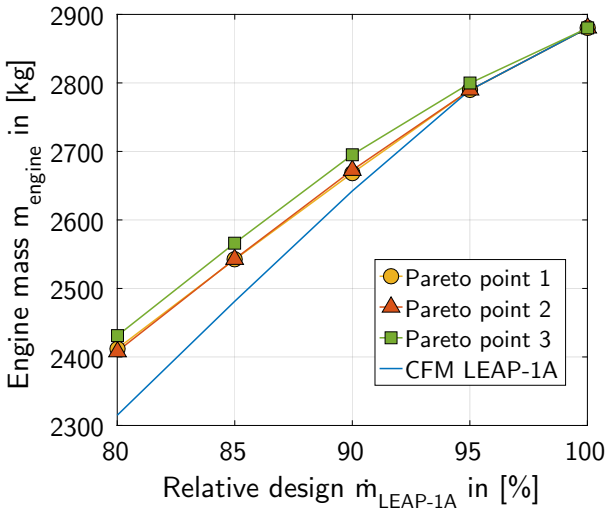

Figure 6.22: Effect of power management strategy and engine scaling on engine mass, assuming modified A320neo with EAPPS (2020+).

The maximum temperatures for the HPT nozzle guide vanes (NGVs) T_{t41} and exhaust gas temperature (EGT) T_{t45} for the various Pareto points and engine sizes are shown in Figure 6.23 and Figure 6.24, respectively. The solid red line indicates the maximum allowable temperature (including a margin of 75°C for EGT). The dashed red line in Figure 6.24 is the T_{t45} limit without margin. The markers will be indicated as grey when these exceed the corresponding temperature limits.

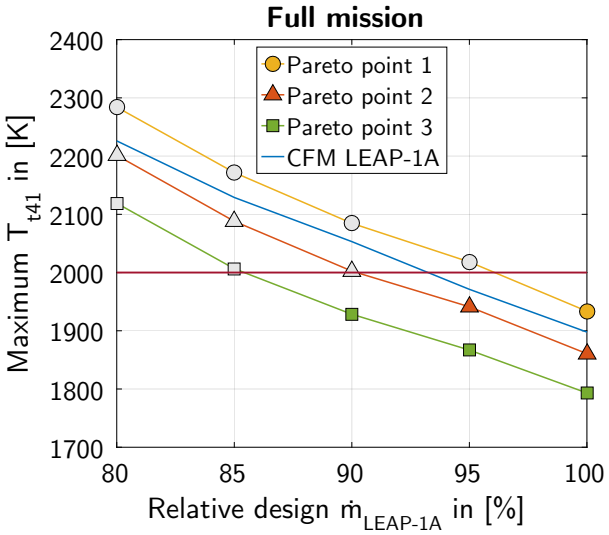

Figure 6.23: Effect of power management strategy and engine scaling on NGV temperature (T_{t41}), assuming modified A320neo with EAPPS (2020+).

According to Figure 6.23, the overall limit of 2,000 K for T_{t41} will be exceeded for engines scaled smaller than 90%. Even for the engine scaled down to 90% and 95%, only specific Pareto points will be able to operate below this T_{t41} limit. On a side note, the maximum T_{t41} temperature in the case of only assistance during climb (Pareto point 1) is slightly higher than for the reference case; this difference is due to the additional electrical system mass that must be carried along. Once a take-off power split $\phi_{takeoff}$ is applied (Pareto points 2 & 3), the maximum T_{t41} temperature drops below the reference temperature line. The most economical option below the T_{t41} limit is the engine scaled down to 90% with a power management of $\phi_{takeoff} = 16.6\%$ and $\phi_{climb} = 9.3\%$ (Pareto point 3).

Figure 6.24 shows the maximum EGT values in different scenarios: ground, take-off and in-flight. The EGT limits used are stated in Table 4.6. The importance of the take-off power split $\phi_{takeoff}$ is once more highlighted in this graph. For the unscaled engine at take-off, it is shown that both Pareto points 1 & 2 will surpass the soft limit; the engine will only perform below this limit if Pareto point 3 is selected. In terms of engine life, this means that the same device can operate longer with a higher take-off power split; the engine deteriorates slower when it is exposed to lower EGT values. In the case of EGT temperature (T_{t45}) limitations, the absolute limit (with EGT margin) is reached at take-off and in-flight phases. The best choice that stays below the T_{t45} limit at all three scenarios is a downscaled engine of 95% operating at Pareto point 3.

To present the options more clearly, the Pareto efficiency map (Figure 6.20) is altered to include the NGV and EGT limitations; if a point surpasses the respective temperature limit of T_{t41} or T_{t45}, this point will be marked grey. The resulting Pareto efficiencies with the NGV and EGT temperatures are displayed in Figure 6.25 and Figure 6.26, respectively.

As mentioned before in Section 4.2, the limits set on EGT (T_{t45}) are only indicative and mainly used for aircraft engine maintenance; it is by no means necessary to set it as a design requirement. Without this EGT limit, the most optimal configuration without exceeding the NGV temperature limitation of 2,000 K becomes the CFM LEAP-1A engine downscaled to 90% with a take-off power split $\phi_{takeoff}$ of 16.6% and a climb power split ϕ_{climb} of 9.3% (Pareto point 3). This setup will be considered as the optimal power split combination and will be further analysed in the following section.

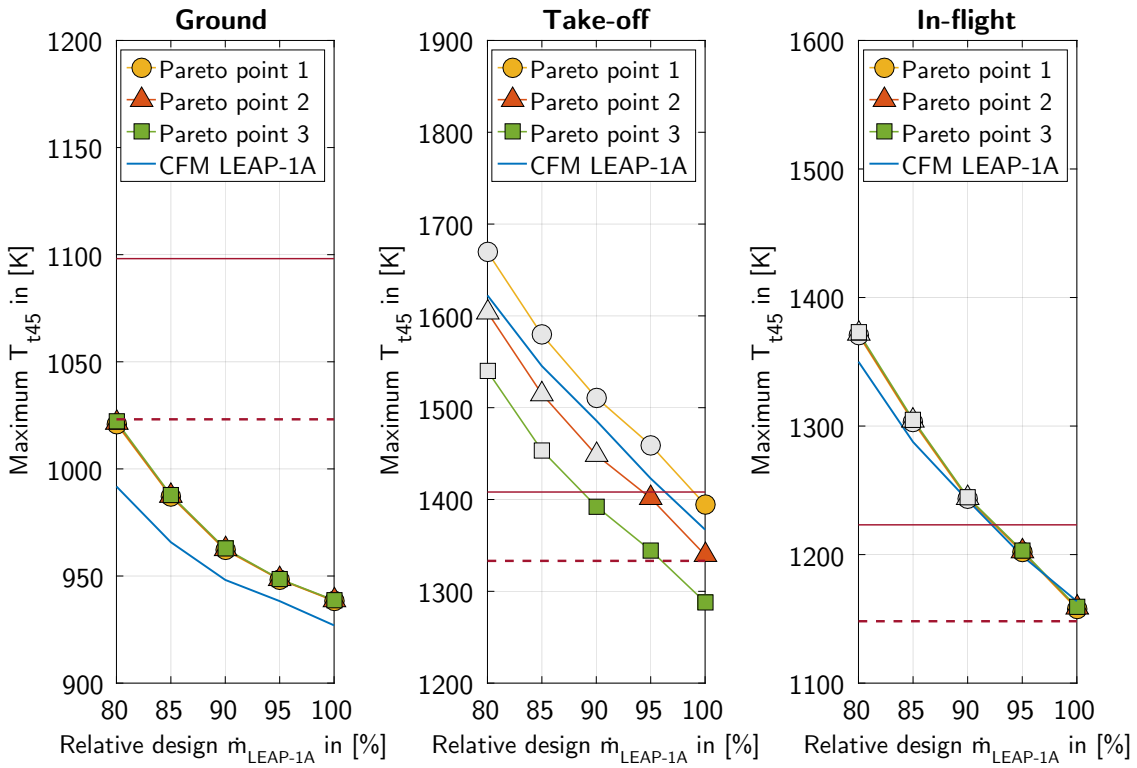

Figure 6.24: Effect of power management strategy and engine scaling on EGT (T_{t45}), assuming modified A320neo with EAPPS (2020+).

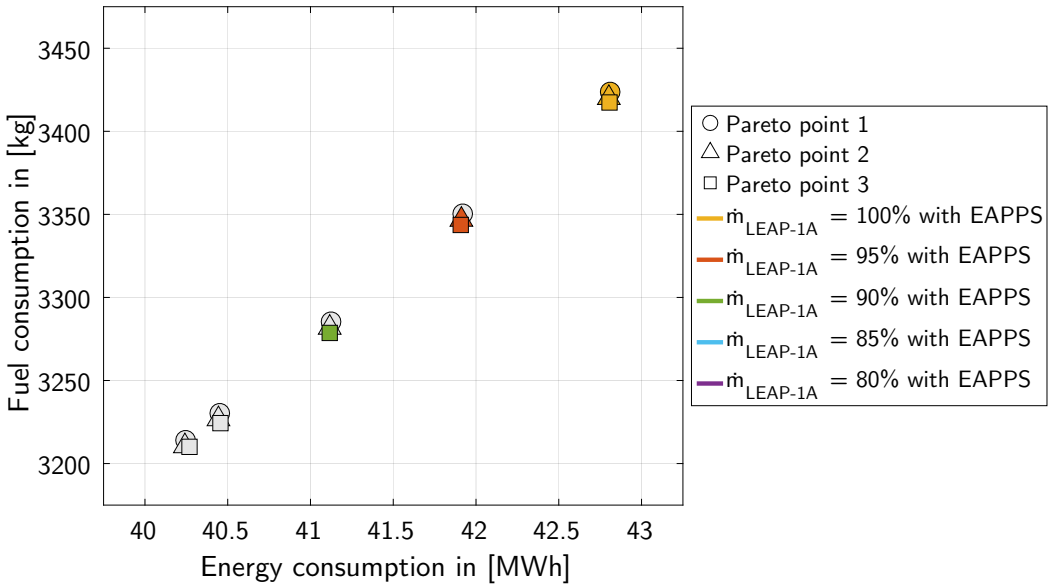

Figure 6.25: Pareto efficiency of modified A320neo with EAPPS (2020+) as function of power management strategy and engine scaling, taking the NGV temperature (T_{t41}) limitations into account.

6.2.6 Effect of Flight Mission on EAPPS Performance

Photovoltaics is largely dependent on location, time and date; to showcase the true potential of photovoltaics, three flight missions (stated earlier in Table 4.9) will be analysed at different times of the day (morning, afternoon and evening). To represent the PV performance throughout the year and account

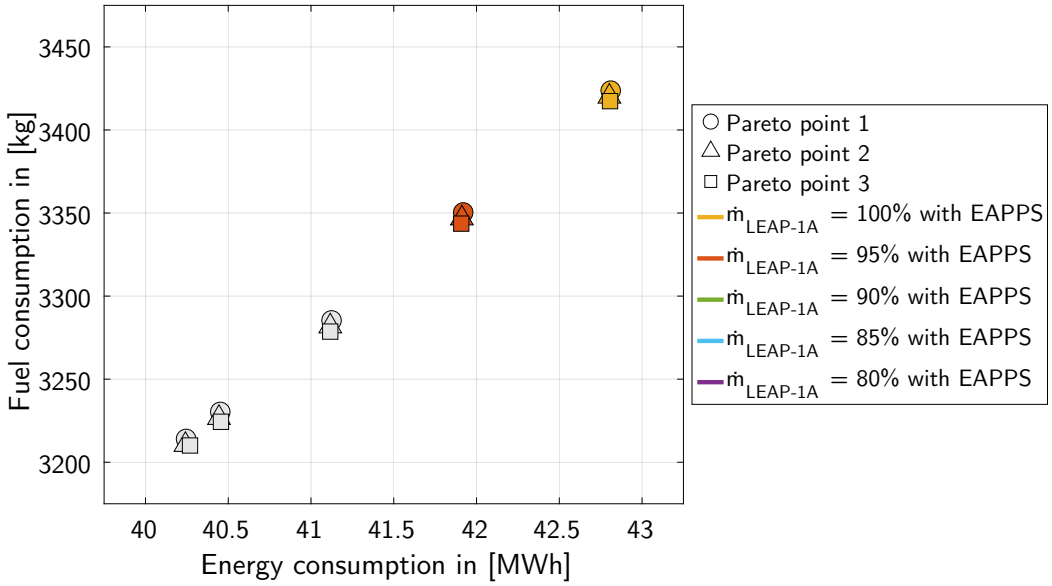

Figure 6.26: Pareto efficiency of modified A320neo with EAPPS (2020+) as function of power management strategy and engine scaling, taking the EGT (T_{t45}) limitations into account.

for the fluctations in sunlight, an annual average solar irradiance will be used; these values are expressed in W/m^2 and found in Table 6.2.

Table 6.2: Annual solar irradiance (in W/m^2) as function of location and time.

Time of the day	TLS-AMS[1]	GYE-BOG[2]	HBA-SYD[3]
Morning (8AM-11AM)	350.3	514.8	421.4
Afternoon (12PM-3PM)	604.9	910.8	735.7
Evening (4PM-7PM)	282.5	391.3	332.7

The fuel and energy consumption will be compared to the same A320neo configuration without photovoltaics. The results are summarised in Table 6.3 and Table 6.4. The average values for fuel and energy throughout the day are indicated as well, in kg and kWh, correspondingly.

Table 6.3: Effect of flight mission on relative reduction in fuel consumption (in %) as function of location, time and date.

Time of the day	TLS-AMS[1]	GYE-BOG[2]	HBA-SYD[3]
Morning (8AM-11AM)	0.029	-0.007	0.014
Afternoon (12PM-3PM)	-0.027	-0.094	-0.056
Evening (4PM-7PM)	0.044	0.020	0.033
Daily average (8AM-7PM)	0.015	-0.027	-0.003
Average amount of fuel burnt [kg]	0.508	-0.879	-0.100

The viability of photovoltaics for a selected flight mission is represented by the daily average in Table 6.3. A negative value implies that the amount of fuel saved due to the power generated by photovoltaics

[1] Flight mission 1: Toulouse (France) to Amsterdam (The Netherlands).
[2] Flight mission 2: Guayaquil (Ecuador) to Bogota (Colombia).
[3] Flight mission 3: Hobart (Tasmania) to Sydney (Australia).

Table 6.4: Effect of flight mission on relative reduction in energy consumption (in %) as function of location, time and date.

Time of the day	TLS-AMS[1]	GYE-BOG[2]	HBA-SYD[3]
Morning (8AM-11AM)	-0.092	-0.183	-0.132
Afternoon (12PM-3PM)	-0.233	-0.402	-0.306
Evening (4PM-7PM)	-0.055	-0.115	-0.083
Daily average (8AM-7PM)	-0.127	-0.233	-0.173
Average amount of energy consumed [kWh]	-52.35	-96.24	-71.50

compensates for the additional mass of the panels; more fuel is saved than burnt throughout the day. Results indicate that installing photovoltaics has more effect on flight missions 2 and 3 than on flight mission 1, although in absolute senses the fuel savings are rather small and can only be achieved during the afternoon.

Table 6.4 shows that relative energy consumption is always negative; from an energy perspective, any power generated through the photovoltaic effect comes without charge. One could argue that for flight mission 1 the amount of 'sustainable' energy generated is worth burning extra fuel for; in this case, an additional 0.508 kg of fuel per flight for 52.35 kWh of generated energy.

The ideal flight mission for the EAPPS configuration would be from Guayaquil to Bogota during the afternoon (12PM-3PM). Relative to the modified A320neo without photovoltaics, a fuel reduction of 0.094% and energy savings of 0.402% can be achieved. If the same mission is flown throughout the day from 8AM till 7PM, 0.879 kg of fuel and 96.24 kWh of energy can be saved on average per flight. A thorough analysis on the Return on Investment (ROI) performance of the PV system is described in Section D.2. Moreover, in Section 6.2.7, the optimised EAPPS setup projected with near future technology (2020+) will be discussed in more detail.

6.2.7 Discussion

Extending the basic HEPS setup with EAPPS modifications has proven to be beneficial in terms of fuel and energy consumption. The optimal EAPPS configuration features an electrical subsystem architecture (MEA), a fuel cell system that delivers a constant supply of 200 kW, 209.91 m^2 of PV panels on the outer skin of the aircraft and a CFM LEAP-1A engine scaled down to 90%. The optimal power management strategy includes fully electric taxiing, a take-off power split $\phi_{takeoff}$ of 16.6% and a climb power split ϕ_{climb} of 9.3%. The electrical system is sized with near future technology (2020+) such that sufficient power and energy are available throughout the whole mission. In terms of solar irradiance, the ideal flight mission departs from Guayaquil towards Bogota such that solar noon occurs midway of the flight. However, in real life, one should look at seasonal or annual averages for a better indication of the PV performance.

Changing the A320neo into a MEA by replacing current subsystems with electrical counterparts seems to be the most effective approach by 2020+. Both the addition of the fuel cell and PV systems leads to minimal fuel and energy savings, but increases the complexity of the EAPPS configuration. In this case, the benefits may not outweigh the penalties; both technologies are still relatively new and may bring additional uncertainties in terms of safety and costs. Nonetheless, both emerging

[1] Flight mission 1: Toulouse (France) to Amsterdam (The Netherlands).
[2] Flight mission 2: Guayaquil (Ecuador) to Bogota (Colombia).
[3] Flight mission 3: Hobart (Tasmania) to Sydney (Australia).

technologies are still included in the optimal EAPPS setup for 2020+. The fuel and energy consumption achieved with this optimised setup become 3276.78 kg and 41.1 MWh, correspondingly. Relative to the conventional A320neo aircraft, this setup lowers the fuel and energy consumption by 16.92% and 12.82%, respectively. The corrected results of this setup will be covered in Section 6.5.1.

6.3 Future A320neo with EAPPS Modifications (2040+)

After identifying the optimised EAPPS configuration, another analysis will be done to investigate the effect of technological advancement. A similar EAPPS setup will be projected with far future technology (2040+), as described in Chapter 3. An overview of the values changed due to projected technological advancement is given in Table 6.5.

Table 6.5: Summary of efficiency and mass-related parameters for near future technology (2020+) and far future technology (2040+) [20, 33, 71, 72, 80, 82, 99].

	Efficiency		Mass-related parameter		
Component	**2020+**	**2040+**	**2020+**	**2040+**	**Unit**
Electric motor/generator	95%	98%	7,500	15,000	W/kg
Battery	92.5%	95%	500	1,000	Wh/kg
Power electronics	95%	98%	7,500	15,000	W/kg
Cables	99%	99.6%	15	10	$\%_{\text{mass,system}}$
Fuel cell system	60%	75%	500	1,000	W/kg
Photovoltaic cells	23.6%	35%	0.4368	0.35	kg/m^2

First, the unscaled engine EAPPS setup with all three modifications (electrical subsystems, fuel cells and photovoltaics), from Section 6.2.4, will be projected with far future technology (2040+) to see how this affects the electrical system mass as well as total fuel and energy consumption. This projection analysis is described in Section 6.3.1 and Section 6.3.2. Based on an updated Pareto plot found in Section 6.3.3, new optimal points will be evaluated by applying engine scaling in Section 6.3.4. Also, an additional PV analysis will be performed in Section 6.3.5. The outcome is an optimised and scaled setup with far future technology (2040+), which will described in Section 6.3.6.

6.3.1 Effect of Technological Development on Electrical System Mass

To show how important the maturity level of electric components is, the total masses of the electrical system, projected in the near and far future, will be compared to each other. Figure 6.27 indicates the differences in electrical system mass for a range of power management strategies, relative to the unscaled fully-equipped configuration described in Section 6.2.4.

The graph clearly shows that huge advancements in electric technology can open up the gateway to hybrid electric aviation. Mass reductions of 3,000 kg to 8,000 kg can be achieved depending on the power management strategy allowed. Despite a limit of 6,700 kg (or 7,499 kg after MEA conversion) on the total EAPPS mass due to MTOM constraints (see Section 3.1), these mass improvements predicted for 2040+ still allow for an increase in hybridisation power. The next section will outline how this translates to fuel and energy consumption.

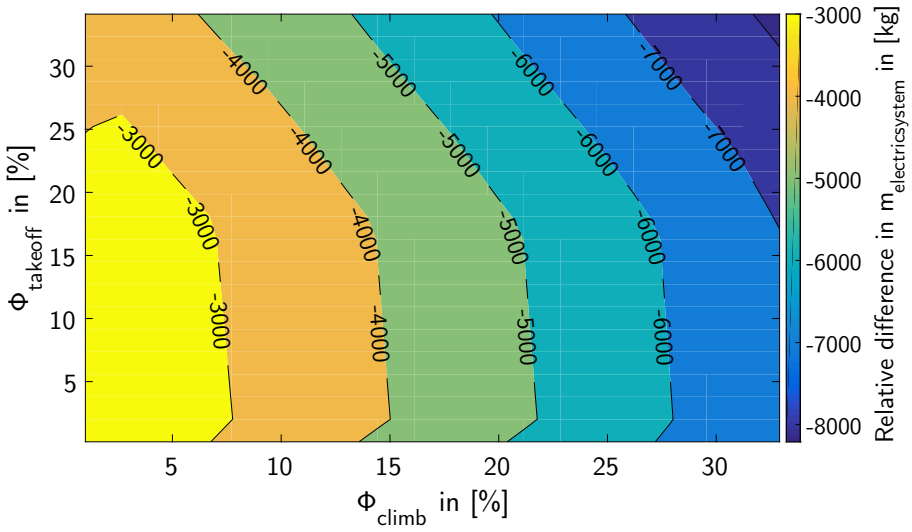

Figure 6.27: Effect of power management strategy on relative difference in electrical system mass, assuming technological development.

6.3.2 Effect of Technological Development on Fuel and Energy Consumption

Figure 6.28 and Figure 6.29 describe the relative fuel and energy savings, respectively, between 2020+ and 2040+ maturity levels for the EAPPS aircraft setup with all three modifications, but with unscaled engines. Note that the shown power split combinations up to 35% do not exceed the electrical system mass limitation at all; power split ratios above 35% are possible.

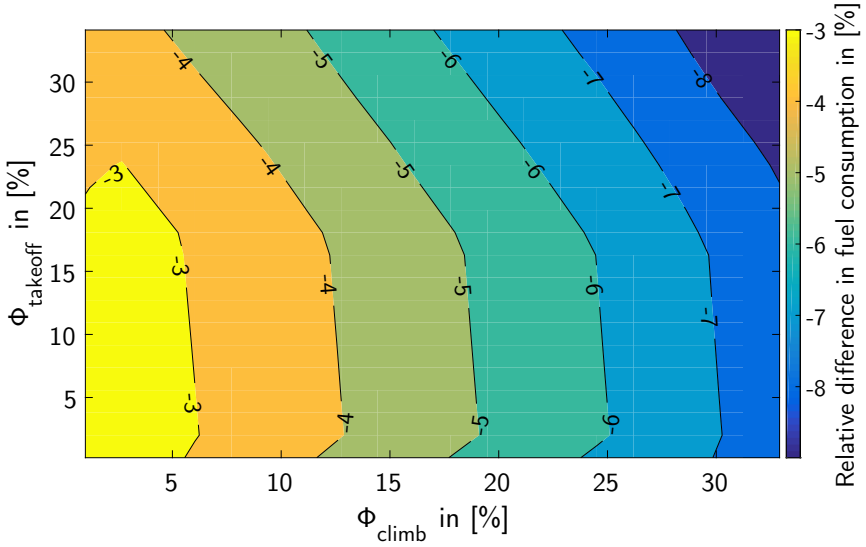

Figure 6.28: Effect of power management strategy on relative difference in fuel consumption, assuming technological development.

As illustrated in Figure 6.28, a reduction in electrical system mass allows for lower total fuel consumption. This happens almost proportionally: for every 900 kg of mass reduced, a fuel reduction of approximately 1% can be accomplished. The reduced total mass of the electrical system allows an increase in electrification, which in turn will bring additional savings in fuel reduction. This snowball effect will also be observed when scaling the engine in Section 6.3.4.

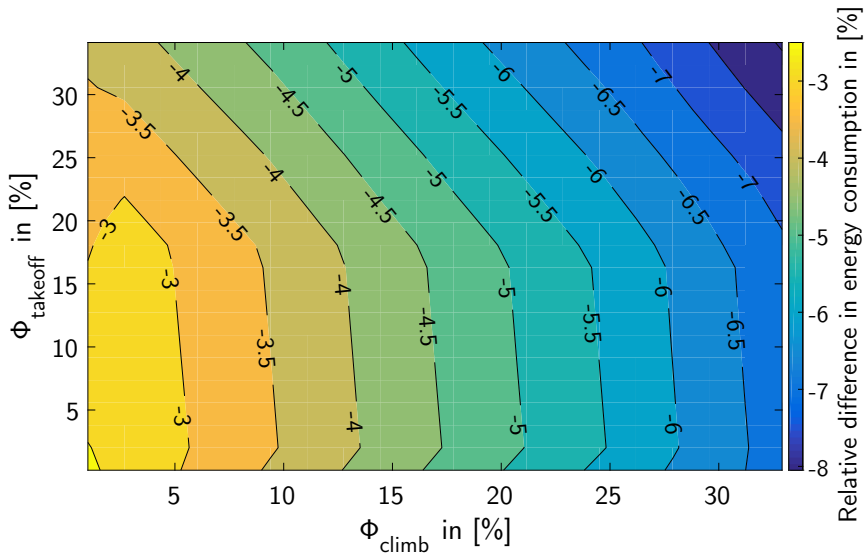

Figure 6.29: Effect of power management strategy on relative difference in energy consumption, assuming technological development.

Figure 6.29 shows a similar relationship as for the fuel consumption, where the system mass reduction and the amount of energy saved are related proportionally. For every 1,000 kg of lowered electrical system mass, an equivalent of around 1% of energy can be saved. Nonetheless, these reductions are limited by the MTOM on the aircraft mass as well as temperature and speed limitations on the CFM LEAP-1A engine. These aspects will be covered in Section 6.3.3 and Section 6.3.4, correspondingly.

6.3.3 Pareto Representation of Future A320neo with EAPPS Modifications (2040+)

The Pareto efficiency for the A320neo with all three modifications (electrical subsystems, fuel cells and photovoltaics) and future technology (2040+) is shown in Figure 6.30. In contrast to Figure 6.19, the number of viable power management strategies without exceeding the mass limit have increased immensely; this is mainly caused by significant mass reduction of the electrical system. Also, a true Pareto optimality is reached, as one has to compromise between either achieving the lowest fuel consumption or the lowest energy consumption throughout a full mission.

In general, increasing the climb power split ϕ_{climb} lowers the overall fuel consumption. In the case of the take-off power split ratio $\phi_{takeoff}$, the overall trend is more difficult to describe. By increasing the take-off power split from 0% up to around 20%, both the fuel and energy consumption become slightly lower. At higher ratios (beyond 20%), this strategy will no longer be beneficial and consumption starts to increase again. The only exception is near the mass limitation area ($\phi_{climb} > 40\%$), where a take-off power split of 25.6% is still favourable.

The selected Pareto points to be further investigated by applying engine scaling are marked purple in Figure 6.30. To give a better and clearer view of the Pareto optimality, a zoomed-in shot is displayed in Figure 6.31. Furthermore, the exact power management strategies of these points are described in Table 6.6.

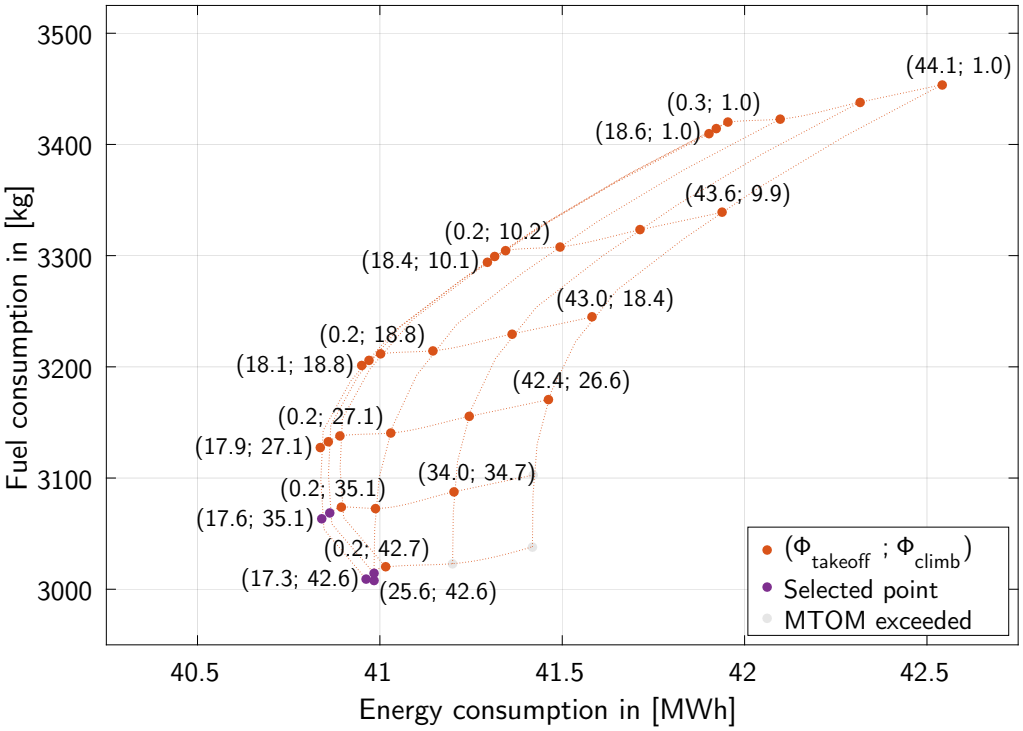

Figure 6.30: Pareto efficiency of future A320neo with EAPPS (2040+).

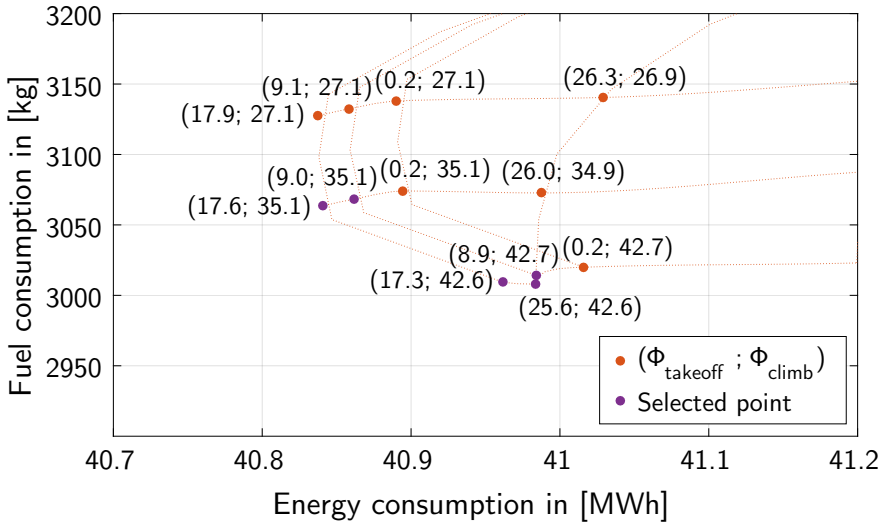

Figure 6.31: Zoomed-in view of the Pareto efficiency of future A320neo with EAPPS (2040+).

Table 6.6: Optimal Pareto points for future A320neo with EAPPS (2040+).

Pareto point	$\phi_{takeoff}$ in [%]	ϕ_{climb} in [%]
1	9.0	35.1
2	17.6	35.1
3	8.9	42.7
4	17.3	42.6
5	25.6	42.6

6.3.4 Effect of Engine Scaling on Future EAPPS Performance

Following a similar procedure as in Section 6.2.5, five varying levels of engine scaling will be applied onto the selected Pareto points in Table 6.6. Figure 6.32 shows the various operating points as shapes (circle, triangle, square, diamond and hexagram), while each colour represents a different level of scaling (yellow, orange, green, light blue and purple).

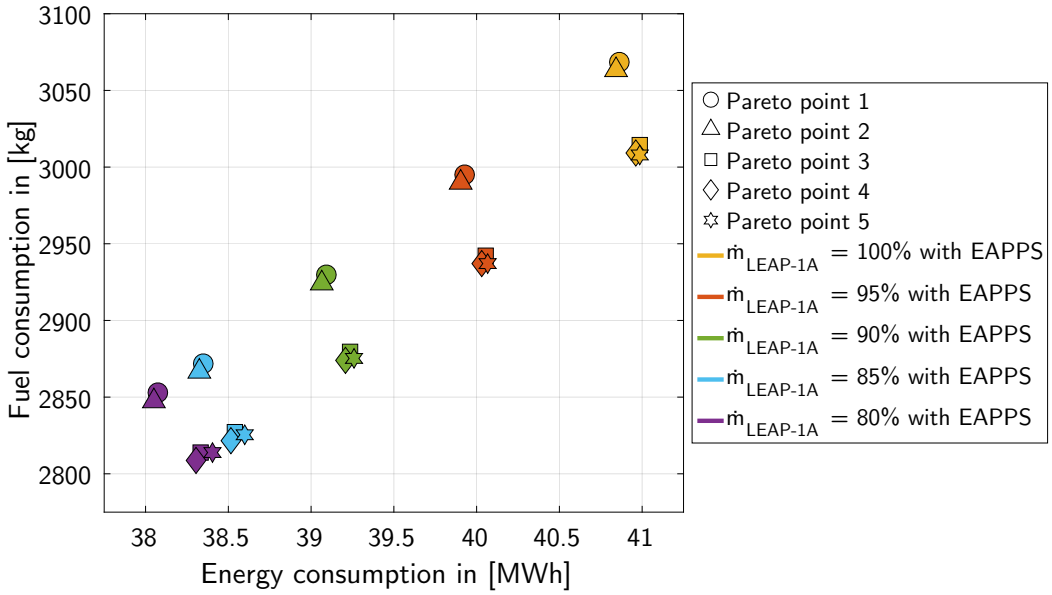

Figure 6.32: Pareto efficiency of future A320neo with EAPPS (2040+) as function of power management strategy and engine scaling, assuming future A320neo with EAPPS (2040+).

Again, downscaling the engine results in lower fuel and energy consumption; as the operating point of the turbine shifts more towards the cruise phase, it will be able to perform more efficiently with lower fuel flow rates. The graph also reveals that the trend of reducing fuel consumption by increasing the climb power split ratio, as shown in Figure 6.31, holds for any magnitude of scaling. The power management strategies with higher climb power split ratios (Pareto points 3, 4 and 5) consume less fuel than those with lower climb power splits (Pareto point 1 and 2) at any engine scale. Essentially, the whole group of Pareto points with the same engine scale moves left and downwards, towards lower fuel and energy consumption, as the engine becomes smaller and lighter. The benefits of scaling is most apparent from 100% to 95% and becomes less effective at smaller scales, eventually reaching a point of saturation.

The effect of power management strategy and engine scaling on the maximum LP and HP shaft speeds (N_1 and N_2) is shown in Figure 6.33. The trends are similar as described in Section 6.2.5: increasing the take-off power split (from point 1 to point 2 and from point 3 to point 5 via point 4) gradually lowers the HP rotational speed N_2. In addition, Figure 6.33 reveals that raising the climb power split (from point 1 to point 3 and from point 2 to point 4) leads to a slight increase in LP speed N_1.

The effect on the engine mass can be found in Figure 6.34. This graph confirms that the technological development on the electrical system does not affect the engine mass nor its performance at all, compared to Figure 6.22; within this study, the engine characteristics and performance are assumed to stay the same throughout the years as mentioned earlier in Section 4.2.

Still, the most important indicator which limits the engine performance is the maximum NGV temperature (T_{t41}) experienced during flight. This temperature is plotted for various Pareto points and engine

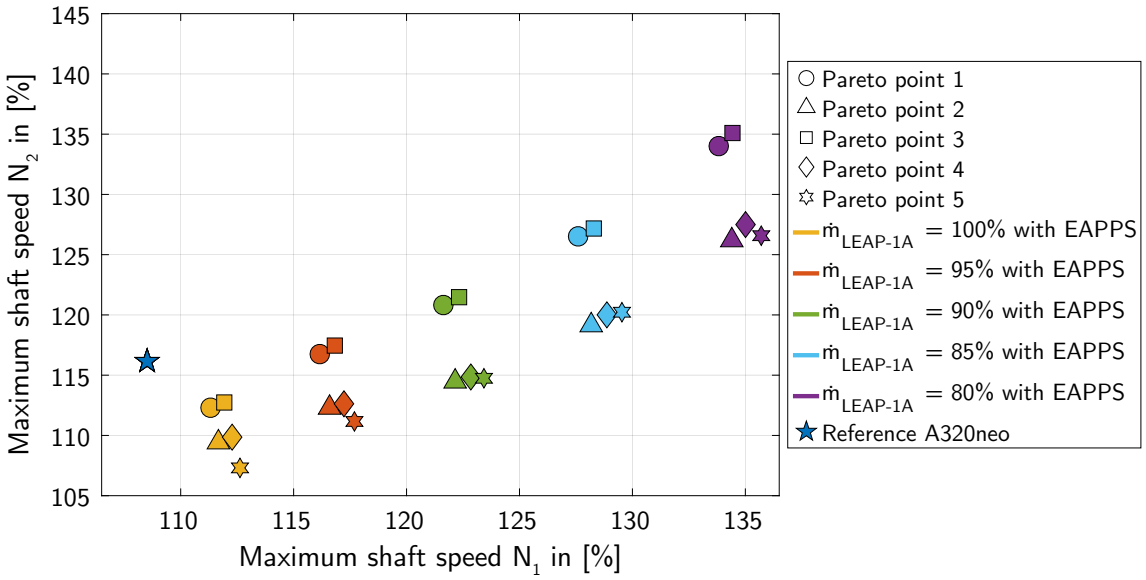

Figure 6.33: Effect of power management strategy and engine scaling on maximum shaft speeds, assuming future A320neo with EAPPS (2040+).

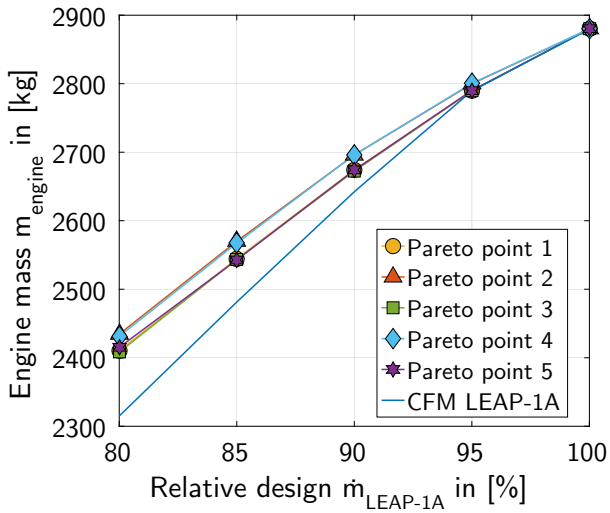

Figure 6.34: Effect of power management strategy and engine scaling on engine mass, assuming future A320neo with EAPPS (2040+).

sizes in Figure 6.35. Again, the solid red line marks the maximum allowable temperature of 2,000 K and the markers will be greyed out when these exceed this temperature boundary. Note that the EGT (T_{t45}) is left out, because it can be treated as a non-critical design constraint; this was also addressed in Section 4.2.

Compared to the previous NGV plot with three Pareto points (Figure 6.23), Figure 6.35 presents many more options below the T_{t41} limit (red solid line). This is mainly possible by the higher take-off power split of 25.6% for Pareto point 5 (purple), which even allows engine downscaling of 85%. All points stay below the reference line of the CFM LEAP-1A engine, as each Pareto point exercises some form of electrical assistance during the take-off procedure ($\phi_{takeoff} > 0$). The variations in climb power split ratio ϕ_{climb} do not affect the maximum operating NGV temperature in any way, as higher NGV temperatures are experienced during the take-off phase than the climb phase.

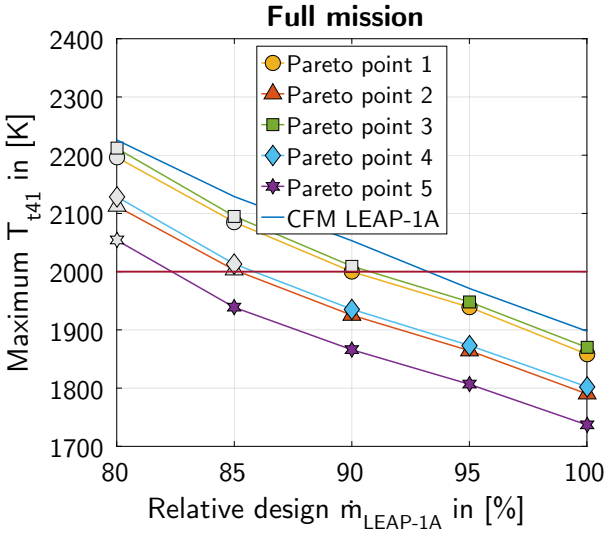

Figure 6.35: Effect of power management strategy and engine scaling on NGV temperature (T_{t41}), assuming future A320neo with EAPPS (2040+).

Once more, the Pareto efficiency map (Figure 6.32) is adjusted by including the NGV limitations in Figure 6.36; a Pareto point will be indicated as grey if that particular setup exceeds the temperature limit of 2,000 K for T_{t41}.

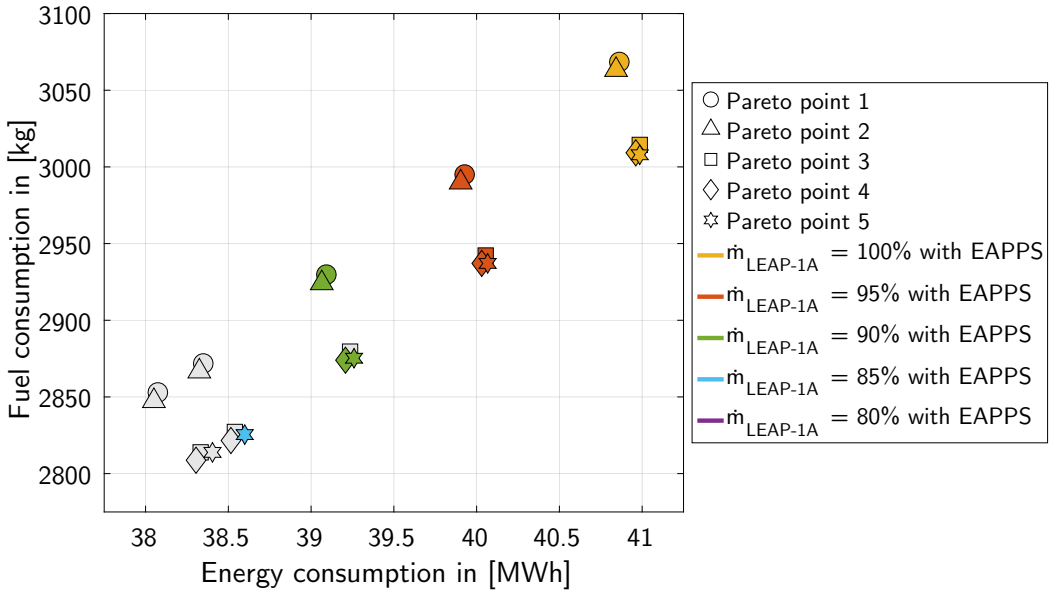

Figure 6.36: Pareto efficiency of future A320neo with EAPPS (2040+) as function of power management strategy and engine scaling, taking the NGV temperature (T_{t41}) limitations into account.

The Pareto efficiency plot in Figure 6.36 shows that the most economical option without exceeding the absolute T_{t41} limitation is an engine downscaled to 85% operating with a power management strategy of $\phi_{takeoff} = 25.6\%$ and $\phi_{climb} = 42.6\%$ (Pareto point 5); this is the best possible setup projected with far future technology (2040+).

To investigate the effect of technological development on the PV performance, another PV study is carried out for the future EAPPS setup in Section 6.3.5.

6.3.5 Effect of Technological Development on Future PV Performance

In Section 6.2.6, the viability of installing PV on the A320neo in the near future (2020+) was investigated; the results were not convincing at all and the perceived benefits were minimal. To see how technological development may increase the potential of PV performance, another PV analysis will be carried out for the EAPPS setup with far future technology (2040+); the same three flight missions (Toulouse - Amsterdam, Guayaquil - Bogota and Hobart - Sydney) and times of the day (morning, afternoon and evening) in Section 6.2.6 will be used.

The changes in fuel and energy consumption relative to the same A320neo configuration without photovoltaics are presented in the same format and shown in Table 6.7 and Table 6.8, respectively. Once again, the average values for fuel and energy will be indicated in kg and kWh, correspondingly.

Table 6.7: Effect of flight mission on relative fuel consumption (in %) as function of location, time and date.

Time of the day	TLS-AMS[1]	GYE-BOG[2]	HBA-SYD[3]
Morning (8AM-11AM)	0.040	0.007	0.026
Afternoon (12PM-3PM)	-0.011	-0.071	-0.036
Evening (4PM-7PM)	0.053	0.031	0.043
Daily average (8AM-7PM)	0.027	-0.011	0.011
Average amount of fuel burnt [kg]	0.766	-0.301	0.303

Table 6.7 reveals that, in terms of fuel consumption, only flight mission 2 is beneficial. Compared to the previous PV study, the relative amount of fuel savings has decreased; even the daily total for flight mission 3 is no longer favourable (negative value). This setback is caused by the relatively poor improvement in PV system mass, compared to other system components. The area mass density in the far future (2040+) is assumed to improve by only 20% (from 0.4368 kg/m^{2}to 0.35 kg/m^2), averaging 1% per year. Since fuel savings are highly sensitive to mass changes and the reduction in PV mass is comparatively low, the overall PV system performance is cut back when measured against Section 6.2.6.

Table 6.8: Effect of flight mission on relative energy consumption (in %) as function of location, time and date.

Time of the day	TLS-AMS[1]	GYE-BOG[2]	HBA-SYD[3]
Morning (8AM-11AM)	-0.162	-0.283	-0.214
Afternoon (12PM-3PM)	-0.350	-0.574	-0.446
Evening (4PM-7PM)	-0.113	-0.192	-0.150
Daily average (8AM-7PM)	-0.208	-0.350	-0.270
Average amount of energy consumed [kWh]	-80.75	-135.57	-104.59

Despite its lacking performance in fuel savings, the reduction in energy consumption has increased considerably. In the worst case (flight mission 1), an extra 0.766 kg of fuel is burnt per flight for 80.75 kWh worth of energy. In the best case scenario (flight mission 2), 0.301 kg of fuel is saved per flight while generating 135.57 kWh of sustainable energy.

[1] Flight mission 1: Toulouse (France) to Amsterdam (The Netherlands).
[2] Flight mission 2: Guayaquil (Ecuador) to Bogota (Colombia).
[3] Flight mission 3: Hobart (Tasmania) to Sydney (Australia).

The ideal flight mission for the future EAPPS setup is still from Guayaquil to Bogota during the afternoon (12PM-3PM). Compared to a PV-less A320neo, a fuel reduction of 0.071% and energy savings of 0.574% can be accomplished. For a full day of flying from 8AM till 7PM, 0.301 kg of fuel and 135.57 kWh of energy can be saved per flight. Details of the optimised EAPPS setup will be provided in Section 6.3.6 and investigated further in Section 6.5.2.

6.3.6 Discussion

The research done on the future A320neo with EAPPS modifications highlights the impact of technological development on aircraft flight performance. The optimal EAPPS setup in 2040+ includes the same three modifications (electrical subsystem architecture, fuel cell system of 200 kW and 209.91 m^2 worth of PV panels) as in Section 6.2.7, but with a different power management strategy and engine size. The same flight mission is flown from Guayaquil towards Bogota. The technological advancements on the individual components significantly decrease the total mass of the electrical system, enabling greater power split ratios: 25.6% for the take-off power split ratio $\phi_{takeoff}$ and 42.6% for the climb power split ϕ_{climb} are now considered optimal. The power management strategy still features fully electric taxiing. Also, the engine can be downscaled to 85%, which is slightly smaller than the engine in 2020+. Compared to the setup in 2020+, the fuel consumption reduces with 13.82% from 3,276.78 kg to 2,823.97 kg and the energy consumed with 6.16% from 41.10 MWh to 38.57 MWh. While adopting EAPPS in 2020+ can already improve the performance of the A320neo greatly, the projected technological enhancements within 20 years time will elevate this performance even further.

6.4 Energy Management System Optimisation of EAPPS

This section covers the findings from the energy management system optimisation tool, also known as the EMS module, described in Chapter 5. This optimisation procedure is carried out for both optimised EAPPS setups defined in Section 6.2.7 and Section 6.3.6. Some individual components (electric motor, PV, PEMFC and battery) of the electrical system will be modelled in more detail and the aim is to identify the optimal battery setup which can meet the power requirements throughout the whole flight mission. From this, a corrected value for the battery specific energy is obtained, which can then be fed back into the EAPPS simulation model. This procedure and the final corrected results can be found in Section 6.5.

First, the simulation will be run for the A320neo configuration with near future technology (2020+), from Section 6.2.7; the details are specified in Section 6.4.1. Then, the same procedure is repeated for the A320neo arrangement with far future technology (2040+) from Section 6.3.6; the results are described in Section 6.4.2. This concludes with insights regarding the effect of technological development on the energy management system optimisation in Section 6.4.3.

6.4.1 Detailed Analysis of A320neo with EAPPS Modifications (2020+)

The first aspect to be discussed is the variable efficiency of the electric motor. In the EAPPS module, a fixed efficiency is assumed; now it depends on the power output and the rotational speed. Figure 6.37 depicts the change in motor efficiency over the whole mission from taxi-out to taxi-in. It shows that the motor efficiency (yellow solid) is highest during both taxi segments averaging 97% and has transitions to around 88% from the take-off to the climb phase. Keep in mind that the electric motor is not used at all during cruise and descent, which is why the efficiency drops to 0%. The average motor efficiency throughout the flight mission, averaged over the time intervals it is being used, equals 91.1% (orange

dashed), which is quite lower than the assumed efficiency of 95% (light blue solid) used within the EAPPS model.

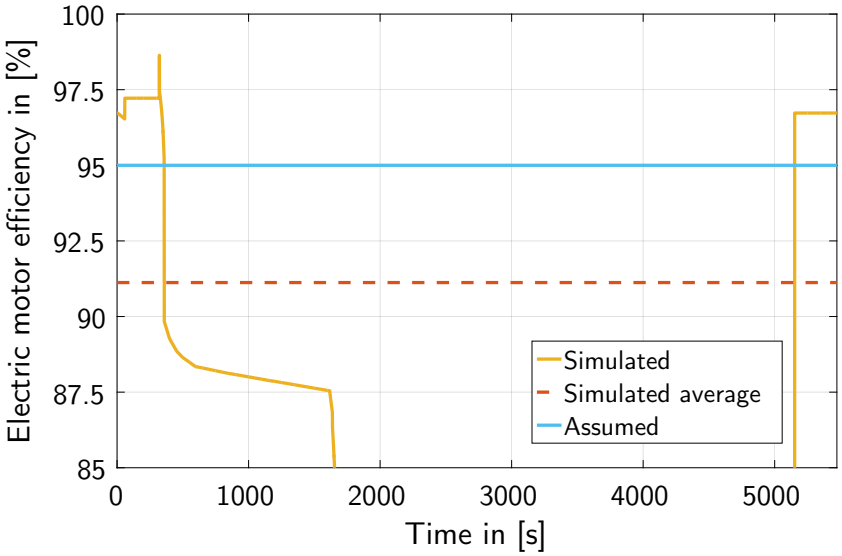

Figure 6.37: Electric motor efficiency throughout the flight mission in the near future (2020+); average motor efficiency (orange dashed line) is 91.1%.

The next component to be analysed is the PV system. This setup consists of Maxeon Gen III cells covering the outer skin of the A320neo aircraft (see Figure C.5), of which 540 cells are arranged in series and 23 in parallel, making a total of 12,420 cells. The solar irradiance plays a crucial role in the performance of this system, therefore the obtained irradiance in the EMS simulation model is plotted in Figure 6.38.

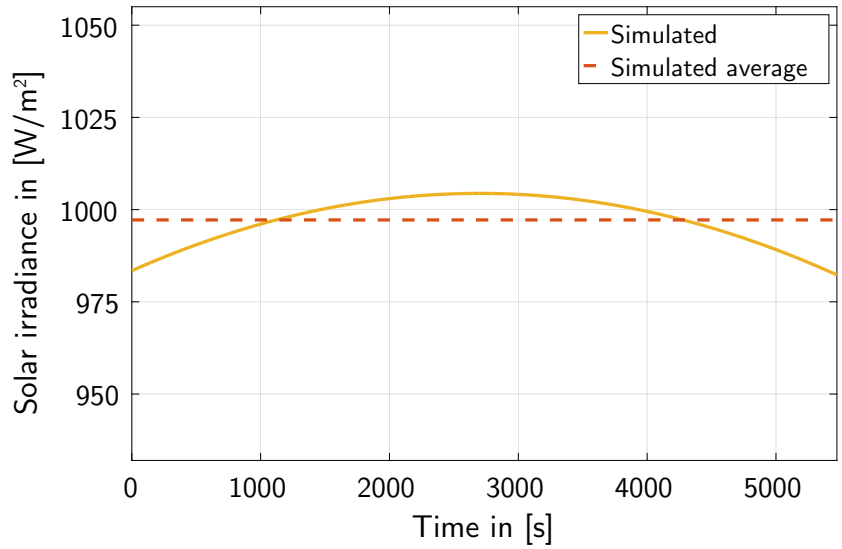

Figure 6.38: Solar irradiance throughout the flight mission in the near future (2020+); average solar irradiance (orange dashed line) is 997.2 W/m^2.

The graph shows that the average solar irradiance throughout the mission (orange dashed line) is equal to 997.2 W/m^2, which is remarkably high; this number almost matches the value of 1,000 W/m^2 used for Standard Test Conditions (STC). The irradiance fluctuates from 983.4 W/m^2 towards its peak value of 1,004 W/m^2 at solar noon, halfway of the flight mission.

Figure 6.39 and Figure 6.40 present the acquired efficiency and power output of the PV system, as a result of this varying solar irradiance.

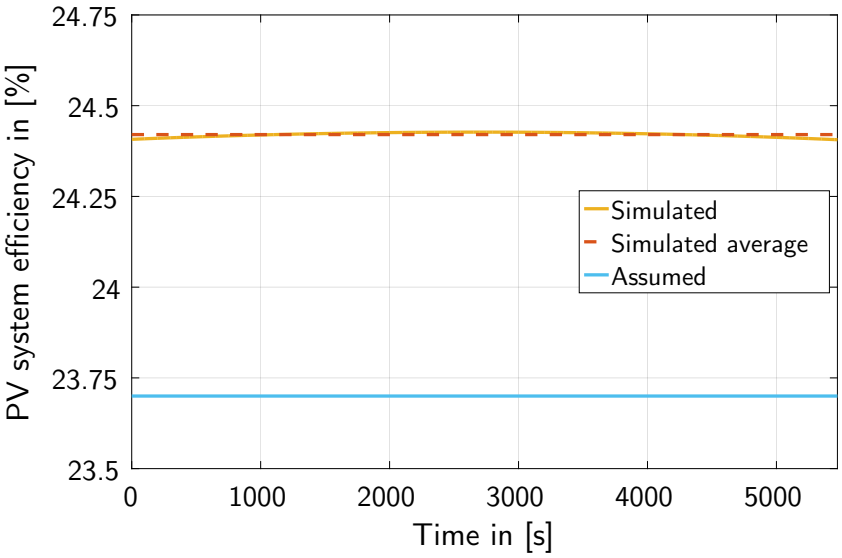

Figure 6.39: PV system efficiency throughout the flight mission in the near future (2020+); average PV system efficiency (orange dashed line) is 24.4%.

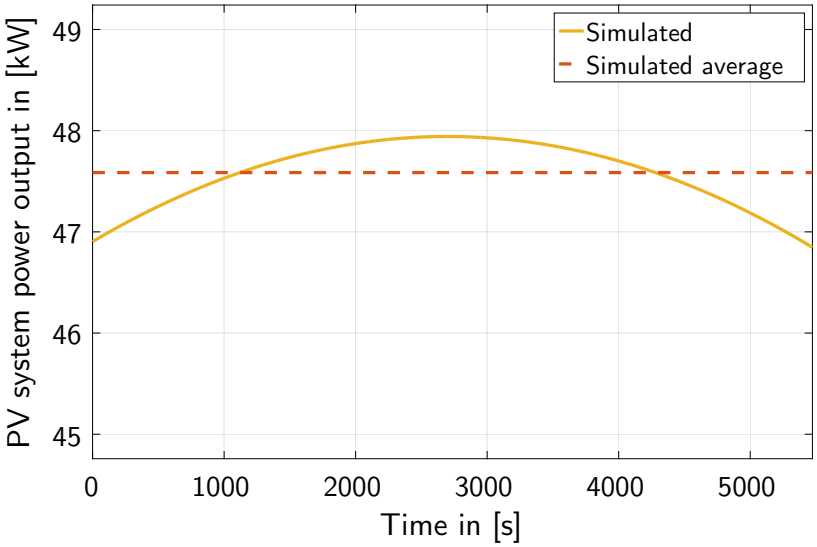

Figure 6.40: PV system power output throughout the flight mission in the near future (2020+); average PV system power output (orange dashed line) is 47.59 kW.

In this particular mission from Guayaquil to Bogota, the PV cells are performing slightly better than the assumed average of 23.7% (light blue solid) due to the selected flight location and its favourable weather conditions. The resulting power output of the PV system is then illustrated in Figure 6.40, which shows that the PV system provides an average power of 47.59 kW during the flight mission.

The hydrogen consumption rate of the fuel cell system is dependent on the operating current, as indicated by Equation 3.71. For better readability, the resulting fuel flow rate in kg/s is presented as a function of net system power output in Figure 6.41. Since the net power supply is kept at 200 kW, this corresponds to $4.092 \cdot 10^{-3}$ kg/s. For a mission of 5,473 seconds, this leads to 22.397 kg of hydrogen consumed throughout flight. In turn, this produces 200.33 kg of H_2O emissions, which should be taken into account as emissions in Section 6.5.1.

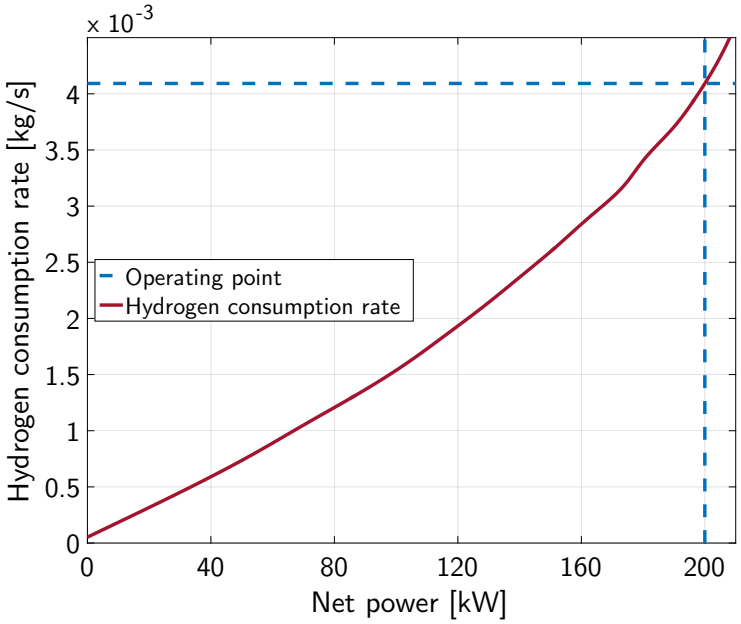

Figure 6.41: Hydrogen consumption rate as a function of net power output by the fuel cell system; for a net power output of 200 kW, the hydrogen consumption rate equals $4.092 \cdot 10^{-3}$ kg/s.

Figure 6.42 displays the state of charge (SOC) of the battery system throughout the entire flight. It is clear that the majority of the battery capacity, around 60%, is discharged during the climb phase to supply sufficient power to the electric motor for hybrid propulsion. The small decrease in SOC during cruise and descent is caused by the aircraft non-propulsive power systems; besides the 200 kW from the PEMFC system, the battery system provides supplementary power to generate sufficient non-propulsive power. The energy required for fully electric taxiing amounts to about 20% of the total battery capacity, which indicates that a significant portion is actually reserved for the taxiing procedure. Also, the graph demonstrates that the battery system never operates below the defined SOC limit of 10% (red dashed); this shows that the limit defined within the battery optimisation tool is implemented correctly.

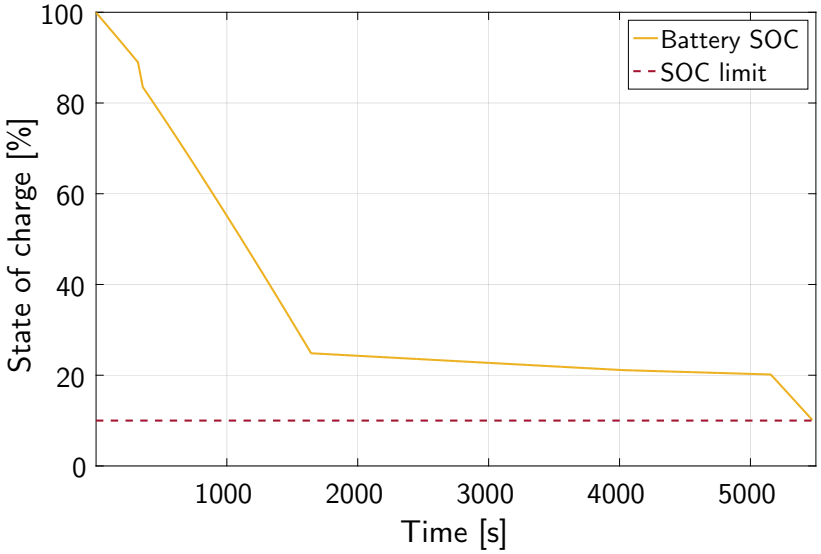

Figure 6.42: Battery state of charge throughout the flight mission in the near future (2020+); the SOC limit of 10% is indicated by the red dashed line.

The discharge current and voltage of the battery system can be found in Figure 6.43 and Figure 6.44,

respectively. Note that the discharge current is plotted against time and the battery system voltage against depth of discharge (DOD).

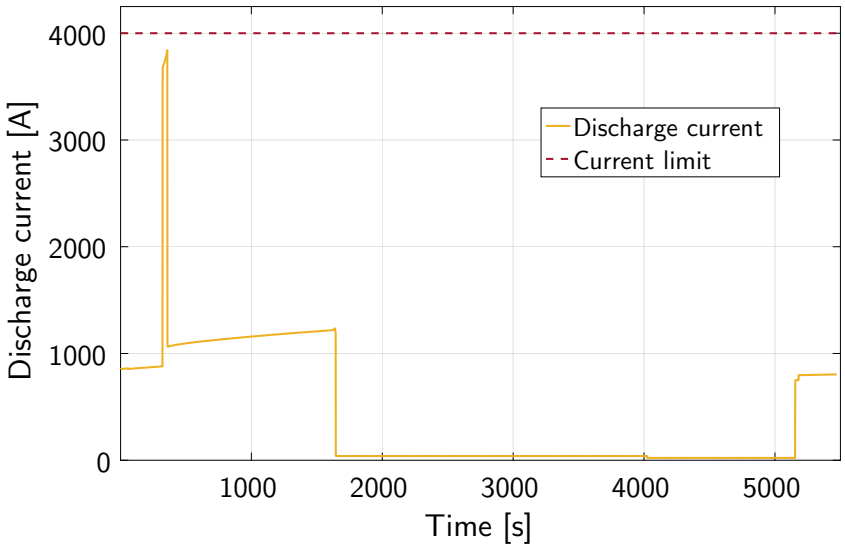

Figure 6.43: Operating discharge current of the battery throughout the flight mission in the near future (2020+).

The user-defined current limit of 4,000 A (see Section 5.2) marked as a red dashed line is only challenged during the take-off phase, where the discharge current peaks at roughly 3,850 A for a short time period. For the remainder of this mission, the discharge current will never operate above 1,250 A. Nevertheless, the electrical cables are still designed for the peak current of 3,850 A during take-off (with a certain safety margin), which results in thicker and heaver cables. This indicates that the operating conditions have a significant effect on the overall system mass, although this aspect has not been taken into account in this study.

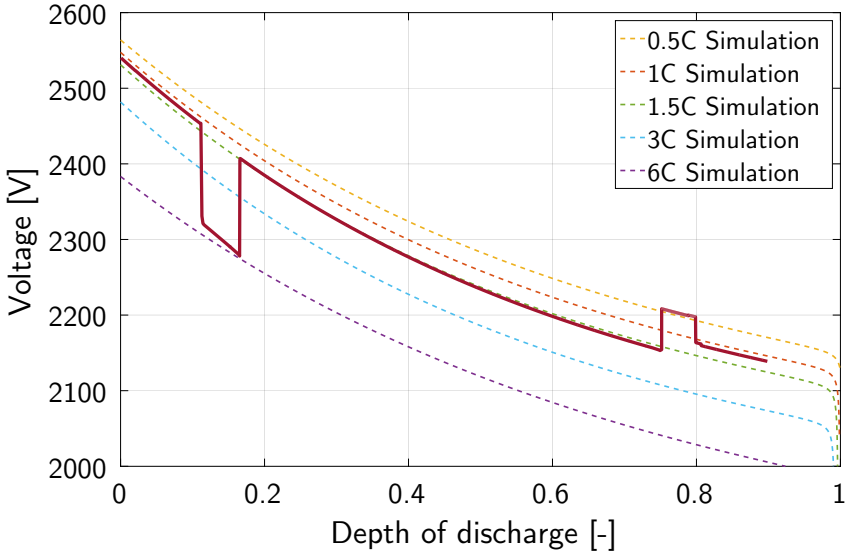

Figure 6.44: Operating voltage of the battery system throughout the flight mission in the near future (2020+), as a function of depth of discharge.

The course of the battery voltage is summarised in Figure 6.44; the curves at various discharge rates are also indicated as dashed lines in different colours. A value of 1C means that the selected discharge current will discharge the entire battery within 1 hour. The plot shows the distinct voltage jumps between the discharge curves, when it transfers from one flight phase to another.

From taxi-out to take-off, the discharge current climbs rapidly from roughly 900 A to 3,850 A; this forces the battery to operate at a higher discharge curve, which explains the voltage drop from 1.5C (green) to 6C (purple). The opposite happens when the aircraft switches from take-off to climb; the discharge current falls from its peak value of 3,850 A to 1,100 A. This allows the battery to switch from 6C (purple) back to 1.5C (green), operating at its previous discharge curve. Another rise in voltage is seen when the aircraft shifts from the climb phase to the cruise phase, corresponding to the curve of 1.5C (green) to the curve of 0.5C (yellow). This allows the battery to operate at a lower and more efficient discharge curve during cruise. Similar to Figure 6.42, the long uninterrupted line from 17% to 75% DOD implies that most of the installed battery capacity is utilised during the climb segment.

Figure 6.45 gives an overview of the power distribution of the electrical system. Each power system is marked in a different colour: light blue for the battery system, yellow for the PV system and green for the fuel cell system. In addition, the total electrical power required for the motor and the non-propulsive power systems is marked in red.

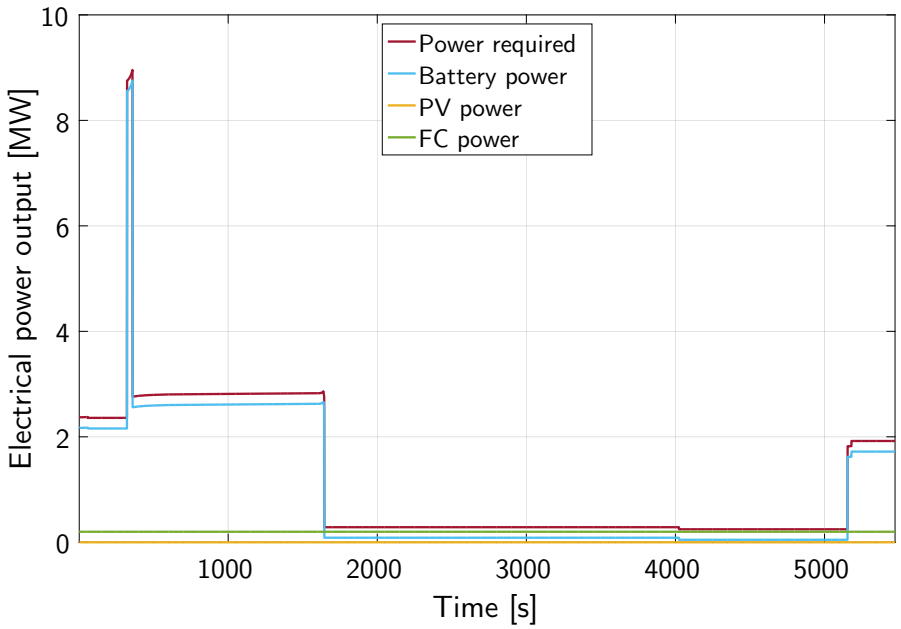

Figure 6.45: Power distribution of the electrical system throughout the flight mission in the near future (2020+); individual systems include battery (light blue), PV system (yellow) and fuel cell system (green).

From this figure can be deduced that the EAPPS is highly dependent on the battery system, as it provides most of the power and energy necessary to enable hybrid electric flight. The presence of the PV and fuel cell systems within EAPPS is mainly to provide electrical power to the aircraft subsystems throughout the mission.

The optimal battery setup for the EAPPS projected in the near future (2020+) has a total of 130,782 cells. In this battery pack, 614 cells are configured in series and 213 cells in parallel, also characterised as 614S213P; this setup can provide a total of 1.437 MWh of energy. The maximum operating voltage $V_{op,max}$ and discharge current $I_{op,max}$ are equal to 2,546.39 V and 3,840.85 A, respectively.

By integrating the battery power (light blue) over the mission time using Figure 6.45, the actual amount of energy extracted from the battery can be calculated. With a given mass of 60 g per cell for the Panasonic NCR20700A Li-ion battery [117] and a correction factor to realise the expected reduction in mass, the specific energy can be derived more accurately. In this particular setup, the corrected specific energy becomes 477 Wh/kg, which is slightly lower than the assumed value of 500 Wh/kg in the EAPPS module. This value can be used to recalculate the mass of the electrical system and fed back into the EAPPS simulation model. For comparison, the specific energy of the PV system can also be derived with a similar method; this leads to a value of 737.89 Wh/kg by incorporating the total masses of the panels and the converter. The higher specific energy of the PV system implies that it is still superior to batteries.

The final performance results of the Airbus A320neo with the updated electrical system mass, projected for the near future (2020+), will be summarised in Section 6.5.1. Furthermore, the fundamental differences with respect to the conventional A320neo aircraft, which flies around in the present moment, will be analysed.

6.4.2 Detailed Analysis of Future A320neo with EAPPS Modifications (2040+)

In similar fashion as Section 6.4.1, the electrical system of the future A320neo aircraft with EAPPS has also been modelled in more detail. Again, the variable efficiency of the electric motor is displayed in Figure 6.46. It can be noticed that the average motor efficiency (orange dashed) is now increased to 96.3%; this is considerably higher than the average value of 91.1% in Section 6.4.1. The increased power split ratios of 25.6% for take-off and 42.6% for climb in 2040+ allow the electric motor to operate more consistently and efficiently throughout the entire mission. This is, however, still slightly below the assumed value of 97.5% (light blue solid).

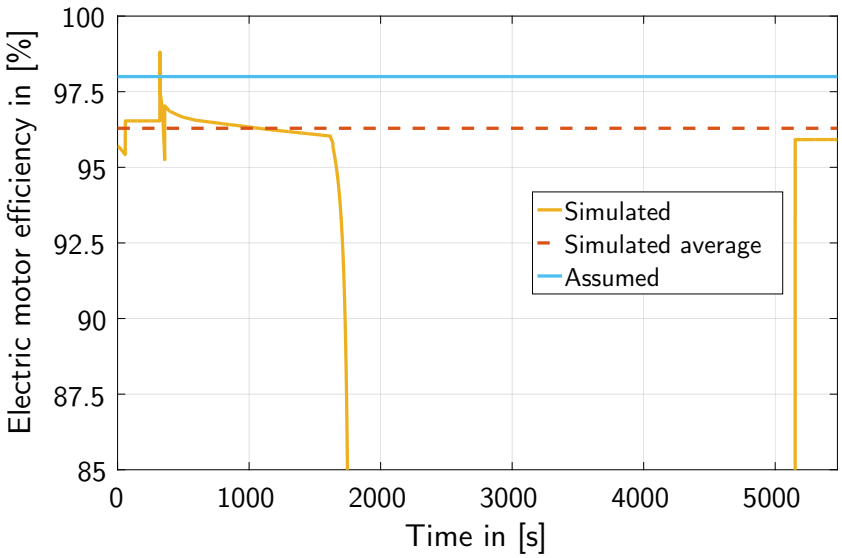

Figure 6.46: Electric motor efficiency throughout the flight mission in the far future (2040+); average motor efficiency (dashed orange line) is 96.3%.

The solar irradiance during this flight mission remain the same as for 2020+; the average irradiance is still 997.2 W/m^2 and its variation throughout flight can be found in Figure 6.38. The effect of technological development on the PV system is witnessed in the system efficiency and its power output; these are shown in Figure 6.47 and Figure 6.48, respectively.

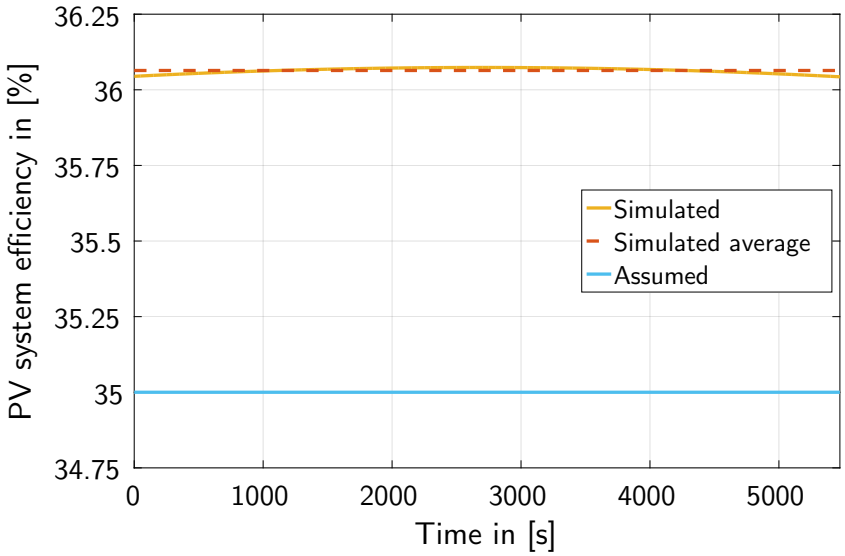

Figure 6.47: PV system efficiency throughout the flight mission in the far future (2040+); average PV system efficiency (dashed orange line) is 36.1%.

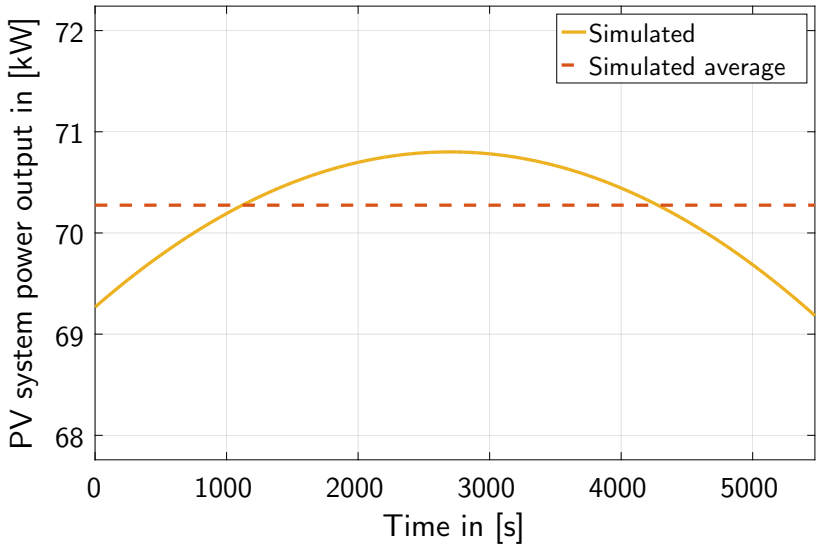

Figure 6.48: PV system power output throughout the flight mission in the far future (2040+); average PV system power output (dashed orange line) is 70.27 kW.

In Figure 6.47 can be seen that, once more, the simulated average PV system efficiency of 36.1% (red dashed line) is higher than the assumed average of 35% in the EAPPS model, due to the desirable PV conditions experienced in flight from Guayaquil to Bogota. This translates to an average system power output of 70.27 kW, as illustrated in Figure 6.48 by the orange dashed line. Compared to the previous PV setup of the near future (2020+), the solar performance has improved by 47.7%, from 47.59 kW to 70.27 kW.

Since the same fuel cell system setup is used, the hydrogen consumption and H_2O emissions remain the same as for 2020+, 22.397 kg of hydrogen and 200.33 kg of water, respectively.

The SOC of the battery system is presented in Figure 6.49. An apparent difference between the two setups from 2020+ and 2040+ is the amount of battery capacity used for hybrid electric propulsion

during take-off and climb phases. For the power management strategy in 2020+, a total battery capacity of 63.86% is used (see Figure 6.42). This number increases to 82.02% for the applied power management strategy in 2040+; this is caused by the increased total battery capacity due to the larger take-off and climb power split values, whereas the total electrical energy needed for taxiing remains more or less the same.

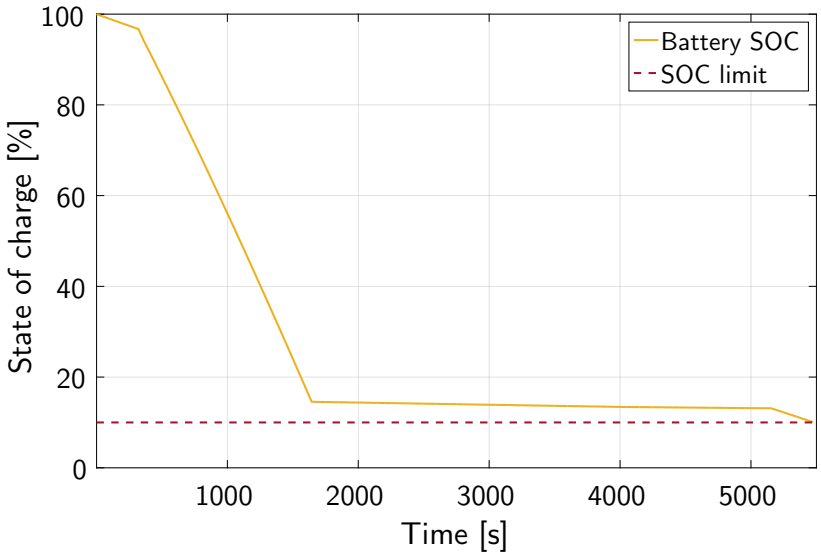

Figure 6.49: Battery state of charge throughout the flight mission in the far future (2040+); the SOC limit of 10% is indicated by the dashed red line.

The discharge current and voltage of the battery system are displayed in Figure 6.50 and Figure 6.51, correspondingly. Note that, again, the discharge current is plotted as a function of time, while the operating voltage is displayed as a function of DOD.

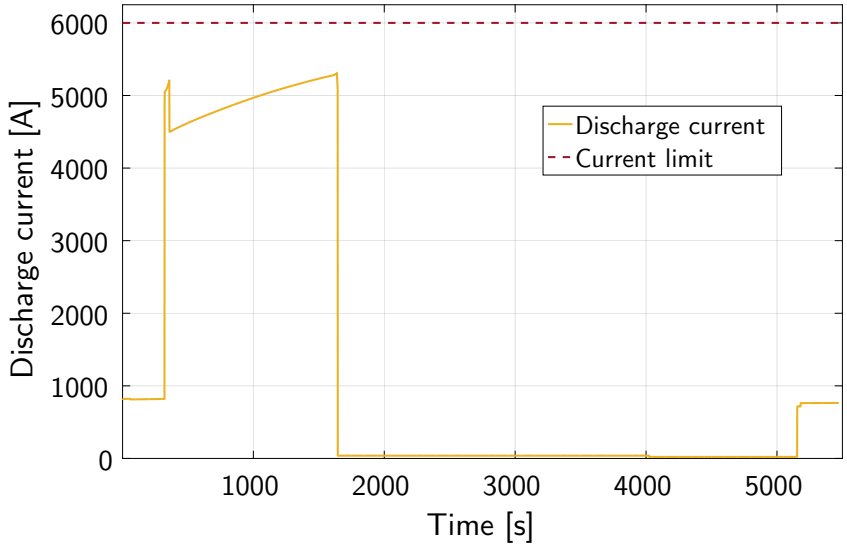

Figure 6.50: Operating discharge current of the battery throughout the flight mission in the far future (2040+).

Compared to Figure 6.43, a higher and better current distribution is achieved for the future battery setup, as shown in Figure 6.50. The discharge current reaches a local peak of 5,208 A during take-off,

followed by a quick drop and a steady climb towards the peak discharge current of 5,312 A at the end of the climb phase. This graph shows that higher peak currents are needed to provide the required electrical power in the far future, with the assumptions described in Section 5.2. This suggests that the cable mass will increase compared to the setup in 2020+, due to the higher operating current; nonetheless, the current-dependence aspects of the cable mass have not been considered in this study. In the future, the option of superconductive systems should be explored in order to minimise the mass and electrical losses of the cables.

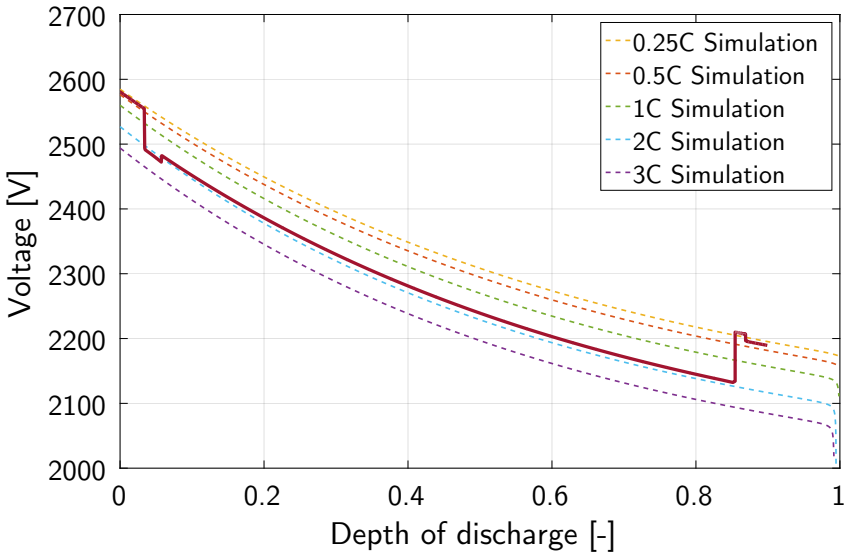

Figure 6.51: Operating voltage of the battery system throughout the flight mission in the far future (2040+), as a function of depth of discharge.

The voltage distribution of the battery system is shown in Figure 6.51; again, several discharge curves are plotted for reference, marked as dashed lines in different colours. The graph reveals that much lower discharge rates are applied for this setup: a maximum C-rate of 2C compared to that of 6C in Figure 6.44. Again, the voltage drop coincides with the switch from taxi-out to take-off: from 0.5C (orange) to 2C (blue). The voltage will significantly rise again, from 2C (blue) to 0.25C (yellow), when the climb phase shifts into the cruise phase. Also, by discharging a battery at lower C-rates, more capacity will be available for use; the energy inside the battery is simply being extracted more effectively. The majority of the battery capacity is extracted during the climb phase from 6% to 85% DOD.

The last graph to be presented is the power distribution of the electrical system in Figure 6.52. The same colour codes are used as for Figure 6.45 in Section 6.4.1: blue for the battery system, yellow for the PV system, green for the fuel cell system and red for the total electrical power required.

The first noticable difference compared to Figure 6.45 is that the power output of the electric motor is increased from 9 MW to 13 MW. This is necessary to supply the increased electrical loads for the power management strategy of $\phi_{\text{takeoff}} = 25.6\%$ and $\phi_{\text{climb}} = 42.6\%$. Furthermore, the power contribution of the battery system has grown immensely; the technological improvement of the battery technology has unlocked the true potential of HEPS. On the contrary, the significant impact of the PV and fuel cell systems within EAPPS have diminished, albeit still beneficial in terms of fuel and energy consumption.

The optimal battery setup for the EAPPS projected in the far future (2040+) becomes a battery pack of 414,007 cells; 617 cells are arranged in series and 671 cells in parallel, characterised as 617S671P. This electrical system can supply a total of 4.551 MWh of energy, which is a growth of 216.7%, relative

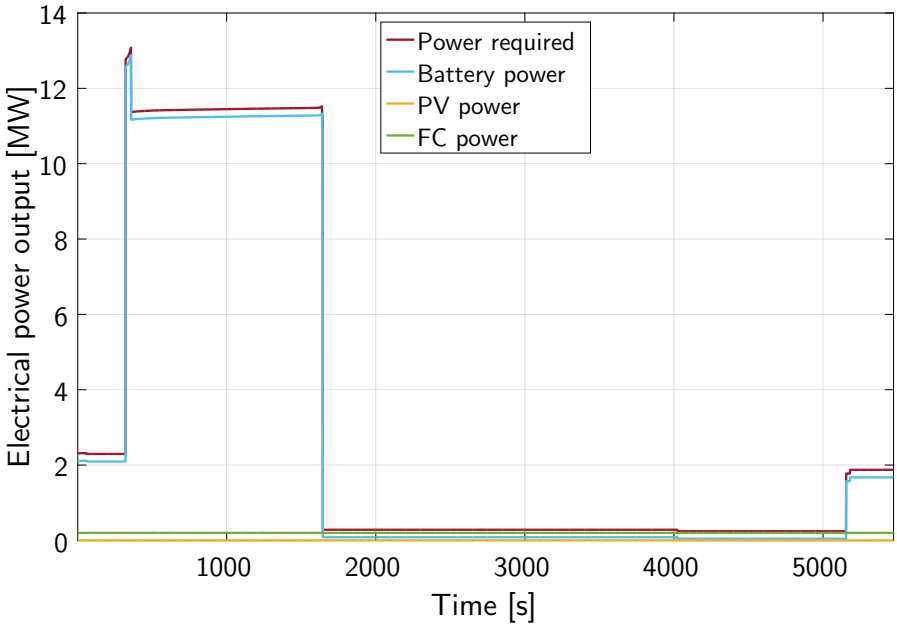

Figure 6.52: Power distribution of the electrical system throughout the flight mission in the far future (2040+); individual systems include battery (light blue), PV system (yellow) and fuel cell system (green).

to the setup described in Section 6.4.1. The maximum operating voltage $V_{op,max}$ and discharge current $I_{op,max}$ are realised at 2,580.54 V and 5,311.55 A, respectively.

Again, the total amount of energy extracted from the battery can be computed by integrating the battery power (light blue) over the mission time using Figure 6.52. For the future EAPPS configuration, the corrected specific energy becomes 954.2 Wh/kg. This result is fed back into the EAPPS module to correct for the low-fidelity simulation of the electrical system. This time the specific energy of the PV system becomes 1,366.77 Wh/kg, which still justifies the use of PV over batteries.

The updated and final results of the overall performance for the future Airbus A320neo aircraft, projected for the far future (2040+), will be discussed in Section 6.5.2. Also, its performance will be compared to the conventional A320neo aircraft, to see how much can be benefitted from EAPPS.

6.4.3 Discussion

The detailed analysis performed on the electrical system of the Airbus A320neo with EAPPS shows the future outlook of PEMFC and PV systems within a HEPS environment. This energy management study reveals that the use of these systems is quite limited due to the maximum power it can provide. Both Figure 6.45 and Figure 6.52 display that the total electrical power received from the PV and PEMFC systems is merely a small fraction of the power required by the electric motor and the non-propulsive power systems.

In the ideal flight mission for 2040+, the PV system may only generate a total of 70.27 kW of electrical power; even with more optimistic values for area mass density and efficiency, the system power will still not improve beyond 100 kW. Nevertheless, this study demonstrates the technical feasibility of PV; limited fuel and energy savings are achievable. Also, the equivalent specific energy of PV is higher than that of batteries, which justifies the use of it in this particular mission. The commercial viability of PV with detailed cost analysis is investigated in Section D.2.

A similar result is found for the PEMFC system; as the maximum power is capped at the minimum electrical power required throughout the whole flight, the benefits of adding fuel cell technology are, similar to PV, minimal. However, the fuel cell system shows more potential in an aircraft environment due to its multifunctional use: first of all, excess heat from the fuel cell may be used to pre-heat the air going into the gas turbine. Secondly, the in-flight production of water allows less water to be carried on-board and can be utilised in galleys as well as lavatories. Last but not least, the fuel cell system may be used as an APU for battery charging and/or redundancy. If the former is the case, the maximum fuel cell power may be increased and less batteries may be carried along. Unfortunately, these potential use cases have not been investigated during this study due to the lack of time.

The main verdict of this thorough energy management system study is that the potential of HEPS or EAPPS is governed by future battery development. The specific energy of the battery is a valuable indicator whether hybrid electric propulsion may or may not be realised; in this case, a battery specific energy of 477 Wh/kg is sufficient for hybrid electric aviation. Also, inherent sizing characteristics of batteries allow numerous battery configurations to be viable.

Additionally, the volume aspects of these EAPPS setups are analysed and described in Appendix B.

6.5 Final Corrected Results

This section provides the final performance results from the EAPPS module for both the near and far future A320neo setups, after a corrective feedback on the electrical system mass has been applied. This correction is derived from the outcome of the EMS module, where the electrical system has been simulated in more detail. Once again, the optimal flight mission is from Guayaquil (Ecuador) to Bogota (Colombia). The optimised A320neo EAPPS arrangements with downscaled engines for near future technology (2020+) and far future technology (2040+) are described in Section 6.5.1 and Section 6.5.2, correspondingly. The findings will be measured against the reference A320neo setup without EAPPS, as was performed with the baseline aircraft in Section 6.1, to discover the full benefits in terms of fuel, energy and emission savings. This is concluded with a brief discussion on the results in Section 6.5.3.

6.5.1 Optimised and Scaled A320neo with EAPPS Modifications (2020+)

The near future EAPPS configuration in 2020+ features a power management strategy with a take-off power split $\phi_{takeoff}$ of 16.6%, a climb power split ϕ_{climb} of 9.3% and a downscaled engine of 90%. The electrical system weighs a total of 6,279.92 kg, after adjusting the assumed specific energy of 500 Wh/kg to 477 Wh/kg. This particular setup can save a total of 661.06 kg of kerosene and 5.97 MWh of energy, relative to the conventional A320neo aircraft without EAPPS.

Figure 6.53 compares the results from the optimised configuration with the reference A320neo, from an overall mission perspective. As shown in Figure 6.53a and Figure 6.53b, the fuel and energy consumption are reduced by 16.8% and 12.7%, respectively. This is a direct consequence of using an efficient electric motor during taxiing, take-off and climb phases, which results in a higher overall system efficiency, as indicated in Figure 6.53c. In order to carry the additional electrical system mass, the required thrust is marginally increased throughout flight, as illustrated in Figure 6.53d.

The difference in total fuel burn dependent emissions, CO_2 and H_2O, is shown in Figure 6.54. A reduction of 15.3% can be achieved in terms of CO_2 and H_2O emissions, which translates to 2,042.3 kg and 610.1 kg, respectively. A part of the H_2O emissions is a by-product of the PEMFC system, namely 200.33 kg.

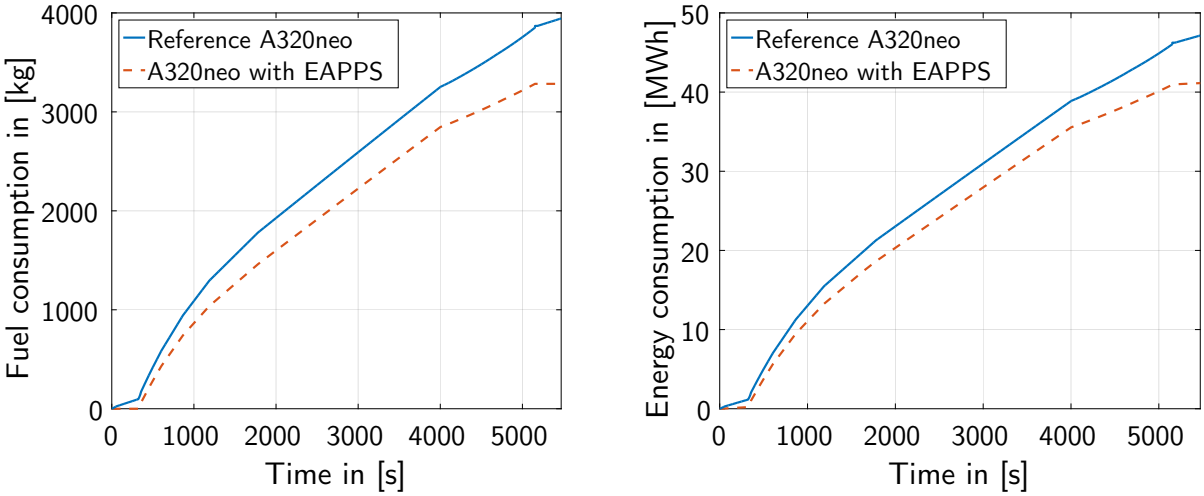

(a) Effect on fuel consumption.

(b) Effect on energy consumption.

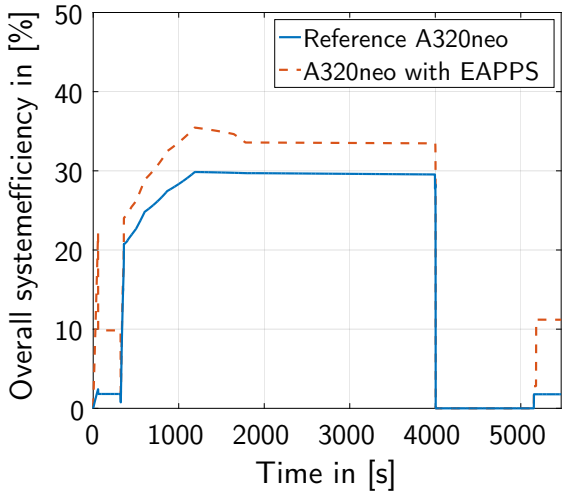

(c) Effect on overall system efficiency.

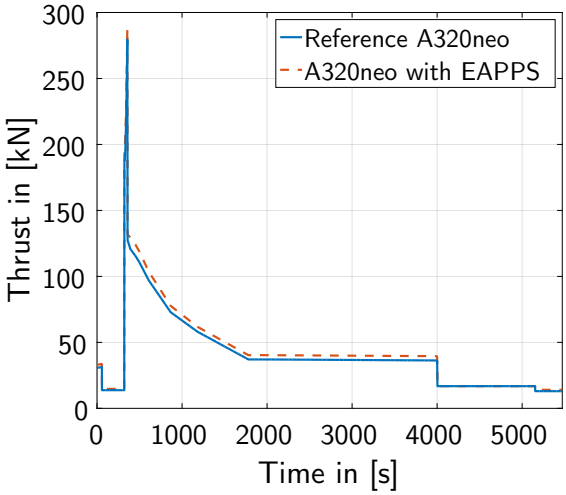

(d) Effect on thrust requirement.

Figure 6.53: Effect of optimised EAPPS (2020+) and downscaled engine on overall mission performance; relative to reference A320neo configuration without EAPPS.

Figure 6.55 presents the engine dependent emissions, CO, UHC, NO_x and soot. In absolute terms, the optimised A320neo setup for 2020+ emits 10.46 kg less pollutants than the reference A320neo; this corresponds to a substantial reduction of 24.7% in engine dependent emissions.

By observing the emission trends in Figure 3.4, it is expected that CO and UHC values will decrease greatly while NO_x and soot values will drop slightly; the use of EAPPS allows the turbofan engine to only operate at higher thrust settings, as the electric motor can provide the required thrust during taxiing. Indeed, both CO and UHC pollutants are heavily reduced by 69.8% and 50.6%, respectively. Also, the NO_x emissions are lowered by 3.8%. Only the amount of soot produced is slightly more than for the reference case, an increase of 0.4 g or 2.1%. This divergence can be explained by the emission data used from Table 4.2. The trends coincide with the numbers used for CO, UHC and NO_x, but not for SN. The smoke numbers should be highest at take-off and lowest at idle; in this case, the smoke numbers chosen remain more or less at 1.3, with the exception of 1.17 during climb. These numerical values assumed for SN are most likely the source of the discrepancies related to soot.

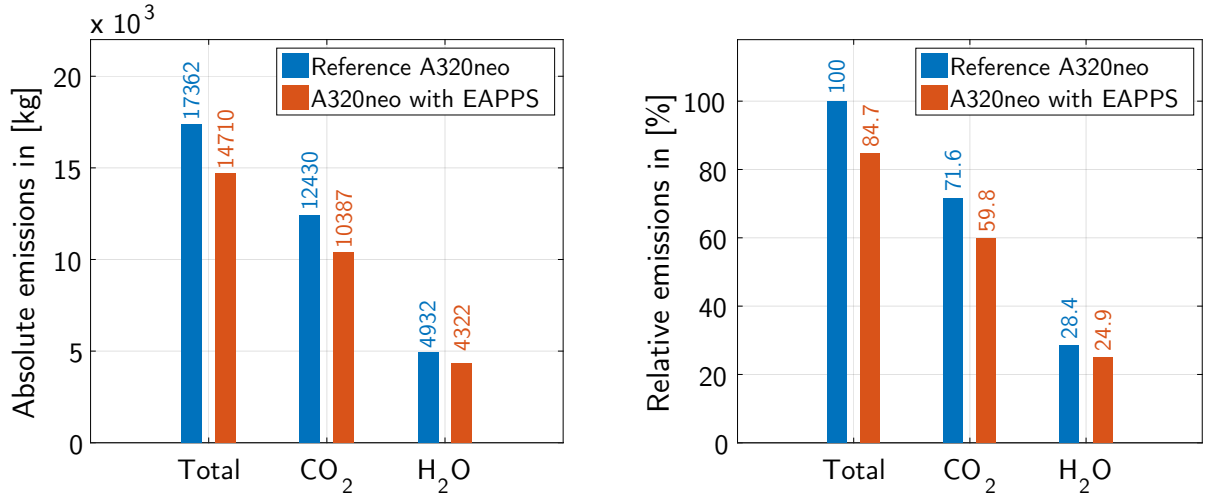

(a) Total emission masses. **(b)** Distribution of emissions.

Figure 6.54: Effect of optimised EAPPS (2020+) and downscaled engine on fuel burn dependent emissions; relative to reference A320neo configuration without EAPPS.

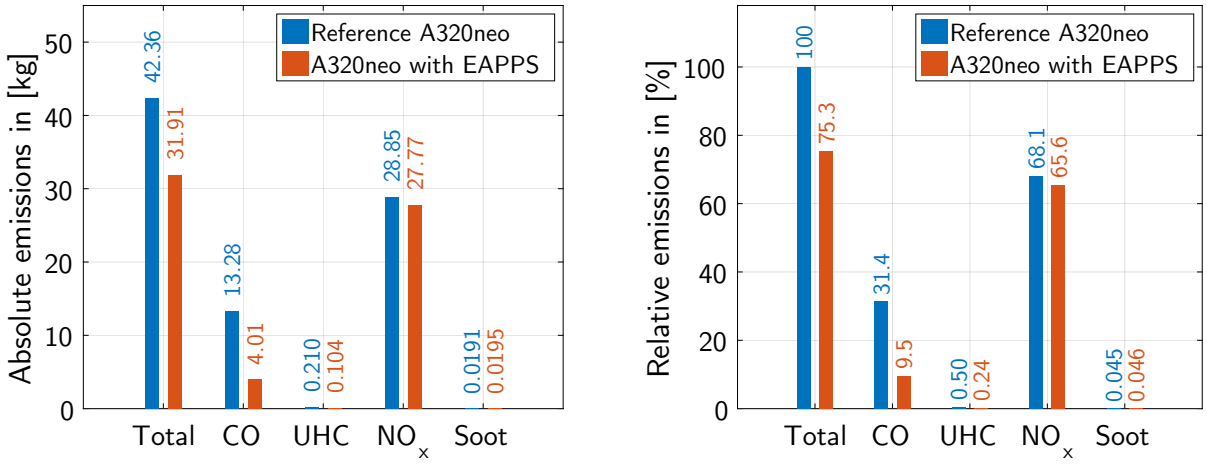

(a) Total emission masses. **(b)** Distribution of emissions.

Figure 6.55: Effect of optimised EAPPS (2020+) and downscaled engine on engine dependent emissions; relative to reference A320neo configuration without EAPPS.

6.5.2 Optimised and Scaled Future A320neo with EAPPS Modifications (2040+)

The optimised EAPPS configuration with far future technology (2040+) includes a take-off power split $\phi_{takeoff}$ of 25.6%, a climb power split ϕ_{climb} of 42.6% and a CFM LEAP-1A engine downscaled to 85% of the original size, while keeping the three modifications (electrical subsystem architecture, fuel cell system of 200 kW and PV installation of 209.91 m^2) intact. Using the corrected specific energy of 954.2 Wh/kg from the EMS module, the final electrical system mass will amount to 7,348.57 kg. This setup brings a total savings of 1,109.8 kg of jet fuel and 8.45 MWh of energy.

The overall mission performance is outlined in Figure 6.56 for the optimised A320neo with EAPPS and the reference A320neo. Figure 6.56a and Figure 6.56b display the differences between the overall fuel and energy consumption; the amounts of fuel and energy used are lowered by 28.1% and 17.9%, respectively. The biggest offsets with respect to the reference aircraft are accomplished during the take-

off and climb phases, where the overall system efficiency reaches above 40%, as shown in Figure 6.56c. The thrust is slightly higher with EAPPS, as the additional mass of the electrical system needs to be carried along the flight. This is depicted in Figure 6.56d.

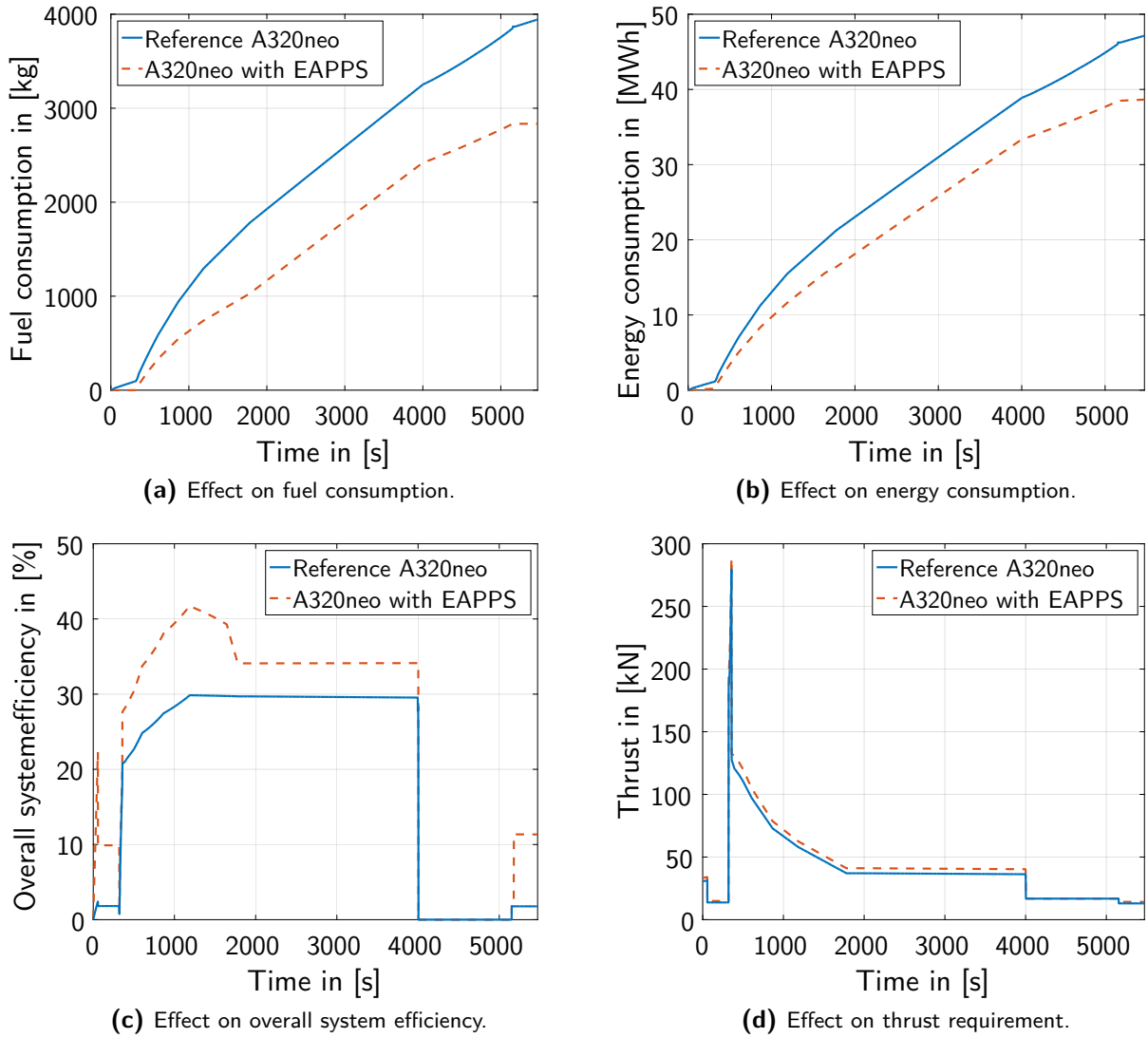

(a) Effect on fuel consumption.

(b) Effect on energy consumption.

(c) Effect on overall system efficiency.

(d) Effect on thrust requirement.

Figure 6.56: Effect of optimised EAPPS (2040+) and downscaled engine on overall mission performance; relative to reference A320neo configuration without EAPPS.

The fuel burn dependent emissions, CO_2 and H_2O, are illustrated in Figure 6.57; the absolute as well as the relative emissions are provided.

The CO_2 and H_2O emissions are lowered by 25.6%: in absolute terms, 3,322.7 kg of CO_2 and 1,118.2 kg of H_2O can be saved. Again, 200.33 kg of the total H_2O emissions comes from the fuel cell system as a by-product. The engine dependent emissions (CO, UHC, NO_x and soot) are shown in Figure 6.58; the total reduction in engine dependent emissions equals 34.7% or the equivalent of 14.68 kg.

Surprisingly, the future EAPPS setup with a power management strategy of 25.6% during take-off and 42.6% during climb manages to cut back on all four pollutants relative to the reference A320neo aircraft. Perhaps the increased use of electrification during take-off allows the soot production to go down. The largest reductions are seen for the CO and UHC pollutants, which are reduced by 73.8% and 57.3%, respectively. The NO_x emissions are lowered by 16.5% or 4.77 kg, while the amount of soot produced is 6.9% lower or 1.32 g less than for the reference aircraft.

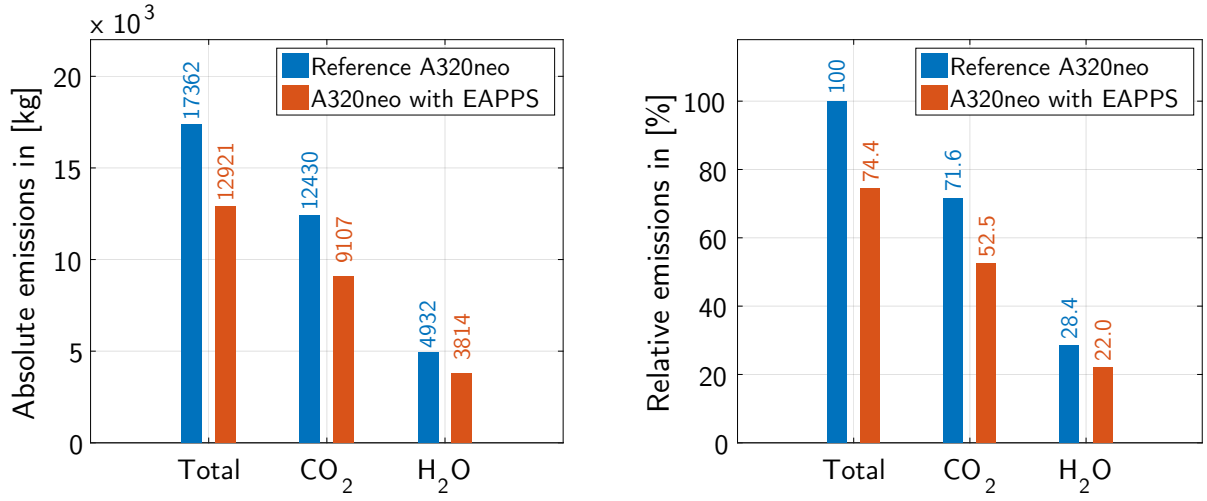

(a) Total emission masses. **(b)** Distribution of emissions.

Figure 6.57: Effect of optimised EAPPS (2040+) and downscaled engine on fuel burn dependent emissions; relative to reference A320neo configuration without EAPPS.

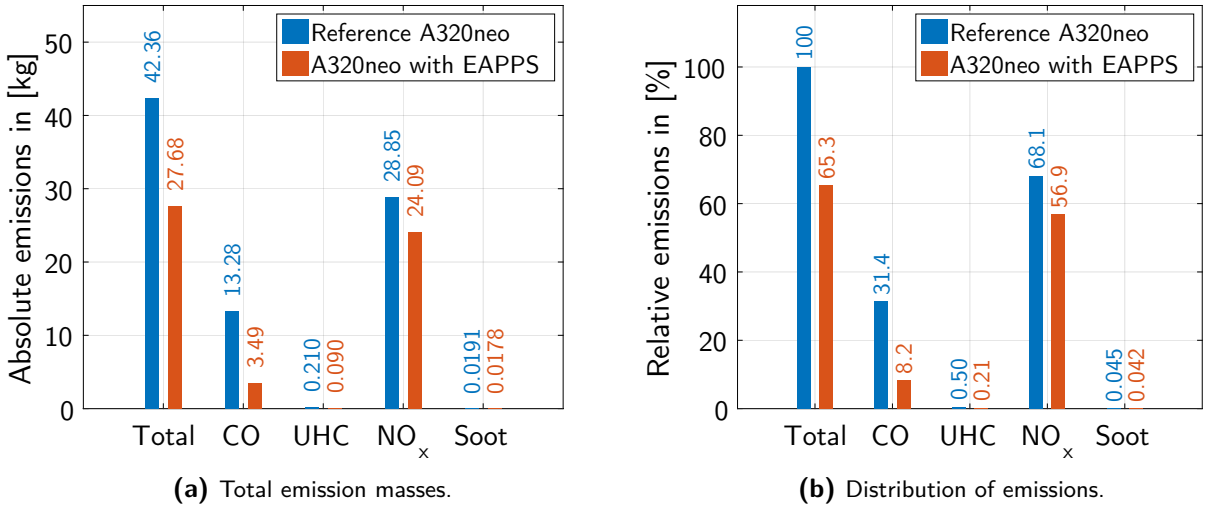

(a) Total emission masses. **(b)** Distribution of emissions.

Figure 6.58: Effect of optimised EAPPS (2040+) and downscaled engine on engine dependent emissions; relative to reference A320neo configuration without EAPPS.

6.5.3 Discussion

The final and corrected results from the EAPPS simulation model in terms of fuel, energy and emission savings are summarised in Table 6.9.

By observing Table 6.9 more closely, one can see that significant reductions in fuel, energy and emissions are possible with the proposed EAPPS configurations. Of course, between the two scenarios, the potential savings in the far future are noticeably greater than in the near future. A noteworthy difference is that the soot emission trend is reversed in the far future, using the same emission data from Table 4.2; instead of an increase in soot production, less substance is actually emitted. This is most likely caused by increasing the take-off power split ratio from 16.6% to 25.6%. Normally, soot production is maximal at high fuel-air ratios (e.g. during take-off) [70], as depicted in Figure 3.4. Since the smoke numbers used are inconsistent with this trend, the exact reasoning for this observation cannot be disclosed.

Table 6.9: Summary of fuel, energy and emission savings for near future technology (2020+) and far future technology (2040+).

	Near future technology (2020+) $\phi_{takeoff}$=16.6%, ϕ_{climb}=9.3% Battery specific energy: 477.0 Wh/kg Electrical system mass: 6,279.92 kg		**Far future technology (2040+)** $\phi_{takeoff}$=25.6%, ϕ_{climb}=42.6% Battery specific energy: 954.2 Wh/kg Electrical system mass: 7,348.57 kg	
Type	**Absolute savings**	**Relative savings**	**Absolute savings**	**Relative savings**
Fuel	-661.06 kg	-16.76%	-1,109.80 kg	-28.14%
Energy	-5.97 MWh	-12.65%	-8.45 MWh	-17.92%
CO_2	-2,042.28 kg	-16.43%	-3,322.66 kg	-26.73%
H_2O	-610.10 kg	-12.37%	-1,118.18 kg	-22.67%
CO	-9.27 kg	-69.79%	-9.80 kg	-73.76%
UHC	-0.11 kg	-50.64%	-0.12 kg	-57.27%
NO_x	-1.08 kg	-3.75%	-4.77 kg	-16.52%
Soot	+0.40 g	+2.11%	-1.32 g	-6.94%

Another interesting point to mention is the huge development in propulsive electrification from 2020+ to 2040+; the take-off power split ratio $\phi_{takeoff}$ increases from 16.6% to 25.6% and the climb power split ratio ϕ_{climb} from 9.3% to 42.6%. While the battery specific energy improves by a factor 2, the take-off and climb power split ratios increase by a factor 1.5 and 4.6, respectively. This can be explained by the following reasons: first of all, the electrical system mass in 2020+ is lower than that of 2040+, indicating that the comparison is unfair; there is room for additional batteries and hybridisation up to the MTOM limit of 7,499 kg. The incremental steps of 10% used in the power management optimisation procedure do not allow for higher power splits; steps of 5% would probably have resulted in a higher climb power split ratio of around 15% in 2020+. Also, the take-off power split ratio $\phi_{takeoff}$ has not doubled, which implies that less battery mass is dedicated towards the take-off phase. Another explanation is that the other system components have also become more efficient and lighter, leaving more mass available for batteries. Taking all these aspects into account, it is likely that the improvement factor for the climb power split ratio ϕ_{climb} would lower to 2.5-3 instead of 4.6.

The aforementioned time frames of 2020+ and 2040+ should be treated as indicative values; a better indicator is to look at the realised battery specific energy, which prominently influences the flight performance of the A320neo and thus the benefits of EAPPS. As mentioned earlier in Section 6.4.3, the feasibility of EAPPS is mainly affected by how fast battery technology can progress and reach its desired specific energy values; surely enough, this cannot be predicted exactly.

CHAPTER 7

Conclusions and Recommendations

Finally, this chapter will conclude the thesis report; first by summarising the key points and discoveries of this study in Section 7.1 and then by providing a few recommendations for further research regarding electrically assisted propulsion & power systems (EAPPS) in Section 7.2.

7.1 Conclusions

With a vastly growing demand for global connectivity, air traffic is expected to double over the next twenty years. Consequently, the consumption of kerosene as fuel and its harmful effect on the natural environment will increase as well. To reduce the environmental impact of aviation and promote sustainable awareness, new innovative solutions need to be developed. An EAPPS integrates a conventional turbofan engine with a network of electrical components, providing assistance to the aircraft propulsion and non-propulsive power systems.

The main objective of this study was to evaluate how gradual EAPPS modifications could affect the overall performance of an Airbus A320neo aircraft in a short-range mission of 1,000 km. In order to analyse these effects, two separate simulation models were developed: the EAPPS module and the energy management system (EMS) module. The former contains a detailed mission analysis tool which, in combination with an in-depth engine model, can compute the flight performance of a hybrid electric aircraft. Within this module, the electrical system and its corresponding mass are simulated in a low-fidelity model, by applying fixed specific energy and power values as well as constant efficiencies throughout the flight mission. The latter is an in-depth model for simulating the internal dynamics of the electrical system more accurately. It features validated models of four different components: the electric motor, the photovoltaic (PV) system, the polymer electrolyte membrane fuel cell (PEMFC) system and the battery system. Both modules can accommodate a variety of EAPPS configurations; to examine the benefits of these setups, a series of trade studies was performed. Since technological development plays a huge role in the realisation of hybrid electric aviation, two different timecframes were considered: near future (2020+) and far future (2040+). For instance, a battery specific energy of 500 Wh/kg is applied in the 2020+ scenario, while in the 2040+ scenario this value is increased to 1,000 Wh/kg.

First, the power management of the HEPS configuration was investigated, similar to a former study [1]. Higher power split ratios (amount of electrical power relative to total power) are desired, within

the aircraft maximum take-off mass (MTOM) limitations, for reduced fuel consumption. During the taxi phase, fully electric propulsion significantly increases the overall system efficiency from 2% to 10%; this results in a fuel reduction of 3%, which is comparable to values obtained from Safran and Airbus [104]. Between increasing the take-off power split $\phi_{takeoff}$ and the climb power split ϕ_{climb}, the latter should be prioritised to maximise the benefits of hybrid electric propulsion in terms of fuel consumption. Unlike the climb phase, the duration of the take-off phase is too short to take advantage of HEPS; the fuel saved in this period of time is less than the additional fuel consumed for the inclusion of the electrical system mass e.g. due to power-based sizing of the electric motor. Another aspect of the power management strategy is the option of charging the batteries during phases with low power requirements e.g. descent. It turned out that in-flight charging is not advantageous; the fuel and energy required to charge the batteries during descent does not offset the lower fuel and energy consumption due to the smaller and lighter electrical system. This implies that the batteries should be recharged while the aircraft is parked at the airport.

In addition, a number of A320neo modifications with various EAPPS arrangements were applied, assessing the effect on the overall performance (i.e. total fuel and energy consumption) in the near future (2020+) and the far future (2040+). The first modification was the conversion to an electrical architecture for the non-propulsive power systems (MEA). This proved to be the most effective approach in terms of fuel and energy reduction, mainly due to the removal of the engine bleed air and shaft power off takes. Also, the use of lighter electrical components allowed a mass reduction of 799 kg. The next modification was the implementation of a fuel cell system; its sizing appeared to be crucial for potential benefits. Due to the low utilisation rate throughout flight, an oversized fuel cell system cannot compensate for its additional mass, leading to higher fuel and energy consumption. A fuel cell system capable of generating 200 kW of power was considered to be optimal between the test cases; it could save a small amount of fuel and energy due to its greater specific energy than batteries. The third modification was the installation of PV panels on the outer skin of the A320neo. This system change also showed some savings in fuel and energy, albeit negligible, due to the greater specific energy of photovoltaic than batteries. Finally, the EAPPS setup was further optimised by scaling the CFM LEAP-1A engine down within the NGV temperature limitation of 2,000 K. Each modification proved to be advantageous in terms of fuel and energy savings, although the addition of PV and fuel cell systems only brings minor improvements; their added value in commercial hybrid electric aviation has yet to be identified.

Both optimal EAPPS setups for 2020+ and 2040+ feature an electrical subsystem architecture (MEA), a fuel cell system that delivers a constant supply of 200 kW, 210 m^2 of PV panels on the outer skin of the aircraft and a downscaled engine. The optimal power management strategy in 2020+ includes fully electric taxiing, a take-off power split $\phi_{takeoff}$ of 16.6% and a climb power split ϕ_{climb} of 9.3%. By 2040+, the take-off power split $\phi_{takeoff}$ increases to 25.6% and the climb power split ϕ_{climb} to 42.6%; the technological advancements on the individual components significantly decrease the total electrical system mass enabling this increase in electrification of the propulsion system. Also, higher take-off power split ratios lower the rotational speed on the HP spool N_2 and the maximum temperature experienced at the nozzle guide vanes T_{t41}. This allows the CFM LEAP-1A engine to be scaled down to 90% in 2020+ and 85% in 2040+. In terms of solar irradiance, the ideal flight mission departs from Guayaquil towards Bogota (991 km) such that solar noon occurs midway of the flight. However, seasonal or annual averages of the solar irradiance should be considered for real-life performance estimations. Furthermore, the energy storage capacity of the A320neo aircraft has been evaluated; there is sufficient space to accommodate the additional batteries and fuel cell system, along with its hydrogen storage.

Moreover, the comprehensive energy management study was performed to demonstrate the dynamic behaviour of four electrical system components: the electric motor, the PV system, the PEMFC system and the battery system. It showed in more detail that emerging technologies such as PEMFC and

PV systems can be beneficial in an aircraft environment. Despite the fact that only a limited amount of power can be generated, the use of these systems still reduces overall aircraft consumption and emissions; in addition, sustainable development in aviation is encouraged. Also, the battery optimisation study showed that the energy stored in the battery system cannot be fully extracted due to discharge inefficiency. This implies that the rated capacity is overestimated and corrective measures should be taken, i.e. lowering the value assumed for the battery specific energy (for 2020+, the assumed value of 500 Wh/kg is corrected into 477 Wh/kg). The corrected and optimised results are compared to the conventional A320neo and show that the optimal EAPPS setup in 2020+ can reduce the fuel and energy consumption by 16.8% and 12.7%, correspondingly. Also, the engine emissions are lowered significantly: CO_2 by 16.4%, CO by 69.8%, UHC by 50.6% and NO_x by 3.8%. The optimal EAPPS setup in 2040+ can save significantly more due to the increased use of electrically assisted propulsion; the total relative savings of fuel and energy are 28.1% and 17.9%, respectively. In terms of pollutants, the following reductions are possible: CO_2 by 26.7%, CO by 73.8%, UHC by 57.3% and NO_x by 16.5%.

In conclusion, several trade studies were performed and verified using two different simulation models developed to expand the knowledge on HEPS in commercial aircraft. The results revealed how the benefits from each modification can be maximised in terms of fuel and energy consumption, leading to an optimal configuration for the near future (2020+) and the far future (2040+). Also, the energy management analysis provided additional insights into the individual performance of the electric motor, the PEMFC system, the PV system and the battery system. Given the projected timeline of technological development, the technical feasibility of EAPPS has already been discussed in this study; the potential use of EAPPS highly depends on future advancements in battery technology. The commercial viability of EAPPS is as equally important as the technical feasibility and financial incentives need to be realised to bring EAPPS into existence. Ultimately, only time will tell how the sustainable nature of future commercial aviation develops.

7.2 Recommendations for Future Research

The two simulation models were developed to analyse the mission performance of an Airbus A320neo aircraft equipped with EAPPS; this EAPPS configuration can be altered to include or exclude certain electrical systems. Nonetheless, further improvements to the simulation models can be made.

In order to advance the knowledge on HEPS in commercial aviation, the following aspects should be considered:

- *Expansion to other electric propulsion architectures*
  Current simulation models only consider the parallel HEPS configuration, where both the turbofan engine and the electric motor are separated from each other. Other variations such as the series HEPS, full and partial turbo-electric can be included to compare the overall mission performance of each architecture. In particular, the partial turbo-electric setup sounds promising; the required electrical power comes directly from the engine via a generator, so the heavy battery systems are not required.

- *Hybrid SOFC-GT setup*
  With the inclusion of fuel cells in EAPPS, a hybrid SOFC-GT setup should be investigated. This arrangement allows an increase in SOFC and engine performance; an exchange of pressurised air and heat benefits both systems. Also, the number of SOFC components can be reduced, as the gas turbine can provide the same functions.

- *Detailed modelling of CFM LEAP-1A engine emissions*
  The GSP® engine model or the emission data used for modelling the emissions of the CFM LEAP-1A26 engine may not be sufficiently accurate and need further validation. A more careful analysis of the actual combustion products throughout the mission is recommended. The validity of these results is essential for a technological breakthrough in future aviation, as engine emissions will remain one of its core problems.

- *Detailed bleed schedule of CFM LEAP-1A engine*
  The current bleed schedules for cooling and off-takes are based on a set of assumptions. To accurately represent this aspect, the actual bleed schedules for the CFM LEAP-1A engine should be implemented in the GSP® model. This includes multi-stage bleed air extractions at different phases of the flight mission.

- *Thermal management of EAPPS*
  The aspect of thermal management has not been taken into account in this study. As electrically assisted propulsion may reach power values above 1-10 MW, cooling equipment need to be installed for electric motors, power electronics and battery systems. Another alternative option is to investigate the potential of advanced superconducting components using cryogenics.

- *Detailed modelling of converter and electric motor interaction*
  Due to the lack of electrical engineering knowledge, detailed models of the converter and the electric motor have been left out in this study. Both components should be defined and modelled accurately, e.g. with simulation software such as Simulink®, to show the dynamic interaction between the two. This step is crucial to understand how a complete EAPPS can be built and realised in the future.

- *Aerodynamic analysis of solar skin and HEPS-integrated engine*
  While the functionality of the solar skin has been demonstrated by Solar Impulse 2, the aerodynamic disturbances of installing this skin on a commercial aircraft have not been investigated yet. A detailed aerodynamic analysis of the aircraft should be done to identify the drag penalty of the applied solar skin. Also, the addition of an electric motor on the LP shaft of the CFM LEAP-1A engine will undoubtedly change the original nacelles and pylons; the effect of this on the aircraft aerodynamics should be investigated as well.

- *Life-cycle cost analysis of the A320neo aircraft*
  To prove the commercial viability of EAPPS, a complete life-cycle cost analysis should be performed. This means that all research & development costs, manufacturing costs, acquisition costs, operating costs and disposal costs should be taken into account. If the results are positive, the aircraft manufacturer Airbus and commercial airline companies can adapt to this and dedicatedly work towards a more sustainable future of aviation.

APPENDIX A

Electrical Power Requirements of A320neo

A.1 Conventional Architecture of A320neo

The electrical power requirements for the conventional architecture of the A320neo are derived from the electrical architecture described in Section A.3 along with a dataset from Ref. [36]. Unwanted electric loads are removed (e.g. for ECS and IPS) and new ones are introduced (e.g. controls for hydraulics). A general assumption here is that the power factor is equal to 1; the total apparent power for AC loads in kVA are equivalent to the real power in kW, allowing the AC and DC power requirements to be added up to obtain a total amount. The results are summarised in Table A.1. An in-depth breakdown of the power requirements can be found in Table A.2.

Table A.1: Electrical power requirements for conventional architecture of Airbus A320neo; adapted from [33, 36].

Subsystem	Taxi-out	Take-off	Climb	Cruise	Descent	Landing	Taxi-in
Actuation & landing gear	9.80	17.10	13.10	12.50	15.10	23.50	9.80
Avionics	31.59	34.13	41.23	41.23	41.23	34.62	31.59
Cabin equipment	7.50	6.50	6.50	49.40	6.50	6.50	7.50
Total AC [kVA]	*19.80*	*12.50*	*18.80*	*61.70*	*18.80*	*12.50*	*19.80*
Total DC [kVA]	*29.09*	*45.23*	*42.03*	*41.43*	*44.03*	*52.12*	*29.09*
Total [kW]	**48.89**	**57.73**	**60.83**	**103.13**	**62.83**	**64.62**	**48.89**

Table A.2: Detailed electrical power requirements for conventional architecture of Airbus A320neo in [kW]; adapted from [33, 36].

Subsystem	Equipment	AC/DC	Taxi-out	Take-off	Climb	Cruise	Descent	Landing	Taxi-in
Actuation & landing gear	Hydraulic systems	DC	9.8	17.1	13.1	12.5	15.1	23.5	9.8
Avionics	Actuator control electronics	DC	1	1	1	1	1	1	1
Avionics	Air data inertial reference system	AC	0.12	0.12	0.12	0.12	0.12	0.12	0.12
Avionics	Anti-collision beacons & ice inspection lights	DC	0.6	0.6	0.6	0.6	0.6	0.6	0.6
Avionics	Cabinet & switch	DC	3.05	3.05	3.05	3.05	3.05	3.05	3.05
Avionics	Communication (HF/VHF) & satellite system	DC	4.3	4.3	4.3	4.3	4.3	4.3	4.3
Avionics	Display units (heater on/off & head-up)	DC	0.49	0.49	0.49	0.49	0.49	0.49	0.49
Avionics	Distance measuring equipment	DC	0.06	0.06	0.06	0.06	0.06	0.06	0.06
Avionics	Electric load management center & PPDU	DC	2.2	2.2	2.2	2.2	2.2	2.2	2.2
Avionics	Electronic equipment cooling	AC	6	6	6	6	6	6	6
Avionics	Emergency lights	DC	0.2	0	0	0	0	0	0.2
Avionics	Enhanced ground proximity warning system	DC	0	0.5	0.5	0.5	0.5	0.5	0
Avionics	Flight data record unit	DC	0.2	0.2	0.2	0.2	0.2	0.2	0.2
Avionics	Fire protection system	DC	0.4	0.4	0.4	0.4	0.4	0.4	0.4
Avionics	GCU1/GCU2/AGCU/EPMU/EGCU	DC	1	1	1	1	1	1	1
Avionics	GPS/ILS/ADF/VOR/marker receivers	AC	0.22	0.22	0.22	0.22	0.22	0.22	0.22
Avionics	Nacelle anti-icing valves & switches	DC	0	0.08	0.08	0.08	0.08	0	0
Avionics	Navigation & landing/taxiing lights	DC	1.05	0.2	0.2	0.2	0.2	1.05	1.05
Avionics	Pump, valves	DC	3	12	12	12	12	12	3
Avionics	Recirculation fan	AC	6.3	0	6.3	6.3	6.3	0	6.3
Avionics	Traffic collision avoidance system	DC	0	0.3	0.3	0.3	0.3	0.3	0
Avionics	Weather radar	DC	0	0	0.8	0.8	0.8	0	0
Avionics	Window heat computer & ice detectors	AC	0.31	0.31	0.31	0.31	0.31	0.03	0.31
Avionics	Windshield wiper	DC	0.9	0.9	0.9	0.9	0.9	0.9	0.9
Avionics	Wing de-icing computer & temperature sensors	DC	0.09	0.09	0.09	0.09	0.09	0.09	0.09
Cabin equipment	Coffee kettle/chiller/oven (galleys)	AC	0	0	0	25.4	0	0	0

Subsystem	Equipment	AC/DC	Taxi-out	Take-off	Climb	Cruise	Descent	Landing	Taxi-in
Cabin equipment	Evacuation equipment	DC	1	0	0	0	0	0	1
Cabin equipment	Heat (lavatory)	AC	0	0	0	5	0	0	0
Cabin equipment	Light	DC	1.5	1.5	1.5	1.5	1.5	1.5	1.5
Cabin equipment	Passenger entertainment system	AC	5	5	5	5	5	5	5
Cabin equipment	Waste water master heater	AC	0	0	0	12.5	0	0	0
		Total AC [kVA]	*19.80*	*12.50*	*18.80*	*61.70*	*18.80*	*12.50*	*19.80*
		Total DC [kVA]	*29.09*	*45.23*	*42.03*	*41.43*	*44.03*	*52.12*	*29.09*
		Total [kW]	**48.89**	**57.73**	**60.83**	**103.13**	**62.83**	**64.62**	**48.89**

A.2 Validation of Shaft Power Off-Takes

To validate the acquired values, the shaft power off-takes of the conventional setup are compared to actual flight data from Hamburg to Toulouse with an Airbus A320. The results are summarised in Table A.3; only the data for the climb, cruise and descent phases swill be compared due to its availability.

Table A.3: Data validation of shaft power off-takes; comparison between estimated and actual power requirements [62].

Description	**Climb**	**Cruise**	**Descent**	**Average**
Estimated values [kW]	60.83	103.13	62.83	75.60
Actual flight data [kW] [62]	83.50	79.00	68.60	77.03
Relative difference	*-27.15%*	*30.55%*	*-8.41%*	*-1.86%*
Description	**Climb**	**Cruise**	**Descent**	**Total**
Segment duration [s]	1,286	2,366	1,143	4,795
Energy used [MJ]	78.23	244.01	71.82	394.05
			Weighted average [kW]	82.18
			Relative weighted difference	**6.68%**

As can be seen from Table A.3, the relative difference of the individual segments is quite large, ranging between -27.15% and 30.55%. If the relative difference of the average power is taken, the offset reduces to an acceptable value of -1.86%. Unfortunately, this is not an accurate representation since the mission segments have varying time durations. A weighted average is calculated by multiplying the power with the segment duration and dividing the total energy by the total duration of the three segments. The resulting difference becomes 6.68%, which is sufficiently accurate for this study. This allows the power requirements stated in Table 3.3 and Table 3.4 to be used.

A.3 Electrical Architecture of A320neo

The electrical power requirements for the electrical architecture of the A320neo are mainly deduced from Ref. [33]. This report describes the load breakdown of a similar-sized aircraft, '*The Flying Crane*'. This aircraft is a 150-seater more electric aircraft for short- and medium-range flights throughout Asia and features near-identical aircraft characteristics. This allows the electrical power requirements to be extracted for the Airbus A320neo. Again, a power factor of 1 is assumed. The electrical power requirements for the various subsystems throughout flight are summarised in Table A.4. A detailed overview of the available aircraft equipment is presented in Table A.5.

Table A.4: Electrical power requirements for electrical architecture of Airbus A320neo; adapted from [33, 36].

Subsystem	Taxi-out	Take-off	Climb	Cruise	Descent	Landing	Taxi-in
Actuation	12.89	43.48	35.48	34.28	35.48	16.74	12.89
Avionics	41.59	34.13	41.23	41.23	51.23	47.92	41.59
Cabin equipment	7.50	6.50	6.50	49.40	6.50	6.50	7.50
ECS	135.00	5.00	125.00	130.40	125.00	5.00	135.00
IPS	4.33	8.23	26.29	26.29	26.29	0.00	4.33
Landing gear	5.10	3.80	0.00	0.00	0.00	31.20	5.10
Total AC [kVA]	*22.44*	*28.04*	*44.40*	*87.30*	*44.40*	*24.84*	*22.44*
Total DC [kVA]	*183.97*	*73.10*	*190.10*	*194.30*	*200.10*	*82.52*	*183.97*
Total [kW]	**206.41**	**101.14**	**234.50**	**281.60**	**244.50**	**107.36**	**206.41**

Table A.5: Detailed electrical power requirements for electrical architecture of Airbus A320neo in [kW]; adapted from [33, 36].

Subsystem	Equipment	AC/DC	Taxi-out	Take-off	Climb	Cruise	Descent	Landing	Taxi-in
Actuation	Aileron actuators	DC	0	3.52	3.52	3.52	3.52	3.52	0
Actuation	Cargo door actuator	DC	2	0	0	0	0	0	2
Actuation	Elevator actuators	DC	2.51	6.8	6.8	6.8	6.8	6.8	2.51
Actuation	High lift actuators	DC	6.76	19.2	19.2	0	19.2	19.2	6.76
Actuation	Horizontal stabiliser	DC	0	1.56	1.56	1.56	1.56	1.56	0
Actuation	Landing gear actuator	AC	0	8	0	0	0	8	0
Actuation	Rudder actuators	DC	1.62	4.4	4.4	4.4	4.4	4.4	1.62
Actuation	Spoilers actuators	DC	0	0	0	18	0	0	0
Avionics	Actuator control electronics	DC	1	1	1	1	1	1	1
Avionics	Air data inertial reference system	AC	0.12	0.12	0.12	0.12	0.12	0.12	0.12
Avionics	Anti-collision beacons & ice inspection lights	DC	0.6	0.6	0.6	0.6	0.6	0.6	0.6
Avionics	APU starter	DC	10	0	0	0	10	0	10
Avionics	Cabinet & switch	DC	3.05	3.05	3.05	3.05	3.05	3.05	3.05
Avionics	Communication (HF/VHF) & satellite system	DC	4.3	4.3	4.3	4.3	4.3	4.3	4.3
Avionics	Display units (heater on/off & head-up)	DC	0.49	0.49	0.49	0.49	0.49	0.49	0.49
Avionics	Distance measuring equipment	DC	0.06	0.06	0.06	0.06	0.06	0.06	0.06
Avionics	Electric load management center & PPDU	DC	2.2	2.2	2.2	2.2	2.2	2.2	2.2
Avionics	Electronic equipment cooling	AC	6	6	6	6	6	6	6
Avionics	Emergency lights	DC	0.2	0	0	0	0	0	0.2
Avionics	Enhanced ground proximity warning system	DC	0	0.5	0.5	0.5	0.5	0.5	0
Avionics	Flight data record unit	DC	0.2	0.2	0.2	0.2	0.2	0.2	0.2
Avionics	Fire protection system	DC	0.4	0.4	0.4	0.4	0.4	0.4	0.4
Avionics	GCU1/GCU2/AGCU/EPMU/EGCU	DC	1	1	1	1	1	1	1
Avionics	GPS/ILS/ADF/VOR/marker receivers	AC	0.22	0.22	0.22	0.22	0.22	0.22	0.22
Avionics	Nacelle anti-icing valves & switches	DC	0	0.08	0.08	0.08	0.08	0	0
Avionics	Navigation & landing/taxiing lights	DC	1.05	0.2	0.2	0.2	0.2	1.05	1.05
Avionics	Pump, valves	DC	3	12	12	12	12	12	3

Subsystem	Equipment	AC/DC	Taxi-out	Take-off	Climb	Cruise	Descent	Landing	Taxi-in
Avionics	Recirculation fan	AC	6.3	0	6.3	6.3	6.3	0	6.3
Avionics	Thrust reverser	AC	0	0	0	0	0	13.3	0
Avionics	Traffic collision avoidance system	DC	0	0.3	0.3	0.3	0.3	0.3	0
Avionics	Weather radar	DC	0	0	0.8	0.8	0.8	0	0
Avionics	Window heat computer & ice detectors	AC	0.31	0.31	0.31	0.31	0.31	0.03	0.31
Avionics	Windshield wiper	DC	0.9	0.9	0.9	0.9	0.9	0.9	0.9
Avionics	Wing de-icing computer & temperature sensors	DC	0.09	0.09	0.09	0.09	0.09	0.09	0.09
ECS	Motor (compressor) & miscellaneous	DC	115	5	115	120.4	115	5	115
ECS	Ram air fan	DC	20	0	10	10	10	10	20
Cabin equipment	Coffee kettle/chiller/oven (galleys)	AC	0	0	0	25.4	0	0	0
Cabin equipment	Evacuation equipment	DC	1	0	0	0	0	0	1
Cabin equipment	Heat (lavatory)	AC	0	0	0	5	0	0	0
Cabin equipment	Light	DC	1.5	1.5	1.5	1.5	1.5	1.5	1.5
Cabin equipment	Passenger entertainment system	AC	5	5	5	5	5	5	5
Cabin equipment	Waste water master heater	AC	0	0	0	12.5	0	0	0
IPS	Fixed window heat elements	AC	1.86	1.86	1.86	1.86	1.86	1.86	1.86
IPS	Sliding window heat elements	AC	1.17	1.17	1.17	1.17	1.17	1.17	1.17
IPS	Windshield heat elements	AC	1.3	5.2	5.2	5.2	5.2	5.2	1.3
IPS	Wing de-icing heat elements	AC	0	0	18.07	18.07	18.07	18.07	0
Landing gear	Braking system	DC	5	0	0	0	0	0	5
Landing gear	Nose wheel steering system	DC	3.8	0	0	0	0	0	0
Landing gear	Parking brake	DC	0.1	0	0	0	0	0	0.1
		Total AC [kVA]	*22.44*	*28.04*	*44.40*	*87.30*	*44.40*	*24.84*	*22.44*
		Total DC [kVA]	*183.97*	*73.10*	*190.10*	*194.30*	*200.10*	*82.52*	*183.97*
		Total [kW]	**206.41**	**101.14**	**234.50**	**281.60**	**244.50**	**107.36**	**206.41**

APPENDIX B

Energy Storage Capacity of A320neo

B.1 Energy Storage Options

The main energy carrier on the Airbus A320neo is kerosene, e.g. Jet A-1, stored in the fuel tanks located in the body and wings of the aircraft. The fuel tank capacities of the A320neo are presented in Table B.1.

Table B.1: Fuel tank distribution of the Airbus A320neo [59].

Tank	Usable fuel [L]	Unusable fuel [L]
Wing	15,476.7	58.9
Center	8,248	23.2
Total	**23,724.7**	**82.1**

Aside from jet fuel, there are two 28V 23 Ah DC batteries present in the electronics and engineering (E & E) bay underneath the cockpit area; this compartment contains sensitive electrical systems such as avionics. These batteries are used as back-up power sources to supply vital loads during emergency situations [33, 127]. On the occasion that fuel cells, hydrogen tanks and supplementary batteries are installed for the electrically assisted propulsion & power system (EAPPS), these devices can be established in the E & E bay.

B.2 Excess Volume in E & E Bay

To ensure that there is enough space for the new EAPPS equipment, the available space of this E & E bay will be approximated. Figure B.1 shows the dimensions of the compartment; the values are estimated using an image tracer [128].

Since this section is curved, the mean values of the front and back sheets are used. Assuming the section curvature is elliptical, the mean major and minor radii, a_{mean} and b_{mean}, can be calculated using Equation B.1 and Equation B.2, accordingly.

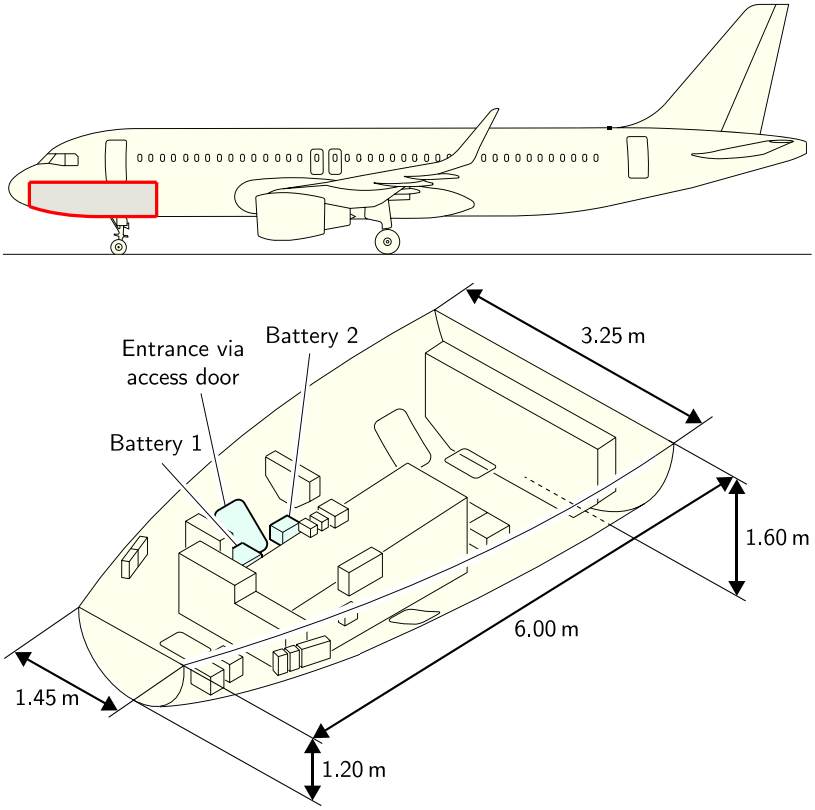

Figure B.1: Location of the E & E bay, including estimated dimensions; adapted from [4].

$$a_{mean} = \frac{a_{front} + a_{back}}{2} \tag{B.1}$$

$$b_{mean} = \frac{b_{front} + b_{back}}{2} \tag{B.2}$$

Inserting $a_{front} = 0.725$ m, $a_{back} = 1.625$ m, $b_{front} = 1.20$ m and $b_{back} = 1.60$ m into Equation B.1 and Equation B.2, the semi major and minor axes become 1.175 m and 1.40 m, respectively. Now, the volume of the E & E compartment can be determined using Equation B.3:

$$V_{EEbay} = \frac{\pi}{2} \cdot a_{mean} \cdot b_{mean} \cdot L_{EEbay} \tag{B.3}$$

where the compartment length L_{EEbay} equals 6.00 m; the resulting volume is 15.5 m^3 or 15,500 L. Assuming a fill factor of 30% due to existing hardware and reserved space for walking, the excess volume becomes 10.85 m^3 or 10,850 L.

B.3 Total Energy Storage Required

Before estimating the total capacity needed, the volumetric density of hydrogen need to be known. The two most favourable architectures currently are based on pressurised and cryogenic tanks for hydrogen supply [129]; the volumetric densities of compressed hydrogen at 350 bar, at 700 bar and liquefied hydrogen are 25 g/L, 40 g/L and 70 g/L, respectively [130]. These values include the volume of the

tanks to store the hydrogen fuel. The important parameters of the EAPPS configurations for near future (2020+) and far future (2040+) scenarios are summarised in Table B.2; these are extracted from Section 6.4.1 and Section 6.4.2.

Table B.2: Overview of essential parameters for energy storage estimations.

Parameter	Near future (2020+)	Far future (2040+)
Number of batteries [-]	130,782	414,007
Installed battery energy [kWh]	1,437.29	4,550.88
Fuel cell system power [kW]	200	200
Hydrogen consumed [kg]	22.397	22.397

Using the dimensions of the Panasonic NCR20700A battery mentioned in the manufacturer's data sheet [117], the energy density can be calculated. This results in a value of 480.7 Wh/L or $22.865 \cdot 10^{-3}$ L per cell for 2020+. Assuming that by 2040+ the battery will improve in terms of mass but also in size, a battery volume reduction of 10% is taken into account. Since Panasonic NCR20700A battery cells are circular in shape, assembling the packs will leave gaps in between the cells such as shown in Figure B.2.

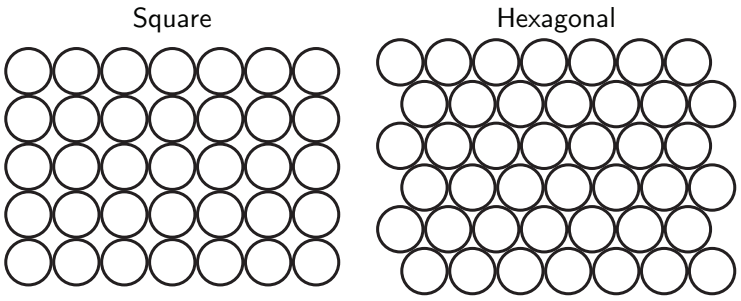

Figure B.2: Two types of battery packing arrangements: square (left) and hexagonal (right).

Square and hexagonal packing are the two most common ways to arrange identical circles in a two-dimensional plane. The latter results in the smallest battery pack and will be preferred over square packing. The packing density of the hexagonal lattice η_h is equal to $\frac{1}{6}\pi\sqrt{3}$ or approximately 0.9069. Assuming the power densities of the fuel cell system as listed in Table 3.15, the total capacity required for each storage option and time frame is outlined in Table B.3.

Table B.3: Total capacity required for each case in 2020+ and 2040+.

Volume [L]	Near future (2020+)			Far future (2040+)		
Battery pack	3297.3			9394.3		
Fuel cell system	585			409.5		
Hydrogen storage option	*25 g/L*	*40 g/L*	*70 g/L*	*25 g/L*	*40 g/L*	*70 g/L*
Hydrogen tank	895.9	559.9	320.0	895.9	559.9	320.0
Total capacity [L]	4,778.2	4,442.3	4,202.3	10,699.7	10,363.7	10,123.8

From the results in Table B.3 can be concluded that no particular case exceeds the available volume of 10,850 L; there is sufficient space on the Airbus A320neo to accommodate the batteries and fuel cell system, along with its hydrogen storage. In case the aircraft centre of gravity significantly shifts forwards, the balance can be restored by moving the bulk of the batteries towards the cargo bay and aircraft wings.

APPENDIX C

Effective PV Surface Area of A320neo

C.1 Estimation Procedure

One of the main parameters for installing PV panels on an aircraft is the total surface area that can be utilised. Based on a top view image of the Airbus A320neo, as shown in Figure C.1, the surface areas of the wings, fuselage, tailplane and various control surfaces are approximated using an area calculator [128]. Assuming that the panels will not be installed on any movable control surfaces, the corresponding values are substracted from the wing and tailplane surface areas. Lastly, the effective areas for the wings, tailplane and fuselage are summed to obtain the total effective surface area.

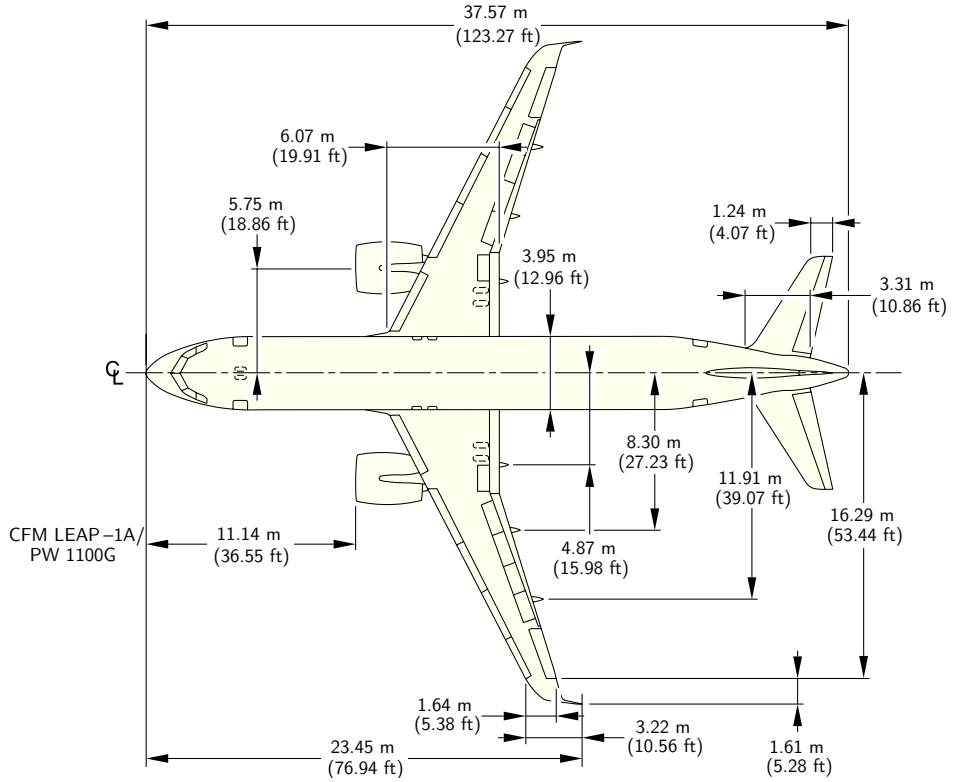

Figure C.1: Top view of the Airbus A320neo, including general dimensions [4].

C.1.1 Aircraft Anatomy

Figure C.2 shows the main parts of the aircraft, with the primary and secondary flight control surfaces. The flight control surfaces include the ailerons, elevators, rudder, flaps, slats and spoilers.

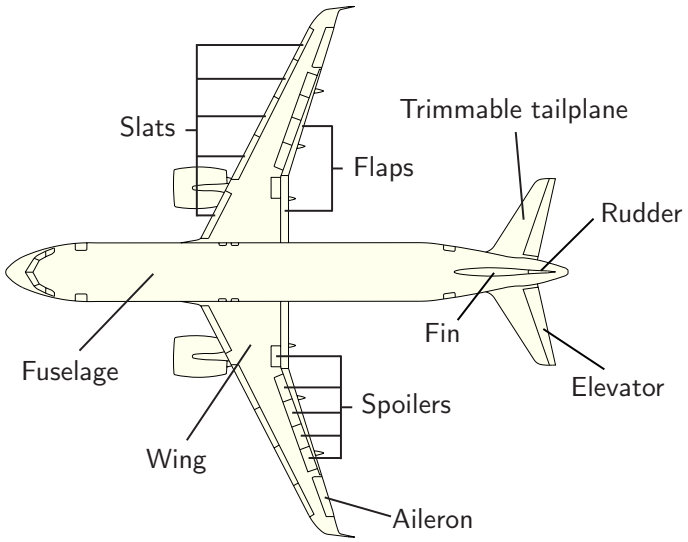

Figure C.2: Aircraft anatomy of Airbus A320neo; adapted from [4].

C.1.2 Wings

The estimated surface areas of the wings and control surfaces are summarised in Table C.1. The total effective wing area $S_{wing,eff}$ equals 69.14 m^2.

Table C.1: Estimated surface areas of wings and control surfaces.

Surface	Area [m^2]
Single wing	52.47
Aileron	1.71
Flaps	4.46
Slats	5.95
Spoilers	5.78
Effective single wing	34.57
Total effective wings	**69.14**

C.1.3 Tailplane

The estimated surface areas of the tailplane and elevators are summarised in Table C.2. The total effective tailplane area $S_{tail,eff}$ equals 16.76 m^2.

Table C.2: Estimated surface areas of tailplane and elevators.

Surface	Area [m^2]
Single tailplane	12.21
Elevator	3.83
Effective single tailplane	8.38
Total effective tailplane	**16.76**

C.1.4 Fuselage

The effective fuselage area can be calculated by multiplying the effective fuselage length by the length of the curvature. This equation becomes:

$$S_{fuse,eff} = L_{fuse,eff} \cdot L_{curve} \tag{C.1}$$

The effective fuselage length $L_{fuse,eff}$ is defined as the distance between the first and last cabin door, as shown in Figure C.3.

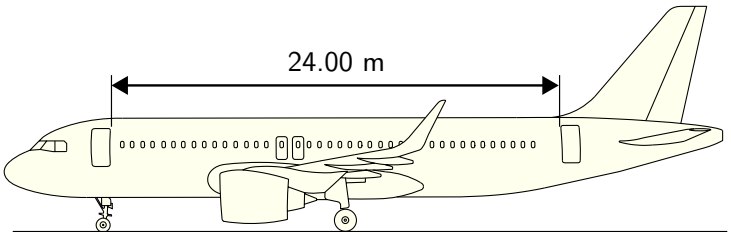

Figure C.3: Side view of the fuselage; adapted from [4].

The length of the curvature L_{curve} is defined as the upper half of the fuselage cross-section. It is assumed that the area below the passenger windows will not be used; it complicates the installment of PV and will not generate significant power as the tilt angle is nearly parallel towards the Sun. Figure C.4 indicates the (dashed) arc length that needs to be determined.

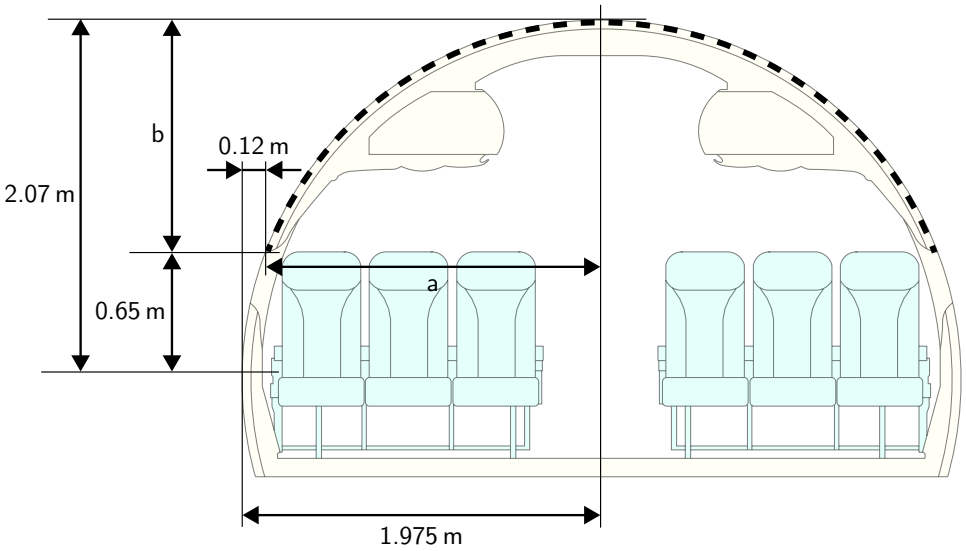

Figure C.4: Cross-sectional view of the fuselage; adapted from [4].

Assuming that the curvature is half elliptical, the following equations may be used:

$$h = \frac{(a-b)^2}{(a+b)^2} \tag{C.2}$$

$$L_{curve} \approx \frac{\pi}{2}(a+b)\left(1 + \frac{3h}{10+\sqrt{4-3h}}\right) \tag{C.3}$$

Substituting $a = 1.855$ m and $b = 1.42$ m into Equation C.2 and Equation C.3, the curvature length L_{curve} becomes 5.1671 m. Inserting $L_{curve} = 5.1671$ and $L_{fuse,eff} = 24$ into Equation C.1, the effective fuselage area $S_{fuse,eff}$ becomes 124.01 m^2.

C.1.5 Total Effective Surface Area of A320neo

The total effective surface area can be expressed as follows:

$$S_{pv,eff} = S_{wing,eff} + S_{tail,eff} + S_{fuse,eff} \tag{C.4}$$

Substituting the values from previous sections, the effective surface area available for PV installation on the A320neo equals 209.91 m^2. An impression of the Airbus A320neo in the specified PV arrangement is depicted in Figure C.5.

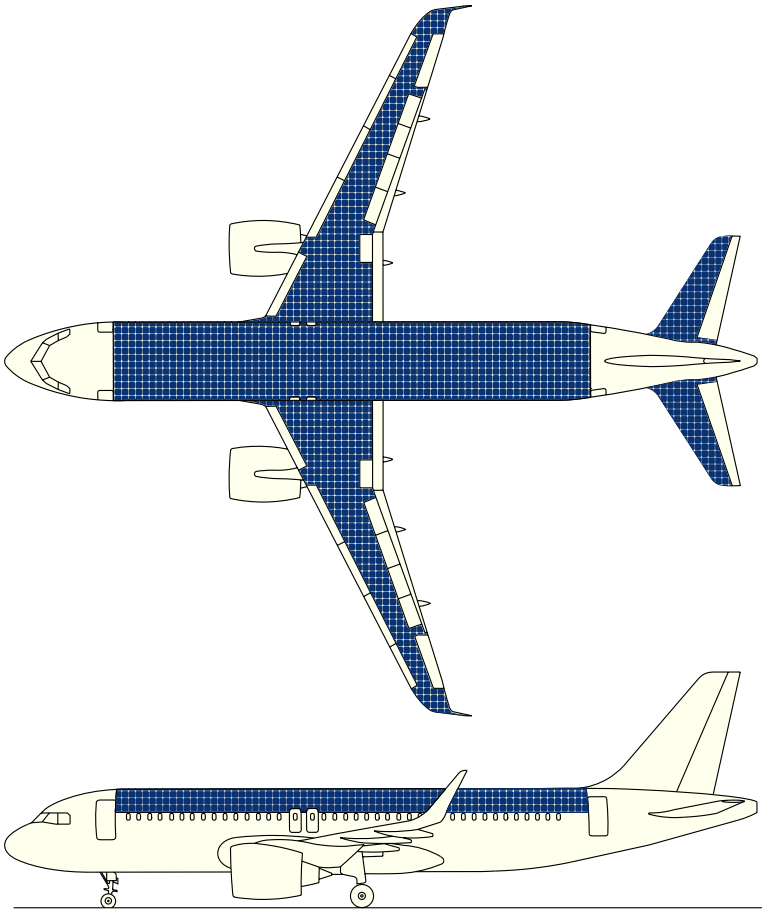

Figure C.5: Airbus A320neo covered in PV panels; adapted from [4].

APPENDIX D

Environmental Impact Assessment

This chapter gives additional insights into the commercial viability of electrically assisted propulsion & power systems (EAPPS) and serves as a project deliverable, as part of pursuing the graduation annotation 'Technology in Sustainable Development (TiSD)'. To avoid any currency conversion, all costs will be expressed in U.S. dollars (US$) for the sake of convenience.

D.1 Operational Energy Cost Analysis of a Single A320neo Flight

In order to evaluate the commercial viability of EAPPS, the operating energy costs will be investigated for the reference and optimised EAPPS setups, in the near future (2020+) as well as in the far future (2040+). These costs will be estimated for a single flight. The total operating costs (TOC) are all the costs incurred while operating an airplane and consists of direct operating costs (DOC) and indirect operating costs (IOC); the to-be-estimated costs will only cover a part of the DOC, which also include the cost of maintenance, depreciation and wages of the flight crew [131].

The three distinguishable energy carriers in this study are kerosene (e.g. Jet A-1), hydrogen and electricity. The fuel economies as well as the electricity market are affected by the laws of supply and demand; fluctuations in fuel and electricity prices are commonly seen.

The kerosene prices will be based on short term forecasts by Airbus [132] and the hydrogen prices on near term projections by National Renewable Energy Laboratory (NREL) using the ARB Vision model, which is a scenario planning tool developed by California Air Resources Board. These fuel prices are projected for a period from 2015 to 2025, as shown in Table D.1, and can be extended to the far future (2040+) using linear regression analysis.

Table D.1: Kerosene and hydrogen price predictions by Airbus and NREL [132, 133].

Parameter	2015	2016	2017	2018	2019	2020	2021	2022	2023	2024	2025
Kerosene [$/gal]	1.52	1.25	1.63	1.63	1.86	2.27	2.41	2.53	2.59	2.71	2.76
Hydrogen [$/kg]	14.00	13.71	13.42	13.13	12.85	12.56	12.27	11.98	11.69	11.40	11.11

Figure D.1a shows the linear price trend for jet fuel from 2015 to 2045 in US$. Although the progression in data points suggests that a price ceiling might be expected, former kerosene prices (prior to 2015) have reached as high as $3.89 per gallon; this implies that the price for kerosene is unpredictable. For

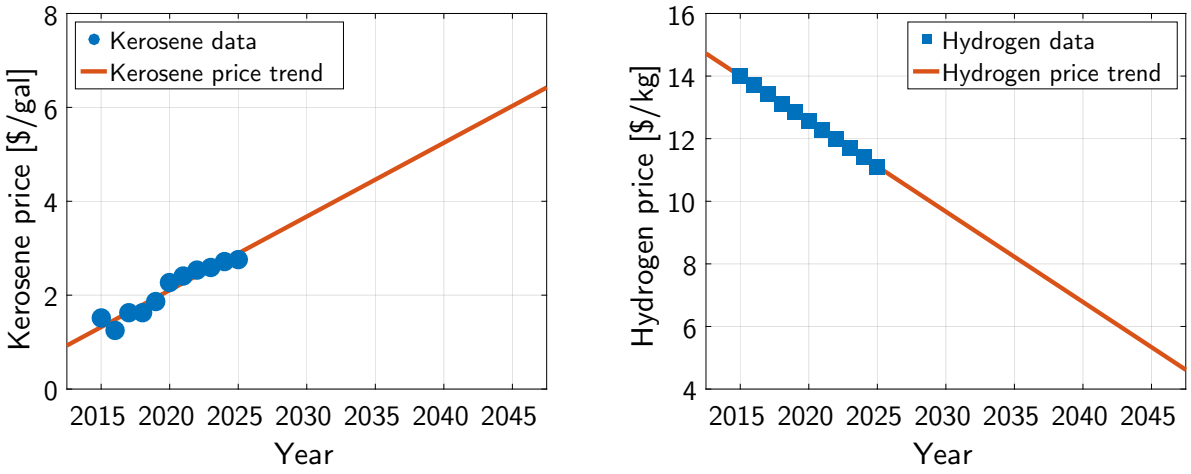

(a) For kerosene [132]. **(b)** For hydrogen [133].

Figure D.1: Fuel price trends based on short term projection data: for kerosene (left) and for hydrogen (right).

simplicity reasons, a linear trend is assumed within this study; the price of kerosene is expected to increase, as the availability of fossil fuels will decline. On the other hand, the price for the alternative fuel hydrogen is predicted to drop significantly, as illustrated in Figure D.1b; new and more efficient ways to produce hydrogen will become available, which in turn drive down the costs and ultimately allow hydrogen to compete with traditional transportation fuels. In 2020, the kerosene and hydrogen prices are $2.27 per gallon and $12.56 per kg, respectively. By 2040, the kerosene price increases to $5.25 per gallon, while the cost for hydrogen decreases to $6.84 per kg.

The projected electricity prices are derived from an annual energy outlook report by the U.S. Energy Information Administration (EIA) [134] and summarised in Table D.2. The prices are categorised in generation, transmission and distribution costs. The total price will remain relatively flat, ranging between 10.55 and 11.23 dollar cents per kilowatt hour. The generation costs remain the largest share of the price and will decrease by 10% due to continued low natural gas prices and increased generation from renewables. The transmission and distribution costs will increase by around 25%, indicating the need to replace ageing infrastructure and improve the grid to accommodate changing reliability standards [134].

Table D.2: Future electricity price predictions by EIA [134].

Electricity price	**2017**	**2020**	**2030**	**2040**	**2050**
Generation [$/kWh]	0.0625	0.0632	0.0596	0.0574	0.0562
Transmission [$/kWh]	0.0132	0.0144	0.0157	0.0165	0.0164
Distribution [$/kWh]	0.0298	0.0316	0.0370	0.0380	0.0373
Total [$/kWh]	0.1055	0.1092	0.1123	0.1119	0.1099

Table D.3 shows the three different cases to be analysed: the reference Airbus A320neo without HEPS and the two A320neo configurations with optimised EAPPS (including all three modifications and scaled engine) for near future (2020+) and far future (2040+).

By applying the aforementioned price predictions (for 2020 and 2040) to the consumption values in Table D.3, the average energy costs per flight can be determined. The total operating costs for the

Table D.3: Overview of three cases with varying energy consumption (kerosene, hydrogen and electricity).

Configuration	Kerosene [kg]	H_2 [kg]	Electricity [kWh]
Reference A320neo without HEPS	3944.29	0	0
A320neo with EAPPS (Section 6.5.1)	3283.23	22.397	1437.294
Future A320neo with EAPPS (Section 6.5.2)	2834.49	22.397	4550.882

reference and the EAPPS-integrated A320neo, in terms of energy consumed, are illustrated in Figure D.2 for both time frames.

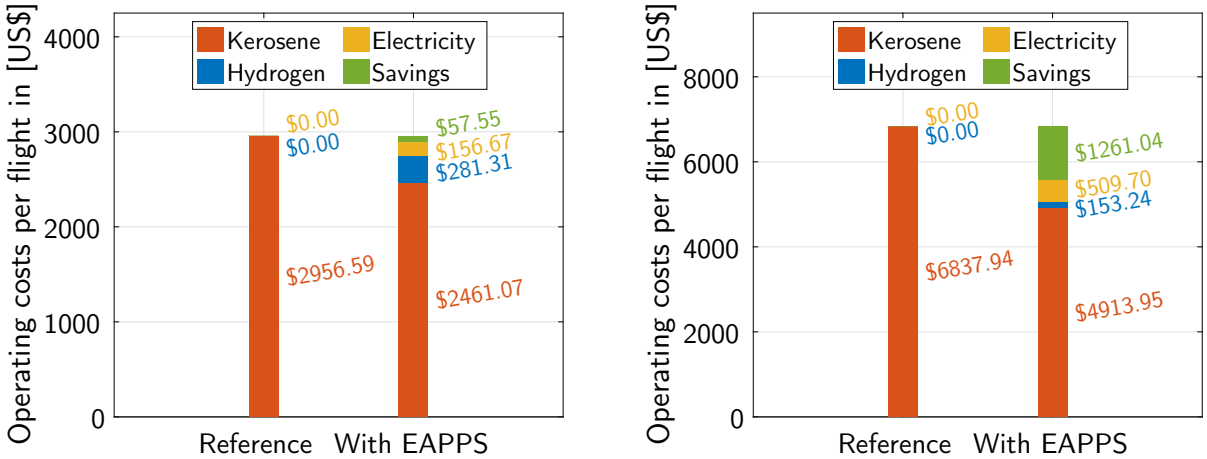

(a) Near future (2020). **(b)** Far future (2040).

Figure D.2: Total operating costs per flight determined by energy consumption, for two different time frames: 2020 (left) and 2040 (right).

Figure D.2a and Figure D.2b present the total operating energy costs for near term (2020) and far term (2040), respectively. A noticeable difference is the amount of dollars saved per flight: \$57.55 in 2020 versus \$1261.04 in 2040. This contrast is largely due to the huge rise in kerosene price; a price increase of 131.3% is expected, as depicted in Figure D.1 earlier. Also, the electricity costs has tripled from \$156.67 to \$509.70 due to the increased use of HEPS. While the hydrogen consumption remains the same, the costs will be cut nearly in half from \$281.31 to \$153.24 due to expected technological advancements in hydrogen production.

A more common definition regarding costs is the fuel costs per available seat mile (ASM). It reflects the fuel costs incurred by an airline to fly a single seat one mile. This number is displayed in Figure D.3 for the two different setups in 2020 and 2040.

As a measure for comparison, the average fuel costs of single-aisle airliners across the U.S. fleet were \$0.021/ASM in 2016 [135]. The reference fuel costs per ASM in 2020 become \$0.015/ASM, adjusted to the fuel price in 2016. This significant difference in costs can be explained by the large range of mission duration and seating arrangements. Although this study is defined by a flight mission of 1,000 km and 190 available seats, this can vary greatly among different airlines. Operators which mainly fly popular long-distance routes and low-cost carriers which maximise the number of seats will bring the average fuel costs per ASM down, while regional operators which fly shorter distances with empty seats may push that average back up. The actual fuel costs for a similar flight as performed in this study are not known.

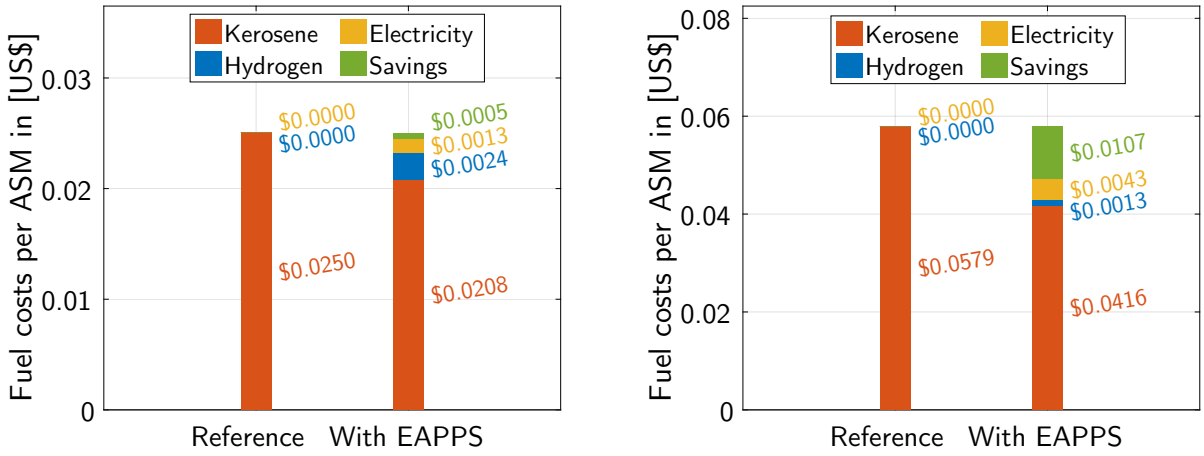

(a) Near future (2020). **(b)** Far future (2040).

Figure D.3: Fuel costs per available seat mile (ASM) for two different time frames: 2020 (left) and 2040 (right).

Another interesting perspective is to look at the relative fractions regarding energy provided and predicted costs for the two different EAPPS setups in 2020 and 2040. The results are presented in Figure D.4.

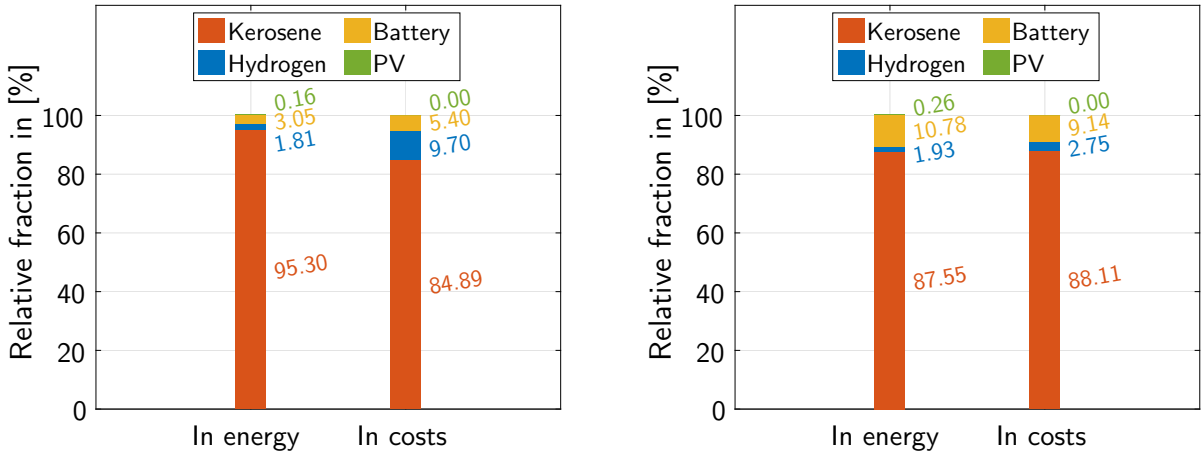

(a) Near future (2020). **(b)** Far future (2040).

Figure D.4: Relative fractions in terms of energy provided and predicted costs for the two optimised EAPPS setups in different time frames: 2020 (left) and 2040 (right).

Observing Figure D.4a more closely, it is noticeable that making use of batteries and hydrogen to provide energy is simply not as cost-effective as using kerosene. This is because the prices for electricity and especially for hydrogen are relatively high compared to the kerosene price. In 2040, the energy-costs proportions are much more balanced, as indicated in Figure D.4b. By then, with exclusion of photovoltaics (PV), the batteries have become the most cost-effective method to provide energy.

Nevertheless, from an operational energy point of view, cost savings can be realised in both time frames by applying EAPPS; albeit more balanced and efficient in the far future (2040) than in the near future (2020) due to the huge differences in fuel prices. Keep in mind that, next to lower energy costs, these setups also emit substantially less pollutants than their reference counterparts, as indicated in Table 6.9.

D.2 ROI Performance of PV Systems in Commercial Aircraft

To prove the viability of photovoltaics on commercial aircraft, the total costs to install, operate and maintain the solar skin will be investigated in more detail. This cost analysis assumes that HEPS is already integrated into the aircraft, thus additional batteries for the PV system are not required.

The total costs consist of the initial investment costs for the system itself, the installation costs and the recurring operations and maintenance (O&M) costs. The initial investment costs include the monocrystalline Maxeon Gen III cells (12,420 units) and a set of solar inverters to take care of power conversion and maximum power point tracking (MPPT); the prices are described in Table D.4. Keep in mind that the expected lifetime of PV cells is at least 20 years, so system components such as inverters are often offered with warranties of up to 20 years; additional PV hardware investments are seldom necessary.

Table D.4: Prices for individual PV components [136–138].

Parameter	Price [$]
Maxeon Gen III Ultra Premium Performance (high quality)	$5.10/unit
Enphase Energy IQ6-60 micro-inverter 240W	$120/unit
Four Star Solar MC4 10 AWG PV wire	$3.28/m

The whole PV system is made of 23 PV strings in parallel, where one string is formed by connecting 9 PV modules in series. Each PV module contains 60 Maxeon Gen III cells in series and is rated at 224W. To ensure independent use between modules, a micro-inverter is required for each module. Also, based on an estimation using Figure C.1, approximately 160 metres of MC4 cables is needed to connect the micro-inverters. According to Ref. [139], the installation costs account for 9% of the initial costs for a commercial PV system up to 200 kW; in this case, the installation costs become $8,773.20. The total investment costs are summarised in Table D.5.

Table D.5: Initial investment costs for installing a complete PV system on the A320neo aircraft.

Parameter	Costs [$]
Single PV module (60 Maxeon Gen III cells)	*$306*
Single PV string (9 modules)	*$2,754*
Complete PV array (23 strings)	*$63,342*
Set of micro-inverters (9 x 23 = 207 units)	*$24,840*
PV wiring (160 metres)	*$524.80*
Total PV hardware	$88,706.80
Installation labor (9% of initial costs)	$8,773.20
Total investment	**$97,480**

The recurring costs are based on average utility-scale O&M costs of a solar PV plant; for monocrystalline, the average is $20.50 per kilowatt-peak per year [140]. With a single Maxeon Gen III cell generating 3.63 Wp [119], the total PV system of 12,420 cells will amount to 45.09 kWp; this suggests that the recurring costs are $924.23 annually.

By using the data for fuel and energy saved from Table 6.3 and Table 6.4 (for 2020+), the savings per flight can be calculated with the price data in Table D.1 and Table D.2. For example, in 2020, the fuel and energy savings become 0.879/(0.8*3.785)*2.27 = $0.66/flight and 96.24*0.1092 = $10.51/flight, respectively, totalling $11.17 saved per flight; this procedure can be repeated for each year with the

predicted prices. Assuming that the average daily number of flights performed per aircraft is 6[1], an aircraft will complete a total of 2,190 flights per year. A cost breakdown chart of a PV system on a commercial aircraft throughout a period of 20 years is shown in Figure D.5 for a flight mission from Guayaquil to Bogota.

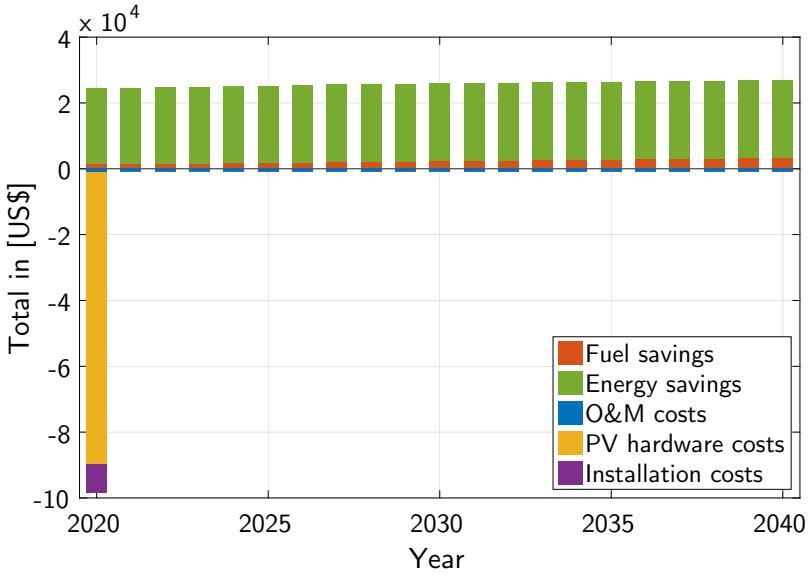

Figure D.5: Cost breakdown of a PV-integrated aircraft designed for a flight mission from Guayaquil to Bogota throughout a period of 20 years.

Then, the ROI performance of the PV system can be determined by mapping out the cumulative costs and savings over a time span of 20 years; this is plotted in Figure D.6 and Figure D.7 for the three selected flight missions, projected from 2020 to 2040 and 2040 to 2060, respectively.

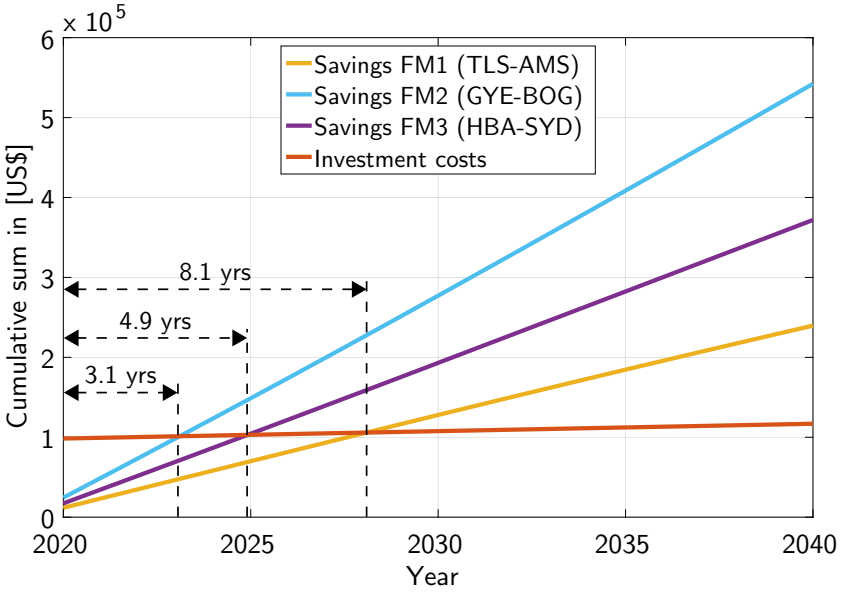

Figure D.6: ROI performance of PV systems for three different flight missions from 2020 to 2040: Toulouse - Amsterdam (yellow), Guayaquil - Bogota (light blue) and Hobart - Sydney (purple).

[1] The daily utilisation rate or the average daily hours flown of a single-aisle airliner like the A320neo aircraft across major airlines in the United States is 9.78 hours in 2016 [135]. Assuming 6 flights of around 1.5 hours per day, the daily utilisation rate within this study equals 9 hours; in comparison to the average of 9.78 hours, the chosen number is conservative.

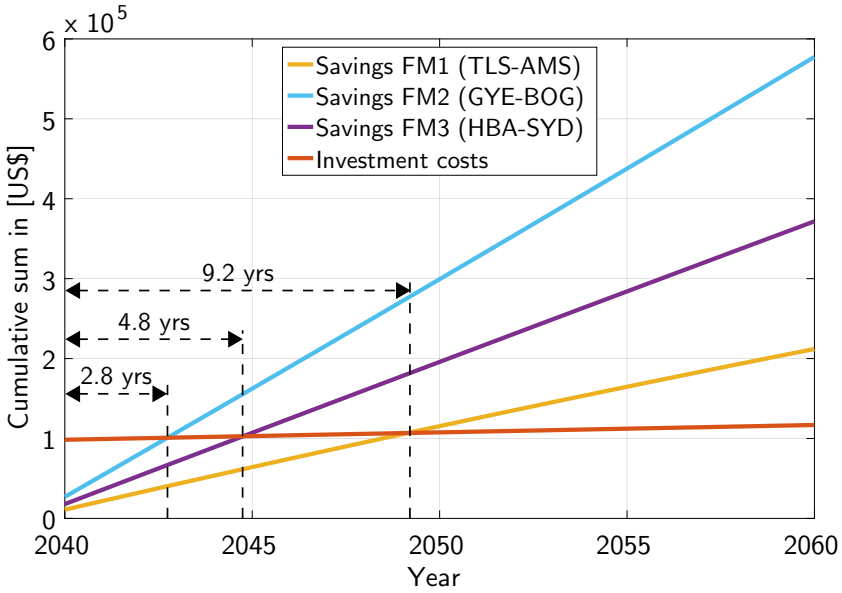

Figure D.7: ROI performance of PV systems for three different flight missions from 2040 to 2060: Toulouse - Amsterdam (yellow), Guayaquil - Bogota (light blue) and Hobart - Sydney (purple).

Figure D.6 and Figure D.7 demonstrate that the investment costs of installing a PV system will eventually be earned back for all three missions. The payback period (PP) and resulting net profits, however, vary for each mission and time period; these values are tabulated in Table D.6.

Table D.6: ROI PV performance results for three different flight missions in the near future (2020+) and the far future (2040+): Toulouse - Amsterdam, Guayaquil - Bogota and Hobart - Sydney.

	Near future (2020+)		Far future (2040+)	
Flight mission	**PP [yr]**	**Net profit [$]**	**PP [yr]**	**Net profit [$]**
FM1: Toulouse - Amsterdam	8.1	$122,791	9.2	$95,089
FM2: Guayaquil - Bogota	3.1	$425,389	2.8	$460,577
FM3: Hobart - Sydney	4.9	$254,978	4.8	$254,851

D.3 Estimated Annual Savings of EAPPS

Based on an average of six flights per day, the annual savings of a A320neo aircraft using EAPPS can be estimated using data from Table 6.9. The estimated results are shown in Table D.7. In addition to that, the savings can also be expressed in equivalent flights, based on the fuel, energy and emissions values of the reference A320neo setup.

This table shows that the adoption of EAPPS can have a positive impact on the natural environment. In the near future (2020+), 4,472.6 tonnes of CO_2 can be saved on a yearly basis, which amounts to roughly 360 equivalent flights. This means that six A320neo aircraft equipped with EAPPS can annually save an equivalent amount of CO_2 emissions produced by a single conventional A320neo aircraft. In the far future (2040+), this number will increase to 585 equivalent flights or 7,276.7 tonnes of CO_2; only four EAPPS-integrated A320neo aircraft are needed to offset the amount of CO_2 emissions produced by one conventional A320neo aircraft. Keep in mind that these values hold for a single A320neo aircraft flying a specific mission from Guayaquil to Bogota, imagine the total savings of a fleet of EAPPS-integrated A320neo aircraft operating throughout the world.

Table D.7: Estimated annual savings and equivalent flights for a single A320neo using EAPPS in the near future (2020+) and the far future (2040+).

	Annual savings		Equivalent flights	
Type	**2020+**	**2040+**	**2020+**	**2040+**
Fuel	1,447.7 t	2,430.5 t	367.0	616.2
Energy	13.1 GWh	18.5 GWh	277.3	392.5
CO_2	4,472.6 t	7,276.6 t	359.8	585.4
H_2O	1,336.1 t	2,448.8 t	270.9	496.5
CO	20.3 t	21.5 t	1,528.5	1,615.9
UHC	240.9 kg	262.8 kg	1,148.2	1,252.6
NO_x	2.4 t	10.5 t	82.0	362.1
Soot	-0.88 kg	2.89 kg	-45.9	151.5

D.4 Discussion

Next to considering the technical feasibility aspects of EAPPS in Chapter 6, an attempt is made to examine the commercial viability of EAPPS and find a stimulus for commercial airlines to adopt hybrid electric propulsion and PV systems.

According to the results in Section D.1, the operating energy costs of EAPPS are significantly lower than for the reference A320neo aircraft, taking price fluctuations into account. This can be a major driver for commercial airlines to integrate EAPPS into their fleet, once the desired technological advancement of batteries and other components is reached.

Also, the ROI performance of PV systems has been investigated in Section D.2. Considering the initial investment and recurring O&M costs of installing photovoltaics, the yearly fuel and energy savings will still result in net profits over the expected lifetime of PV modules (20 years) for all three flight missions. This adds another incentive for commercial airlines to install PV and promote environmental awareness.

Lastly, the annual savings in terms of fuel, energy and emissions were evaluated in Section D.3. On a yearly basis, the savings of a single A320neo flight become much more significant and could make a notable impact on the natural environment.

All in all, these analyses have shown that EAPPS can be considered as one of the solutions to improve the environmental impact of future aviation and create incentives for commercial airlines to adopt this technology. In a hopeful sense, it could bring us one step closer towards a sustainable future.

Bibliography

[1] A. W. X. Ang, "Integrated Performance Analysis Applied on Short-Range Aircraft," Delft University of Technology, Tech. Rep., 2016.

[2] A. W. X. Ang, A. G. Rao, T Kanakis, and W Lammen, "Performance Analysis of an Electrically Assisted Propulsion System for a Short-Range Civil Aircraft," *Journal of Aerospace Engineering*, pp. 1–13, 2018. DOI: 10.1177/0954410017754146.

[3] S. C. Tan, "AE4020 Literature Study: Electrically Assisted Propulsion & Power Systems for Short-Range Missions - Energy Management System Optimisation of Airbus A320," Delft University of Technology, Delft, Tech. Rep. May, 2017.

[4] Airbus Group, "Airbus A320: Aircraft Characteristics Airport and Maintenance Planning," Tech. Rep., 2016, pp. 1–387.

[5] Boeing, "Current Market Outlook: 2016-2035," Tech. Rep., 2016, p. 54. arXiv: arXiv:1011.1669v3.

[6] European Commission, "Flightpath 2050: Europe's Vision for Aviation," *Report of the High Level Group on Aviation Research*, p. 28, 2011. DOI: 10.2777/50266.

[7] National Science and Technology Council, "National Plan for Aeronautics Research and Development and Related Infrastructure," Tech. Rep., 2008, p. 124.

[8] D. S. Lee, G. Pitari, V. Grewe, K. Gierens, J. E. Penner, A. Petzold, M. J. Prather, U. Schumann, A. Bais, T. Berntsen, D. Iachetti, L. L. Lim, and R. Sausen, "Transport Impacts on Atmosphere and Climate: Aviation," *Atmospheric Environment*, vol. 44, no. 37, pp. 1–57, 2009, ISSN: 1352-2310. DOI: 10.1016/j.atmosenv.2009.06.005.

[9] K. Davies, P. Norman, C. Jones, S. Galloway, and M. Husband, "A Review of Turboelectric Distributed Propulsion Technologies for N+3 Aircraft Electrical Systems," in *Proceedings of the Universities Power Engineering Conference*, 2013, ISBN: 9781479932542. DOI: 10.1109/UPEC.2013.6714885.

[10] C. C. Chan, "The State of the Art of Electric, Hybrid, and Fuel Cell Vehicles," *Proceedings of the IEEE*, vol. 95, no. 4, pp. 704–718, 2007, ISSN: 00189219. DOI: 10.1109/JPROC.2007.892489.

[11] L. Lorenz, A. Seitz, H. Kuhn, and A. Sizmann, "Hybrid Power Trains for Future Mobility," in *Paper 1316, Deutscher Luft- und Raumfahrtkongress*, Stuttgart, 2013, pp. 1–17. arXiv: 301316.

[12] National Academies of Sciences, *Commercial Aircraft Propulsion and Energy Systems Research: Reducing Global Carbon Emissions*. Washington, DC: The National Academies Press, 2016, ISBN: 978-0-309-44096-7. DOI: 10.17226/23490.

[13] J. Y. Hung and L. F. Gonzalez, "On Parallel Hybrid-Electric Propulsion System for Unmanned Aerial Vehicles," *Progress in Aerospace Sciences*, vol. 51, pp. 1–17, 2012, ISSN: 03760421. DOI: 10.1016/j.paerosci.2011.12.001.

[14] L. Faleiro, "Beyond the More Electric Aircraft," *Aerospace America, AIAA*, vol. 44, no. September 2005, pp. 35–40, 2006, ISSN: 0740722X.

[15] M. Hepperle, "Electric Flight - Potential and Limitations," NATO Science and Technology Organization, Brussels, Tech. Rep., 2012, pp. 1–30.

[16] C. A. Luongo, P. J. Masson, T. Nam, D. Mavris, H. D. Kim, G. V. Brown, M. Waters, and D. W. Hall, "Next Generation More-Electric-Aircraft: A Potential Application for HTS Superconductors," in *Applied Superconductivity*, vol. 19, 2009, pp. 1055–1068, ISBN: 1051-8223 VO - 19. DOI: 10.1109/TASC.2009.2019021.

[17] A. S. Gohardani, G. Doulgeris, and R. Singh, "Challenges of Future Aircraft Propulsion: A Review of Distributed Propulsion Technology and Its Potential Application for the All Electric Commercial Aircraft," *Progress in Aerospace Sciences*, vol. 47, no. 5, pp. 369–391, 2011, ISSN: 03760421. DOI: 10.1016/j.paerosci.2010.09.001.

[18] M. J. Armstrong, C. A. H. Ross, M. J. Blackwelder, and K. Rajashekara, "Propulsion System Component Considerations for NASA N3-X Turboelectric Distributed Propulsion System," *SAE International Journal of Aerospace*, vol. 5, no. 2, 2012, ISSN: 1946-3901. DOI: 10.4271/2012-01-2165.

[19] D. Blanding, "Subsystem Design and Integration for the More Electric Aircraft," in *25th International Congress of the Aeronautical Sciences*, 2006, p. 8, ISBN: 9781604232271. DOI: doi: 10.2514/6.2007-4828.

[20] G. Abbe and H. Smith, "Technological Development Trends in Solar-Powered Aircraft Systems," *Renewable and Sustainable Energy Reviews*, vol. 60, pp. 770–783, 2016, ISSN: 18790690. DOI: 10.1016/j.rser.2016.01.053.

[21] C. Barchasz, F. Molton, C. Duboc, J. C. Leprêtre, S. Patoux, and F. Alloin, "Lithium/Sulfur Cell Discharge Mechanism: An Original Approach for Intermediate Species Identification," *Analytical Chemistry*, vol. 84, no. 9, pp. 3973–3980, 2012, ISSN: 00032700. DOI: 10.1021/ac2032244.

[22] A. F. Hofmann, D. N. Fronczek, and W. G. Bessler, "Mechanistic Modeling of Polysulfide Shuttle and Capacity Loss in Lithium-Sulfur Batteries," *Journal of Power Sources*, vol. 259, pp. 300–310, 2014, ISSN: 0378-7753. DOI: 10.1016/j.jpowsour.2014.02.082.

[23] A. Fotouhi, D. J. Auger, K. Propp, S. Longo, and M. Wild, "A Review on Electric Vehicle Battery Modelling: From Lithium-ion toward Lithium-Sulfur," *Submitted to Renewable & Sustainable Energy Reviews*, vol. 56, no. 2016, pp. 1008–1021, 2015.

[24] G. Lampič, G. Gotovac, H. Geaney, and C. O. Dwyer, "Comparing the Suitability of Lithium Ion , Lithium Sulfur and Lithium Air Batteries for Current and Future Vehicular Applications," 2016.

[25] OXIS Energy, "Lithium Sulfur Rechargeable Batteries," p. 16, 2016.

[26] N. Imanishi and O. Yamamoto, "Rechargeable Lithium-Air Batteries: Characteristics and Prospects," *Biochemical Pharmacology*, vol. 17, pp. 24–30, 2014, ISSN: 1369-7021. DOI: 10.1016/j.mattod.2013.12.004.

[27] P. G. Bruce, S. A. Freunberger, L. J. Hardwick, and J.-M. Tarascon, "Li-O_2 and Li-S Batteries with High Energy Storage," *Nature Materials*, vol. 11, pp. 19–29, 2011, ISSN: 1476-1122. DOI: 10.1038/nmat3237.

[28] S. Stückl, J. van Toor, and H. Lobentanzer, "VOLTAIR - The All Electric Propulsion Concept Platform – A Vision For Atmospheric Friendly Flight," *28th Congress of the International Council of the Aeronautical Sciences*, pp. 1–11, 2012.

[29] T. Zhang, N. Imanishi, Y. Shimonishi, A. Hirano, Y. Takeda, O. Yamamoto, and N. Sammes, "A Novel High Energy Density Rechargeable Lithium/Air Battery," *Chemical Communications*, vol. 46, no. 10, pp. 1661–3, 2010, ISSN: 1364-548X. DOI: 10.1039/b920012f.

[30] H. Nagata and Y. Chikusa, "A Lithium Sulfur Battery with High Power Density," *Journal of Power Sources*, vol. 264, pp. 206–210, 2014, ISSN: 03787753. DOI: 10.1016/j.jpowsour.2014.04.106.

[31] S. J. Visco, V. Y. Nimon, A. Petrov, K. Pridatko, N. Goncharenko, E. Nimon, L. De Jonghe, Y. M. Volfkovich, and D. A. Bograchev, "Aqueous and Nonaqueous Lithium-Air Batteries Enabled by Water-Stable Lithium Metal Electrodes," *Journal of Solid State Electrochemistry*, vol. 18, no. 5, pp. 1443–1456, 2014, ISSN: 14328488. DOI: 10.1007/s10008-014-2427-x.

[32] M. F. Ozcan, I. Chakraborty, and D. N. Mavris, "Impact of Subsystem Secondary Power Requirements on Gas Turbine Sizing and Performance," *16th AIAA Aviation Technology, Integration, and Operations Conference*, no. June, pp. 1–19, 2016. DOI: 10.2514/6.2016-3146.

[33] X. Xia, "Dynamic Power Distribution Management for All Electric Aircraft," PhD thesis, Cranfield University, 2011.

[34] R. Seresinhe, C. Lawson, A. Shinkafi, and D. Quaglia, "Airframe Systems Power Off-Take Modelling in More-Electric Large Aircraft for Use in Trajectory Optimisation," in *29th International Congress of the Aeronautical Sciences*, 2014, pp. 1–20, ISBN: 3932182804.

[35] A. Faidi, "Effect of Accessory Power Take-Off Variation on a Turbofan Engine Performance," PhD thesis, Air Force Institute of Technology, Ohio, 2012.

[36] I. Chakraborty, D. N. Mavris, M. Emeneth, and A. Schneegans, "An Integrated Approach to Vehicle and Subsystem Sizing and Analysis for Novel Subsystem Architectures," in *Proceedings of the Institution of Mechanical Engineers, Part G: Journal of Aerospace Engineering*, vol. 230, 2016, pp. 496–514. DOI: 10.1177/0954410015594399.

[37] M. Provost, "The More Electric Aero-Engine: A General Overview from an Engine Manufacturer," in *International Conference on Power Electronics Machines and Drives*, vol. 2002, 2002, pp. 246–251, ISBN: 0 85296 747 0. DOI: 10.1049/cp:20020122.

[38] G. Romeo, F. Borello, G. Correa, and E. Cestino, "ENFICA-FC: Design of Transport Aircraft Powered by Fuel Cell & Flight Test of Zero Emission 2-Seater Aircraft Powered by Fuel Cells Fueled by Hydrogen," *International Journal of Hydrogen Energy*, vol. 38, no. 1, pp. 469–479, 2013, ISSN: 03603199. DOI: 10.1016/j.ijhydene.2012.09.064.

[39] Honeywell, "More Electric Architecture Vision," pp. 1–5, 2007.

[40] C. Huynh, L. Zheng, and D. Acharya, "Losses in High Speed Permanent Magnet Machines Used in Microturbine Applications," *Journal of Engineering for Gas Turbines and Power*, vol. 131, no. 2, p. 022 301, 2009, ISSN: 07424795. DOI: 10.1115/1.2982151.

[41] J. E. Vrancik, "Prediction of Windage Power Loss in Alternators," NASA Lewis Research Center, Cleveland, Ohio, Tech. Rep. October, 1968.

[42] P. Andrada, M. Torrent, J. I. Perat, and B. Blanqué, "Power Losses in Outside-Spin Brushless DC Motors," *Renewable Energy & Power Quality Journal (RE & PQJ)*, vol. 1, no. 2, pp. 507–511, 2004.

[43] K. R. Shah, "Measurement of Stray Load Loss of DC Machines," PhD thesis, University of Missouri, 1965.

[44] E. De Kreij, "Comparative Techno-Economic Analysis Between a Novel Series Hybrid Powertrain and Conventional Series Hybrid Powertrain," Delft University of Technology, Tech. Rep., 2014.

[45] A. Hughes and B. Drury, *Electric Motors and Drives: Fundamentals, Types and Applications*, 4th. 2013.

[46] Nidec Corporation, *Basic Motor Information*, 2017.

[47] Y. Miyairi, C. Perullo, and D. N. Mavris, "A Parametric Environment for Weight and Sizing Prediction of Motor/Generator for Hybrid Electric Propulsion," in *51st AIAA/SAE/ASEE Joint Propulsion Conference*, 2015, pp. 1–19, ISBN: 978-1-62410-321-6. DOI: 10.2514/6.2015-3887.

[48] G. Ramírez-Díaz, V. Nadal-Mora, and J. Piechocki, "Descriptive Analysis of Viability of Fuel Saving in Commercial Aircraft Through the Application of Photovoltaic Cells," *Renewable and Sustainable Energy Reviews*, vol. 51, pp. 138–152, 2015, ISSN: 18790690. DOI: 10.1016/j.rser.2015.06.008.

[49] V. K. Vashishtha, A. Kumar, R. Makade, and S. Lata, "Solar Power the Future of Aviation Industry," *International Journal of Engineering Science and Technology (IJEST)*, vol. 3, no. 3, pp. 2051–2058, 2011.

[50] K. Jäger, O. Isabella, A. H. Smets, R. A. Van Swaaij, and M. Zeman, *Solar Energy: Fundamentals, Technology and Systems*. Delft, 2014, p. 404.

[51] J.-G. Werthen, "Climate and Trends in Solar Cell Technologies," *ECN Magazine*, 2010.

[52] National Renewable Energy Laboratory, *Best Research Cell Efficiencies*, 2016.

[53] X. Z. Gao, Z. X. Hou, Z. Guo, R. F. Fan, and X. Q. Chen, "The Equivalence of Gravitational Potential and Rechargeable Battery for High-Altitude Long-Endurance Solar-Powered Aircraft on Energy Storage," *Energy Conversion and Management*, vol. 76, pp. 986–995, 2013, ISSN: 01968904. DOI: 10.1016/j.enconman.2013.08.023.

[54] F. Fazelpour, M. Vafaeipour, O. Rahbari, and R. Shirmohammadi, "Considerable Parameters of Using PV Cells for Solar-Powered Aircrafts," *Renewable and Sustainable Energy Reviews*, vol. 22, pp. 81–91, 2013, ISSN: 13640321. DOI: 10.1016/j.rser.2013.01.016.

[55] A. K. Sehra and W. Whitlow, "Propulsion and Power for 21st Century Aviation," *Progress in Aerospace Sciences*, vol. 40, no. 4-5, pp. 199–235, 2004, ISSN: 03760421. DOI: 10.1016/j.paerosci.2004.06.003.

[56] U.S. Department of Energy, "Fuel Cell Technical Team Roadmap," *U.S. Drive Partnership*, no. June, p. 26, 2013. DOI: 10.2172/1220127.

[57] Airbus Group, *Airbus: Orders & Deliveries*, 2017.

[58] P. Jackson and Fellowship of the Royal Aeronautical Society (FRAeS), *IHS Jane's All the World's Aircraft: A320*. IHS, 2016.

[59] European Aviation Safety Agency, "Type-Certificate Data Sheet No. EASA.A.064: Airbus A318 - A319 - A320 - A321," Blagnac, France, Tech. Rep., 2017, pp. 1–138.

[60] CFM International, *CFM Engines*, 2017.

[61] European Aviation Safety Agency, "Type-Certificate Data Sheet No. E.110: LEAP-1A & LEAP-1C Series Engine," Paris, France, Tech. Rep. December, 2016, pp. 1–13.

[62] D. Scholz, R. Seresinhe, I. Staack, and C. Lawson, "Fuel Consumption Due to Shaft Power Off-Takes from the Engine," *4th International Workshop on Aircraft System Technologies (AST 2013), 23-24 April 2013, Hamburg, Germany*, pp. 169–179, 2013.

[63] R. Schleicher, *Wing Anti-Icing Model*, 2003.

[64] P. Sforza, "Refined Weight and Balance Estimate," in *Commercial Airplane Design Principles*, 2014, ch. 8, pp. 301–347, ISBN: 9780124199538. DOI: 10.1016/B978-0-12-419953-8.00008-5.

[65] P. P. Walsh and P. Fletcher, "Dimensionless, Quasidimensionless, Referred and Scaling Parameter Groups," in *Gas Turbine Performance*, 2nd, 2008, ch. 4, pp. 143–158.

[66] J. D. Singleton and W. T. Yeager, "Important Scaling Parameters for Testing Model-Scale Helicopter Rotors," *20th AIAA Advanced Measurement and Ground Testing Technology Conference*, no. AIAA-98-2881, pp. 1–11, 1998, ISSN: 0021-8669. DOI: 10.2514/2.2639.

[67] E. R. Rademaker, "Scaling of Compressor and Turbine Maps on Basis of Equal Flow Mach Numbers and Static Flow Parameters," Tech. Rep., 2012.

[68] J. Kurzke, "GasTurb 9 User's Manual," Tech. Rep., 2001.

[69] International Civil Aviation Organization, "Environmental Protection: ICAO Annex 16 Volume II, including Amendment 8 (CAEP/8)," International Civil Aviation Organization, Tech. Rep. July, 2008.

[70] T. J. Mulder, *AE4421 Air Traffic Noise and Emissions*, Delft, 2012.

[71] G. V. Brown, "Weights and Efficiencies of Electric Components of a Turboelectric Aircraft Propulsion System," *AIAA Aerospace Sciences Meeting including the New Horizons Forum and Aerospace Exposition*, no. January, pp. 1–18, 2011. DOI: 2011-225.

[72] H. Kuhn, A. Seitz, L. Lorenz, A. T. Isikveren, and A. Sizmann, "Progress and Perspectives of Electric Air Transport," in *28th Congress of the International Council of the Aeronautical Sciences 2012, ICAS 2012*, vol. 6, 2012, pp. 4886–4899, ISBN: 9781622767540 (ISBN).

[73] N. Madavan, "Hybrid-Electric and Distributed Propulsion Technologies for Large Commercial Air Transports : A NASA Perspective "Advanced Air Transport Technology Project"," *Presentation at Special Session on Future Electric Aircraft-Systems*, 2015.

[74] J. Welstead and J. L. Felder, "Conceptual Design of a Single-Aisle Turboelectric Commercial Transport with Fuselage Boundary Layer Ingestion," in *54th AIAA Aerospace Sciences Meeting*, 2016, pp. 1–34, ISBN: 978-1-62410-393-3. DOI: 10.2514/6.2016-1027.

[75] C. Bowman, *NASA Investments in Electric Propulsion Technologies for Large Commercial Aircraft*, 2016.

[76] C. E. Lents, L. W. Hardin, J. Rheaume, and L. Kohlman, "Parallel Hybrid Gas-Electric Geared Turbofan Engine Conceptual Design and Benefits Analysis," in *52nd AIAA/SAE/ASEE Joint Propulsion Conference*, 2016, pp. 1–12, ISBN: 978-1-62410-406-0. DOI: 10.2514/6.2016-4610.

[77] F. Anton, *Siemens - Electric Drive System for Aircraft*, Hirschaid, 2017.

[78] M. K. Bradley and C. K. Droney, "Subsonic Ultra Green Aircraft Research: Phase II – Volume II – Hybrid Electric Design Exploration," Tech. Rep., 2015, p. 207. DOI: 2060/20150017039.

[79] A. Nawawi, C. F. Tong, S. Yin, A. Sakanova, Y. Liu, Y. Liu, M. Kai, K. Y. See, K. J. Tseng, R. Simanjorang, C. J. Gajanayake, and A. K. Gupta, "Design and Demonstration of High Power Density Inverter for Aircraft Applications," *IEEE Transactions on Industry Applications*, vol. 53, no. 2, pp. 1168–1176, 2017, ISSN: 00939994. DOI: 10.1109/TIA.2016.2623282.

[80] O. Schmitz and M. Hornung, "Unified Applicable Propulsion System Performance Metrics," *Journal of Engineering for Gas Turbines and Power*, vol. 135, no. November 2013, pp. 1–9, 2013, ISSN: 07424795. DOI: 10.1115/GT2013-95724.

[81] S. Datta, "Switched Reluctance Motor," Yanam, India, 2014.

[82] K.-P. Kairies, *Battery Storage Technology Improvements and Cost Reductions to 2030*, Aachen, 2017.

[83] D. Novak, "Design of a Li-Ion Battery Pack Emulator," Universidad de Oviedo, Tech. Rep., 2015.

[84] D. Verstraete, A. Gong, D. D. Lu, and J. L. Palmer, "Experimental Investigation of the Role of the Battery in the AeroStack Hybrid, Fuel-Cell-Based Propulsion System for Small Unmanned Aircraft Systems," *International Journal of Hydrogen Energy*, vol. 40, no. 3, pp. 1598–1606, 2015, ISSN: 03603199. DOI: 10.1016/j.ijhydene.2014.11.043.

[85] Mathworks Simscape Power Systems, *Generic Battery Model*, 2017.

[86] P. Y. Yi, L. F. Peng, X. M. Lai, Z. Q. Lin, and J. Ni, "Performance Improvement of Wave-Like PEMFC Stack with Compound Membrane Electrode Assembly," *Fuel Cells*, vol. 12, no. 6, pp. 1019–1026, 2012, ISSN: 16156846. DOI: 10.1002/fuce.201200097.

[87] PowerCell Sweden AB, *PowerCell MS-100: Mobile System (50-100 kW) Data Sheet*, Gothenburg, 2017.

[88] J. Larminie and A. Dicks, *Fuel Cell Systems Explained*, 2nd. Wiley, 2003, p. 406, ISBN: 047084857X. DOI: 10.1002/9781118878330. arXiv: arXiv:1011.1669v3.

[89] C. Kunusch, P. Puleston, and M. Mayosky, "Sliding-Mode Control of PEM Fuel Cells," in, 1st, Springer-Verlag London, 2012, ch. 2, ISBN: 978-1-4471-2430-6. DOI: 10.1007/978-1-4471-2431-3.

[90] V. Ramani, "Fuel Cells," *The Electrochemical Society Interface*, pp. 41–44, 2006.

[91] D. Verstraete, K. Lehmkuehler, A. Gong, J. R. Harvey, G. Brian, and J. L. Palmer, "Characterisation of a Hybrid, Fuel-Cell-Based Propulsion System for Small Unmanned Aircraft," *Journal of Power Sources*, vol. 250, no. 2014, pp. 204–211, 2014, ISSN: 03787753. DOI: 10.1016/j.jpowsour.2013.11.017.

[92] A. Datta and W. Johnson, "Requirements for a Hydrogen Powered All-Electric Manned Helicopter," *American Institute of Aeronautics and Astronautics*, no. September 2012, pp. 1–28, 2012. DOI: doi:10.2514/6.2012-5405.

[93] European Space Agency (ESA), *Solar Plane Flying High*, 2013.

[94] Solvay, "The Future Starts Today - Introducing Solar Impulse 2," 2014.

[95] P. Prozeller, *Solar Impulse HB-SIB: Pushing the Boundaries in Chemistry*, 2014.

[96] Solar Impulse, *Solar Cells*, 2016.

[97] Solvay, *Halar ECTFE: Films for Photovoltaic Front-Sheets*, 2016.

[98] ——, *Solef PVDF: Typical Properties*, 2016.

[99] D. D. Smith, P. J. Cousins, A. Masad, A. Waldhauer, S. Westerberg, M. Johnson, X. Tu, T. Dennis, G. Harley, G. Solomon, S. Rim, M. Shepherd, S. Harrington, M. Defensor, A. Leygo, P. Tomada, J. Wu, T. Pass, L. Ann, L. Smith, N. Bergstrom, C. Nicdao, P. Tipones, and D. Vicente, "Generation III High Efficiency Lower Cost Technology: Transition to Full Scale Manufacturing," in *Conference Record of the IEEE Photovoltaic Specialists Conference*, 2012, pp. 1594–1597, ISBN: 9781467300643. DOI: 10.1109/PVSC.2012.6317899.

[100] F. H. Alharbi and S. Kais, "Theoretical Limits of Photovoltaics Efficiency and Learned from Photosynthesis and Quantum Coherence," vol. 43, pp. 1073–1089, 2014, ISSN: 1364-0321. DOI: 10.1016/j.rser.2014.11.101. arXiv: arXiv:1402.1923v1.

[101] H. B. Vika, "Modelling of Photovoltaic Modules with Battery Energy Storage in Simulink/Matlab," Norwegian University of Science and Technology, Tech. Rep. June, 2014.

[102] International Civil Aviation Organization, "ICAO Aircraft Engine Emissions Databank," Tech. Rep., 2017.

[103] T. F. Johnson, *Electric Green Taxiing System (EGTS) for Aircraft*, 2014.

[104] Safran, "Electric Taxiing by Safran - Environmental Benefits," Tech. Rep., 2017.

[105] G. Warwick, *Commercial Aviation - NASA Studies Early Option For Hybrid-Electric Airliners*, 2016.

[106] Airbus Customer Services, "Getting to Grips with Aircraft Performance," *The International Standard Atmosphere*, pp. 11–16, 2002. DOI: 10.1017/CBO9781107415324.004.

[107] P. Van Der Geest, "The AMAAI Modelling Toolset for the Analysis of In-Trail Following Dynamics - Deliverable D2: Description and User Guide," Netherlands Aerospace Centre (NLR), Tech. Rep. March, 2002, pp. 1–74.

[108] GasTurb GmbH, "GasTurb 12 - Design and Off-Design Performance of Gas Turbines," Tech. Rep., 2015. DOI: 10.1017/CBO9781107415324.004. arXiv: arXiv:1011.1669v3.

[109] A. J. Colozza, "NASA/CR-2003-212084: Convective Array Cooling for a Solar Powered Aircraft," Brook Park, Ohio, Tech. Rep., 2003, p. 23.

[110] ITACA, *Part 3: Calculating Solar Angles*, 2017.

[111] W. B. Stine and M. Geyer, *Power From the Sun*. 2001.

[112] D. Simos, *Piano-X*, 2017.

[113] S. Ackert, "Engine Maintenance Management," 2015.

[114] B. Fehrm, *Fundamentals of Airliner Performance, Part 6; The Engine*, 2015.

[115] G. Warwick and T. Osborne, *Airbus E-Fan X To Pave Way For Electric Regional Aircraft*, 2017.

[116] Battery University, *Elevated Self-Discharge*, 2017.

[117] Panasonic Corporation, *Panasonic NCR20700A Data Sheet*, 2017.

[118] J. C. Lagarias, J. A. Reeds, M. H. Wright, and P. E. Wright, "Convergence Properties of the Nelder-Mead Simplex Method in Low Dimensions," *SIAM Journal of Optimization*, vol. 9, no. 1, pp. 112–147, 1998.

[119] SunPower Corporation, *Maxeon™ Gen III Solar Cells Data Sheet*, 2016.

[120] Mathworks Simscape Power Systems, *PV Array Model*, 2016.

[121] PowerCell Sweden AB, *PowerCell MS-20: Mobile System (10-20 kW) Data Sheet*, Gothenburg, 2017.

[122] ——, *PowerCell S2: Scalable (5-35 kW) Data Sheet*, Gothenburg, 2017.

[123] O. S. Joshua, G. J. Ejura, V. E. Essien, I. B. Olokungbemi, A. Y. Oluwaseun, and E. P. Okon, "Fuel Cell Types and Factors Affecting Them," vol. 2, no. 8, pp. 11–14, 2014.

[124] B. Xu, A. Oudalov, A. Ulbig, G. Andersson, and D. Kirschen, "Modeling of Lithium-Ion Battery Degradation for Cell Life Assessment," *IEEE Transactions on Smart Grid*, no. June 2016, pp. 1–1, 2016, ISSN: 1949-3053. DOI: 10.1109/TSG.2016.2578950. arXiv: ''''.

[125] M. Mújica, M. Soler, and I. Flores, "Development and Simulation of a New Scheme for the Aircraft Cleaning Service," in *European Modeling and Simulation Symposium (EMSS) 2013*, 2013, ISBN: 9788897999225.

[126] K. Seeckt and D. Scholz, "Jet Versus Prop, Hydrogen Versus Kerosene for a Regional Freighter Aircraft," p. 12, 2009.

[127] Airbus Training, *A320 Flight Crew Operating Manual: Electrical*, 2016.

[128] iCalc Inc., *SketchAndCalc - Area Calculator*, 2017.

[129] G. Renouard-Vallet, M. Saballus, P. Schumann, J. Kallo, K. A. Friedrich, and H. Müller-Steinhagen, "Fuel Cells for Civil Aircraft Application: On-Board Production of Power, Water and Inert Gas," *Chemical Engineering Research and Design*, vol. 90, no. 1, pp. 3–10, 2012, ISSN: 02638762. DOI: 10.1016/j.cherd.2011.07.016.

[130] K. Kunze and O. Kircher, *Cryo-Compressed Hydrogen Storage*, Oxford, 2012.

[131] Institute of Aviation, "D4.2 Operating Cost Analysis," Tech. Rep., 2008, pp. 1–104.

[132] Airbus, "Global Market Forecast: Growing Horizons 2017/2036," Tech. Rep., 2017, pp. 1–128.

[133] California Air Resources Board, "Joint Agency Staff Report on Assembly Bill 8: Assessment of Time and Cost Needed to Attain 100 Hydrogen Refueling Stations in California," California, Tech. Rep. December, 2015.

[134] Energy Information Administration, "Annual Energy Outlook 2018 - With Projections to 2050," Washington, DC, Tech. Rep., 2018. DOI: DOE/EIA-0383(2017). arXiv: arXiv:1011.1669v3.

[135] MIT Global Airline Industry Program, *Airline Data Project*, 2017.

[136] SunPower Corporation, *SunPower Cell Price Sheet*, 2017.

[137] WholeSaleSolar, *Four Star Solar MC4 10 AWG - 100' Cable*, 2018.

[138] FreeCleanSolar, *Enphase Energy IQ6-60 Micro-Inverter 240 Watt 240V*, 2018.

[139] R. Fu, D. Feldman, R. Margolis, M. Woodhouse, and K. Ardani, "U.S. Solar Photovoltaic System Cost Benchmark: Q1 2017," Tech. Rep. September, 2017. DOI: 10.2172/1390776.

[140] Electric Power Research Institute, "Budgeting for Solar PV Plant Operations & Maintenance: Practices and Pricing," Tech. Rep. December, 2015, p. 11.